The Dissertation Committee for Oyinkansola Modupe Ajayi Certifies that this is the approved version of the following dissertation:

Numerical Simulation and Interpretation of Neutron-Induced Gamma-Ray Spectroscopy Measurements

Committee:

Carlos Torres-Verdín, Supervisor

Ekwere J. Peters

William E. Preeg

Erich A. Schneider

Kamy Sepehrnoori

Numerical Simulation and Interpretation of Neutron-Induced Gamma-Ray Spectroscopy Measurements

by

Oyinkansola Modupe Ajayi, B.S.; M.S.E.

Dissertation

Presented to the Faculty of the Graduate School of

The University of Texas at Austin

in Partial Fulfillment

of the Requirements

for the Degree of

Doctor of Philosophy

The University of Texas at Austin

December 2015

Dedication

To my family, thank you for your unwavering support, countless sacrifices, and love.

Acknowledgements

The work reported in this dissertation was funded by University of Texas at Austin Research Consortium on Formation Evaluation, jointly sponsored by Anadarko, Aramco, Baker-Hughes, BG, BHP Billiton, BP, Chevron, COSL, ConocoPhillips, DEA Deutsche Erdoel AG, Det Norske, ENI, ExxonMobil, Halliburton, Hess, Maersk Oil, Paradigm, Petrobras, PTTEP, Repsol, Schlumberger, Shell, Southwest Energy, Statoil, TOTAL, Weatherford, Wintershall and Woodside Petroleum Limited.

Numerical Simulation and Interpretation of Neutron-Induced Gamma-Ray Spectroscopy Measurements

Oyinkansola Modupe Ajayi, Ph.D.

The University of Texas at Austin, 2015

Supervisor: Carlos Torres-Verdín

Neutron-induced spectroscopy measurements are commonly used to quantify in-situ elemental and mineral compositions of rocks from the processing of measured gamma-ray energy spectra. However, geometrical effects on measured spectroscopy logs, such as thin beds, dipping beds, and deviated well trajectories, can cause shoulder-bed averaging that compromises the assessment of true layer elemental and mineral compositions. Traditional methods of interpreting neutron-induced gamma-ray spectroscopy measurements typically neglect such shoulder-bed averaging effects in the estimation of elemental and mineral compositions. Monte Carlo methods accurately reproduce borehole and formation geometrical effects on spectroscopy measurements but are extremely time consuming and impractical for use in routine interpretation. Reliable measurement interpretation must therefore begin with the development of a fast and accurate forward simulation method that explicitly incorporates measurement physics, borehole, tool, and formation geometry.

This dissertation introduces a new algorithm to rapidly simulate elemental and

mineral compositions from neutron induced spectroscopy measurements. The algorithm utilizes neutron-gamma ray spatial sensitivity functions to account for environmental and three-dimensional (3D) effects of formation porosity, fluids, dipping beds, thin beds, and arbitrary well trajectories. Simulations assume a logging-while-drilling (LWD) spectroscopy tool furbished with a 14-MeV pulsed-neutron source in the interpretation of gamma ray spectra obtained from high energy inelastic neutron scattering and thermal neutron capture. Results obtained with the rapid simulation method are benchmarked against rigorous Monte Carlo spectroscopy calculations for synthetic conventional and unconventional thinly-bedded reservoirs penetrated by vertical and high angle/horizontal (HA/HZ) wells. The fast simulation method yields calculations in approximately 1e6 the time required by Monte Carlo simulations, with an average difference below 5% between Monte Carlo and fast simulated logs.

An inversion-based interpretation method is next introduced to accurately evaluate mineral concentrations from measured spectroscopy elemental logs based on the analytical relationship between elements and minerals through their chemical formulas. In the presence of geometrical effects, spectroscopy elemental and mineral logs are corrected for shoulder-bed averaging by the inclusion of spatial sensitivity maps, which account for such geometrical effects, in the inversion-based interpretation. Calculations are performed with both inelastic and capture gamma-ray spectroscopy measurements which arise from high-energy inelastic neutron scattering and low-energy thermal neutron capture, respectively. This strategy provides two sets of data that can ascertain chemical

elements or minerals detectable in only one measurement mode and also independently validates estimated elemental and mineral compositions. In laminated formations, where layer thicknesses are below the vertical resolution of the tool, it is impossible to quantify layer properties with inversion methods. An additional interpretation method based on a new spectroscopy mixing law is therefore developed to estimate elemental and mineral compositions within individual laminae.

The new inversion-based interpretation methods are successfully implemented in diverse synthetic and field cases with varying lithology types and well trajectories including vertical and HA/HZ wells. Results show that the developed methods reduce shoulder-bed averaging effects on measured spectroscopy logs by as much as 0.4 yield fraction, 0.17 weight fraction, and 0.34 mineral volume fraction. Finally, a new spectroscopy-based petrophysical interpretation method is introduced that utilizes estimated mineralogy to overcome the common assumption of homogeneous lithology in measured porosity logs, thereby improving the estimation of porosity and water saturation. Inclusion of shoulder-bed averaging effects on spectroscopy mineral logs also increases the accuracy of spectroscopy-based petrophysical interpretation.

Table of Contents

List of Tables

List of Figures

Figure 4.10: Comparison of inverted layer elemental weight concentrations (blue solid lines) to model values (red solid lines) for Synthetic Case No. 2. Panel (a) displays a cumulative plot of MCNP-simulated inelastic elemental weight concentrations shown as purple solid lines in panels (c) to (l). Panel (b) exhibits a cumulative plot of inverted elemental weight concentrations shown as blue solid lines in panels (c) to (l). Black dashed lines, black uncertainty bars, and purple solid lines describe the initial guess of the inversion, 95% confidence interval, and MCNP-simulated elemental weight concentrations, respectively; $C_{formation}$, $C_{kerogen}$, Na, S, Mg, Al, Si, K, Ca, and Fe represent carbon present in the formation, carbon present in kerogen, sodium, sulfur, magnesium, aluminum, silicon, potassium, calcium, and iron, respectively, while I to IX identify distinct layers in the synthetic case. 188

Figure 4.13: Comparison of inverted layer elemental relative yields (blue solid lines) to model values (red solid lines) for Synthetic Case No. 4. Panel (a) displays a cumulative plot of MCNP-simulated capture elemental relative yields shown as purple solid lines in panels (c) to (i). Panel (b) exhibits a cumulative plot of inverted elemental relative yields shown as blue solid lines in panels (c) to (i). Black dashed lines, black uncertainty bars, purple solid lines, and magenta solid lines describe the initial guess of the inversion, 95% confidence interval, MCNP-simulated, and reconstructed elemental relative yields, respectively; Mg, Al, Si, S, K, Ca, and Fe are the elements magnesium, aluminum, silicon, sulfur, potassium, calcium, and iron, respectively; I to V identify distinct layers in the synthetic case, while A to D identify laminations within layers.191

Chapter 1: Introduction

Quantifying in-situ elemental and mineral compositions is a fundamental task in formation evaluation because it can impact practically every other petrophysical interpretation step, including the estimation of matrix properties, porosity, and water saturation. Spectroscopy well-log measurements have been used for more than 30 years to assess in-situ elemental and mineral compositions reliably through the analysis of measured neutron-induced gamma-rays with respect to energy. The recent introduction of spectroscopy measurements into a 14-MeV pulsed neutron logging-while-drilling (LWD) tool facilitates well-log-based lithology evaluation in the complex formation geometries and well trajectories that are typically drilled with LWD tools. However, these complex environments are subject to significant geometrical effects, such as shoulder-bed averaging, that current spectroscopy interpretation methods do not address.

This dissertation introduces efficient numerical methods that improve estimations of elemental and mineral compositions by correcting geometrical effects on measured spectroscopy logs through the application of borehole measurement physics and inverse theory. These methods are used to establish accurate, spectroscopy-based, petrophysical-interpretation workflows via joint interpretation of improved spectroscopy measurements with nuclear and resistivity logs. In this chapter, I review relevant literature in the field of spectroscopy logging, conventional interpretation methods, and limitations of these interpretation methods as a reference to advance the interpretation of spectroscopy logs. The objectives, methods, and outline of the dissertation are also described in this chapter.

1.1 BACKGROUND

Spectroscopy includes the acquisition and interpretation of measured neutron-induced gamma rays. Neutron-induced gamma rays arise from nuclear interactions between source neutrons and subsurface elemental atoms. These interactions result in an atomic nucleus in an excited state that decays back into its ground state through the emission of gamma rays.

Measured gamma rays can be analyzed within specific energy intervals, in the form of gamma-ray spectra, to quantify formation elemental concentrations based on the distinct gamma- ray spectrum of each element. The two major nuclear interactions that give rise to gamma rays used in spectroscopy interpretation include high-energy inelastic neutron scattering and low-energy thermal neutron capture. These two distinct nuclear interactions result in two sets of spectroscopy measurement modes: inelastic and capture. Some elements have discernable cross sections and consequently useable spectra in only one of these measurement modes. For example, carbon and oxygen are detectable in the inelastic mode alone, whereas hydrogen and chlorine are discernible solely in the capture mode (Westaway et al., 1980; Pemper et al., 2006; Radtke et al., 2012). In pulsed neutron tools, inelastic and capture spectra are typically differentiated through the use of timed gate sections based on the assumption that gamma rays within the early time section of the neutron burst are inelastic and late time sections record capture measurements. However, due to the existence of some capture contribution, even in the early neutron burst time segment, late thermal capture spectra are usually used to correct early time inelastic spectra of background capture spectra contributions (Hertzog et al., 1978).

Elements routinely measured in spectroscopy tools are hydrogen (H), chlorine (Cl), silicon (Si), aluminum (Al), calcium (Ca), magnesium (Mg), iron (Fe), potassium (K), titanium (Ti), sulfur (S), oxygen (O), carbon (C), and gadolinium (Gd) (Westaway et al., 1980; Neville et al., 2005; Pemper et al., 2006; Radtke et al., 2012). Aluminum is difficult to measure directly due to its strong linear dependence with respect to iron, and it is commonly modeled from other measured elements (Herron and Herron, 1996; Pemper et al., 2006). Silicon, calcium, magnesium, iron, potassium, sulfur, and aluminum are the most relevant elements in lithologic interpretation because they are typically constituents of only rock-forming minerals (Hertzog, 1989; Neville et al., 2005). Hydrogen and chlorine are related to porosity and salinity responses, respectively, whereas gadolinium and titanium are present in trace amounts in clay minerals. Spectroscopy tools have limited applications in the assessment of porosity (through the analysis of capture hydrogen and rock-formation elemental spectra), salinity (through the analysis of capture chlorine and hydrogen elemental spectra), and hydrocarbon saturation (through the analysis of inelastic carbon and oxygen elemental spectra) (Hertzog et al., 1978; Gilchrist et al., 1982; Schweitzer et al., 1984). The reliability of such assessments is compromised by the presence of hydrogen, chlorine, carbon, and oxygen outside of saturating fluids, and these methods are not routinely used in petrophysical interpretation.

Improvements in the robustness of pulsed neutron technology (Neville et al., 2005; Weller et al., 2005; Radtke et al., 2012) permitted the introduction of 14-MeV pulsed neutron sources into LWD tools for geochemical logging of spectroscopy measurements. LWD tools present several advantages over wireline tools because they are sturdy and can log in any direction and at high deviation angles. They also usually

acquire azimuthal images as the tool rotates, and they are less affected by hole conditions than are wireline tools. Several other measurements alongside spectroscopy are co-located at the collar of the LWD tool (Weller et al., 2005), which facilitates integration of spectroscopy with other borehole measurements. In LWD spectroscopy field measurements, low signal-to-noise ratios are recorded at the long-spaced detector due to low count rates. Low signal-to-noise ratios are also measured in the inelastic spectra because the energy cross sections that govern gamma ray production are extremely small for inelastic measurements (Ellis et al., 2007). LWD spectroscopy field measurements are therefore only provided in the capture-spectra mode of the short-spaced gamma-ray detector, but this limits the interpretation of certain minerals consisting entirely of inelastic elements (Weller et al., 2005).

Due to the existence of a unique gamma-ray spectrum for each element, measured gamma-ray spectra can be interpreted to determine formation elemental compositions as elemental yields and weight concentrations. Elemental yields are commonly interpreted through the spectral fitting of total measured spectra to experimentally predetermined standard elemental and tool spectra. Spectral fitting is implemented in a linear least-squares optimization algorithm to estimate yields as the fractional contribution of each standard spectrum to the total measured spectrum. The total measured spectrum is expressed as

$$d_z = y_1 s_{z1} + y_2 s_{z2} + y_3 s_{z3} + \ldots + y_m s_{zm} + \varepsilon_z$$
$$d_z = \left(\sum_{i=1}^{m} y_i s_{zi} \right) + \varepsilon_z \quad , \qquad (1.1)$$

where subscript *z* designates the index of each spectral energy data channel for *v* spectral energy data channels, and subscript *i* designates the index of each element for *m*

elements; d_z is the measured data spectrum in the z^{th} spectral energy data channel, y_i is the yield of measured element i, s_{zi} is the elemental spectral standard for the i^{th} element in the z^{th} spectral energy data channel, and ε_z is the inherent uncertainty of the spectral fit in each z^{th} spectral energy data channel.

A solution of the above linear system of equation via a weighted least squares method is given by

$$\mathbf{y} = \left[\left(\mathbf{S}^T \mathbf{W}_d \mathbf{S} \right)^{-1} \mathbf{S}^T \mathbf{W}_d \right] \mathbf{m} \quad , \qquad \mathbf{y} = \mathbf{E}\,\mathbf{m} \tag{1.2}$$

where **S** is a spectral matrix composed of s_{zi} standards (v x m), **y** is the vector of elemental yields (m x 1), $\mathbf{W}_d$ is a data-weighting matrix (v x v), **m** is the vector of measured spectrum data (v x 1), and **E** is the estimator matrix (m x n) (Hertzog, 1978; Galford and Hertzog, 1989; Pemper et al., 2006). Note that in this formulation, the tool is defined as an additional element, i, in order to remove tool spectra contributions from spectroscopy measurements. Complications in this method arise due to underdetermined problems where the number of spectral standards is lower than the number of estimated elemental yields. Additional complexities may arise from errors in elemental and tool spectra standards that propagate into estimations of elemental yields and from the assumption that predefined spectra standards contribute to measured spectra. Spectral fitting methods are further complicated by low count rates, poor detector resolution, and overlapping elemental spectral peaks.

Estimated elemental yields are converted into elemental weights with a weight-balance closure condition achieved through an oxide closure model. The closure model accounts for unmeasured formation rock elements such as hydrogen, carbon, and oxygen

by their correlation with measured elements in minerals often encountered in the sedimentary environment (Galford and Hertzog, 1989; Grau et al., 1989, 1990; Hertzog et al., 1989; Galford et al., 2009). The implementation of closure normalization assumes that the sum of these minerals is unity by

$$F\sum_{i=1}^{m}\frac{X_i y_i}{Se_i}=1, \qquad (1.3)$$

where X_i is a factor used to account for the weights of elements that are not measured but are associated with element i, and Se_i is a known relative detection sensitivity of element i to the production of gamma rays. F is a depth-varying normalization factor that accounts for the variability of neutron flux due to changes in environmental parameters, as can be calculated through the constraint in equation 1.3. Elemental weights, M_i, can then be estimated through

$$M_i = F\frac{y_i}{Se_i}. \qquad (1.4)$$

Spectroscopy interpretation also comprises the estimation of mineralogy from elemental concentrations. Such interpretation can accurately quantify complex lithologies consisting of several minerals in varying compositions based on the direct relationship between elements and minerals through their chemical formulas. Commercial, elemental-based mineralogic interpretations vary from one tool to another, but they all typically utilize empirical methods based on core calibration (Herron and Herron, 1996; Pemper et al., 2006) or probabilistic element- to-mineral transforms (Galford et al., 2009; Eslinger and Boyle, 2013). The conventional spectroscopy interpretation workflow for the estimation of elemental and mineral compositions from measured gamma-ray spectra is summarized in Figure 1.1.

Several existing petrophysical-interpretation algorithms quantify matrix properties, porosity, and saturations, but these methods seldom apply spectroscopy measurements (Gonçalves et al., 1995; Cuddy, 2000; Liu et al., 2007; Sanchez-Ramirez et al., 2009; Heidari et al., 2012; Ijasan et al., 2013). Existing spectroscopy-based petrophysical-interpretation techniques include probabilistic error minimization that uses elemental logs as well as other logging data to estimate mineralogy, porosity, and saturations (Galford et al., 2009). Other approaches quantify matrix density, density porosity, matrix neutron response, matrix-adjusted neutron porosity, total porosity, and permeability on the basis of empirical correlations of spectroscopy-derived elemental weight and mineral data (Herron and Herron, 2000; Herron et al., 2002; ZuoAn et al., 2010).

Spectroscopy measurements can be modeled numerically by solving the coupled neutron and gamma-ray transport Boltzmann equation for inelastic neutron scattering and thermal neutron capture (Lewis and Miller, 1993). Although this technique is accurate, it is very slow and is not robust enough to handle complex geometries. Monte Carlo techniques also provide accurate numerical spectroscopy solutions and are applicable in complex geometries, but they are also very slow and therefore computationally expensive. Research has shown that solutions to the Boltzmann's equation in borehole nuclear measurements can be rapidly and accurately approximated with flux perturbations based on *a priori* tool responses and detector spatial sensitivities (Mendoza et al., 2010a, 2010b; Mimoun et al., 2011a), but this application has not been extended to spectroscopy in published literature.

Shoulder-bed and well deviation effects compromise the interpretation of well logs through the averaging of true layer petrophysical properties. Use of fast simulation methods (based on flux perturbation techniques) in inversion algorithms has considerably improved the estimation of nuclear and petrophysical properties such as neutron porosity, bulk density, Sigma, and hydrocarbon pore volume through the correction of shoulder-bed and well deviation effects on measured logs (Sanchez-Ramirez et al., 2009; Mimoun et al., 2011b; Heidari et al., 2012; Ijasan et al., 2013; Mendoza et al., 2012Ortega, 2014b;). Thinly-bedded formations introduce additional difficulties in the interpretation of well logs because conventional inversion methods cannot resolve the properties of laminations that are thinner than the vertical resolution of the logging tool. Mixing laws have been developed to address this problem in resistivity (Poupon and Leveaux, 1971) and Sigma measurements (Haley, 1995), thereby improving the quantification of petrophysical properties within laminations. None of the techniques that address shoulder-bed, well deviation, or thin-bed effects have been implemented for spectroscopy measurements in the published literature.

1.2 PROBLEM STATEMENT

Difficulties in conventional spectra interpretation limit the accuracy of elemental and mineral concentrations estimated through these methods. These difficulties include low signal-to-noise ratios due to low count rates, overlapping elemental spectral peaks, the assumption that predefined standard spectra contribute to measured spectra, underdetermined spectral fitting problems where the number of elemental yields to be estimated exceeds the number of elemental standard spectra, the need to differentiate inelastic from capture gamma-ray spectra, and the need to distinguish borehole and tool

effects from formation responses. Therefore, development of an improved numerical spectra interpretation method that addresses these impediments is necessary to enable more reliable spectroscopy calculations.

It is common practice to use only non-spectroscopy lithology-sensing logs such as gamma- ray and photoelectric factor (PEF) logs to estimate matrix compositions. However, spectroscopy elemental logs express a direct relation to formation matrix lithology, and they should be included in the characterization of matrix compositions and subsequent petrophysical interpretation. On the other hand, existing spectroscopy-based mineral quantification techniques typically do not include other lithology-sensing well logs and usually do not invoke further petrophysical interpretation based on spectroscopy-derived mineral concentrations. A more robust interpretation method is required that incorporates spectroscopy and other lithology-sensing logs into accurate, petrophysically consistent interpretation models. Such a method will increase the accuracy and uniqueness of estimated mineralogy.

Because neutron and density porosity logs are usually presented in homogeneous limestone or sandstone units, these porosity logs need to be corrected for the homogeneous matrix assumption to quantify fluid effects, total porosity, and hydrocarbon saturation accurately. A few published studies quantify total porosity through the correction of matrix effects on measured porosity logs, but no method exists in which matrix correction is achieved using mineral compositions obtained from spectroscopy logs within a petrophysically consistent framework.

Geometrical effects due to complex well trajectories, thin beds, and dipping beds further compromise spectroscopy interpretation through the averaging of true layer

properties. Previous advances in the correction of such geometrical effects on other measurements suggest that the introduction of a numerical fast-forward simulation model that accurately quantifies geometrical effects on spectroscopy measurements can facilitate the correction of these effects through inversion methods. In laminated formations, in which layer thicknesses are below the vertical resolution of the logging tool, inversion methods break down, and additional interpretation is required to accurately resolve layer elemental or mineral compositions.

1.3 RESEARCH OBJECTIVES

The main purpose of this dissertation is to improve the interpretation of spectroscopy measurements through the reduction of shoulder-bed averaging effects on measured spectroscopy logs and thereby introduce a reliable spectroscopy-based petrophysical interpretation workflow. Specifically, the objectives of the dissertation are as follows:

- To develop and validate Monte Carlo based LWD spectroscopy simulation and interpretation methods that quantify elemental spectra, elemental relative yields, elemental weights, and mineral concentrations in inelastic and capture measurement modes. Developed Monte Carlo methods will be designed to circumvent inaccuracies due to limitations in conventional spectra interpretation. Validation will be achieved by comparison between Monte Carlo simulated elemental gamma-ray spectra and elemental gamma-ray spectra obtained from laboratory experiments. Monte Carlo simulations are performed in the presence of the LWD logging tool, borehole, and formation, and thereby they include geometrical effects and borehole-measurement physics.

- To develop and validate an accurate fast-forward model that numerically simulates LWD spectroscopy elemental and mineral logs in inelastic and capture measurement modes. The fast simulation method should reliably reproduce geometrical effects by incorporating borehole-measurement physics and environmental effects into the forward model. Similar to Monte Carlo methods, the forward model should also be designed to circumvent inaccuracies that arise from conventional spectra interpretation. Monte Carlo simulated elemental and mineral compositions will validate results from the spectroscopy forward model.
- To develop an interpretation method that quantifies petrophysically consistent mineral concentration logs from spectroscopy elemental weight logs through joint inversion of spectroscopy and other lithology-sensing logs such as gamma ray, matrix Sigma, matrix PEF, and matrix density. Estimated mineralogy will be integrated with fluid-sensitive well logs, such as neutron porosity, density porosity, and resistivity, to quantify total porosity and hydrocarbon saturation. The method should remain valid independent of tool configuration, well trajectory, formation geometry, or formation lithology, and it will be validated with several synthetic and field cases.
- To develop inversion algorithms that quantify layer elemental and mineral compositions in inelastic and capture measurement modes along with uncertainties in estimated layer properties. The inversion method will be implemented using the LWD spectroscopy fast-forward model and should significantly decrease geometrical effects, such as shoulder-bed averaging, on measured elemental relative yields, elemental weight, and mineral concentration

logs. Mineral concentrations will also be estimated through joint inversion of spectroscopy and other lithology-sensing logs to ensure that results are petrophysically consistent with other logs.

- To integrate LWD spectroscopy measurements with other borehole nuclear and resistivity measurements and thereby improve petrophysical calculations of porosity and hydrocarbon saturation.
- To develop additional interpretation methods that quantify elemental and mineral compositions within laminated formations where layer thicknesses are below the vertical resolution of the LWD tool such that conventional inversion methods fail. Interpretation methods will also include the assessment of hydrocarbon saturation within laminations using an appropriate saturation model.
- To validate the developed LWD interpretation methods with several synthetic and field cases that evaluate the accuracy and applicability of the developed workflow in a range of well trajectories and formation geometries.

1.4 METHOD OVERVIEW

The first part of this dissertation describes the main technical basis of this research, which is the development and benchmarking of a new, fast, and reliable numerical-spectroscopy simulation method in an LWD tool. The spectroscopy-based fast simulation method quantifies formation elemental and mineral compositions in inelastic and capture spectroscopy measurement modes. Spectroscopy logs are rapidly modeled through flux perturbations based on known tool responses and spatial sensitivity of the detectors. Perturbations are based on a nuclear property that controls spectroscopy responses in inelastic and capture measurement modes. This property is determined

through extensive analysis of spatial sensitivity detector responses with respect to various nuclear properties. Results of this analysis indicate that migration length is the property that most significantly and predictably affects spectroscopy responses in both inelastic and capture-measurement modes. Tool responses are based on an earth model property of elemental absolute yields; this choice prevents complications that arise in transforming spectra into yields through equations 1.1 and 1.2. The spatial detector sensitivity that is included in the simulation of elemental absolute yield logs accounts for tool physics, formation geometry, well deviation, and environmental effects. The forward model also includes the interpretation of simulated elemental absolute yields in the estimation of elemental relative yields, elemental weight concentrations, mineral volumetric concentrations, and mineral weight concentrations through oxide closure and inversion models.

The first part of the dissertation also describes the simulation and benchmarking of gamma-ray spectra based on rigorous and accurate Monte Carlo calculations in the Monte Carlo N-Particle (MCNP) code (X-5 Monte Carlo Team, 2005). The MCNP-simulated gamma-ray spectra are also interpreted to quantify elemental (including elemental relative yields and weight concentrations) and mineral (including mineral volumetric and weight concentrations) logs and can therefore validate results from the forward model.

The second part of this dissertation presents the use of an inversion-based interpretation method to quantify matrix mineralogy from spectroscopy elemental weight logs. The method exploits the analytical forward relationship between elemental weights and mineral concentrations in a nonlinear iterative algorithm to quantify mineral logs

(including mineral volumetric and weight concentrations). Nonlinear inversion of elemental weight logs is implemented in conjunction with matrix sensitive logs to ensure petrophysically consistent mineralogy results. Estimated mineralogy is used to correct the assumption of a homogeneous lithology in measured porosity logs and thereby quantify porosities and water saturations devoid of matrix effects. The developed methodology is benchmarked with synthetic cases and implemented in field cases where core data are acquired.

In the third part of this dissertation, I implement a nonlinear inversion algorithm based on the developed LWD spectroscopy fast-forward model. The inversion method quantifies layer elemental relative yields and weight concentrations devoid of geometrical and environmental effects. The uncertainty in estimated elemental relative yields and weight concentrations is quantified using covariance-derived error bars. I introduce a new spectroscopy mixing law to quantify elemental compositions in thin-bedded formations, within thin laminations where conventional inversion methods fail because layer thicknesses are below the vertical resolution of the logging tool. The developed methods are validated with synthetic and field cases that exhibit varying well trajectories and formation lithologies.

The final part of the dissertation utilizes the LWD spectroscopy fast-forward model in a nonlinear inversion method to obtain detailed mineral concentrations and associated covariance-derived uncertainties in results. This method includes joint inversion of spectroscopy elemental logs in conjunction with lithology-sensing logs, which ensures that mineralogy results are petrophysically consistent with other well logs, as discussed in the second part of this dissertation. Estimated mineral volumetric

concentrations also improve petrophysical calculations of porosity and water saturation by replacing the homogeneous matrix lithology assumed in measured neutron and density porosity logs. I introduce additional interpretation methods that quantify mineralogy, porosity, and water saturation in thin-bedded formations using the developed spectroscopy mixing law and a shaly-sand saturation model. Synthetic and field cases validate the accuracy and flexibility of the developed methods by testing various formation lithologies and well trajectories.

1.5 DISSERTATION OUTLINE

This dissertation consists of four parts and six chapters. The first chapter introduces spectroscopy measurements, summarizes conventional interpretation procedures, outlines the challenges in current spectroscopy-interpretation techniques, and cites relevant literature. I also describe the methods introduced in this dissertation to advance the interpretation of spectroscopy measurements, particularly in relation to LWD tools.

Chapter 2 comprises the first and central part of the dissertation, which is the introduction of a new, rapid method for simulating LWD spectroscopy elemental and mineral concentrations. The method includes a first-order perturbation method of layer spectroscopy properties (elemental absolute yields) using Monte Carlo derived flux sensitivity functions that account for high-energy inelastic neutron scattering and thermal neutron capture. I validate the model with detailed Monte Carlo simulations achieved using a modified version of the Monte Carlo N-Particle (MCNP) code, which directly simulates elemental gamma-ray spectra and facilitates the interpretation of elemental relative yields, elemental weight concentrations, and mineral concentrations. The

accuracy of MCNP-simulated spectra is benchmarked with laboratory-obtained elemental spectra. The forward model is implemented in three synthetic cases comprising various well trajectories and formation lithologies.

Chapter 3, the third part of the dissertation, outlines a technique that quantifies mineral logs and associated uncertainties from elemental weight concentration logs. The technique is particularly useful when the specific tool model architecture is unavailable because it is applicable to any tool model, formation lithology, formation geometry, or well trajectory. Because the tool model is not included in the solution, inverted mineralogy data are quantified depth-by-depth and exclude geometrical effects such as shoulder-bed averaging. However, estimated mineralogy improves petrophysical calculations of porosity and water saturation by replacing the homogeneous lithology assumed in porosity logs with the estimated mineralogy. Results are validated with two synthetic cases and implemented in four field examples in which core measurements are available.

The third part of this dissertation, in Chapter 4, describes the implementation of the LWD spectroscopy fast-forward model in a nonlinear inversion method. The inversion method corrects geometrical and environmental effects on measured spectroscopy elemental logs and thereby quantifies true layer elemental relative yields and weight concentrations. The fast-forward model, which is implemented in the inversion algorithm, is significantly faster than MCNP simulations and is therefore more efficient in the estimation of layer spectroscopy elemental and mineral compositions. In the presence of thin beds that are below the vertical resolution of the logging tool, I implement a spectroscopy mixing law that quantifies elemental weight concentrations

within thin laminations. I validate the developed methods with four synthetic and two field cases in different well trajectories and formation lithologies.

The fourth and final part of this dissertation, presented in Chapter 5, includes a joint nonlinear inversion of spectroscopy and lithology sensing logs, based on the LWD spectroscopy forward model, to quantify mineral concentrations and associated uncertainties in estimations. I introduce a workflow that utilizes estimated mineral concentrations to improve porosity and water saturation calculations through the reduction of shoulder-bed averaging effects and the replacement of the homogeneous matrix lithology assumed in measured neutron and density porosity logs with the solution of mineral concentrations. The method is modified in the presence of thin laminations, based on the developed spectroscopy mixing law and a shaly-sand saturation model, to quantify matrix compositions and petrophysical properties within laminations. Four synthetic cases and two field examples test the accuracy and flexibility of the method.

Finally, Chapter 6 summarizes the contributions, conclusions, and recommendations stemming from this dissertation.

1.6 LIST OF PUBLICATIONS

Several research articles from this dissertation have been published by various journals; others have been or will be submitted for peer review. A list of these publications is presented below.

1.6.1 Refereed Journal Publications

Ajayi, O., C. Torres-Verdín, and W. E. Preeg, 2015, Fast numerical simulation of logging-while-drilling gamma-ray spectroscopy measurements: Geophysics, **80**, no. 5, D501-D523.

Ajayi, O., C. Torres-Verdín, and W. E. Preeg, 2015, Petrophysical Interpretation of LWD, Neutron-Induced Gamma-Ray Spectroscopy Measurements: An inversion-based approach: Petrophysics: Petrophysics, **56**, No. 4, 358-378.

Ajayi, O., C. Torres-Verdín, and W. E. Preeg, 2015, Inversion-based interpretation of logging-while-drilling gamma-ray spectroscopy measurements: Geophysics *(accepted for publication)*.

Ajayi, O. and C. Torres-Verdín, 2015, Improved mineral and petrophysical analysis using neutron-capture gamma-ray spectroscopy elemental logs: Interpretation *(under review)*.

1.6.2 Conference Proceedings

Ajayi, O., C. Torres-Verdín, and W. E. Preeg, 2014, Rapid simulation and inversion-based interpretation of gamma ray spectroscopy logs in high-angle and horizontal wells: Transactions of the Society of Petrophysicists and Well Log Analysts, 55th Annual Logging Symposium, paper VVV.

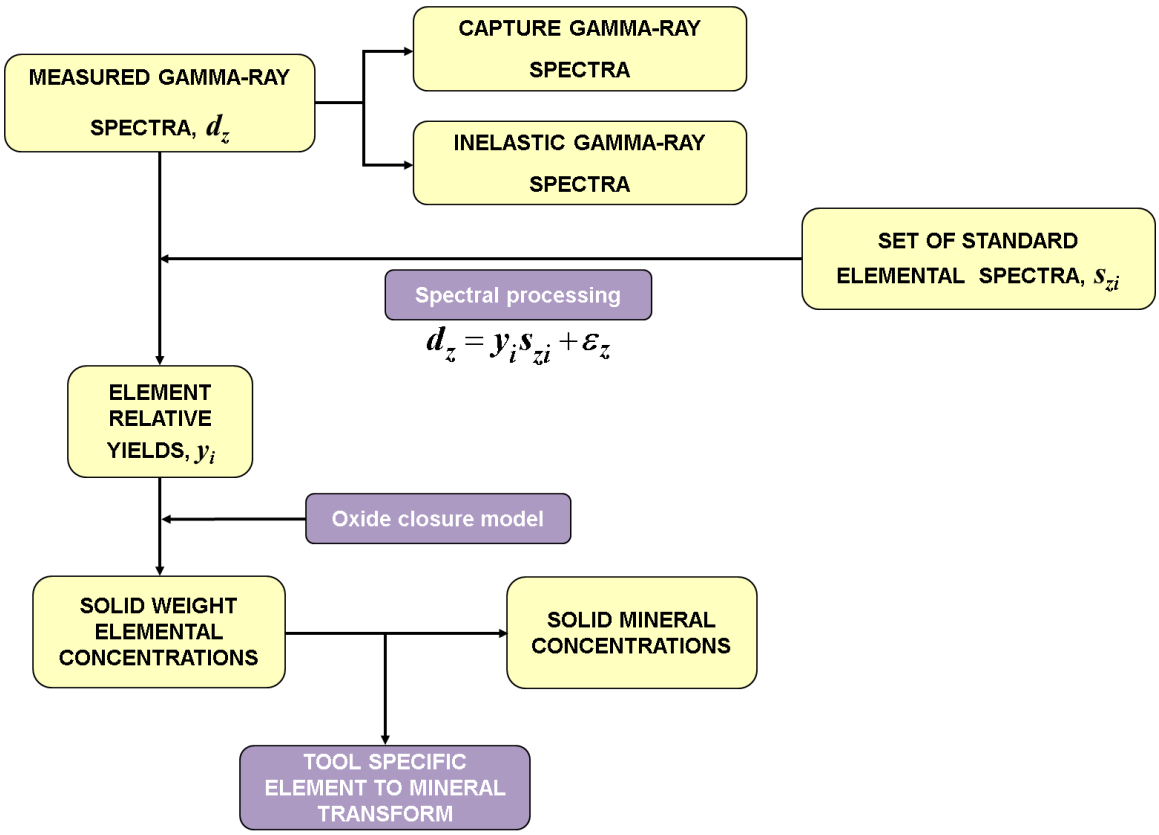

Figure 1.1. Conventional interpretation method typically adopted in the analysis of measured gamma-ray spectra. Subscript z designates the index of each spectral energy data channel, d_z is the measured data spectrum in the z^{th} spectral energy data channel, y_i is the yield of measured element i, s_{zi} is the elemental spectral standard for the i^{th} element in the z^{th} spectral energy data channel, and ε_z is the inherent uncertainty of the spectral fit in each spectral energy data channel.

[1]Chapter 2: Fast Numerical Simulation of Logging-While-Drilling Gamma-Ray Spectroscopy Measurements

Neutron-induced gamma-ray spectroscopy measurements originate from inelastic neutron scattering and thermal neutron capture of chemical elements excited by neutrons; they are widely used to quantify in-situ elemental and mineral compositions of rocks in boreholes. Traditional methods of interpreting neutron-induced gamma-ray spectroscopy measurements neglect layer-boundary and layer-thickness effects in the estimation of elemental and mineral compositions. Such effects can cause significant averaging of true layer properties in thinly-bedded formations or in formations penetrated by high-angle/horizontal (HA/HZ) wells. Reliable measurement interpretation must therefore begin with the development of a fast and accurate forward simulation model that explicitly incorporates measurement physics, borehole, tool, and formation geometry. Monte Carlo methods accurately reproduce averaging effects but are extremely time consuming and impractical for use in routine spectroscopy interpretation. I introduce a rapid and accurate numerical method that utilizes spatial coupled neutron-gamma ray sensitivity functions to account for environmental and three-dimensional (3D) effects of formation porosity, fluids, dipping beds, thin beds, and arbitrary well trajectories in the simulation of elemental and mineral compositions. Simulations are performed assuming a logging-while-drilling (LWD) spectroscopy tool furbished with a 14-MeV pulsed-neutron source. I benchmark results obtained with the rapid simulation method against rigorous

[1] The information within this chapter has been published in Geophysics journal as "Ajayi, O., C. Torres-Verdín, and W. E. Preeg, 2015, Fast numerical simulation of logging-while-drilling gamma-ray spectroscopy measurements: Geophysics, **80**, no. 5, D501-D523". Co-authors Torres-Verdín and Preeg supervised the research presented in this publication.

Monte Carlo spectroscopy calculations for synthetic conventional and unconventional thinly-bedded reservoirs penetrated by vertical and HA/HZ wells. Fast simulations are obtained in approximately 1e6 the time required for Monte Carlo simulations, with an average difference below 5% between them. Similar to Monte Carlo simulated logs, fast simulated logs accurately reproduce geometrical effects on measurements affected by shoulder-bed averaging of layer elemental and mineral compositions. The fast-forward simulation method facilitates the development of efficient inversion-based spectroscopy interpretations which can mitigate geometrical effects that mask true layer elemental and mineral compositions.

2.1 INTRODUCTION

Interpretation of borehole nuclear spectroscopy measurements begins with the analysis of measured gamma-ray spectra, which are defined by the distribution of gamma-ray counts within specified energy spectral channels. Gamma-ray spectra include inelastic and capture measurements that arise, respectively, from inelastic high-energy neutron scattering and thermal low-energy neutron capture of formation elemental nuclei when the latter are bombarded with a neutron source (Westaway et al., 1980). The analysis of borehole gamma-ray spectra to evaluate elemental and mineral compositions is complex because of the numerous processes involved, such as differentiation of inelastic from capture gamma-ray spectra, removal of the background response of the logging tool, evaluation of elemental spectra, elemental composition, and quantification of the relationship between elements and minerals (Hertzog, 1978; Pemper et al., 2006; Galford et al., 2009).

Solutions to the coupled neutron and gamma-ray Boltzmann equation using appropriate nuclear cross sections for inelastic and capture measurements are commonly used to model spectroscopy transport mechanisms (Lewis and Miller, 1993). Numerical methods such as discrete ordinates and Monte Carlo random sampling have been used to solve the Boltzmann equation when modeling measurements acquired with borehole nuclear instruments. The discrete ordinates method is extremely slow and generally cannot account for general 3D geometries, such as those involved in complex well trajectories and spatially heterogeneous formations. Calculations of detailed gamma-ray spectra are hindered by the lack of sufficient energy resolution in discrete ordinates methods due to presence of multigroup cross sections (Tsang and Evans, 1983). Solutions approximated with Monte Carlo methods are customarily implemented with the Monte Carlo N-particle (MCNP) software (X-5 Monte Carlo Team, 2005); MCNP is the industry standard for spectroscopy simulation because of its accuracy and flexibility to solve elaborate 3D neutron and gamma-ray transport problems in arbitrary well-logging environments.

There exist few published well-logging applications of spectroscopy numerical modeling and are limited to Monte Carlo simulations of spectra acquired with wireline tools in thick homogeneous formations. Tsang and Evans (1983) performed Monte Carlo simulations of wireline inelastic and capture total gamma-ray spectra in homogeneous formations and compared results to tool measured spectra. Elemental composition was determined by tracking the origin and parent nuclide of each gamma ray measured at the detector. Additionally, they performed depth-of-investigation calculations and studied the spatial distribution of elemental signals. Galford et al. (2009) exploited recent

improvements in the quality of MCNP elemental cross section data libraries (Cywicka-Jakiel, 2007) to accurately simulate elemental spectral data, which was previously impractical. MCNP simulations are also frequently used to optimize tool design via sensitivity analysis of the measured spectra (Galford et al., 2009; Radtke et al., 2012). A major limitation of Monte Carlo simulation methods is that they are extremely CPU-time consuming, and therefore not practical for routine interpretation.

Watson (1992) used a first-order perturbation method to approximate tool nuclear measurements based on the spatial sensitivity of the detector in homogeneous materials of known cross section. Mendoza et al. (2010) used the first-order perturbation method to rapidly and accurately simulate nuclear logs based on Monte Carlo-derived spatial sensitivity functions, referred to as flux sensitivity functions (FSFs), in the presence of the tool itself, shoulder beds, mud-filtrate invasion, and irregular borehole environmental conditions.

However, no published works address (a) 3D spectroscopy simulation with LWD tools in complex lithologies and well trajectories or (b) development of fast numerical simulation for spectroscopy measurements. A fast-forward spectroscopy simulation method will enable the development of inversion-based interpretation algorithms to explicitly account for 3D geometrical effects on spectroscopy measurements in the estimation of layer-by-layer elemental and mineral compositions. Such a method can be further implemented in a joint interpretation framework with other borehole measurements to improve the estimation of petrophysical properties, such as porosity and hydrocarbon saturation (Liu et al., 2007; Sanchez-Ramirez et al., 2009; Heidari et al., 2010).

The following sections describe the development and application of a new spectroscopy fast-forward method for quantifying elemental and mineral compositions with a 14-MeV pulsed-neutron LWD tool via independent inelastic and capture gamma-ray simulations. Rigorous Monte Carlo calculations are performed for synthetic cases and results are compared to those obtained with the fast simulation method for validation. The method is implemented in vertical wells, deviated wells, and complex thinly-bedded heterogeneous formations of varying lithology. The studied cases confirm the reliability and accuracy of the new simulation method in efficiently simulating 3D LWD spectroscopy measurements over a wide range of lithologies, formation geometries, and well trajectories.

2.2 LWD SPECTROSCOPY MEASUREMENTS

2.2.1 Tool Description

Recent advances in pulsed-neutron generator technology enabled the introduction of 14-MeV pulsed-neutron sources in LWD tools for geochemical logging with spectroscopy measurements (Neville et al., 2005; Weller et al., 2005; Radtke et al., 2012). The commercial 14-MeV pulsed-neutron LWD spectroscopy tool considered in this chapter provides spectroscopy measurements for capture gamma-ray spectra at a short-spaced gamma-ray sodium iodide (NaI) scintillator detector located between two neutron detectors. For this tool, inelastic spectra have a low signal to noise ratio because energy cross sections that govern inelastic gamma-ray production are extremely small (Ellis and Singer, 2007), and early-capture gamma rays and the tool body itself can have significant contributions in inelastic spectra. As shown in Figure 2.1, the tool provides an industry

standard suite of formation evaluation measurements using only a single short collar located close to the drill bit. This acquisition and sensor co-location strategy facilitates the integration of spectroscopy measurements with other well logs acquired in the same borehole, ensures that measurements are recorded almost simultaneously, and minimizes invasion effects (Weller et al., 2005).

LWD spectroscopy data typically acquired in the field include elemental measurements of capture hydrogen (H), chlorine (Cl), silicon (Si), aluminum (Al), calcium (Ca), magnesium (Mg), iron (Fe), potassium (K), titanium (Ti), sulfur (S), and gadolinium (Gd). Silicon, calcium, magnesium, iron, potassium, sulfur and aluminum are the most relevant elements in lithology interpretation because they are the primary elements contained within common rock forming minerals.

2.2.2 Spectra Modes

Pulsed-neutron sources have repetitive cycles of neutron burst packets composed of neutron burst, early capture, and late capture segments differentiated by timed gate sections. Inelastic gamma rays arise from interactions between the high-energy fast neutrons, and the atoms in the wellbore, and rock formations in the vicinity of the source measured within the neutron burst period. Fast neutrons are quickly slowed to their thermal state, causing some capture contributions to inelastic spectra. In the late capture section of the burst packet, capture gamma rays are free of the inelastic background response. Logging tools commonly use these ‘uncontaminated’ capture gamma-ray spectra to correct for the background capture response present in inelastic spectra (Hertzog, 1978).

Modeling of both inelastic and capture spectra modes improves elemental spectra characterization, particularly for elements that exhibit only one dominant spectral mode, such as inelastic carbon present in kerogen of organic shales (Hertzog, 1978; Pemper et al., 2006; Radtke et al., 2012). Carbon is a unique identifier of kerogen because other kerogen components, such as hydrogen and oxygen, are simultaneously present in several other fluids and minerals. I therefore model inelastic measurements in addition to conventional LWD capture measurements.

2.2.3 Monte Carlo simulation of Spectroscopy Measurements

This section describes techniques developed to simulate elemental spectra as well as elemental and mineral compositions based on detailed Monte Carlo calculations performed with the Monte Carlo N-particle (MCNP) software. Due to limited availability of experimental spectroscopy data, the MCNP-based spectroscopy workflow is a useful alternative to validate results obtained from the forward model. The workflow is analogous to methods adopted in the interpretation of measured field spectra and is therefore applicable to field cases. However, I do not calculate elemental spectra via conventional least-squares methods due to poor statistical precision of MCNP-simulated spectra when there are low formation gamma-ray counts. I circumvent this limitation by modifying the MCNP code to directly output each elemental spectrum and validate the accuracy of the modification by benchmarking MCNP-simulated spectra against available experimental spectra.

2.2.3.1 *MCNP Modifications*

Improvements in the quality of MCNP elemental cross section data libraries enable the accurate simulation of gamma-ray spectral data (Cywicka-Jakiel, 2007). Modifications were made to the MCNP code through the use of non-standard tallies to introduce (a) the capability to record detected gamma rays by elemental isotope, and (b) a neutron energy cut-off that distinguishes inelastic from capture gamma rays.

The detection of gamma rays by isotope enables the spectrum of each formation element to be separately recorded by tracking the spatial origin of each gamma ray produced and its parent nuclide. Such an approach allows for direct simulation of each element's spectrum in MCNP without introducing subjective external processing methods on the total measured spectrum. This helps one to focus on formation elements and eliminates the need to distinguish between non-essential borehole fluid components, tool-body responses, and varying fluid pore content.

A neutron energy cut-off corresponding to 0.5-MeV is implemented in the modified MCNP code to define inelastic (greater 0.5-MeV) and capture (less than 0.5-MeV) gamma ray production (Tsang and Evans, 1983). This approach is preferable to using the timed gate sections of pulsed-neutron sources because it decreases contamination of inelastic spectra with capture gamma rays, thereby eliminating the need to subtract a background capture response from inelastic spectra. MCNP simulation statistics are improved by excluding all neutrons with energies less than or greater than 0.5-MeV in inelastic and capture simulations, respectively. Variance reduction techniques such as weight-window generators and importance cards are also included in each MCNP

simulation to further improve simulation statistics by decreasing the statistical uncertainty of results.

2.2.3.2 *Spectra Modeling and Benchmarking*

Pulse-height spectrum is dependent upon a detector response function that quantifies the random nature of the scintillation process and the photo-multiplier response (Evans, 1981). Spectroscopy measurements are therefore modeled as pulse height spectra to incorporate the unique tool detector response into spectral data. Currently, MCNP pulse height measurements cannot be acquired while using variance reduction techniques described in the previous section to improve simulation statistics. Measured pulse-height spectra are therefore approximated following a two-step process including modeling of particle transport from source to detector as MCNP-simulated gamma-ray surface current spectra (which can be modeled in conjunction with variance reduction techniques), and the conversion of the detector response to pulse-height spectra using a tool detector response function calculated with GAMRES (Evans, 1981). Accordingly, I calculate pulse-height spectra as

$$\mathbf{p} = \mathbf{R} \cdot \boldsymbol{\psi} , \qquad (2.1)$$

where $\mathbf{p}$ is the vector of calculated pulse height spectrum (t x 1) for each element, i, and t designates the number of pulse-height channels; $\mathbf{R}$ is the GAMRES-calculated detector response function matrix (t x v) with values at each pulse-height and gamma-ray energy, where v designates the number of gamma-ray energy bins, and $\boldsymbol{\psi}$ is a vector of MCNP-simulated gamma-ray spectrum at the detector surface (v x 1) for each element i. Vector $\boldsymbol{\psi}$ is calculated as relative counts at each gamma-ray energy bin using the surface current tally in MCNP, where the energy bins correspond to the same energies included in $\mathbf{R}$.

Synthetic 20 porosity units (p.u.) water-saturated homogeneous formation models are imported into MCNP to calibrate simulated elemental spectra to experimental results. Each element is simulated with a synthetic case of a common rock forming mineral associated with the element, such as silicon for quartz. Elemental gamma-ray current spectra output by MCNP are used to calculate pulse height spectra through equation 2.1. Calculations are performed only in the capture measurement mode where experimental capture spectra are available (the tool operates commercially in the capture mode only).

Results of this application are displayed in Figure 2.2 and show good agreement between simulated and experimental spectra. Due to the difference between noise present in experimental spectra (which are acquired in the laboratory) and in MCNP simulations (which are modeled according to realistic reservoir conditions in the field), there are some discrepancies between gamma-ray Compton scattering for both spectral measurements particularly for hydrogen, sulfur, and potassium at higher energies. Despite these differences, it is important to note that the principal spectral peaks align for all the elements studied such as the main hydrogen gamma-ray spectrum peak located at 2.2233 MeV.

Statistical noise in MCNP simulations originates from the variance of the measured gamma-ray count population, which is inversely related to the number of particles considered by the Monte Carlo algorithm. This condition results in low statistical precision of simulated gamma-ray spectra for formation elements that are present in low concentrations. MCNP statistical precision can primarily be improved through previously described variance reduction techniques as well as by running the simulation problem for a longer period of time to increase the population of measured

gamma rays. In field spectroscopy measurements, besides low concentrations of formation elements, the statistics of gamma ray field spectra is also dependent upon logging parameters such as the rate of penetration of the logging tool, sampling depth, and the number of depth levels averaged into one single gamma-ray spectra. These logging parameters are optimized to increase measured gamma-ray counts, and thereby improve the statistics of measured gamma-ray field spectra. In terms of statistical noise, MCNP-simulated spectra should exhibit good agreement with such optimized field spectra when variance reduction techniques are appropriately implemented and the simulation problem runs for an ideal length of CPU time.

2.2.3.3 *From Spectra to Elemental Yields*

Elemental yields describe individual elemental contributions to the measured spectrum within a specific energy interval. Tool spectroscopy processing methods compute yields as the fitting coefficients of a linear combination of the elemental standard spectrum that yield the best match to the measured spectrum using least-squares minimization. The elemental standard spectrum is defined as the measured spectrum in a homogeneous rock formation composed of a mineral that contains predominantly the element to be evaluated. Yield calculations using least-squares minimization introduce a limitation on how many elements can be quantified, as too many elemental standard spectra decrease the statistical precision of spectral fitting. Least-squares minimization relies on accurate definitions of elemental standard spectra and assumes that predetermined elemental standard spectra in homogeneous formations contribute to spectra measured in widely heterogeneous formations. Spectral fitting methods are

further complicated by low count rates that decrease statistical precision, poor detector resolution, and overlapping elemental spectral peaks.

I calculate elemental relative yields directly using the modified MCNP code that outputs each elemental spectrum separately, such that

$$y_i = \frac{y_{abs,i}}{\sum_{i=1}^{m} y_{abs,i}}, \qquad (2.2)$$

where $y_{abs,i}$ is the energy-integrated MCNP-simulated spectrum of element *i* within the energy measurement range of the tool (elemental absolute yield) and $\sum_{i=1}^{m} y_{abs,i}$ is the sum of energy-integrated measured spectra for the *m* elements present in the formation within the energy measurement range of the tool. Because only formation elemental spectra are used to determine y_i, equation 2.2 is representative of normalized formation relative yields and defines the fraction of each element present in rock forming minerals.

2.2.3.4 *From Elemental Yields to Elemental Weight Concentrations*

Elemental yields are indicative of elemental concentrations, but do not provide quantitative elemental composition information typically used in petrophysical analysis. This necessitates the conversion of elemental yields into a more useful parameter: absolute elemental weight fractions. Conversion into absolute elemental weight fractions, M_i, is commonly achieved through an oxide closure model that assumes that primary measured formation elements sum to unity and exist as oxides or carbonates (Galford and Hertzog, 1989; Hertzog et al., 1989; Grau et al., 1990; Galford et al., 2009). This oxide closure model is represented by

$$F\sum_{i=1}^{m}\frac{X_i y_i}{Se_i}=1, \qquad (2.3)$$

where X_i is a factor used to account for the weights of elements that are not measured but are associated with element i (such as oxygen and carbon in oxides and carbonates), F is a depth-varying normalization factor that accounts for the variability of neutron flux due to changes in environmental parameters, Se_i designates the relative detection sensitivity of element i to the production of gamma rays, and m is the number of elements present in the analysis (Hertzog et al., 1989; Grau et al., 1990). The solid weight concentration of element i, M_i, is calculated according to the relationship

$$M_i = F\frac{y_i}{Se_i}, \qquad (2.4)$$

where F is obtained from equation 2.3.

2.2.3.5 *From Elemental Composition to Lithology*

Spectroscopy lithology quantification is usually based on interpretative models that invoke predefined linear correlations between elements and minerals (Herron and Herron, 1996) or probabilistic minimization techniques (Quirein et al., 1986; Galford et al., 2009). This empirical approach relies on the accuracy of existing databases, and does not consider 3D complex geometrical effects that are prevalent in LWD logging environments. Other lithology quantification techniques include combined linear inversion of well logs, but they do not typically include spectroscopy logs or 3D geometrical effects on measurements (Mayer and Sibbit, 1980; Doveton, 1994). Such non-spectroscopy based techniques also invoke the often erroneous assumption that log measurements are approximately linear functions of rock mineral volumetric

concentrations. In this chapter, I employ nonlinear inversion of simulated elemental yield logs or weight concentrations, outlined in Appendix A, to estimate mineral concentrations.

2.3 FAST SPECTROSCOPY SIMULATION

2.3.1 Formulation

2.3.1.1 *Spectroscopy Model Parameter*

MCNP spectroscopy calculations are accurate in quantifying elemental and mineral compositions but often require up to 20 hours of CPU time to simulate one measurement along the well trajectory. I therefore seek to develop a fast method to numerically approximate elemental and mineral compositions through a first-order perturbation of an assumed spectroscopy model layer parameter.

Gamma-ray spectra are an ideal choice for the spectroscopy layer parameter because they are directly measured by spectroscopy logging tools. However, low spectra resolution arising from low count rates, poor detector resolution, and overlapping elemental spectral peaks, make spectra impractical for use as a model parameter. As shown in Figure 2.2, gamma-ray spectra can also be significantly affected by noise, which can cause appreciable inaccuracies in estimated elemental and mineral compositions. Limitations in conventional spectra-to-yields least-squares minimization introduce further inaccuracies in interpreting simulated total spectra. These limitations include the need to eliminate tool background response from measured spectra and underdetermined minimization problems where the number of elements in the solution is less than the number of available spectral standards. It is also computationally demanding

to simulate gamma-ray spectra directly in the forward model because this requires estimation of perturbations in gamma-ray counts for each element within each gamma-ray energy channel.

I therefore approximate the numerical simulation of spectra by modeling energy-integrated elemental gamma-ray spectra in the form of elemental absolute yields. Elemental absolute yields describe energy integrated gamma-ray spectra because they include the relative detection sensitivity of element *i* to the production of gamma rays and the weight concentration of element *i* within the sensitivity region of the detector (Flaum and Pirie, 1981; Grau et al., 1989). This condition is represented by the relationship

$$y_{abs,i} = Se_i M_i . \qquad (2.5)$$

Elemental sensitivities account for element-dependent differences in thermal neutron cross sections, effective gamma ray multiplicities, gamma-ray transport, gamma-ray detection efficiencies, and elemental atomic weights (Hertzog, 1989). Elemental absolute yields in Equation 2.5 describe spectra integrated within the energy limits of the tool by including elemental sensitivities that are calculated within the energy measurement range of the tool.

Figure 2.3 shows results obtained with MCNP numerical experiments where synthetic homogeneous porous dolomite formations with distinct formation elemental weight concentrations exhibit a linear variation of magnesium and calcium capture yields with respect to weight fractions. This behavior suggests a relatively constant sensitivity value for each element, as expressed by equation 2.5, and validates the use of a single sensitivity value for each element when defining elemental yields at different solid elemental weight concentrations. Formation elemental yields obtained from one of the

synthetic cases in Figure 2.3, with constant solid elemental weight concentrations, are studied at conditions of varying formation porosities, saturating fluids, and borehole sizes. Results in Figure 2.4 show that these elemental yields are largely invariant with respect to changes in environmental parameters at a constant formation elemental weight concentration; they indicate that formation elemental yields are predominantly affected by changes in solid elemental weight concentrations.

I calculate distinct elemental sensitivity values through numerical experiments for both inelastic and capture gamma-ray spectra using silicon as the reference element with a sensitivity of 1 (Flaum and Pirie, 1981; Grau et al., 1990). It follows from equation 2.5 that elemental sensitivities are computed as

$$Se_i = \frac{y_{abs,i}\, M_{Si}}{y_{abs,Si}\, M_i}, \qquad (2.6)$$

where M_{Si} is the weight fraction of silicon and $y_{abs,Si}$ is the elemental absolute yield of silicon obtained within the energy measurement range of the tool. Synthetic cases of common porous rock (20-p.u.) forming minerals in typical logging environments are used to compute elemental sensitivities; if silicon is not present in the mineral mixture, quartz (SiO_2) is included as a mineral baseline to include silicon. Table 2.1 summarizes the results obtained from these calculations for inelastic and capture gamma-ray sensitivities. Estimated capture elemental sensitivities are comparable to published values for a wireline tool operating in the capture measurement mode (Grau et al., 1989). I do not expect these values to be equal because elemental sensitivities are tool dependent (every tool has a distinct source, detector type, and geometrical arrangement.)

2.3.1.2 *Forward Approximation Method*

I achieve a first-order perturbation of layer elemental absolute yields using an approximation of a Taylor series expansion. The Taylor series expansion describes nonlinear detector responses as a function of the nuclear interaction cross section that controls a specific type of measurement (Watson, 1984; X-5 Monte Carlo Team, 2005).

A background homogeneous formation of established spectroscopy cross section, Σ_B, and detector response at detector position $\mathbf{r}_R$, $N_B(\mathbf{r}_R)$, can be used to approximate the corresponding z-th order change in detector response, expressed with the Taylor series expansion

$$\Delta N^z(\mathbf{r}_R) = N_B(\mathbf{r}_R) \sum_{z=1}^{\infty} \int d\mathbf{r} \frac{1}{z!} \frac{d^z N}{d\Sigma^z}(\mathbf{r}_R, \mathbf{r}) \left[\frac{\Delta\Sigma(\mathbf{r})}{\Sigma_B(\mathbf{r})} \right]^z , \quad (2.7)$$

where $\Delta\Sigma$ is the change in cross section, and $\frac{1}{z!}\frac{d^z N}{d\Sigma^z}$ is the z-th order response sensitivity coefficient defined by the flux sensitivity function, FSF. It follows that

$$N(\mathbf{r}_R) = N_B(\mathbf{r}_R) + \Delta N^z(\mathbf{r}_R), \quad (2.8)$$

where N is the perturbed detector response due to $\Delta\Sigma$ at detector location $\mathbf{r}_R$. Higher-order terms in equation 2.7 that account for flux perturbation effects can be neglected when $\Delta\Sigma << \Sigma_B$, such that a first-order perturbation is an accurate representation of the physics of the problem. This condition is achieved provided that the choice of Σ_B is as close as possible to $\Sigma_B + \Delta\Sigma$. By neglecting higher-order terms in equation 2.7 I obtain

$$N(\mathbf{r}_R) \approx N_B(\mathbf{r}_R) + N_B(\mathbf{r}_R) \int d\mathbf{r} \mathrm{FSF}_\mathrm{B}(\mathbf{r}_R, \mathbf{r}) \left\lceil \frac{\Delta \Sigma(\mathbf{r})}{\Sigma_B(\mathbf{r})} \right\rceil, \quad (2.9)$$

where FSF_B is the background flux sensitivity function associated with Σ_B and N_B ; FSF_B is calculated in a homogeneous formation and explicitly includes the borehole as well as both tool geometry and tool chemical composition.

2.3.1.3 *FSF Modeling with MCNP*

Although formation elemental yield and weight values are insensitive to changes in borehole and formation properties, neutron flux can vary rapidly with these changes in the logging environments. Flux sensitivity functions explicitly account for neutron flux variations by constructing a 3D map of absorbed neutrons that emit gamma rays measured at the detector in the presence of the tool, borehole, and formation. Therefore, these maps explicitly include environmental and 3D effects due formation porosity, fluid saturation, dipping beds, thin beds, and arbitrary well trajectories.

I use iterative mesh-based energy-dependent weight windows as a variance reduction technique in MCNP simulations to give precedence to particles in spatially significant regions through the use of a forward-adjoint generator implemented in MCNP (Booth and Hendricks, 1984). This method outputs a space and energy importance function map for each MCNP-simulated measurement, which is the FSF.

It would be ideal to compute sensitivity maps as pulse height neutron gamma-ray sensitivity functions because pulse height spectra measurements explicitly incorporate the detector response described by the spectra modeling in equation 2.1. However, as encountered in pulse height spectra modeling, limitations in MCNP prevent the use of pulse height measurement tallies concurrently with variance reduction techniques that

generate sensitivity functions. I thus approximate pulse height spectra and sensitivity maps as flux in numerical simulations. This approximation is validated by the consistency between normalized gamma-ray counts measured in flux and pulse height spectra calculations.

2.3.1.4 *Inelastic and Capture FSFs*

Inelastic FSFs describe sensitivity functions of neutrons that produce gamma rays at a high neutron energy level, while capture FSFs describe sensitivity functions of capture gamma rays from the absorption of thermal neutrons. I account for inelastic and capture measurement modes in FSFs by defining energy weight windows corresponding to neutron energy cut-offs for each measurement mode: greater than and less than 0.5-MeV for inelastic and capture spectra, respectively. Neutron FSFs corresponding to an MCNP simulation for neutron energies and energy weight windows greater than or less than 0.5-MeV define inelastic and capture sensitivity functions, respectively; they are calculated in sixteen azimuthal sectors at the short-spaced NaI gamma-ray detector.

2.3.1.5 *Accounting for Gamma-ray Interactions in the Forward Model*

In coupled neutron gamma-ray transport problems such as spectroscopy, it is imperative to synthesize both the physics of neutron capture and subsequent gamma-ray emission in the numerical simulations. This is achieved by defining each spectroscopy calculation as a coupled neutron gamma-ray transport problem using MCNP's neutron-photon mode, n-p, such that neutron maps incorporate the complete measurement physics. Furthermore, the use of elemental sensitivities in defining the spectroscopy modeling parameter (elemental absolute yields) incorporates unique gamma-ray spectra

into the analysis by accounting for element-dependent differences in thermal neutron cross sections, effective gamma ray multiplicities, gamma-ray transport, gamma-ray detection efficiencies, and elemental atomic weights.

2.3.1.6 *FSF Library Construction*

I seek to quantify a cross section parameter that controls the spatial variations in spectroscopy FSFs in the most uniform and linear fashion. This facilitates fast computation of spectroscopy-based sensitivity functions through approximate linear perturbations of the determined cross section parameter. Subsequently, fast calculation of FSFs enables the development of a rapid and efficient spectroscopy forward simulation method.

Independent sensitivity studies are performed for inelastic and capture gamma-ray spectra and sensitivity functions through MCNP calculations over a wide range of borehole conditions, formation types, porosities, and fluid types. I observe that gamma-ray spectra and sensitivity functions, for both inelastic and capture measurements, are most influenced by perturbations of effective migration length. Figure 2.5 shows the results obtained from these MCNP calculations, where the variations in spectra and FSFs only exhibit appreciable linearity and uniformity with respect to perturbations in migration length for both inelastic and capture measurements. Migration length represents the combination of the distance traveled by neutrons during the slowing-down phase (L_s) and in the thermal phase (L_d) before being captured (Ellis and Singer, 2007).

Due to the high energy levels wherein inelastic interactions occur, they are actually not significantly affected by changes in most cross section parameters. Therefore, there are negligible variations of inelastic spectra and the shape of FSFs

resulting from changes in migration length. The most linear variations in inelastic gamma-ray spectra and FSFs are observed with perturbations in migration length as shown in Figures 2.5(a) to (c) where responses are color coded according to migration length. Excited nuclei in inelastic interactions usually have short half-lives (less than 10^6 microseconds) and decay promptly with the emission of gamma rays before travelling far into the formation (Hertzog, 1978). Consequently, as shown in panel (c) in Figure 2.5, there is a small depth of investigation of neutrons into the formation before gamma rays are emitted (Tsang and Evans, 1983). This is in contrast to capture spectra and FSFs that have larger depths of investigation and also more variation with changes in migration length, as shown in panels (d) to (f) of Figure 2.5. Such a behavior arises because source neutrons have substantial nuclear interactions with formation atoms before they are captured and gamma rays are emitted. Inelastic FSFs are also observed to have higher vertical resolution than capture measurements, as shown when comparing panels (b) and (e) in Figure 2.5. Therefore, the volume of investigation for inelastic measurements is smaller than that of capture measurements.

Both inelastic and capture measurements exhibit higher gamma-ray counts, greater depth of investigation, and "shrinking" of normalized 1-D vertical neutron FSFs with an increase in migration length. Variations in migration length correlate to the hydrogen content of the formation because hydrogen considerably slows down neutrons that produce gamma-rays. I therefore observe a decrease in migration length with an increase in hydrogen index such as observed in shales and high-porosity formations. I account for these variations by constructing an MCNP-derived library of 91 FSFs, associated with closely spaced migration lengths for both inelastic and capture

measurements. The chosen migration lengths, between 10.57-cm to 36.2-cm for a standard freshwater-filled borehole with a diameter of 21.59-cm and collar size of 17.54-cm LWD, cover the range of migration lengths typically encountered during well-logging operations. The introduction of a closely spaced library ensures that perturbations are minimized, which in turn validates the first-order approximation technique. Migration lengths are computed with Schlumberger's Nuclear Parameter program, SNUPAR (McKeon and Scott, 1989).

2.3.1.7 *FSF fast calculations*

An iterative calculation technique is used in the fast calculation of sensitivity functions where iterations are initialized with a background migration length, $L_{m,B}$, and its associated FSF, FSF_B, of the formation material adjacent to the detector. A first-order perturbation of layer migration length is used to compute an effective migration length, L_m, at each measurement point, given by

$$L_m(\mathbf{r}_R) \approx L_{m,B}(\mathbf{r}_R) + L_{m,B}(\mathbf{r}_R) \int d\mathbf{r} FSF_B(\mathbf{r}_R, \mathbf{r}) \left\lceil \frac{\Delta L_m(\mathbf{r})}{L_{m,B}(\mathbf{r})} \right\rceil, \quad (2.10)$$

where ΔL_m is the perturbation in model layer migration length.

At each iteration, an FSF_{calc} is computed via linear interpolation (interpolation of FSFs with respect to L_m) of the two library FSFs closest to the computed L_m and an updated L_m is calculated using this FSF_{calc}. This procedure continues until differences between calculated effective migration lengths within two successive iterations are equal to or below a specified threshold value. When this threshold limit is reached, FSF_{calc} becomes the final input for spectroscopy fast simulation. This workflow is depicted in

Figure 2.6 and takes approximately 0.009s to calculate the sensitivity function for each depth level.

2.3.1.8 *Spectroscopy forward simulation*

Forward simulation of spectroscopy logs is performed using a first-order 3D perturbation of layer elemental absolute yields, $y_{abs,i}$, given by

$$y_{abs,i}(\mathbf{r}_R) \approx y_{B_{abs,i}}(\mathbf{r}_R) + y_{B_{abs,i}}(\mathbf{r}_R) \int d\mathbf{r} \mathrm{FSF}_{\mathrm{calc}}(\mathbf{r}_R, \mathbf{r}) \left[\frac{\Delta y_{abs,i}(\mathbf{r})}{y_{B_{abs,i}}(\mathbf{r})} \right], \quad (2.11)$$

where $\mathrm{FSF}_{\mathrm{calc}}$ is the 3D neutron gamma-ray FSF calculated through iterative refinement of library FSFs, $y_{abs,i}$ is the simulated absolute yield for element *i*, $y_{B_{abs,i}}$ is a background absolute yield for element *i*, and $\Delta y_{abs,i}$ is the first-order perturbation in absolute yields for element *i*. All parameters are defined in 3D space, thereby enabling the simulation of image logs and complex 3D geometry features such as invasion, dipping beds, and deviated wells.

I process elemental absolute yields into normalized formation elemental relative yields, y_i, with the relationship expressed by equation 2.2 whereby I normalize each element's absolute yield by the sum of absolute yields for elements present in the formation matrix only. This is a key step in the formulation because I desire to assess formation elemental compositions and mineralogy. Elemental weight concentrations are obtained using the oxide closure model described by equations 2.3 and 2.4. I implement a fast, nonlinear inversion method of simulated elemental yield or weight concentration logs outlined in the Appendix to estimate mineral concentrations based on stoichiometric relationships between elements and minerals.

2.4 NUMERICAL RESULTS

In this section, I document three synthetic cases that benchmark the accuracy and reliability of the developed forward simulation method to reproduce inelastic and capture spectroscopy logs for varying well trajectories and lithologies. MCNP spectroscopy data are obtained every 7.62-cm (3-in) and serve as the standard for fast-simulated logs in the absence of analogous spectral data. Each measurement location along the well trajectory is defined by the geometrical center and depth of investigation of the FSFs used in the spectroscopy fast-forward simulation (Ijasan et al., 2011). Uncertainties in inverted mineral volumetric concentrations are described as uncertainty bars on inverted mineral data. Table 2.2 displays the chemical properties of elements and minerals assumed in the synthetic examples. Migration lengths and elemental compositions are calculated from mineral and fluid compositions with Schlumberger's Nuclear Parameter program, SNUPAR (McKeon and Scott., 1989). Comparisons between sub-cases in Synthetic Case 1 and 2 are made along true vertical depth (TVD).

2.4.1 Synthetic Case No. 1

In view of the difference in volume of investigation between inelastic and capture measurements, I anticipate a difference in their spatial resolution. Well deviation effects due to the relative angle between well axis and formation dip plane impact the distance along the exposed formation, which also affects the precision of the borehole measurement. This example, shown in Figures 2.7 and 2.8, illustrates the effect of spectroscopy measurement modes and well deviation on simulated well logs in an oil-bearing formation that transitions into a water zone in the bottom layer.

The synthetic formation is composed of mixed clean sand (quartz) and carbonate (dolomite) that is penetrated by vertical and deviated wells in inelastic and capture measurement modes. This includes (a) capture measurement mode in a vertical well, (b) capture measurement mode in a 60-degree deviated well, and (c) inelastic measurement mode in a 60-degree deviated well. True stratigraphic thickness (TST) of the synthetic model is 4.57-m with bed thicknesses ranging from 30.48-cm to 91.44-cm. Table 2.3 displays layer thicknesses and migration lengths; layer elemental, mineral, and fluid compositions adopted in this example.

I show fast-simulated results benchmarked against MCNP-simulated data for case (a) and comparisons of fast-simulated results from synthetic case (a), (b), and (c). Results from case (a), shown in Figures 2.7 and 2.8, indicate that the rapid simulation method accurately quantifies the shape and values of elemental relative yields and weight logs, including measurements acquired within the oil-water transition zone between layers VI and VII. There is less than 2% error observed between fast-simulated and MCNP-simulated capture spectroscopy logs for both elemental relative yields and weight concentrations. Results for cases (b) and (c) compared to MCNP simulations are not shown, but also accurately predict the values of elemental relative yields and weight logs. Differences of less than 2% and 3% for cases (b) and (c), respectively, are observed between fast-simulated and MCNP elemental relative yield and weight logs.

Figures 2.9 and 2.10 compare elemental weight concentrations and mineralogy, respectively, for cases (a), (b), and (c). Comparisons exclude elemental relative yields because of differences in inelastic and capture model values due to variations in their neutron transport mechanisms. Elemental weight concentrations and mineralogy are

consistent in cases (a), (b), and (c) but I observe that spectroscopy measurements are "sharper" in deviated wells compared to vertical wells. This is because measurements in HA/HZ wells are controlled by the radial FSF response instead of the vertical FSF response (as is the case in vertical wells). Well-log resolution is also improved for inelastic compared to capture simulations because inelastic FSFs exhibit a smaller volume of investigation than capture FSFs. Regardless of observed log vertical-resolution improvements in inelastic measurements and deviated wells, there is still an appreciable discrepancy between log and layer values in layers II and V, shown in Figures 2.7 to 2.10, due to shoulder-bed averaging effects in these 30.48-cm thick beds. I observe a false increase in the representation of silicon in layer V from actual layer values by as much as 0.25 yield fraction (155%) and 0.15 weight concentration (170%). I also observe a false increase of quartz in layer V from true layer values of up to 0.32 volume fraction (533%). Such behavior emphasizes the importance of developing inversion-based interpretation methods that can reduce shoulder-bed effects on the measurements.

I observe in cases (a), (b), and (c) that the shoulder-bed averaging effects on elemental spectroscopy measurements propagate into inverted mineral logs shown in panels (a), (b), and (c), respectively, of Figure 2.10. Uncertainties in inverted mineral volumetric concentrations tend to be slightly higher in layers more affected by shoulder-bed averaging, such as layers II, III, V, and VI. On average, computed uncertainties in matrix inversion are 3.5% 3.5%, and 4% of the inverted mineral volumetric concentration values for cases (a), (b), and (c), respectively. This represents a high degree of confidence in inverted mineral volumetric concentrations. Forward simulation results were obtained

in 1.66, 2.51, and 2.33 seconds using the fast-forward method, which compares to 25.82, 51.47, 46.92 days of CPU time using MCNP for cases (a), (b), and (c), respectively.

2.4.2 Synthetic Case No. 2

This example is a typical unconventional gas-bearing shale reservoir that consists of a low-porosity 5.64-m TST formation with several minerals in varying compositions along the well trajectory. The presence of several minerals leads to a high number of elements in the formation, which tends to increase numerical noise, uncertainty, and non-uniqueness in MCNP simulated data. The fast-forward model does not include noise on simulated logs; it is therefore important to assess the reliability of the fast-forward model in this case. Porosities range from 3.5 to 7-p.u. and layer thicknesses from 21.34-cm to 91.44-cm. Low-porosity, gas-filled formations lead to higher migration lengths than typically encountered in practice, thereby testing an extreme of the linear iterative refinement FSF technique. This example also highlights the importance of inelastic well logs in evaluating total organic carbon content and kerogen in organic shale reservoirs. I analyze (a) inelastic spectra mode in a 70-degree deviated well and (b) capture spectra mode in a vertical well. The two examples include the simultaneous effect of changes in well deviation and spectra simulation mode on spectroscopy measurements.

Results are benchmarked against MCNP simulations for case (a) and comparisons are made between fast-simulated results from cases (a) and (b). Tables 2.4 and 2.5 display layer thicknesses and migration lengths, as well as layer elemental, mineral, and fluid compositions assumed in this example.

Figures 2.11 and 2.12 show results of case (a) for fast-simulated elemental relative yields and weight concentrations, respectively, benchmarked against MCNP

simulations. I observe that several elements are present in very low concentration (less than an average of 5% weight concentration). Consequently, there are low counts hence relatively high numerical noise in elemental logs quantified with MCNP, which causes slight discrepancies with respect to fast-simulated logs. However, fast-simulated well logs reproduce the shape and shoulder-bed averaging effects observed in MCNP-simulated logs. This behavior suggests that the fast-forward model is reliable in reproducing well logs when MCNP simulations are affected by numerical noise. Elements less affected by noise exhibit less than 1% difference between fast-simulated and MCNP-simulated elemental well logs, thereby confirming the accuracy of the fast-forward model in gas-bearing shale formations with large migration lengths. Analysis of inelastic spectra permits the simulation of carbon from inorganic and organic sources and, ultimately, kerogen estimation. Such calculations are not possible in case (b), where only capture spectroscopy elemental data are available. I distinguish total organic carbon present in kerogen from inorganic carbon present in carbonates through the use of different carbon isotopes by the recompilation of MCNP that allows detected gamma rays to be recorded by isotope.

Spectroscopy measurements in layers II (24.384-cm), VI (21.34-cm), and VIII (30.48-cm) show that it is difficult to distinguish elemental and mineral compositions in thin beds. The extent of spatial averaging is dependent on bed thickness, adjacent layer mineral and elemental compositions, as well as on the magnitude of the flux sensitivity map. Benchmarking results for case (b) are similar to those observed in case (a), excluding the inability to simulate carbon and kerogen.

I observe enhancements in spectroscopy log resolution in thin layers II (24.38-cm) and VI (21.34-cm) for case (a) over case (b), as shown in Figures 2.13 and 2.14, for elemental weight and mineral volumetric concentrations, respectively. This behavior results from the increase in well deviation and inelastic spectra mode in case (a). Average uncertainties in inverted mineral volumetric compositions are 4.6% and 3% for cases (a) and (b), respectively. Similar to Synthetic Case No. 1, uncertainties tend to be slightly higher in measurements acquired in thin layers that are more affected by shoulder-bed averaging. Forward simulation results were obtained in 6.73 and 4.16 seconds using the fast-forward method compared to 45.16 and 11.55 days of CPU time using MCNP for cases (a) and (b), respectively.

2.4.3 Synthetic Case No. 3

This example tests the application of the developed numerical simulation method in a complex case of an 85-degree well trajectory. Layer compositions include oil-bearing shaly-sands with depth-periodic mineral compositions and large contrasts in migration length. Tables 2.6 and 2.7 describe the layer thicknesses and migration lengths; layer elemental, mineral, and fluid compositions assumed in this example. The large difference in migration lengths between layers, coupled with the complex well trajectory considered in this example, tests an extreme case of the fast-simulation method. The synthetic model consists of 15.24-cm to 52.93-cm layer thicknesses in a formation of 3.65-m TST wherein I perform spectroscopy simulations in the capture measurement mode.

Elemental relative yield image logs, shown in Figure 2.15, are obtained from multisector fast-forward simulations and represent the azimuthal distribution of simulated elemental relative yield data. Similar images are constructed for elemental absolute yields

and weight concentrations. Sinusoids in image logs are indicative of the relative angle between well axis and formation dip plane.

In HA/HZ wells, each angular tool sector senses different relative proportions of layered formations, which can cause the tool response at any point along the well trajectory to be an average of several bed properties. Results in Figure 2.16 for elemental relative yields show that layer averaging effects lead to false representations of up to 0.18 yield fraction (208%) by simulated calcium yields compared to the true model value in layer III (15.24-cm). Similarly, Figure 2.17 shows false representations of up to 0.08 weight fraction (309.6%) by simulated calcium weight logs compared to the true model value in layer III. This suggests that measurements will benefit greatly from inversion-based interpretation techniques to reduce shoulder-bed effects on elemental/mineral concentrations.

I observe scatter in magnesium relative yields and weight concentrations in panel (a) of Figures 2.15 and panel (c) 2.16, respectively, due to its low concentration in the formation (less than 0.005 yield fraction and 0.06 weight fraction). This leads to a higher discrepancy between fast-simulated and MCNP-simulated logs for magnesium measurements compared to other elements, which exhibit a maximum discrepancy of 5% between fast-simulated and MCNP-calculated logs. Such an error in fast-simulated logs is the highest observed in all synthetic cases studied because of the complex well trajectory and large perturbations in layer migration lengths.

Uncertainties average 7.3% of inverted mineral volumetric and are relatively uniform in magnitude across the well. The reason for this behavior is that all beds are severely influenced by shoulder-bed effects, except the thickest 52.93-cm top and bottom

layers I and XIII, which exhibit slightly smaller uncertainty in the measurements. Simulation results were obtained in 9.82 seconds of CPU time using the fast-forward method compared to 113.65 days of CPU time using MCNP.

2.5 COMPUTATIONAL SPEED

MCNP simulations were made using a parallelized version of MCNP5 on Stampede, a Linux cluster in the Texas Advanced Computing Center, which consists of a Dell PowerEdge C8220 cluster with Intel Xeon Phi coprocessors. Each simulation was performed with a single node (composed of 16 core processors) on the Stampede Linux cluster. Table 2.8 summarizes the number of measurement points, simulation time for fast-forward and MCNP simulations, simulation errors, and uncertainty in matrix inversion for each synthetic case. The fast-forward simulation model is approximately 1e6 times faster than Monte Carlo methods in computing elemental relative yields.

2.6 DISCUSSION

A reliable forward-simulation method is necessary to quantify spectroscopy logs over a wide range of geometric, formation spatial heterogeneity, and environmental conditions. I tested extreme cases of the developed fast-simulation method, including HA/HZ wells, large migration lengths, large perturbations in migration length, formation fluid changes, and noisy measurements, wherein I obtained accurate results that represent geometrical averaging effects on the measurements. The extent of spatial averaging effects depends on the measurement mode (inelastic vs. capture), well geometry, formation geometry, changes in rock mineralogy, and shape of FSFs. Changes in FSFs

primarily occur due to perturbations in migration length typically from variations in fluid volumes and properties or presence of hydroxyls in shales.

Even though I use only Monte Carlo simulations as verification for the forward model, experimental or field data (when formation layer elemental compositions are known in the field cases) can also be used whenever available for further validation. It is important to note that for the tool assumed in our study, I had no access to any such data and could therefore not include that additional validation step in this chapter. However, Monte Carlo calculations are accurate and detailed enough to satisfactorily serve as a standard for the forward model. Monte Carlo simulated spectra were also acceptably benchmarked against laboratory-obtained spectra while Monte Carlo-derived elemental sensitivities were comparable to values published in the open technical literature. I have also closely followed the interpretation methods adopted in field acquisition and interpretation procedures to ensure that our results are consistent with field measurements.

Invasion effects were not considered in this chapter because of the assumption of negligible invasion in LWD tools. However, invasion is not expected to significantly impact simulation results unless there is a large contrast in migration length between invading and formation fluids, such as water-base mud invading a gas-bearing formation. I expect the developed fast simulation algorithm to accurately reproduce measurements for this case given that its reliability was verified in cases of large perturbations of migration length.

Considering that mineral volumetric concentrations are obtained via inversion methods, it is important to solve for concentrations of minerals which are known to be

present in the formation to avoid false representations of non-existing minerals. This is essential in ill-posed cases such as underdetermined problems, where the number of minerals to be estimated exceeds the number of available elemental data. The inversion method also assumes fixed chemical formulas and properties for minerals which may exhibit variations from one formation to another.

2.7 CONCLUSION

The developed spectroscopy fast simulation method accounts for the most realistic changes in well-logging environments by explicitly including 3D tool and formation geometry, as well as environmental effects on the measurements through the use of Monte Carlo pre-calculated FSFs. Simulation results accurately quantify the effects of 3D formation heterogeneities on the measurements and reproduce spatial averaging effects observed in MCNP inelastic and capture simulations.

Shoulder-bed effects have the largest impact on the measurements, particularly in thinly-bedded formations, and lead to errors in simulated logs that cause biased representations of elemental and mineral layer values by as much as 170%. The largest errors between fast-simulated and MCNP-simulated logs were observed in complex wells trajectories, such as HA/HZ wells, and in the presence of large perturbations in layer migration lengths. However, differences between fast-simulated and MCNP-simulated logs in these challenging cases did not exceed 5%.

The LWD spectroscopy tool assumed in this chapter operates only in the capture mode, but the inclusion of inelastic measurements in synthetic cases is necessary to quantify (a) carbon and kerogen in unconventional gas-bearing shales, and (b) elements with high statistical variation or elements that are not detectable in the capture

measurement mode. It is important to note that the developed numerical simulation method can be implemented with any other spectroscopy tool, including tools that acquire inelastic measurements.

Due to the speed and reliability of the developed fast-forward algorithm, it can be efficiently used with inversion-based interpretation methods to reduce averaging effects and to quantify true subsurface elemental and mineral composition devoid of geometrical effects. Results from such a method could be readily integrated with other nuclear and resistivity measurements for use in joint petrophysical analysis.

Table 2.1: Calculated elemental inelastic and capture sensitivities. Hyphens indicate negligible values.

Element Name	Element Formula	Calculated Inelastic Sensitivity	Calculated Capture Sensitivity
Aluminum	Al	1.08	1.21
Carbon	C	0.60	-
Calcium	Ca	0.76	1.65
Chlorine	Cl	-	104.93
Iron	Fe	0.72	6.48
Gadolinium	Gd	-	28,364
Hydrogen	H	-	13.10
Potassium	K	0.51	6.03
Magnesium	Mg	0.77	0.40
Oxygen	O	0.75	-
Sulfur	S	0.77	2.54
Silicon	Si	1	1
Titanium	Ti	0.84	17.98

Table 2.2: Elemental and mineral properties assumed in synthetic cases examined in this chapter.

Element Name	Element Formula	Molecular Weight (g/gmol)		Mineral Name	Mineral Formula	Molecular Weight (g/gmol)	Mineral Density (g/cm^3)
Aluminum	Al	26.982		**Quartz**	SiO_2	60.09	2.65
Carbon	C	12.011		**Dolomite**	$CaMg(CO_3)_2$	184.41	2.87
Calcium	Ca	40.078		**Albite**	$NaAlSi_3O_8$	262.24	2.62
Iron	Fe	55.845		**Calcite**	$CaCO_3$	100.091	2.71
Potassium	K	39.1		**Pyrite**	FeS_2	119.97	5.01
Magnesium	Mg	24.305		**Illite**	$K_{0.8}Al_{1.6}Fe_{0.2}Mg_{0.2}Si_{3.4}Al_{0.6}O_{10}O_2H_2$	396.189	2.78
Sulfur	S	32.06		**Mg-Chlorite**	$Mg_5AlSi_3AlO_{10}O_8H_8$	555.819	2.65
Silicon	Si	28.09		**Kaolinite**	$Al_2Si_2O_5O_4H_4$	184.41	2.62
				K-Feldspar	$KAlSi_3O_8$	278.35	2.57
				Kerogen	$C_{102}H_{94}O_{17}$	1591.9	1.4
				Hydrocarbon-Oil	C_8H_{18}	114.232	0.82
				Hydrocarbon-Gas	CH_4	16.043	0.178
				Water	H_2O	18.015	1

Table 2.3: Layer true stratigraphic thickness (TST), migration lengths, layer elemental, mineral, and fluid compositions assumed in Synthetic Case No. 1.

Layer	Layer TST (cm)	L_m (cm)	Volumetric Concentrations (%)				Formation Elemental Weight Concentrations (%)		
			Solids		Fluids				
			Quartz	Dolomite	Hydrocarbon-Oil	Water	Magnesium	Silicon	Calcium
I	91.44	16.25	65	10	15	10	1.7	36.07	2.79
II	30.48	14.51	10	60	15	15	10.05	5.48	16.56
III	60.96	15.33	20	55	10	15	8.89	10.59	14.66
IV	91.44	21.12	80	10	3	7	1.51	39.62	2.49
V	30.48	17.07	70	15	3	12	11.77	2.47	19.39
VI	60.96	15.12	10	65	2.5	22.5	10.35	5.21	17.06
VII	91.44	17.06	60	20	0	20	3.2	31.44	5.28

Table 2.4: Layer true stratigraphic thickness (TST), migration lengths, layer mineral, and fluid compositions assumed in Synthetic Case No. 2.

Layer	Layer TST (cm)	L_m (cm)	Volumetric Concentrations (%)								
			Solids							Fluids	
			Quartz	Albite	Calcite	Pyrite	Kerogen	Illite	Mg-Chlorite	Hydro Carbon -Gas	Water
I	91.44	19.59	7.72	2.14	66.69	1.21	4.09	9.14	2.02	4.76	2.23
II	24.38	20.51	6.26	1.59	73.04	0.65	3.64	6.9	1.32	5.01	1.59
III	91.44	19.03	7.01	2.62	66.61	1.49	6.45	8.17	1.08	4.67	1.91
IV	30.48	19.21	10.17	3.96	61.05	1.32	5.46	11.1	1.15	3.53	2.26
V	91.44	18.93	11.93	4.94	59.85	1.21	5.87	8.47	0.94	3.49	3.49
VI	21.34	23.38	37.83	3.96	47.67	0.77	1.06	1.54	3.67	1.91	1.59
VII	91.44	23.15	10.78	2.65	76.97	0.76	1.13	1.3	0.96	4.13	1.31
VIII	30.48	24.13	14	1.81	75.99	0.38	0.57	1.1	1.37	3.8	0. 98
IX	91.44	23.71	7.25	1.62	82.9	0.29	1.14	1.54	0.66	3.62	0.98

Table 2.5: Layer elemental compositions assumed in Synthetic Case No. 2.

Layer	Formation Elemental Weight Concentrations (%)									
	Formation carbon	**Kerogen carbon**	**Sodium**	**Sulfur**	**Magnesium**	**Aluminum**	**Silicon**	**Potassium**	**Calcium**	**Iron**
I	10.43	0.48	0.14	0.15	0.17	0.48	4.50	0.13	34.81	0.30
II	9.57	0.24	0.16	0.20	0.32	0.50	7.80	0.09	31.92	0.38
III	9.75	0.48	0.24	0.39	0.24	0.59	6.56	0.11	32.54	0.73
IV	5.96	0.44	0.35	0.40	0.84	1.02	20.26	0.13	19.89	0.74
V	7.80	2.54	0.46	0.65	0.33	2.05	10.02	0.75	26.04	1.40
VI	7.88	2.34	0.36	0.70	0.41	2.37	9.46	0.97	26.28	1.57
VII	8.71	2.79	0.24	0.80	0.36	1.76	6.75	0.72	29.06	1.66
VIII	9.45	1.56	0.15	0.35	0.40	1.45	5.67	0.60	31.54	0.82
IX	8.65	1.76	0.20	0.65	0.59	1.96	7.30	0.80	28.86	1.41

Table 2.6: Layer true stratigraphic thickness (TST), migration lengths, layer mineral, and fluid compositions assumed in Synthetic Case No. 3.

Layer	Layer TST (cm)	L_m (cm)	Volumetric Concentrations (%)					
			Solids				Fluids	
			Calcite	Illite	Kaolinite	Quartz	Hydrocarbon-Oil	Water
I	52.93	18.17	38	40	10	10	0	2
II	30.48	12.44	5	5	54	6	29	1
III	15.24	14.15	30	10	45	5	5	5
IV	30.48	18.17	38	40	10	10	0	2
V	15.24	12.44	5	5	54	6	29	1
VI	30.48	14.15	30	10	45	5	5	5
VII	15.24	18.17	38	40	10	10	0	2
VIII	30.48	12.44	5	5	54	6	29	1
IX	15.24	14.15	30	10	45	5	5	5
X	30.48	12.44	38	40	10	10	0	2
XI	15.24	14.49	5	5	54	6	29	1
XII	30.48	14.15	30	10	45	5	5	5
XIII	52.93	18.17	38	40	10	10	0	2

Table 2.7: Layer elemental compositions assumed in Synthetic Case No. 3.

Layer	Formation Elemental Weight Concentrations (%)					
	Magnesium	**Aluminum**	**Silicon**	**Potassium**	**Calcium**	**Iron**
I	0.51	8.23	16.69	3.26	15.33	1.17
II	0.14	11.54	15.45	0.88	13.04	0.31
III	0.08	15.1	19.83	0.52	02.59	0.19
IV	0.51	8.23	16.69	3.26	15.33	1.17
V	0.14	11.54	15.45	0.88	13.04	0.31
VI	0.08	15.1	19.83	0.52	2.59	0.19
VII	0.51	8.23	16.69	3.26	15.33	1.17
VIII	0.14	11.54	15.45	0.88	13.04	0.31
IX	0.08	15.1	19.83	0.52	2.59	0.19
X	0.51	8.23	16.69	3.26	15.33	1.17
XI	0.14	11.54	15.45	0.88	13.04	0.31
XII	0.08	15.1	19.83	0.52	2.59	0.19
XIII	0.51	8.23	16.69	3.26	15.33	1.17

Table 2.8: Comparison of CPU times required to calculate MCNP and fast-simulated logs for the synthetic cases reported in this chapter and average difference for each case.

Case		Measurement Points	CPU time		Error (%)	
			MCNP (days)	Fast Simulation (s)	Average Relative Error in y_i and M_i	Average Uncertainty in Inverted C_j
1	a	61	25.82	1.66	2	3.5
	b	122	51.47	2.51	2	3.5
	c	122	46.96	2.33	3	4
2	a	29	11.55	4.16	1	3
	b	110	45.16	6.73	1	4.6
3		275	113.65	9.82	5	7.3

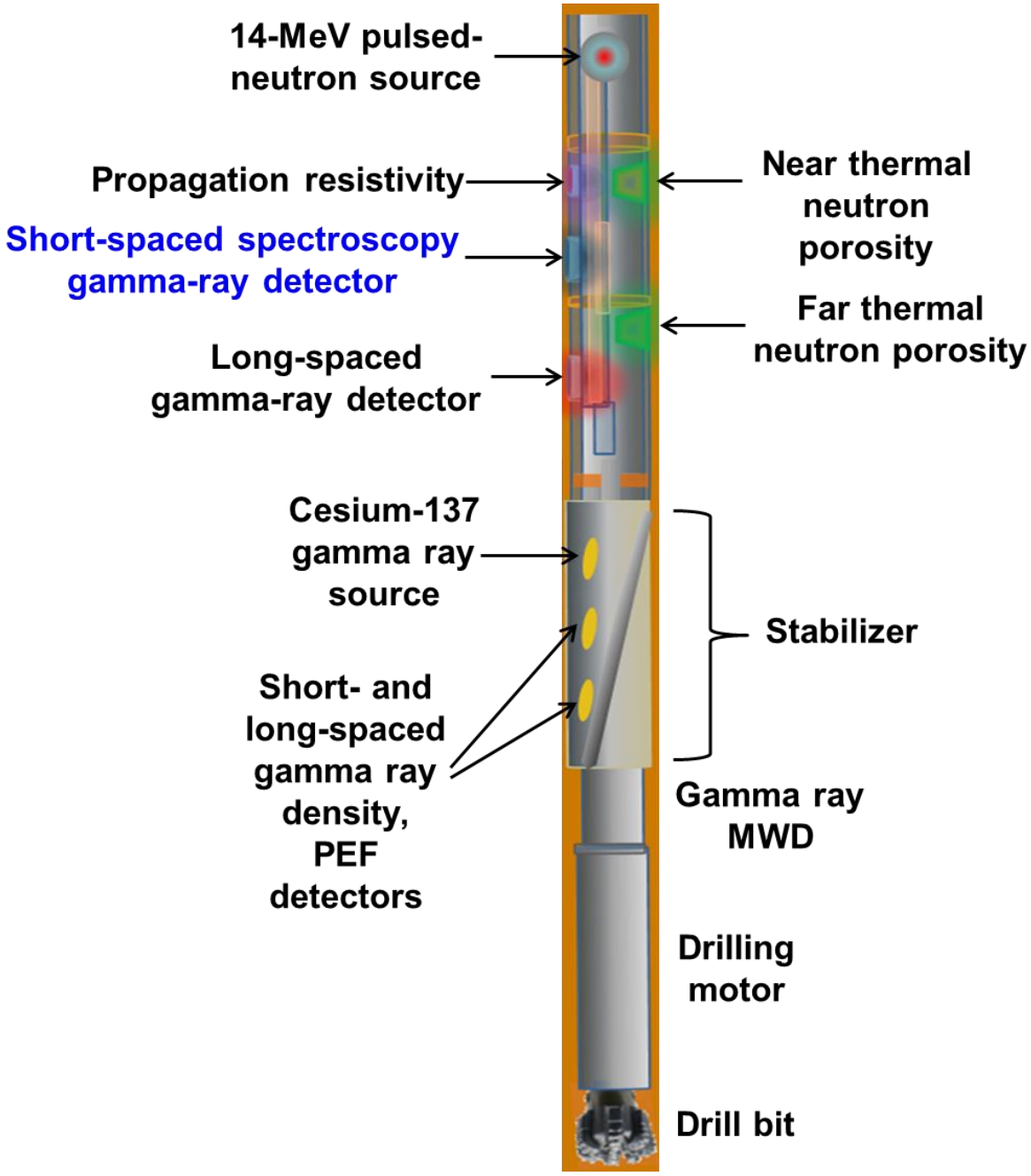

Figure 2.1: Schematic of the commercial LWD spectroscopy tool assumed in this chapter (modified from Ortega et al. 2014a).

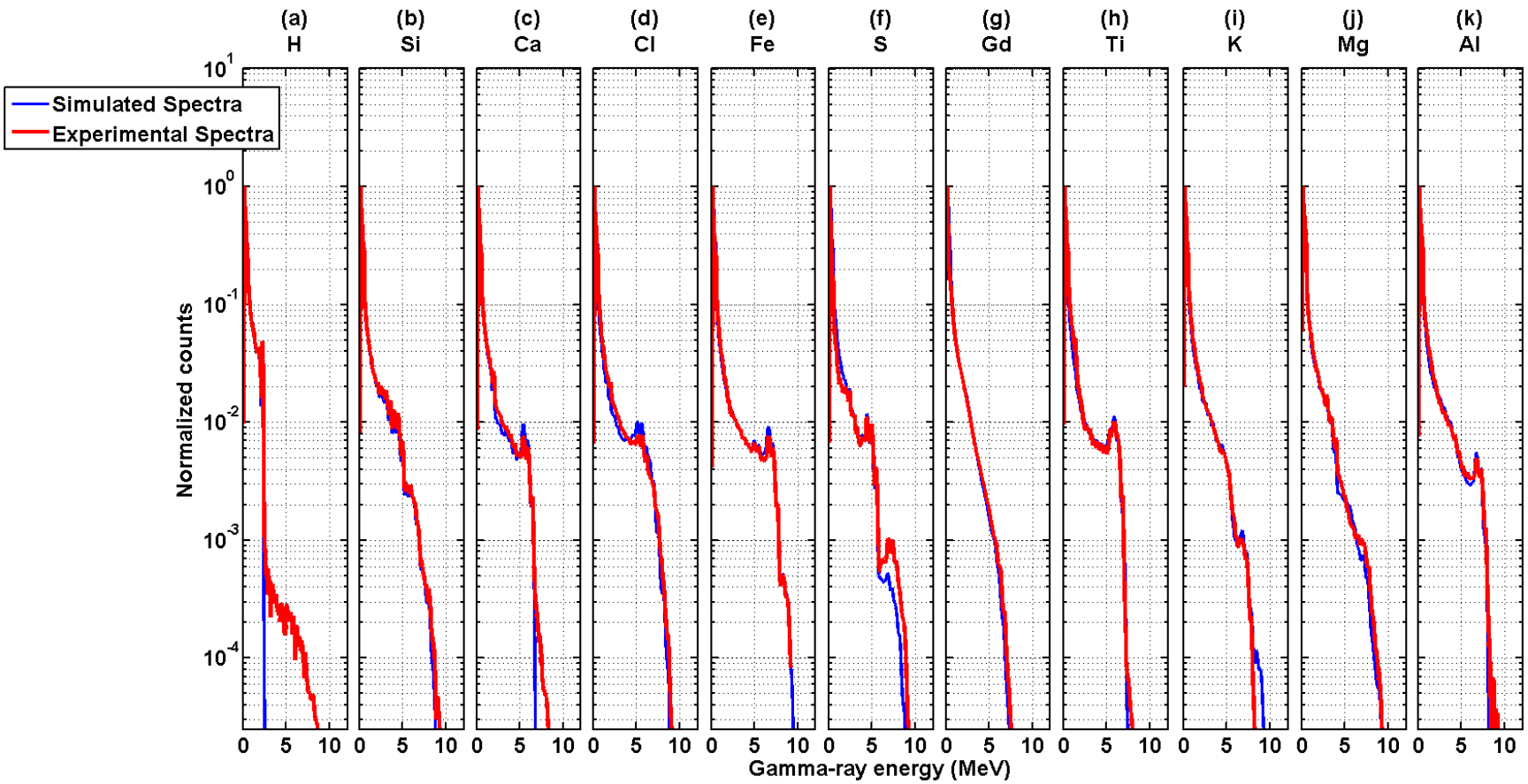

Figure 2.2: Comparison between MCNP-simulated capture pulse height spectra in panel (a) and tool experimental capture spectra standards in panel (b). Note: the vertical axis on panels (a) and (b) is not shown because spectroscopy count data of the commercial tool under study are confidential.

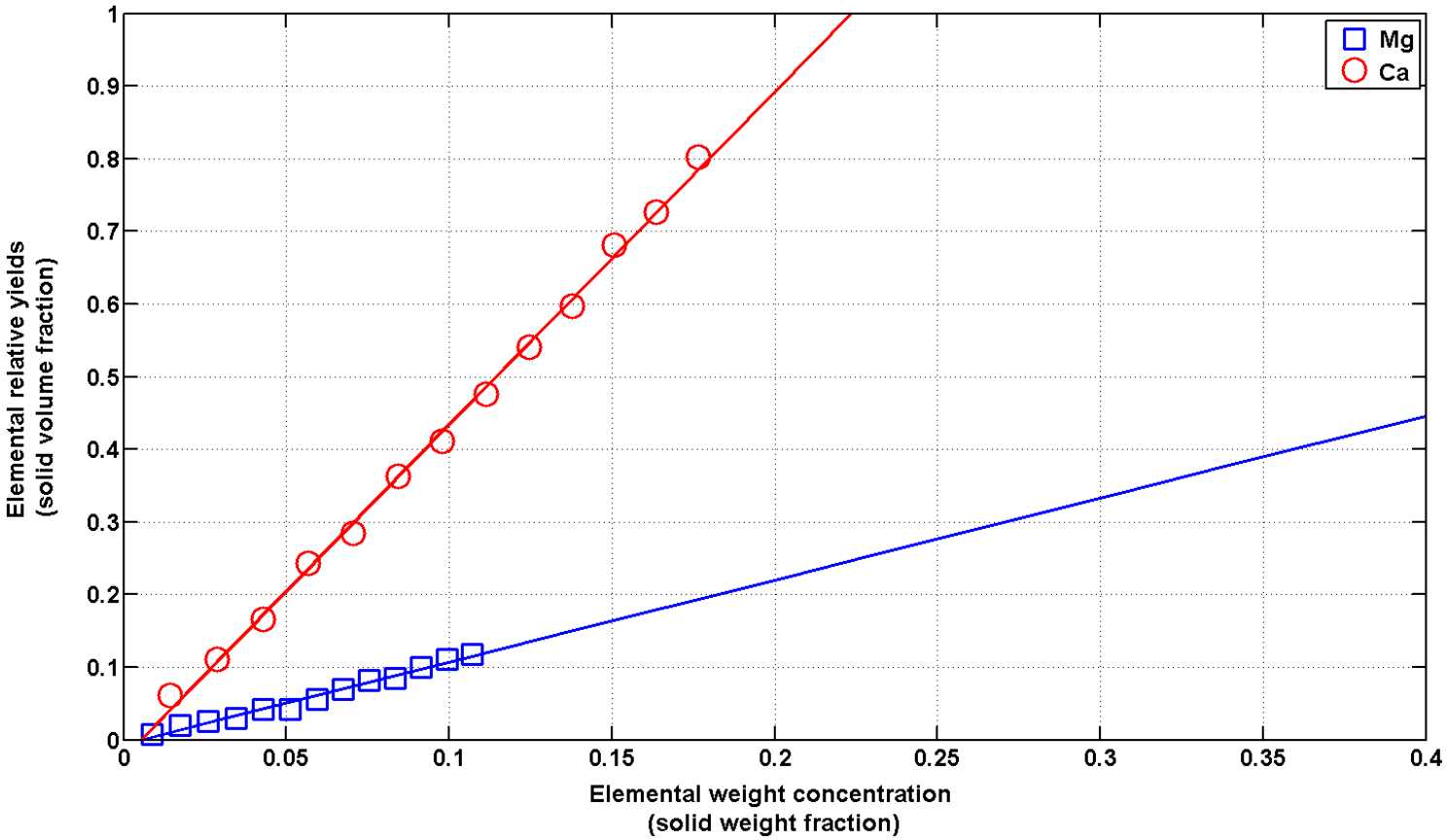

Figure 2.3: Constant linear relationship between capture elemental relative yields and weight concentrations.

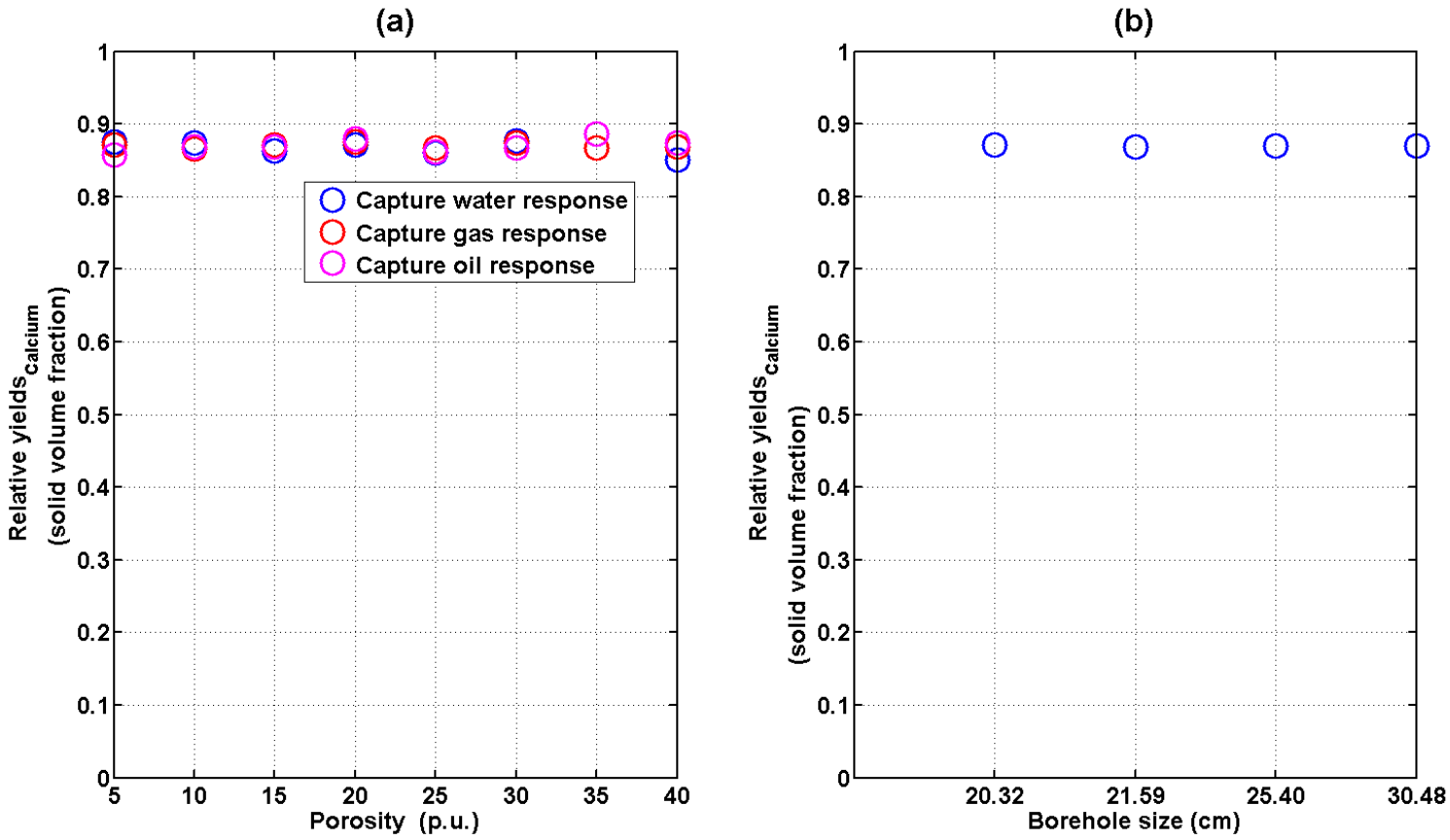

Figure 2.4: Insensitivity of capture calcium relative yields in porous dolomite to variations of (a) porosity and fluid type, and (b) borehole size.

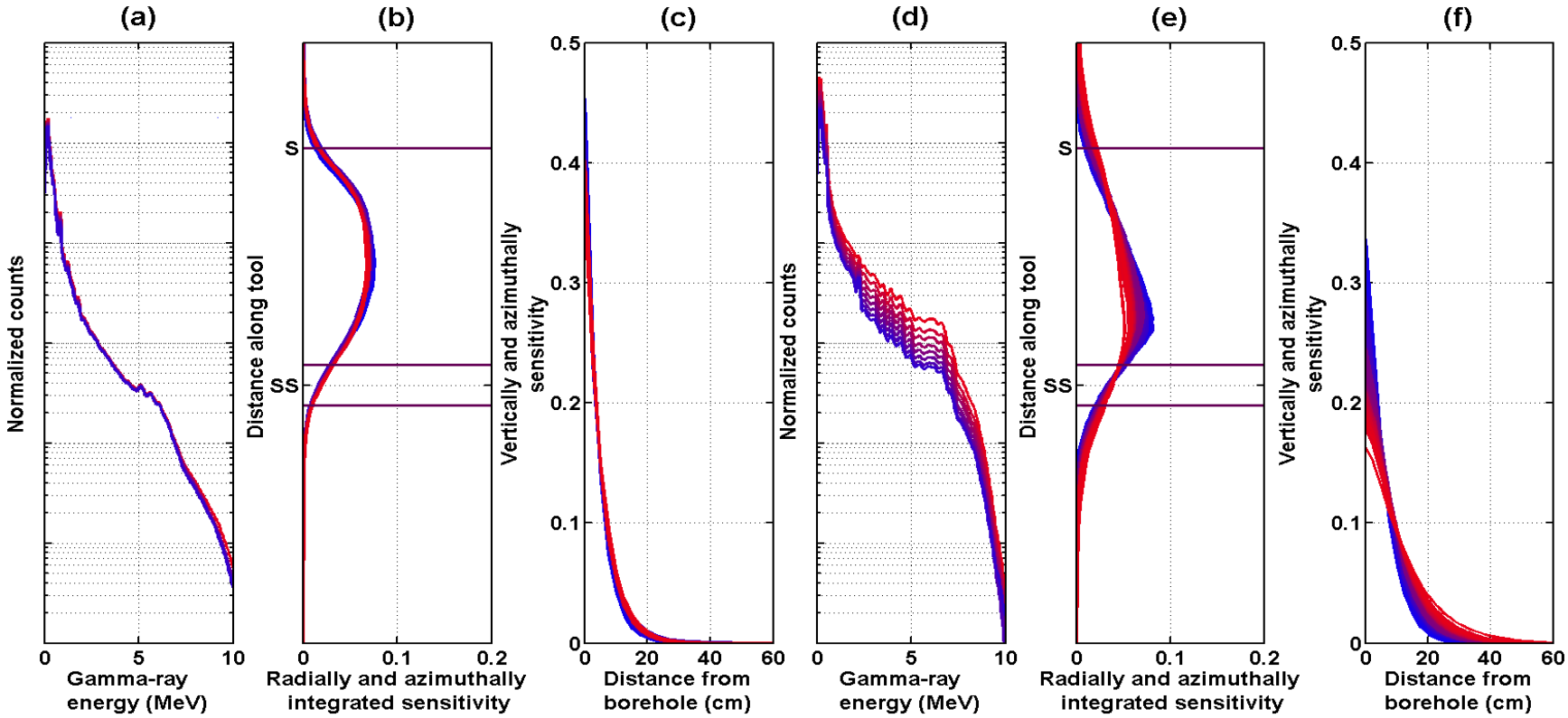

Figure 2.5: Impact of variations in migration length on formation spectra and neutron FSFs for both inelastic and capture spectra. Panels (a) and (d) show inelastic and capture spectra, respectively. Panels (b) and (e) show radially and azimuthally integrated inelastic and capture neutron FSFs along the tool, respectively, where purple lines at S and SS identify the pulsed-neutron source, short-spaced detector, and long-spaced detector positions along the tool, respectively. Panels (c) and (f) show vertically and azimuthally integrated inelastic and capture neutron FSFs as a function of radial distance into the formation, respectively. The transition from blue to red colors indicates increase in migration length. Note: the vertical axis on panels (a), (b), (d), and (e) is not shown because spectroscopy count data, location of the neutron source and gamma-ray detectors of the commercial tool under study are confidential.

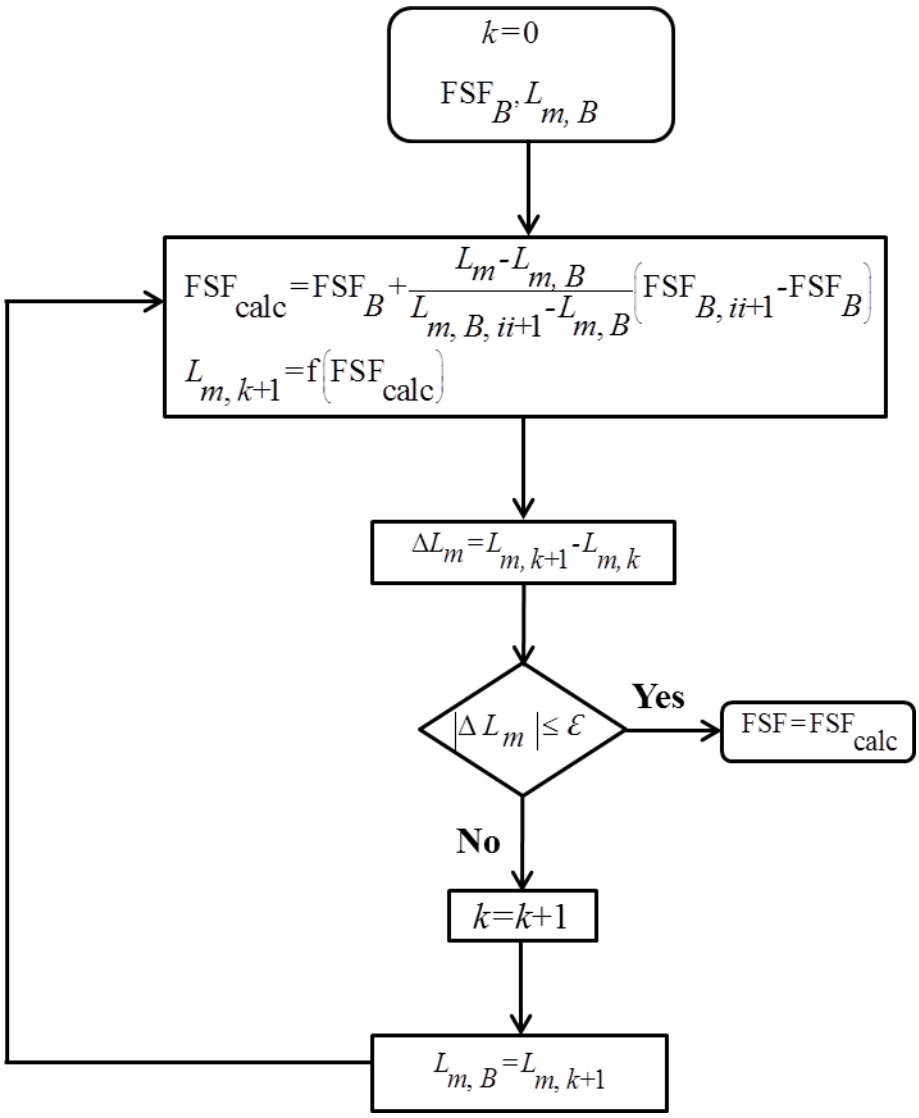

Figure 2.6: Flow chart describing the calculation of flux sensitivity functions used in the spectroscopy forward model at each measurement point. FSF is the flux sensitivity function (depends on the value of migration length) while $\mathrm{FSF}_{\mathrm{calc}}$ describes an FSF calculated through linear interpolation and is used to update the migration length, L_m, at each iteration. Subscript B denotes the selected reference base-case formation effective migration length and FSF, k is the iteration number, and subscript ii denotes the index of the background migration length and FSF in the library. The symbol ε describes a pre-specified threshold used to diagnose convergence.

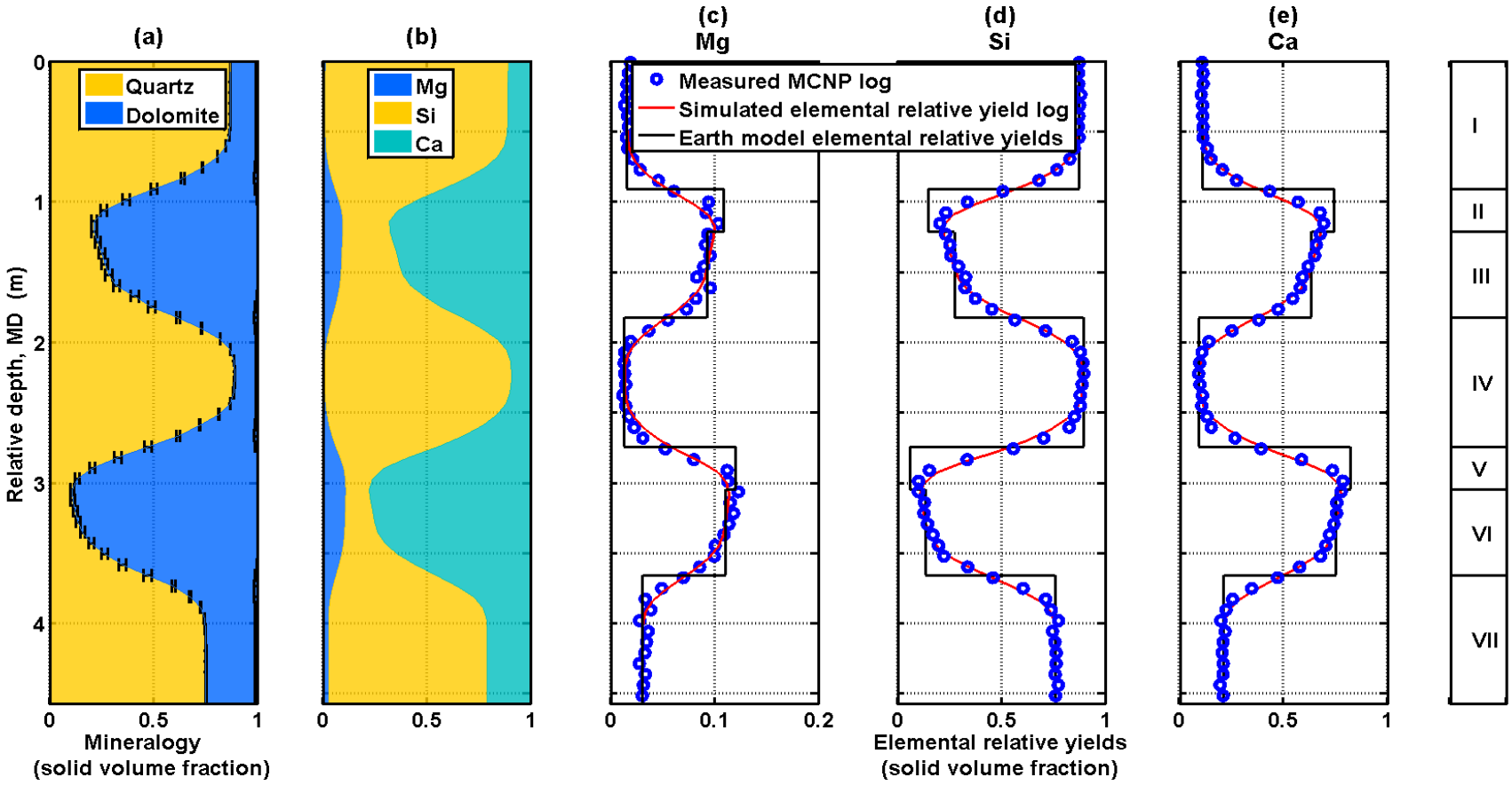

Figure 2.7: Comparison of numerically simulated (red solid lines) and MCNP-simulated capture elemental spectroscopy logs (blue open circles) in panels (c) to (e) for Synthetic Case No. 1(a). Panel (a) displays inverted mineral volumetric concentrations and error bars describe the uncertainty in their estimation. Panel (b) is a cumulative plot of simulated elemental relative yield logs displayed in panels (c) to (e). Mg, Si, and Ca refer to elements magnesium, silicon, and calcium, respectively; I to VII identify distinct layers in the synthetic case. Black blocky logs describe layer elemental relative yields.

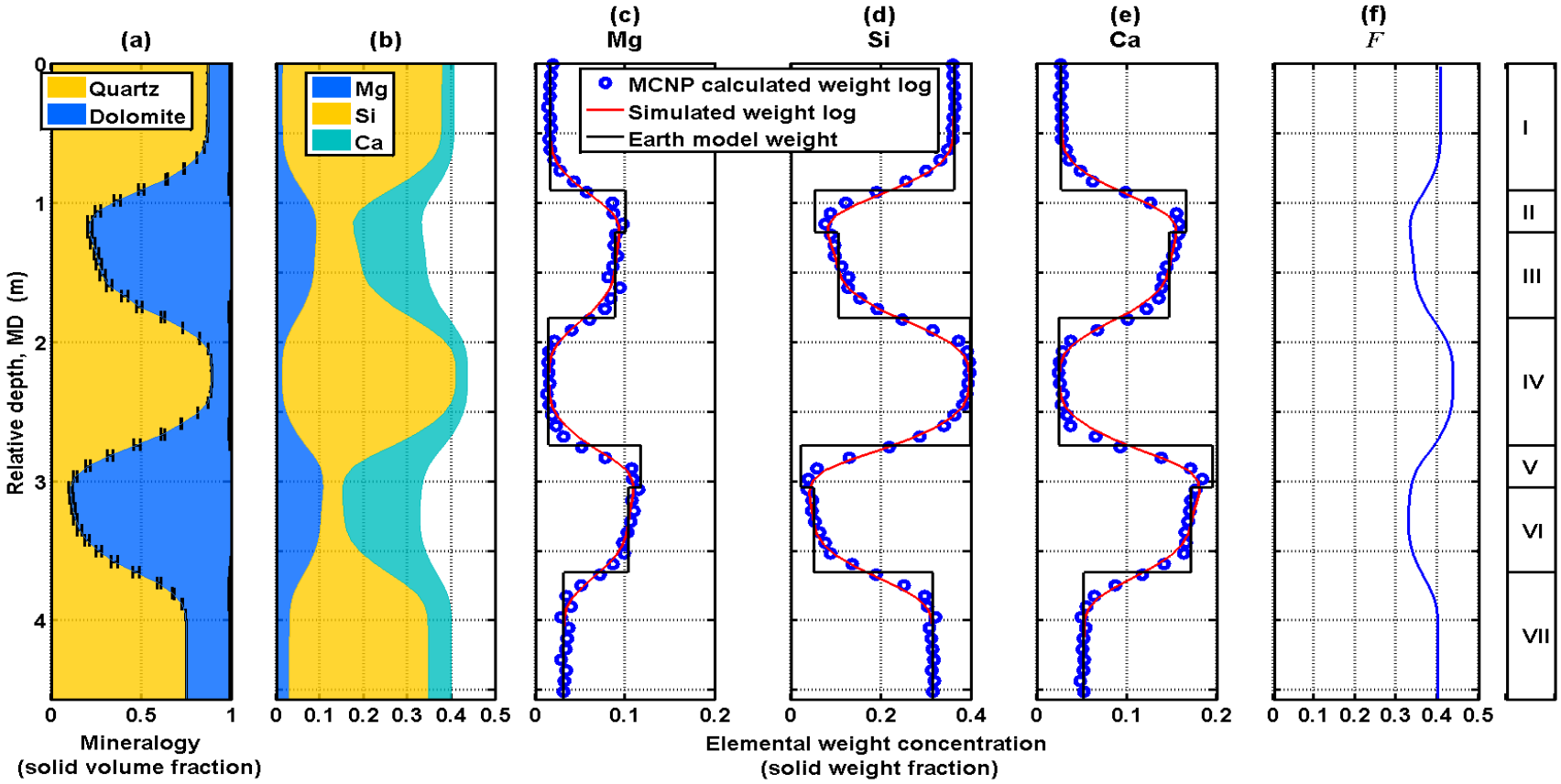

Figure 2.8: Comparison of elemental weight concentrations calculated from numerically simulated capture relative yield logs (red solid lines) to elemental weight concentrations calculated from MCNP-simulated capture relative yield logs (blue open circles) shown in panels (c) to (e) for Synthetic Case No. 1(a). Black blocky logs describe model values of layer elemental weight concentrations. Panel (a) displays inverted mineral volumetric concentrations and error bars describe the uncertainty in their estimation. Panel (b) is a cumulative plot of simulated elemental weight concentrations shown in panels (c) to (e). The blue continuous log in panel (f) describes the depth-varying normalization factor, F, calculated from equation 2.3, while I to VII identify distinct layers in the synthetic case.

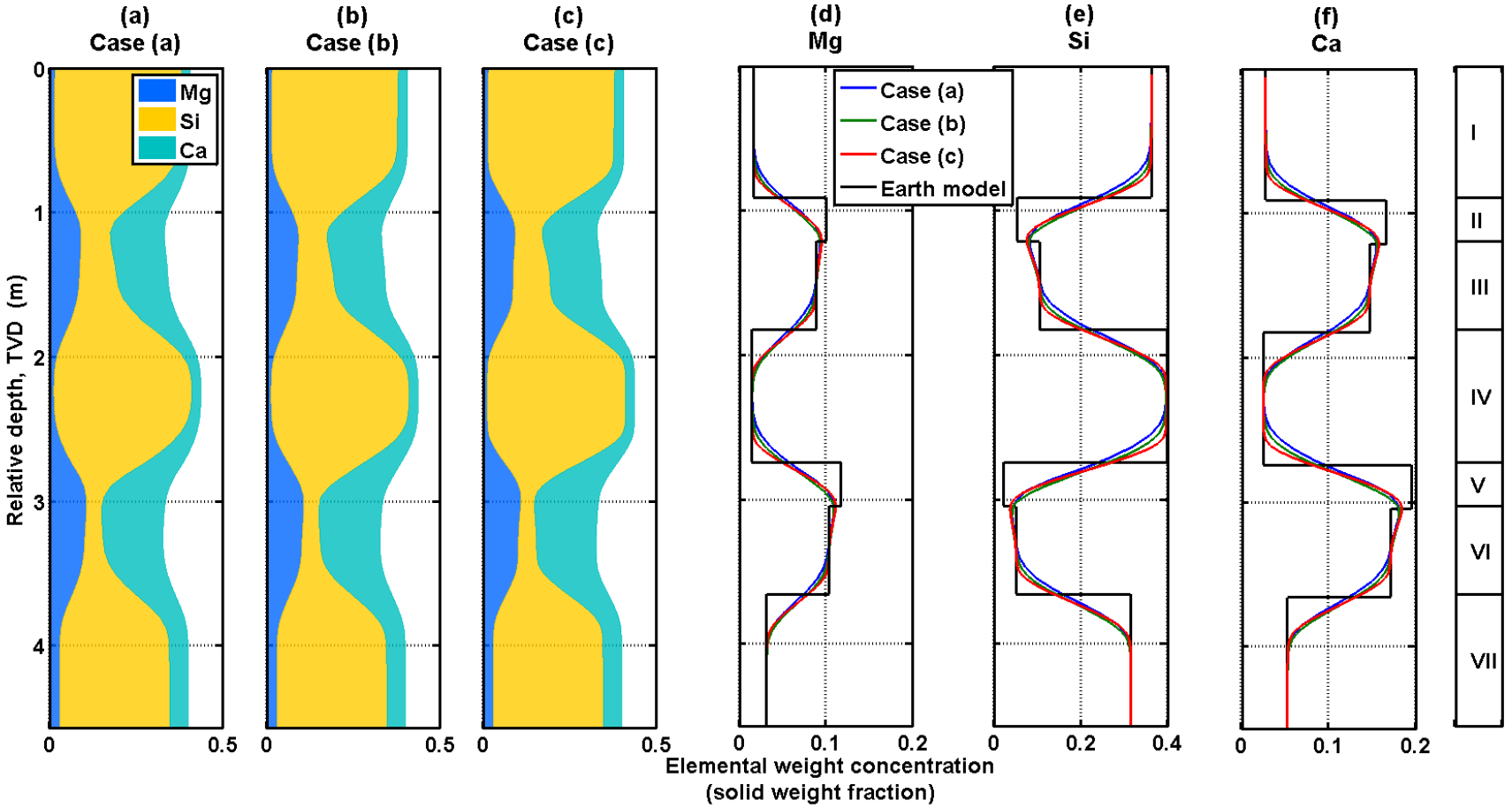

Figure 2.9: Comparison of elemental weight concentrations in Synthetic Case No. 1 for cases (a), (b), and (c). Panels (a) to (c) display cumulative plots of simulated elemental weight logs for cases (a), (b), and (c), respectively. Panels (d) to (f) show comparative plots of the cases displayed in panels (a) to (c) for each element. Black blocky logs describe model values of layer elemental weight concentrations; I to VII identify distinct layers in the synthetic case.

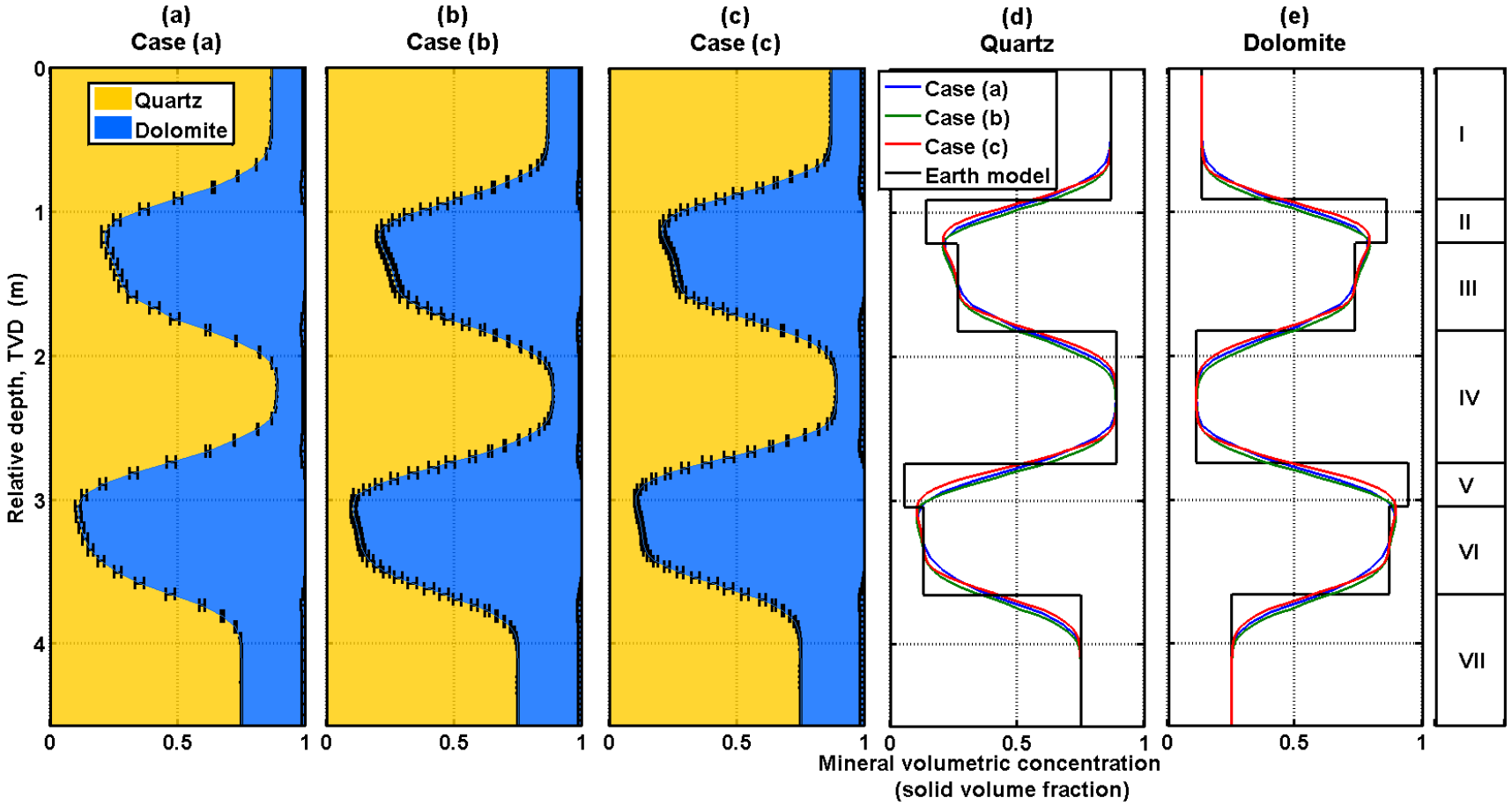

Figure 2.10: Comparison of inverted mineral volumetric concentrations in Synthetic Case No. 1 for cases (a), (b), and (c). Panels (a) to (c) display cumulative plots of mineral logs for cases (a), (b), and (c), respectively, and error bars describe the uncertainty in their estimation. Panels (d) to (e) show comparative plots of the cases displayed in panels (a) to (c) for each mineral; black blocky logs describe the model values of layer mineral volumetric concentrations; I to VII identify distinct layers in the synthetic case.

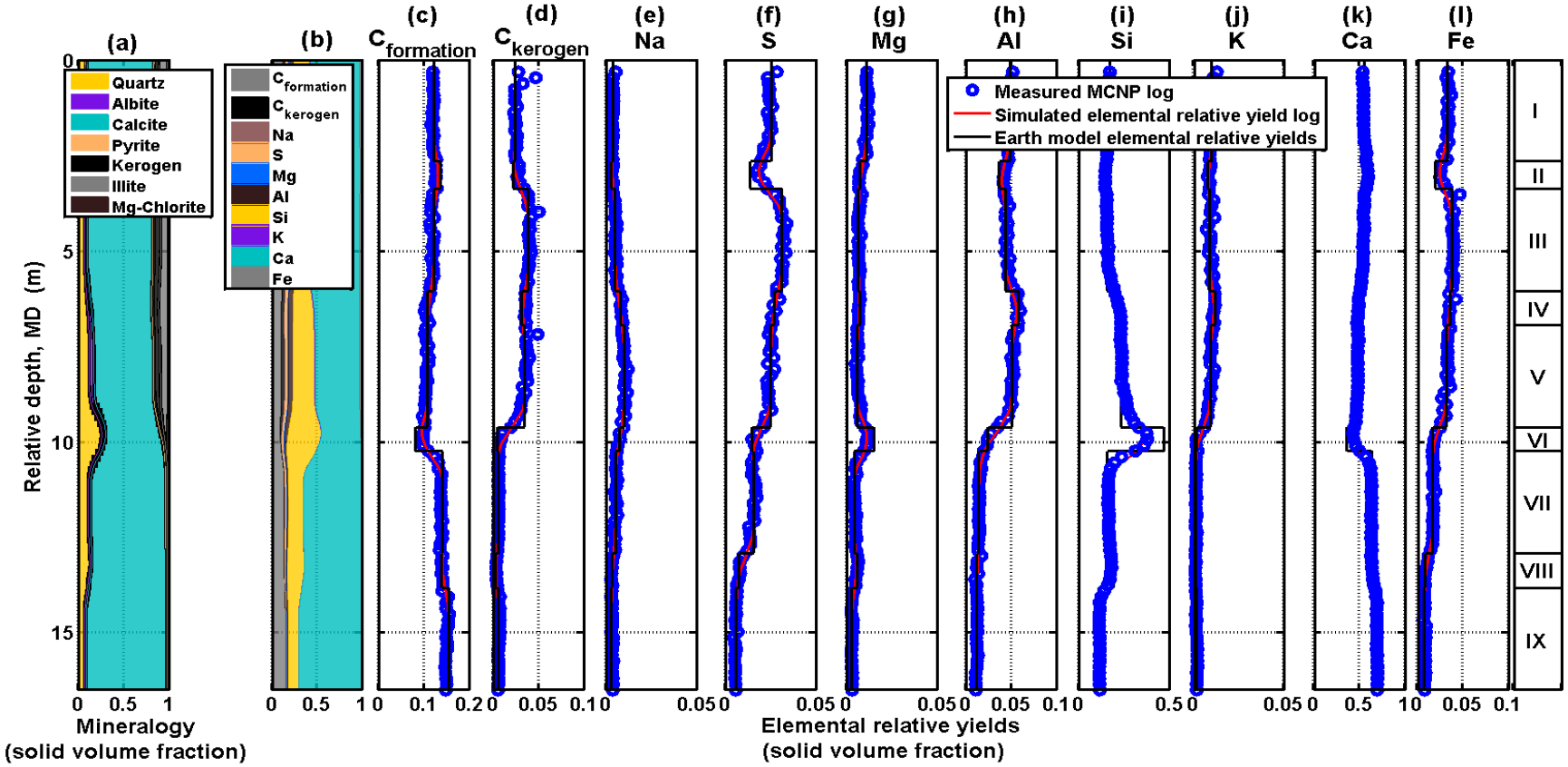

Figure 2.11: Comparison of numerically simulated (red solid lines) and MCNP-simulated inelastic elemental spectroscopy logs (blue open circles) in panels (c) to (l) for Synthetic Case No. 2(a). Panel (a) displays inverted mineral volumetric concentrations and error bars describe the uncertainty in their estimation. Panel (b) is a cumulative plot of simulated elemental relative yield logs displayed in panels (c) to (l). $C_{formation}$, $C_{kerogen}$, Na, S, Mg, Al, Si, K, Ca, and Fe refer to carbon present in the formation, carbon present in kerogen, sodium, sulfur, magnesium, aluminum, silicon, potassium, and calcium, respectively; I to IX identify distinct layers in the synthetic case. Black blocky logs describe layer elemental relative yields.

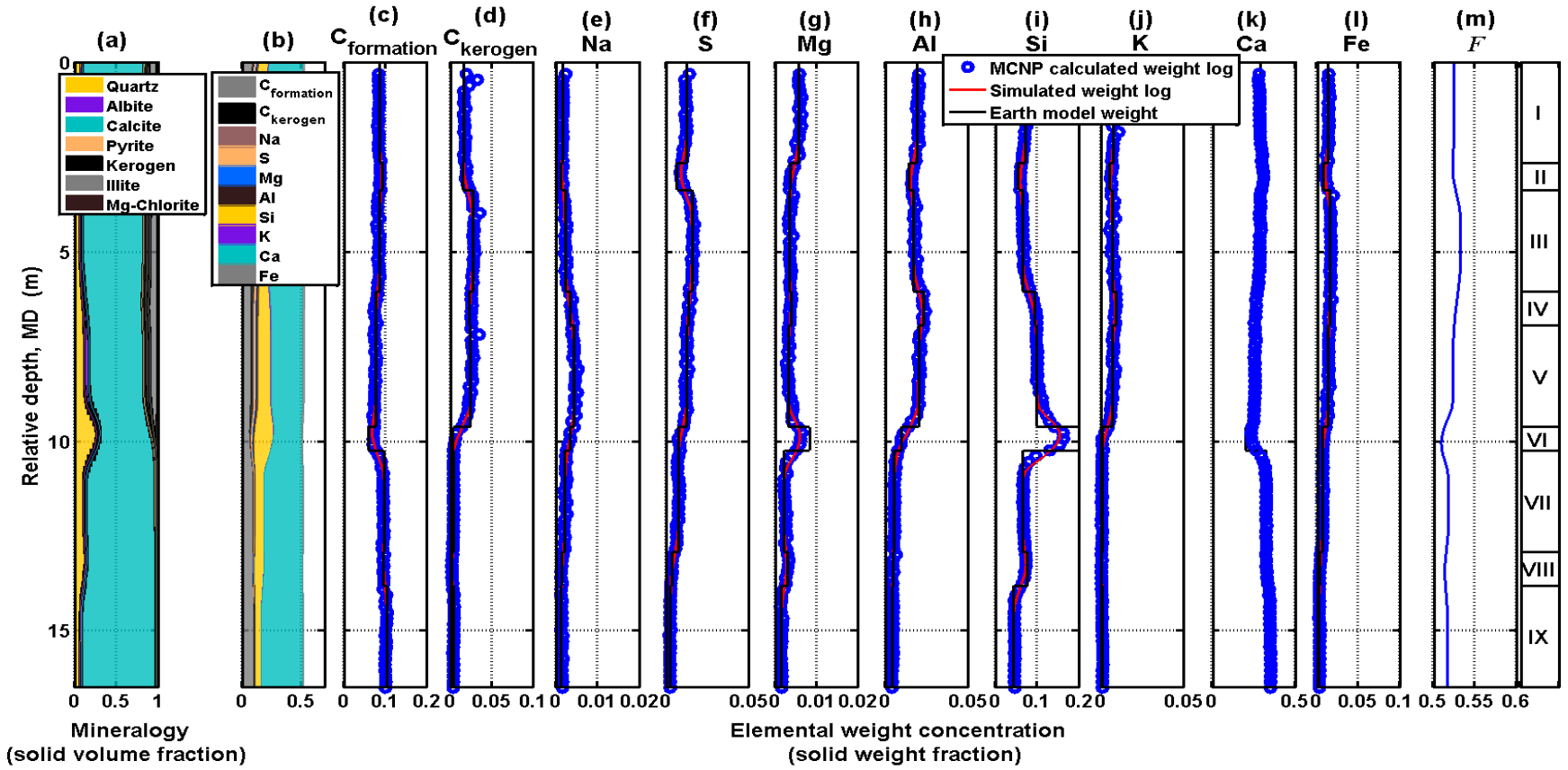

Figure 2.12: Comparison of elemental weight concentrations calculated from numerically simulated inelastic relative yield logs (red solid lines) to elemental weight concentrations calculated from MCNP-simulated inelastic relative yield logs (blue open circles) shown in panels (c) to (l) for Synthetic Case No. 1(a). Black blocky logs describe model values of layer elemental weight concentrations. Panel (a) displays inverted mineral volumetric concentrations and error bars describe the uncertainty in their estimation. Panel (b) is a cumulative plot of simulated elemental weight concentrations shown in panels (c) to (l). The blue continuous log in panel (m) describes the depth-varying normalization factor, F, calculated from equation 2.3, while I to IX identify distinct layers in the synthetic case.

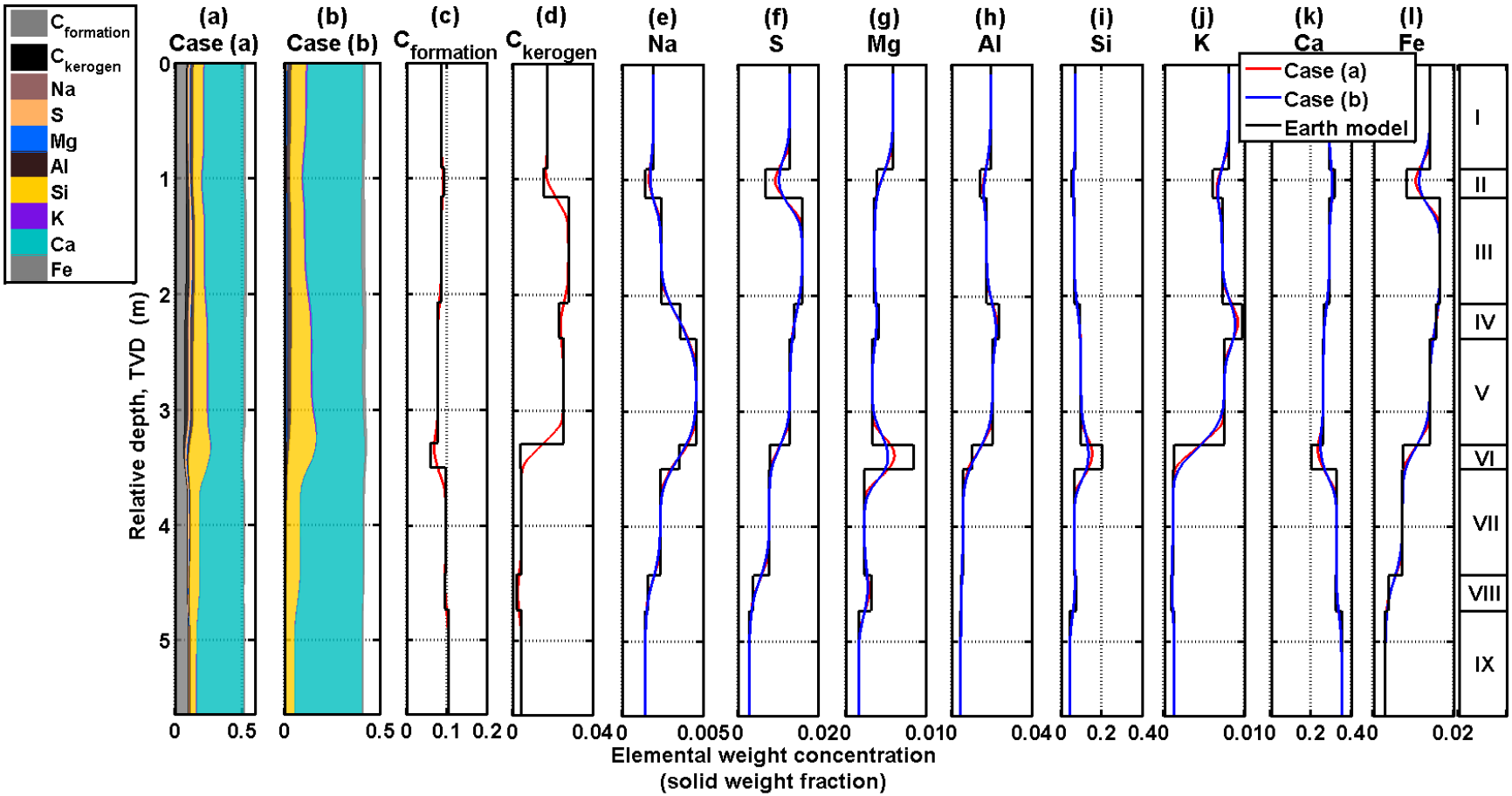

Figure 2.13: Comparison of elemental weight concentrations in Synthetic Case No. 2 for cases (a) and (b). Panels (a) and (b) display cumulative plots of simulated elemental weight logs for cases (a) and (b), respectively. Panels (c) to (l) show comparative plots of the panels displayed in panels (a) and (b) for each element; black blocky logs describe model values of layer elemental weight concentrations; I to IX identify distinct layers in the synthetic case.

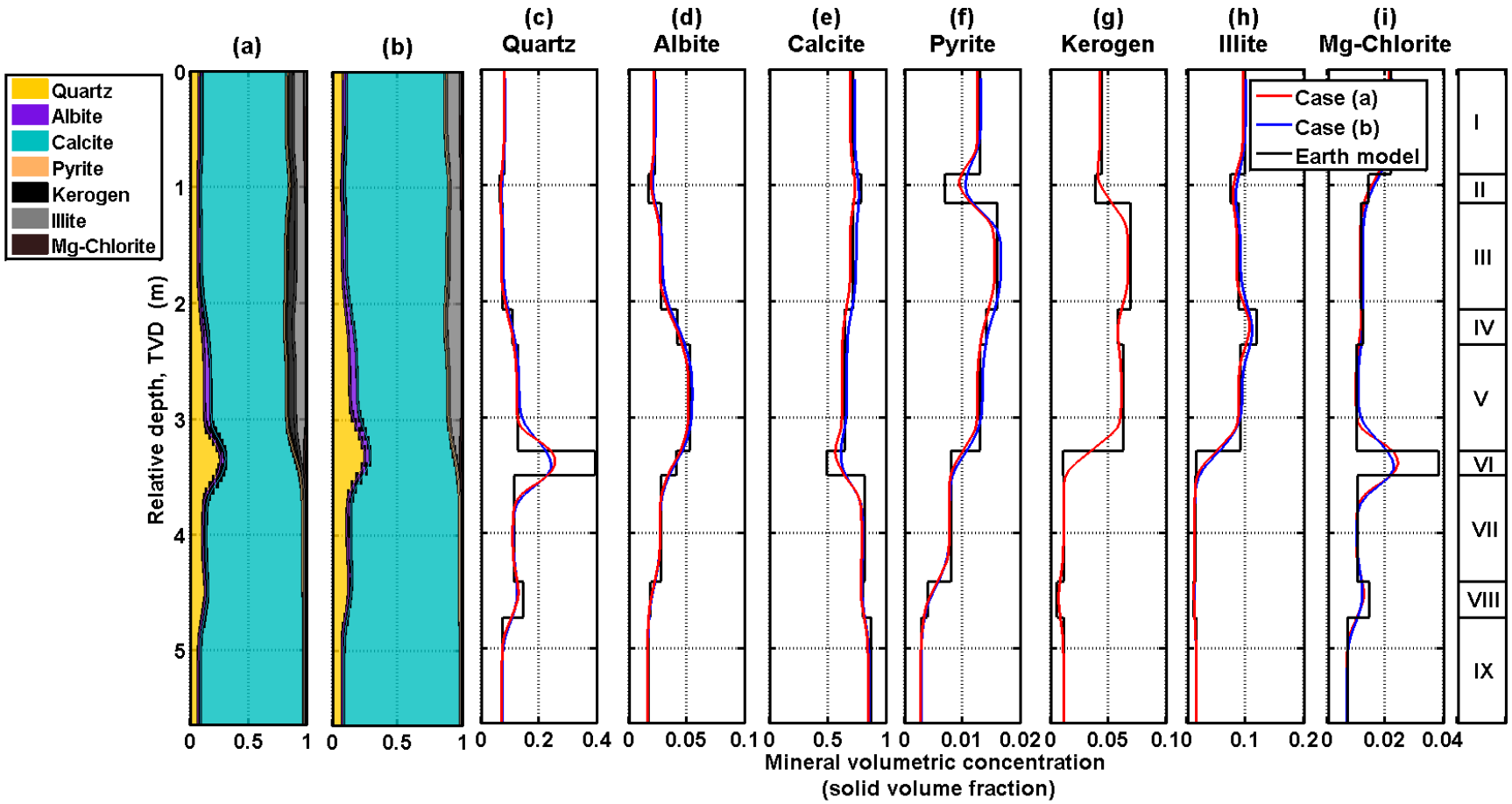

Figure 2.14: Comparison of mineral volumetric concentrations in Synthetic Case No. 2 for cases (a) and (b). Panels (a) and (b) display cumulative plots of mineral logs for cases (a) and (b), respectively. Panel (a) displays inverted mineral volumetric concentrations and error bars describe the uncertainty in their estimation. Panels (c) to (i) show comparative plots of the cases displayed in panels (a) and (b) for each element; black blocky logs describe model values of layer mineral volumetric concentrations; I to IX identify distinct layers in the synthetic case.

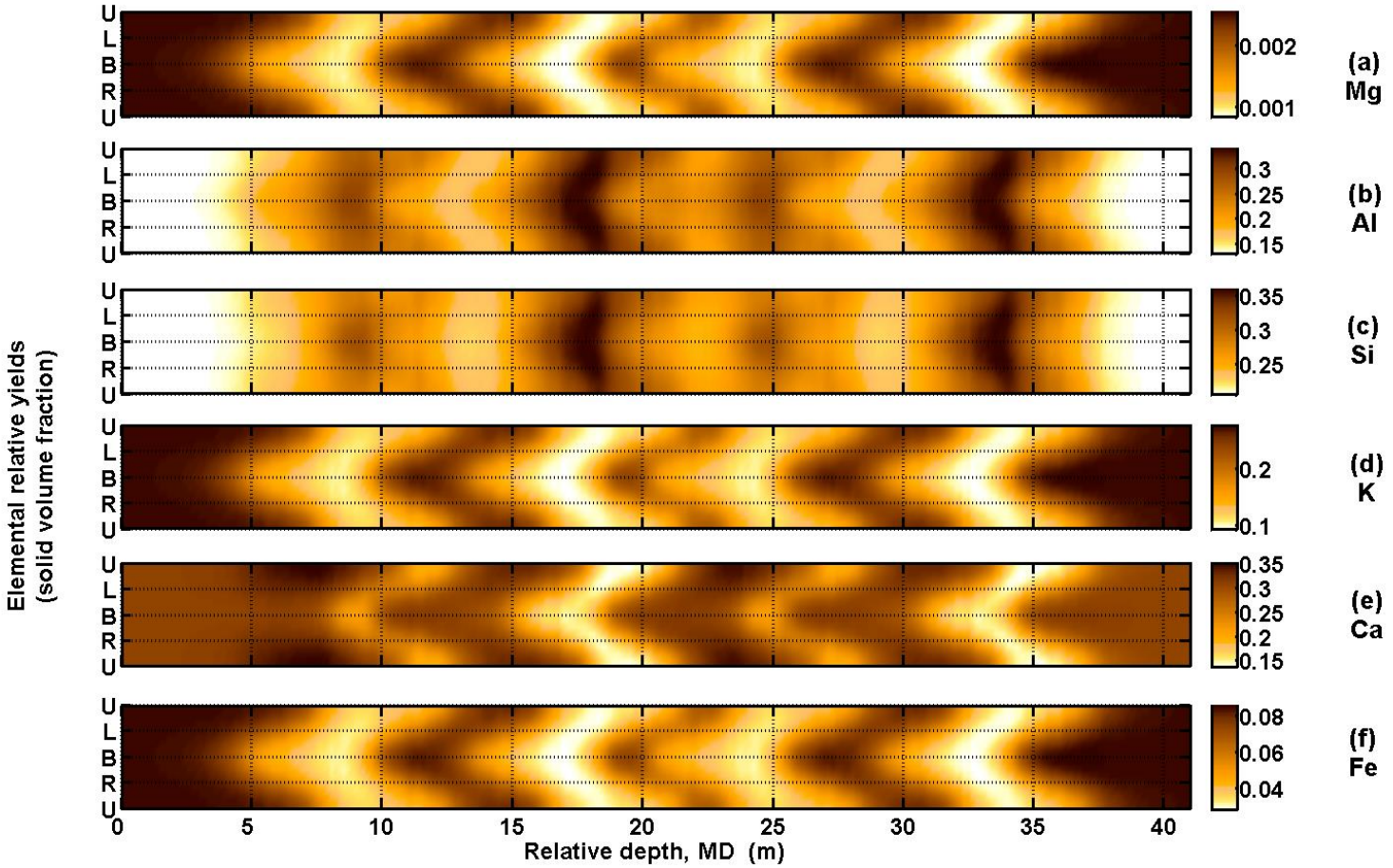

Figure 2.15: Simulated elemental spectroscopy capture image logs. Panels (a) to (f) display the azimuthal distribution of magnesium, aluminum, silicon, potassium, calcium, and iron relative yields, respectively, for Synthetic Case No. 3; U, L, B, R on the y axes identify upper, left, bottom, and right quadrants, respectively.

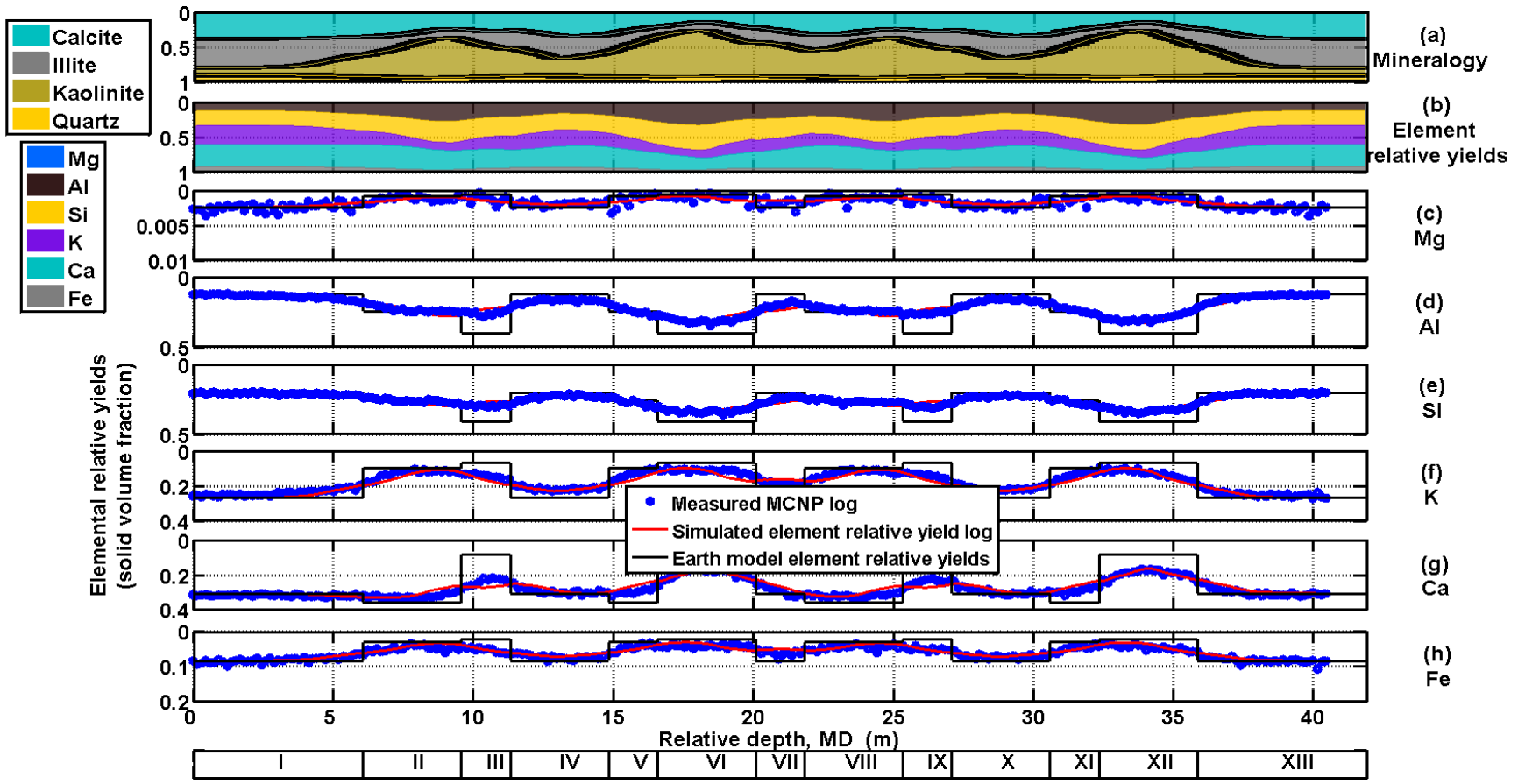

Figure 2.16: Comparison of numerically simulated (red solid lines) and MCNP-simulated capture elemental spectroscopy logs (blue open circles) in panels (c) to (h) for Synthetic Case No. 3. Panel (a) displays inverted mineral volumetric concentrations and error bars describe the uncertainty in their estimation. Panel (b) is a cumulative plot of simulated elemental relative yield logs displayed in panels (c) to (h). Mg, Al, Si, K, Ca, and Fe refer to elements magnesium, aluminum, silicon, potassium, calcium, and iron, respectively; I to XIII identify distinct layers in the synthetic case. Black blocky logs describe layer elemental relative yields.

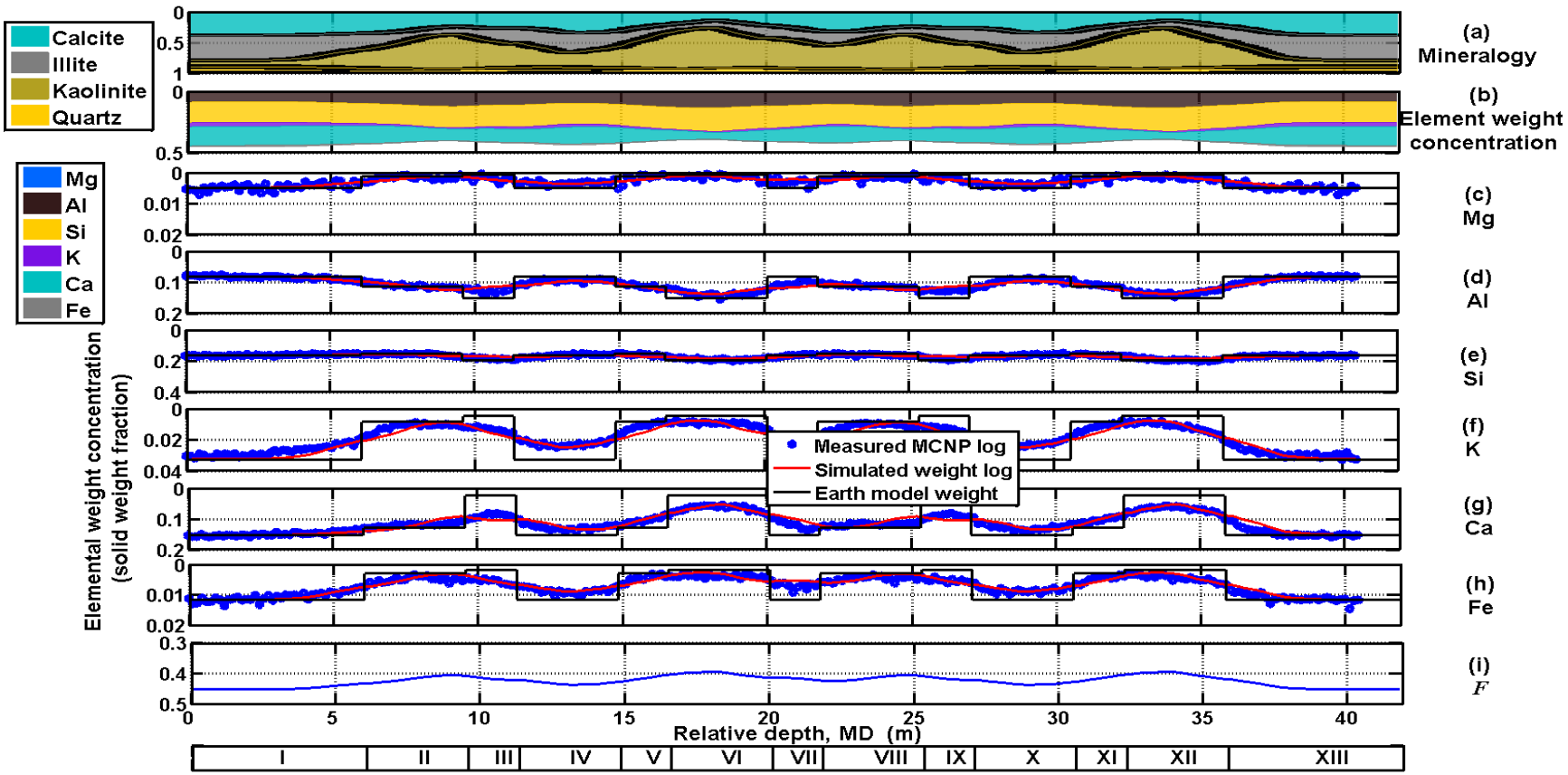

Figure 2.17: Comparison of elemental weight concentrations calculated from numerically simulated capture relative yield logs (red solid lines) to elemental weight concentrations calculated from MCNP-simulated capture relative yield logs (blue open circles) shown in panels (c) to (h) for Synthetic Case No. 3. Black blocky logs describe model values of layer elemental weight concentrations. Panel (a) displays inverted mineral volumetric concentrations and error bars describe the uncertainty in their estimation. Panel (b) is a cumulative plot of simulated elemental weight concentrations shown in panels (c) to (h). The blue continuous log in panel (i) describes the depth-varying normalization factor, F, calculated from equation 2.3, while I to XIII identify distinct layers in the synthetic case.

Chapter 3: Improved Mineral and Petrophysical Analysis using Neutron-Capture Gamma-Ray Spectroscopy Elemental Logs

Neutron and density porosity logs are typically acquired based on the assumption of a freshwater saturated homogeneous formation comprising sandstone or limestone. Realistically, formations are extremely heterogeneous and consist of different minerals and fluids in varying proportions which cause simultaneous matrix and fluid effects in measured porosity logs that have an assumed single matrix and fluid type. Detailed quantification of formation mineral compositions facilitates the correction of matrix effects and reveals fluids effects on measured porosity logs which enables accurate quantification of true porosities and water saturations. Neutron-capture gamma-ray spectroscopy is the most direct means to reliably quantify complex formation mineralogy in-situ using well logs but is rarely implemented in a petrophysical interpretation framework. The few existing spectroscopy based interpretation methods are usually tool dependent and incorporate workflows that are largely based on empirical correlations. I introduce a new quantitative method to assess detailed mineral concentrations through joint nonlinear matrix inversion of measured spectroscopy elemental weight concentrations and matrix-sensitive logs such as gamma ray, matrix photoelectric factor (PEF), matrix Sigma, and matrix density. Estimated mineralogy is used in the correction of matrix effects on porosity logs and subsequent calculation of true formation porosities. Water saturations are quantified through joint petrophysical interpretation of matrix-corrected porosities and resistivity measurements using an appropriate saturation model. The developed method is applicable to a wide range of formation lithologies, well trajectories, well-logging environments (including open and cased hole environments),

and is independent of a specific tool or neutron source type. Results of the implementation of the spectroscopy-based algorithm, in both synthetic and field cases, benchmark the method as reliable and accurate in the quantification of mineral concentrations, matrix properties, porosity, and hydrocarbon saturation.

3.1 INTRODUCTION

Due to the importance of the accurate assessment of formation lithology in petrophysical interpretation, several mineral quantification methods exist. One of the earliest methods is the use of charts that include cross plots between well log pairs such as density-sonic, density-PEF, neutron-sonic, gamma-ray spectral data, and neutron-density (Clavier and Rust, 1976; Schlumberger, 2009). The use of these charts in quantifying lithology is limited because they evaluate only major mineral types such as quartz, limestone, and dolomite; they also do not properly account for mixtures of more than two minerals or quantify organic content in unconventional plays. Cross plots of spectral gamma ray-data including thorium, uranium, and potassium identify but do not quantify specific clay types present in the formation.

Commercial multi-mineral and petrophysical interpretation software are widely used in the petroleum industry to quantify complex mineralogy as well as fluid saturations. However, these techniques rely on the erroneous assumption that there is a linear relationship between all measured logs and formation mineral volumetric compositions. Mineralogy is therefore quantified using inadequate linear inversion techniques that minimize the difference between linearly estimated and field measurements (Mayer and Sibbit, 1980; Doveton, 1994). The linear relationships used in this interpretation method are based on empirical or approximate formulas that require

reliable well log responses across pure lithologies which are difficult to define. The linear inversion method also does not typically include spectroscopy measurements although elemental logs have the most direct relationship to formation minerals through mineral chemical formulas.

Certain numerical methods implement a joint nonlinear inversion of resistivity, gamma-ray, density, neutron porosity, and sonic transit time data (Liu et al, 2007; Sanchez-Ramirez et al, 2009; Heidari et al, 2012) but these methods also do not incorporate spectroscopy logs in their formulations. Other numerical techniques include artificial neural networks, fuzzy logic, and neuro-fuzzy models to diagnose and quantify lithofacies. However, such numerical methods require extensive training, are not applicable in formations with complex mineralogy, and also do not include spectroscopy logs in their formulation (Gonçalves et al., 1995; Cuddy, 2000).

Core data is one of the most accurate methods to quantify lithology but due to the high costs associated with this technique, it is not always practical to acquire core data in every well. Moreover, some methods of analyzing core data such as Fourier Transform-Infrared spectroscopy (FT-IR) and X-Ray Diffraction (XRD) do not detect total organic carbon or kerogen present in unconventional gas-bearing shales.

Neutron-capture gamma-ray spectroscopy measurements have significantly improved since they were first introduced into logging tools in the 1970s (Hertzog, 1978) and are now the most reliable means to quantify complex lithology in-situ (Galford et al., 2009; Radtke et al, 2012). Neutron-capture gamma-ray spectroscopy data measure gamma rays generated during nuclear interactions between source neutrons and formation element atoms at thermal neutron energies. Gamma-ray spectra quantify the distribution

of measured gamma-ray counts with respect to energy, and are used to quantify elemental compositions in the form of elemental relative yields and weight concentrations. In this chapter, I use elemental weight concentrations estimated from neutron-capture spectra measurements to quantify mineral volumetric concentrations because elemental weight data are more commonly acquired than elemental relative yield measurements. Measured elements vary from one tool to another but elemental weight concentrations frequently obtained and used in mineral analysis include silicon, calcium, iron, and sulfur (Herron and Herron, 1996).

Algorithms that transform spectroscopy elements to minerals (Herron and Herron, 1996; Pemper et al., 2006) are typically tool specific and rely on a database of geochemical correlations that use empirical or approximate formulations. Furthermore, petrophysical consistency with other matrix-sensitive logs is not usually included as a constraint in the interpretation even though spectroscopy problems are usually underdetermined in nature (due to the number of spectroscopy elemental data typically being less than the number of minerals present in the formation). Some probabilistic techniques used to estimate mineralogy (Galford et al. 2009; Eslinger and Boyle, 2013) are based on spectroscopy elements but do not include combined petrophysical interpretation with other well logs. Published works of spectroscopy-based joint petrophysical interpretation with other well logs assume linear relationships in quantifying neutron porosity and total porosity or do not include neutron porosity at all in the interpretation (Herron et al., 2002, ZuoAn et al., 2010).

Prior to the discovery of shale gas plays, kerogen was not a mineral of interest to the petroleum industry and is not characterized by conventional neutron-capture

spectroscopy logs, because a main component of kerogen, inelastic carbon, is not quantified by neutron-capture spectroscopy logs. I quantify kerogen in this chapter through a joint nonlinear inversion of spectroscopy elements with matrix-sensitive logs. More recent spectroscopy tools that measure inelastic spectra acquired during high-energy inelastic nuclear interactions can quantify total organic carbon and kerogen (Radtke et al., 2012).

The following sections describe the workflow developed to estimate mineral volumetric concentrations, porosity, and fluid saturations. Two synthetic and four field examples appraise the reliability of the method in mineralogy estimation and petrophysical interpretation of both conventional and unconventional formations.

3.2 NONLINEAR MATRIX INVERSION OF SPECTROSCOPY LOGS

3.2.1 Forward Model

The spectroscopy forward model that describes the nonlinear relationship between spectroscopy elements and minerals is given by

$$M_i = \frac{\sum_{j=1}^{n} \frac{\rho_j C_j N_{ij} MM_i}{MM_j}}{\sum_{i=1}^{m}\sum_{j=1}^{n} \frac{\rho_j C_j N_{ij} MM_i}{MM_j}} \text{ (Bishop, 2008),} \quad (3.1)$$

where subscripts *i* and *j* designate the index for *m* elements and *n* minerals, respectively, ρ_j is mineral density, C_j is mineral volumetric concentration, MM_i is the molar mass of element *i*, MM_j is the molar mass of mineral *j*, and N_{ij} is the number of atoms of the *i-th*

element in the *j-th* mineral. The terms MM_j and N_{ij} are obtained from predefined mineral chemical formulas which invoke a fixed elemental composition for minerals based on the assumption that the chemistry of elements that constitute minerals is fairly constant.

I confirm the reliability of the spectroscopy forward model in field cases by implementing equation 3.1 in a field case where both spectroscopy elemental and mineral logs are available. The field case includes the entire logged interval of a gas-bearing shale in the Bakken formation where measured spectroscopy elements include aluminum, calcium, iron, silicon, and sulfur and spectroscopy mineral logs include clay, siderite, pyrite, carbonate, and the quartz-feldspar-mica (QFM) mineral group. The geology of the formation indicates that the main minerals present within the clay, QFM, and carbonate mineral groups are illite, quartz, and calcite, respectively (Sarg, 2012). The analyzed interval consists of both the middle and lower Bakken formation which include low and high volumetric concentration of shale, respectively. Measured mineral logs in this example do not quantify kerogen because the neutron-capture spectroscopy logs do not include any element associated with the assumed chemical composition of kerogen. Table 3.1 lists assumed elemental and mineral parameters used in equation 3.1 to convert spectroscopy mineral to elemental data. Figure 3.1 shows that results of reconstructed elemental weights from forward calculations exhibit good agreement with measured spectroscopy elemental weights. This behavior is indicative of the accuracy of the forward model and assumed elemental and mineral parameters within the forward model. The relationship expressed in equation 3.1 remains valid independent of tool type, source or nuclear detectors, well trajectory or logging environment (open or cased hole logs).

The relationship is however dependent upon the assumption that measured spectroscopy elemental logs are indicative of formation matrix concentrations and have been corrected for environmental effects. Examples of environmental effects include the presence of barite in mud which could falsely decrease sulfur weight measurements, or a false increase in iron weight measurements due to additional iron detected from tool housing or steel casing in steel-cased logs.

3.2.2 Joint Nonlinear Matrix Inversion

Due to the nonlinearity between spectroscopy elements and minerals indicated by equation 3.1, matrix inversion is implemented using a nonlinear iterative inverse algorithm. The quadratic misfit cost function, $C(\mathbf{x})$ to be minimized in the inversion is given by

$$C(\mathbf{x}) = \left\| \mathbf{W}_d \cdot \left[\mathbf{g}(\mathbf{x}) - \mathbf{d}_m \right] \right\|_2^2 + \lambda^2 \left\| \left(\mathbf{x} - \mathbf{x}_{ref} \right) \right\|_2^2, \qquad (3.2)$$

where λ is a regularization parameter that stabilizes the inversion problem by improving the convergence of the solution, $\mathbf{x}$ is a vector of mineral volumetric compositions, $\mathbf{W}_d$ is a data-weighting matrix, $\mathbf{d}_m$ is the vector of measured elemental relative yield logs, and $\mathbf{g}$ is the forward spectroscopy model given by equation 3.1.

Equation 3.2 is subject to $0 \le \mathbf{x}_j \le 1$ and $\sum_{i=1}^{n} \mathbf{x}_j = 1$ which ensures that the solution is positive and sums up to zero at each iteration step within the inversion algorithm. Joint nonlinear inversion with matrix-sensitive logs is achieved by implementing the mixing laws that govern these measurements as constraints in the solution. The mixing laws

compute the measured response as a volumetric average of individual mineral responses and are given by

$$
\begin{aligned}
&GR_{matrix,\,log} = \sum_{j=1}^{n} C_j \times GR_j, \\
&\text{where } GR_j = \alpha U_j + \beta Th_j + \gamma K_j, \\
&\mathrm{PEF}_{matrix,\,log} = \sum_{j=1}^{n} C_j \times \mathrm{PEF}_j, \\
&\rho_{matrix,\,log} = \sum_{j=1}^{n} C_j \times \rho_j, \\
&\Sigma_{matrix,\,log} = \sum_{j=1}^{n} C_j \times \Sigma_j,
\end{aligned}
\qquad (3.3)
$$

where GR_j, PEF_j, ρ_j, and Σ_j are the gamma-ray, PEF, density, and Sigma values, respectively, associated with each mineral *j*; $GR_{matrix,\,log}$, $\mathrm{PEF}_{matrix,\,log}$, $\rho_{matrix,\,log}$, and $\Sigma_{matrix,\,log}$, are gamma-ray, matrix PEF, matrix density, and matrix Sigma logs, respectively. The parameter U_j is the mass concentration in ppm of uranium for mineral *j*, Th_j is the mass concentration in ppm of thorium for mineral *j*, and K_j is the mass concentration in % of potassium for mineral *j*; the coefficients α, β, and γ depend on the detector and tool design details (Ellis and Singer, 2007). In order for a matrix-sensitive log to be included in the inversion, it must be corrected of environmental effects such that it indicates only the properties of the formation minerals that are included in the solution.

An iterative nonlinear minimization using the regularized Occam's method (Hansen, 1994; Aster et al., 2013) is implemented, depth-by-depth, to obtain a solution for mineral volumetric concentrations, **x** beginning with an initial guess of **x** whereby,

$$\left\{\left[\mathbf{J}^T\left(\mathbf{x}^k\right)\cdot\mathbf{W}_d^T\cdot\mathbf{W}_d\cdot\mathbf{J}\left(\mathbf{x}^k\right)\right]+\lambda^2\mathbf{I}\right\}\mathbf{x}^{k+1}=\mathbf{J}^T\left(\mathbf{x}^k\right)\left[\left(\mathbf{W}_d{}^T\cdot\mathbf{W}_d\right)\cdot\hat{\mathbf{e}}\right]+\lambda^2\mathbf{x}_{ref}, \quad (3.4)$$

where

$$\hat{\mathbf{e}}=\left[\mathbf{d}_m-\mathbf{g}\left(\mathbf{x}^k\right)+\mathbf{J}\left(\mathbf{x}^k\right)\mathbf{x}^k\right], \quad (3.5)$$

where $\mathbf{x}^k$ and $\mathbf{x}^{k+1}$ indicate the vector of model properties at iteration k and the updated trial model at iteration $k+1$, respectively, $\hat{\mathbf{e}}$ is the modified vector of data misfit, $\mathbf{x}_{ref}$ is a reference vector, superscript T indicates transposition, and **J** is the Jacobian or sensitivity matrix.

The regularization parameter is obtained using the L-curve strategy (Hansen, 1994) which calculates a value that best minimizes the norm of the error between numerically simulated and measured logs. The impact of λ progressively diminishes from the quadratic cost function expressed in equation 3.2 as the algorithm reaches convergence. The data-weighting matrix is defined by a diagonal matrix with diagonal entries that correspond to the inverse of spectroscopy elemental weights for spectroscopy elemental data and unity for matrix-sensitive data. This strategy minimizes the relative error between measured and reconstructed elemental weight logs and yields data weighting diagonal entries for spectroscopy elements that are higher than the value of one assigned to matrix-sensitive logs (because elemental weight concentrations are less than one and their reciprocals are subsequently higher than one). This technique ensures that higher emphasis is placed on spectroscopy elements in matrix inversion because elemental data directly indicate mineral chemical compositions. This approach can be modified to place more emphasis on matrix-sensitive logs if there is not a high degree of confidence in measured elemental weight concentration data.

Synthetic and field results shown in this chapter indicate that the inversion solution converges to a unique value which is independent of the initial guess of mineral volumetric concentrations. I therefore assume a constant equal initial guess for each mineral, equal to the reciprocal of the number of minerals present in the formation, at each depth station. The initial guess is updated every iteration until the norm of the difference between measured and numerically simulated logs is equal to or less than 0.0001 for a maximum of ten iterations. This cut off in the number of iterations is implemented because sensitivity analysis shows that after ten iterations, maximum convergence has typically been achieved. A reference vector is included in underdetermined inversion problems when the number of measured input data is less than that of minerals to be estimated in the solution. This approach stabilizes and enhances convergence of the inversion algorithm. The choice of reference vector can be guided by measured spectroscopy mineral logs, core data, or geological reports.

It is important to include minerals in the inversion that are actually present in the formation to avoid false representations of non-existent minerals in the formation. Core mineralogy data at depths within the logged formation, or from nearby cored wells, or geological data can be used to choose the minerals included in the inversion. If spectral gamma-ray logs are available, they can be used to identify the clay types present in the formation through thorium-potassium cross plots.

Entries of the Jacobian matrix are computed as the derivative of the forward model in equation 3.1, $\frac{\partial M_i}{\partial C_j}$, where

$$\frac{\partial M_i}{\partial C_j} = \frac{\sum_{i=1}^{m} \frac{\rho_j \times C_j \times N_{ij} \times MM_i}{MM_j} \left[\sum_{i=1}^{m} \frac{\rho_j \times N_{ij} \times MM_i}{MM_j} + \sum_{j=1}^{n} \sum_{ii=1}^{m} \left(\frac{\rho_j \times C_j \times N_{ij} \times MM_i}{MM_j} \right)_{ii \neq i} \right]}{\left[\sum_{j=1}^{n} \sum_{i=1}^{m} \left(\frac{\rho_j \times C_j \times N_{ij} \times MM_i}{MM_j} \right) \right]^2} -$$

$$\frac{\left[\sum_{j=1}^{n} \sum_{ii=1}^{m} \left(\frac{\rho_j \times C_j \times N_{ij} \times MM_i}{MM_j} \right)_{ii \neq i} \right] \left[\frac{\rho_j \times N_{ij} \times MM_i}{MM_j} + \sum_{ii=1}^{m} \left(\frac{\rho_j \times C_j \times N_{ij} \times MM_i}{MM_j} \right)_{ii \neq i} \right]}{\left(\sum_{j=1}^{n} \sum_{i=1}^{m} \frac{\rho_j \times C_j \times N_{ij} \times MM_i}{MM_j} \right)^2}, \qquad (3.6)$$

where subscript *ii* designates the index for *m* elements excluding element *i*.

I quantify inversion stability and uncertainty in the estimated mineralogy with a 95% confidence interval parameter which is calculated via a modification to the covariance matrix obtained from the nonlinear inversion (Aster et al., 2013). The modified covariance matrix, **Cov(x)** is defined by

$$\mathbf{Cov(x)} = \left[\frac{\left\| \mathbf{W}_d \cdot \mathbf{e}(\mathbf{x}) \right\|_2^2}{\sqrt{q}} \right] \cdot \left[\left(\mathbf{W}_d \cdot \mathbf{J} \right)^T \cdot \left(\mathbf{W}_d \cdot \mathbf{J} \right) \right]^{-1}, \qquad (3.7)$$

where q is the number of degrees of freedom, and $\frac{\left\| \mathbf{W}_d \cdot \mathbf{e}(\mathbf{x}) \right\|_2^2}{\sqrt{q}}$ is the standard deviation of the weighted error between simulated and measured logs. The modified covariance matrix includes $\mathbf{W}_d$ which integrates the preferential data weighting of spectroscopy

measurements, implemented in the inversion, into 95% confidence interval calculations. The 95% confidence interval in estimated properties is given by

$$\pm 1.96\sqrt{diag\left[\mathbf{Cov(x)}\right]}\ , \qquad (3.8)$$

where *diag* describes diagonal covariance matrix entries. This approach assumes that the distribution of estimated properties follows a normal distribution.

Mineral weight concentrations, $C_{w,j}$, can be estimated from volumetric compositions as

$$C_{w,j} = \frac{\rho_j C_j}{\sum_{j=1}^{n} \rho_j C_j}. \qquad (3.9)$$

3.3 PETROPHYSICAL INTERPRETATION

Porosity logs are typically presented in major lithology units of sandstone, or limestone assuming freshwater-saturated porosity. The use of an inaccurate matrix results in a suppression of fluid effects on measured porosity logs and a misrepresentation of true porosity values. This "matrix-effect" phenomenon is commonly exhibited due to the presence of hydroxyl, -OH groups in shales which increases formation hydrogen index, decreases formation migration length, and in turn increases apparent neutron porosities such that neutron porosities are higher than density porosities.

Estimated mineral volumetric concentrations are used to correct matrix effects on porosity logs thereby unmasking fluid effects on measured porosity logs which allows one to diagnose the fluid types present in the formation through an overlay of neutron and density porosity logs. Because porosity logs are typically expressed in freshwater-saturated units, equal neutron and density-porosities indicate the presence of water.

Neutron-density crossover (when the neutron porosity is less than density porosity) is indicative of a fluid lighter than water in the formation and an increase in neutron-density crossover corresponds to an increasingly lighter fluid. Neutron-density crossovers occur due to the low hydrogen index of hydrocarbons which causes an increase in migration length and a decrease in apparent neutron porosity.

I proceed to calculate total porosity and hydrocarbon saturation using matrix corrected total porosities in conjunction with resistivity logs and an applicable saturation model.

3.3.1 Matrix-Corrected Neutron Porosity

Neutron porosity is best characterized using migration length because it accounts for the slowing-down and diffusion phenomena that control the measurement (Allen et al., 1967). Schlumberger's Nuclear Parameter calculation program, SNUPAR (McKeon and Scott, 1989) is used to establish transforms between neutron porosity log values and the inverse of migration length, ξ, in apparent freshwater-saturated limestone and sandstone lithology units (the nonlinearity between migration length and neutron porosity is decreased by using the inverse of migration length). I calculate ξ values with the established transform and measured neutron porosity logs. Using SNUPAR, the lithology assumed in measured neutron porosity logs is replaced with detailed inverted mineralogy, and I dynamically adjust porosity values until SNUPAR-calculated and log-derived ξ values are equal. This technique thereby corrects matrix effects on neutron porosity logs in freshwater-saturated units. In SNUPAR, I can specify the nuclear source present in the

logging tool which is typically either Americium Beryllium (AmBe) or a 14-MeV pulsed neutron source.

3.3.2 Matrix-Corrected Density Porosity

Similar to neutron porosity, density porosity, ϕ_D, logs are typically presented in freshwater-saturated sandstone, or limestone porosity units. However unlike neutron porosity logs, there is a direct relationship density porosity and formation density which is expressed as,

$$\phi_D = \frac{\rho_{bulk} - \rho_{matrix}}{\rho_{fluid} - \rho_{matrix}} \qquad (3.10)$$

where ρ_{bulk} is measured bulk density, ρ_{matrix} is matrix density and ρ_{fluid} is fluid density. In order to correct for matrix effects, I calculate ρ_{matrix} using the estimated mineralogy according to equation 3.3, ρ_{bulk} is obtained from measured well logs, and ρ_{fluid} is one due to the assumption of fresh-water saturated porosity.

3.3.3 Porosity and Water-Saturation Calculations

Matrix-corrected total porosity, ϕ_t^C, is computed by applying a root-mean-square averaging method to matrix-corrected neutron and density porosity logs (Gaymard and Poupon, 1968) whereby

$$\phi_t^C \approx \sqrt{\frac{\left(\phi_D^C\right)^2 + \left(\phi_N^C\right)^2}{2}}, \qquad (3.11)$$

where ϕ_D^C is matrix-corrected density porosity and ϕ_N^C is matrix-corrected neutron porosity.

Calculated total porosity is used in conjunction with an appropriate resistivity saturation model to determine water saturations and subsequently hydrocarbon saturations. Previous research has shown that although the relationship between electrical resistivity, porosity, water saturation, and clay is poorly understood in gas-bearing shales, most saturation models including Archie, Dual water, Indonesia, Modified Simandoux, and Poupon yield comparable and accurate estimations of water saturation provided the petrophysical properties used in these models honor available measurements (Adiguna, 2012). In this chapter, I use Archie's saturation model to compute water saturation in gas-bearing shales and Table 3.2 lists petrophysical properties assumed in the calculations in the field cases studied. Archie's equation (Archie, 1942) is given by

$$R_t = \frac{aR_w}{\phi_t^m S_w^n}. \qquad (3.12)$$

where R_t is the total resistivity, R_w is the resistivity of formation water, a is Archie's Winsauer constant, m is Archie's porosity exponent, n is Archie's saturation exponent, ϕ_t is the total porosity, and S_w is the total water saturation. If formation water salinity and formation temperature are known, formation water resistivity can be computed with

$$R_w \approx \left[0.0123 + \frac{3647.5}{\left(NaCl_{ppm}\right)^{0.955}}\right] \cdot \frac{81.77}{\mathrm{T} + 6.77} \text{ (Schlumberger, 2009),} \qquad (3.13)$$

where $NaCl_{ppm}$ and T is formation water salinity in parts per million and temperature in degrees Farenheit, respectively.

Figure 3.2 outlines the petrophysical workflow adopted in this chapter.

3.4 SYNTHETIC EXAMPLES

The synthetic examples presented in this chapter include a conventional oil-bearing formation and a gas-bearing shale. Synthetic elemental weight concentration and matrix-sensitive logs (including gamma ray, matrix PEF, matrix Sigma, and matrix density) are obtained using a spectroscopy fast forward model (Ajayi et al., 2014) where measurements are acquired with a 14-MeV pulsed neutron source LWD tool. Neutron and density porosity logs are calculated in freshwater-saturated limestone measurement units. Synthetic neutron porosities are calculated through a SNUPAR-derived transform between apparent freshwater-saturated neutron porosity in limestone units and inverse of migration length, ξ, using ξ values calculated with SNUPAR from model properties.

The initial guess is selected as a uniform average value of the reciprocal of the number of minerals present in the formation. A data-weighting weighting matrix with diagonal entries corresponding to the inverse of elemental weight concentrations for elemental measurements and one for matrix-sensitive data is included in the inversion. The regularization parameter is obtained using the L-curve strategy and Table 3.1 lists elemental and mineral physical properties assumed in synthetic examples. Results from synthetic cases quantify mineral volumetric compositions, matrix-sensitive data, and total porosities.

3.4.1 Synthetic Case No. 1

This synthetic case includes a 152.4-cm true stratigraphic thickness (TST) formation composed of ten 15.24-cm thick beds. The formation is an oil-bearing shaly

sand with mineralogy composed of quartz, illite, and calcite. Porosities are relatively high and range from 10 to 25 porosity units (p.u.). The aim of this synthetic case is to evaluate the applicability of developed interpretation methods in a conventional formation model with typical sub-surface lithologies and porosities. Tables 3.3 and 3.4 list layer thicknesses, migration lengths, bulk densities, elemental, mineral, and fluid compositions assumed in this example. Simulated elemental data include weight concentrations of magnesium, silicon, aluminum, potassium, calcium and iron.

Convergence of the inversion problem is achieved within ten iterations and in 1.08 seconds of computer processing unit (CPU) time. The norm of the error between numerically simulated and measured logs at the final iteration is 9.9885e-5. Figure 3.3 shows that estimated mineral volumetric concentrations exhibit a good agreement to model values. Uncertainty bars on estimated mineralogy are very low (an average of 0.38 percent of mineral volumetric concentrations) which indicates a high degree of confidence in the results.

Prior to matrix correction of porosities, the assumption of an inaccurate limestone matrix results in neutron porosities being higher than density porosities as shown in Figure 3.4 (a). In order to reveal the effect of hydrocarbons on the crossover between neutron and density porosities, I correct the assumed limestone matrix with the estimated mineralogy. Results of this procedure, shown in Figure 3.4 (b), indicate that the crossover between neutron and density porosity logs is not significant because the hydrocarbons (oil) present in the formation have nuclear properties (density and the inverse of migration length, ξ) similar to that of freshwater. The crossover between neutron and density porosities decrease from layers I to IX and overlap in layer X, because water

saturation increases from 0.1 in layer I to 1 in layer X. Figure 3.4 (c) shows that total porosity calculated using root-mean-square methods exhibit good agreement with model values. Results in Figure 3.4 (d) to (g) demonstrate that estimated mineralogy generates matrix sensitive logs that are consistent with model values. These results indicate that the inclusion of a data-weighting matrix in the inversion with higher emphasis on spectroscopy elements than matrix-sensitive logs is adequate to accurately assess mineralogy consistent with lithology-sensing logs.

3.4.2 Synthetic Case No. 2

Unconventional gas-bearing shale formations exhibit lower porosities and more complex lithology than that observed in conventional formations. It is therefore important to investigate the applicability of the developed interpretation methods in gas-bearing shales. Another crucial consideration is that neutron capture spectroscopy logs do not typically include weight concentrations of any elements, such as carbon, associated with the kerogen present in shale formations. I therefore use this synthetic example to evaluate the reliability of the implementation of joint inversion of spectroscopy and matrix-sensitive logs in the estimation of formation kerogen content.

The synthetic case includes ten 15.24-cm thick layers with distinct lithology and petrophysical properties. Tables 3.5 and 3.6 list layer thicknesses, migration lengths, bulk densities, elemental compositions, mineral compositions, and fluid compositions**,** assumed in this synthetic case. Elemental data include sodium, magnesium, aluminum, silicon, sulfur, potassium, calcium, and iron, while the formation lithology is composed of quartz, albite, calcite, pyrite, kerogen, illite, and mg-chlorite. The inversion converges

after 2.47 seconds of CPU time and eight iterations when the norm of the error between numerically simulated and measured logs is 6.1343e-4.

Figure 3.5 shows that estimated mineralogy, including kerogen, exhibit good agreement with model mineral volumetric concentrations. These results validate the joint interpretation method as a reliable means to estimate kerogen in shale formations when there are no measured elements associated with kerogen. Results shown in Figure 3.6, where estimated mineral volumetric concentrations yield matrix-sensitive logs that are consistent with model values, further validate the joint interpretation method. Uncertainty in mineralogy is an average of 10.45 percent of estimated mineral volumetric concentrations and is shown in Figure 3.5 as error bars on mineralogy values. This uncertainty is higher than that observed in Synthetic Case No. 1, because the mineralogy is more complex due to the high number of minerals in this case.

Due to the high concentration of clay in the formation, there are significant matrix effects on porosity logs that mask the presence of gas. However, I observe substantial crossover between neutron and density porosity logs, after matrix correction of these logs using the estimated mineralogy, which is clearly indicative of the presence of gas. There are slight discrepancies (less than 1.2-p.u.) between total porosity, calculated using root-mean-square methods, and model porosities due to low porosities, the presence of gas and high shale concentration in this formation.

3.5 FIELD EXAMPLES

The spectroscopy tool used in field examples quantifies matrix-sensitive logs including gamma ray, matrix density, matrix PEF, and matrix Sigma. The tool directly measures gamma-ray logs but other matrix properties are calculated from elemental

weight concentrations using a tool-specific algorithm which does not include kerogen in the calculations. Similarly, measured mineral log values are estimated from elemental weight measurements and do not include kerogen in the estimations. Certain measured minerals are grouped including quartz-feldspar-mica (QFM), clays, and carbonates. Measured well logs in field examples have been corrected for environmental effects such that spectroscopy elemental weight concentrations are truly representative of formation lithology.

Inversion parameters chosen in field cases are similar to those adopted in synthetic cases. The diagonal entries of the data-weighting matrix correspond to the inverse of spectroscopy elemental weights for weight data and unity for matrix-sensitive data. The regularization parameter is calculated with the L-curve strategy and the initial guess is chosen to be a uniform constant value equal to the reciprocal of the number of minerals present in the formation.

Table 3.1 lists the elemental and mineral chemical and petrophysical properties assumed in field examples. Table 3.2 lists the parameters *a*, *m*, and *n* which are obtained from an average of the values that generate the best fit to saturation core data (in the field cases where core water saturation measurements are available) using Archie's saturation model. Total porosities used in saturation calculations are obtained by root-mean-square methods. Formation water resistivity is obtained from formation water salinity and temperature logs through equation 3.13. Other properties used in saturation calculations are listed in Table 3.2 and water saturations are estimated with deep resistivity wireline logs (AT90) and Archie's equation.

Gamma-ray coefficients, α, β, and γ are obtained from least-squares fitting of total measured gamma-ray to spectral gamma-ray logs for Thorium (*Th*), Potassium (*K*), and Uranium (*U*). In the absence of spectral gamma ray data, I assume values of 4, 8, and 16 for α, β, and γ, respectively. Gamma-ray coefficient values implemented in all field cases are listed in Table 3.2.

3.5.1 Field Case No. 1

This field case is a vertical open-hole well within the Barnett shale gas formation located in the Bend Arch-Fort Worth Basin and is logged with wireline neutron-capture spectroscopy tools (Ortega, 2014). The formation is the source rock, reservoir rock, and acts as its own seal. The Barnett formation is composed of approximately 2-8% organics, 20-30% clay minerals (mainly illite), 45-55% silt (quartz and feldspar), 15-19% carbonates (mainly calcite), and trace amounts of siderite and pyrite (Givens and Zhao). Clay typing using spectral gamma ray logs indicates that the main clay mineral present in the formation, for the depth interval under study, is mixed layer clay. Measured chemical elements include calcium, iron, sulfur, silicon, and aluminum. X-ray diffraction (XRD) core data indicate that individual minerals present in the formation are illite, montmorillonite, fe-chlorite, calcite, pyrite, quartz, and kerogen. Although pyrite exists in trace amounts (less than 0.02 volume fraction), I include it in the analysis of this field case and other subsequent field cases, because research shows that it has a strong relationship with total organic carbon content, TOC (Witkowsky et al., 2012).

I decrease the non-uniqueness in this field case (due to a lower number of elements than minerals) by joint inversion of spectroscopy elemental logs with gamma-ray measurements. This strategy also facilitates the estimation of kerogen because even

though there is a small amount of sulfur present in the assumed chemical composition of Barnett kerogen, sulfur is simultaneously present in pyrite. Dependence on sulfur in the quantification of both kerogen and pyrite will lead to an ill-posed problem because iron, the other constituent of pyrite, is present in almost all clay minerals.

I do not include matrix grain density or matrix Sigma in the joint inversion because these properties are calculated without including kerogen in the neutron-capture spectroscopy tool used in this field case. The section of the well under study is 287-m thick and includes two sections, at the top and bottom of the section, where core data is acquired. Log-calculated spectroscopy minerals include clay, carbonates, pyrite, and QFM and I split the clay group into individual clay minerals based on average ratios (0.4-illite, 0.3-montmorillonite, and 0.3-fe-chlorite) estimated from core mineralogy data.

The inclusion of gamma ray in the inversion still yields a slightly underdetermined estimation problem (7 output logs, 6 measured input logs). I therefore include a reference vector to improve the stability and convergence of the solution. Reference vector values are obtained from split measured spectroscopy mineral logs and a constant value for kerogen (which is averaged from core data: 0.0965 solid volume fraction) since kerogen is not included in measured mineral logs. The solution converges after four iterations, when the norm of the error between measured and numerically simulated logs is 0.0061, and the CPU time consumed is 8.42 seconds. Figure 3.7 shows the comparison between estimated, measured spectroscopy mineral logs, and core mineralogy data. Estimated mineral volumetric concentrations exhibit good agreement to core data and calculated uncertainty bars are very low (2.2780e-4 percent of calculated mineral volumetric concentrations). Estimated mineralogy also exhibit relatively good

agreement with split spectroscopy mineral logs. Realistically, it is important to note that comparison to spectroscopy mineral logs is limited by the availability of core data to estimate the proportion of each mineral within mineral groups and the inability of spectroscopy mineral logs to quantify kerogen.

Figure 3.8 shows the agreement between simulated and measured lithology-sensing logs which include gamma-ray, matrix grain density, and matrix Sigma logs. Simulated gamma-ray data exhibit good agreement with measured gamma-ray logs, which is an expected outcome, because gamma-ray measurements are included in the joint interpretation method. Simulated matrix densities are less than corresponding spectroscopy log values because unlike spectroscopy-obtained matrix densities, simulated matrix densities account for kerogen which has a much lower density (1.1 g/cc) than other minerals present in the formation. Consequently, estimated matrix densities display improved agreement with core data than log matrix densities. However, estimated matrix Sigma values agree well with log values because the Sigma of kerogen (20.097 c.u.) is comparable to some of the other minerals present in the formation and the volumetric concentration of kerogen itself is low.

Figure 3.8 also displays porosity, resistivity, and calculated saturation logs as well as core porosity and saturation data. Measured neutron and density porosity logs are acquired in limestone units and exhibit matrix effects (where neutron porosities are greater than density porosities) that mask the presence of hydrocarbons in the formations. This masking effect is greater in sections with higher clay content (X345-X399-m, X618-X632-m) due to the presence of hydroxyls, -OH in shales which lead to higher apparent neutron porosities. The correction of matrix effects on porosity logs leads to a crossover

between neutron and density logs where neutron porosities are less than density porosities. I do not detect substantial neutron density crossovers in this field case due to low formation porosities. Low porosities result in a low effective volume of gas which further decreases in intervals with high water saturations. The crossover in the upper interval of the well, between X345 and X541-m, where there are higher water saturations (average 0.7 volume fraction) is approximately 4-p.u. In the lower section, between X541.5 and X632-m, there is an approximately 8 p.u. crossover which correlates with lower water saturations (average 0.1 volume fraction). Results of water saturation calculations exhibit reasonable agreement with core data in sections where core data is available. Formation water resistivity is calculated using formation salinity (FSAL) and temperature (TEMP) logs. Total porosity, as seen in Figure 3.8 (c), is calculated using root-mean-square methods with measured apparent neutron and density porosities as well as matrix-corrected neutron and density porosities. Total apparent porosity is higher than matrix-corrected total porosity because hydroxyls present in clay lead to a higher apparent porosity. Matrix-corrected porosities therefore exhibit improved agreement to core data porosities compared to apparent porosities.

3.5.2 Field Case No. 2

Field Case No. 2 is located within the Haynesville shale which is an East Texas formation. The Haynesville shale is a gas source rock which includes laminated calcareous and siliceous mudstone; it is underlain by the Smackover limestone formation and overlain by the Cotton Valley group sandstone formation. The formation under study is 67.056-m thick (which is the cored segment of the well), penetrated by a vertical open-hole well, and logged with a wireline neutron-capture spectroscopy tool.

The inversion converges after ten iterations when 4.13 seconds CPU time has elapsed. At the final iteration, the norm of error between measured and numerically simulated data is 2.1343e-4. Measured chemical elements include calcium, iron, sulfur, silicon, and aluminum and mineral logs are QFM, carbonates, clays, and pyrite. Clay typing using spectral gamma-ray logs indicates the presence of illite and mixed layer clays. Measured XRD data show that major clay minerals present are illite and fe-chlorite and carbonates and QFM are composed primarily of calcite and quartz, respectively. I split clays into individual minerals based on the average ratios obtained from core data (0.33-illite, 0.67-fe-chlorite). Joint spectroscopy inversion of elements is performed with gamma-ray because it is the only matrix property that is indicative of all minerals present in the formation. Figure 3.9 shows that mineralogy results from spectroscopy inversion generally compare better to core mineralogy data than measured spectroscopy mineral logs. The estimation method also allows for the estimation of kerogen which agrees considerably well with core data. The uncertainty on estimated mineral volumetric compositions is an average of 7.4644e-5 percent and is depicted by error bars shown in Figure 3.9.

Panels (f) to (i) in Figure 3.10 display the comparison between reconstructed and measured matrix sensitive logs wherein I observe a considerably good fit between measured and simulated gamma-ray measurements. The absence of kerogen in the calculation of matrix density and PEF leads to lower estimated values than log measurements because the density (1.4 g/cc) and PEF (0.19 b/e) of kerogen are significantly lower than that of other minerals. The good agreement between estimated and core matrix densities as seen in Figure 3.10 (g) validates the accuracy of calculated

mineralogy. Estimated Sigma logs are lower than measured log values particularly in the upper section of the well (between X239 and X289-m) even though kerogen has an assumed Sigma of 16.72 c.u., which is comparable to Sigmas of most other minerals. This behavior can be attributed to the presence of trace quantities of elements with high capture cross sections, such as gadolinium and titanium, which are included in log matrix Sigma calculations but not in our calculations because I compute matrix Sigmas from mineral properties. The magnitude of the discrepancies between well log and estimated matrix Sigmas can therefore be indicative of the amount of these trace elements present in the formation.

Neutron and density porosities are acquired in freshwater-saturated limestone units and exhibit matrix effects that mask the presence of gas in the formation as seen in Figure 3.10 (a). The presence of gas in the formation leads to a separation between neutron and density porosity logs as large as the total porosity of the formation (an average of 10 p.u.) as seen in Figure 3.10 (b). Matrix-corrected total porosities exhibit improved agreement with core data compared to well-log calculated total apparent porosities. This behavior is largely due to hydroxyl shale effects that increase apparent total porosity calculated using actual porosity measurements as shown in Figure 3.10 (c).

Formation water resistivity used in saturation calculations is calculated with an assumed formation water salinity of 140 NaCl kppm and temperature log data. Computed water saturations in Figure 3.10 (e) show reasonable agreement with core water saturation values except in the bottom depths of the well between X289 and X305-m. Although calculated water saturations do not agree with core data at the bottom interval of the well (X289 to X305-m), as seen in Figure 3.10 (e), calculated water saturations are

consistent with variations observed in neutron-density crossovers. The extent of the neutron-density crossover and water saturation is fairly constant except at the bottom of the analyzed formation where the crossover decreases due to increase in calculated water saturations.

3.5.3 Field Case No. 3

This field case is also located within the Haynesville gas-bearing shale and includes 91.44-m of unconventional formation penetrated by a vertical open-hole well and logged with neutron-capture spectroscopy wireline logs. The section of the formation where porosity logs are acquired includes only two mineralogy core data such that I cannot perform extensive comparison to core data in this example. I however have sufficient confidence in the developed interpretation methods based on results from synthetic cases and previous field cases. The only available matrix-sensitive log is gamma-ray which I include in the joint matrix inversion method. The spectroscopy tool measures calcium, iron, sulfur, silicon, and aluminum, clay, QFM, carbonate, and pyrite. The two available mineralogy core data indicate that clay minerals include illite and fe-chlorite while carbonates and QFM are composed primarily of calcite and quartz, respectively. I use these core measurements to ascertain the average proportion of individual clay minerals within the clay mineral group (0.8-illite, 0.2-fe-chlorite).

The solution of estimated mineralogy converges after nine iterations in 4.98 seconds when the norm of the error between measured and numerically simulated logs is equivalent to 5.5094e-5. Figure 3.11 shows that estimated mineralogy exhibit good agreement with spectroscopy mineralogy logs but I observe some discrepancies in illite and calcite at depth X140-m between log and core data. It is however not reasonable to

conclude based on the disparity between core data and estimated mineralogy, at a single depth station, that estimated mineralogy is inaccurate particularly because there are only two core lithology measurements available. I can ascertain the reliability of estimated mineral volumetric concentrations through results shown in Figure 3.12 where gamma-ray values reconstructed from estimated mineralogy compare extremely well to log measurements. Uncertainty bars computed on inverted mineral volumetric concentrations are also very low (6.5086e-5 percent) and further indicate a high degree of confidence in estimated mineralogy.

Figure 3.12 (a) shows measured neutron and density porosity logs which are acquired in freshwater-saturated sandstone units. This is the only field case studied in this chapter in which porosity logs are not acquired in limestone units. In this example, I observe the largest matrix effects on measured porosity logs of all field cases studied which is mainly due to high formation clay content. Figure 3.12 (b) shows that estimated mineralogy correct the significant matrix effects observed in measured porosity logs which cause a substantial reduction in total porosities obtained using matrix-corrected porosity logs compared to that derived from measured porosity logs as seen in Figure 3.12 (c). Low formation porosities cause a lack of significant crossover between neutron and density logs even though water saturation is relatively low within the interval under study. In the estimation of water saturation, formation water resistivity is calculated based on an assumed formation water salinity of 140 NaCl kppm and temperature is obtained from temperature logs. Computed total water saturation exhibit an increase towards the bottom interval of the well, between depths X133 and X162-m, which corresponds to a decrease in resistivity logs.

3.5.4 Field Case No. 4

The formation examined in Field Case No. 4 is a vertical open-hole well also located within the gas-bearing Haynesville shale. The formation is logged with a wireline neutron-capture spectroscopy tool with lithology similar to the other Haynesville field examples (Field Case Nos. 2 and 3) which includes illite, fe-chlorite, calcite, pyrite, and kerogen. Measured spectroscopy data are calcium, iron, sulfur, silicon, aluminum, QFM, clays, pyrite, and carbonates. Similar to the other field examples, individual clay minerals are obtained from measured mineral groups based on proportions estimated from core data (0.95-illite, 0.05-fe-chlorite).

I perform joint matrix inversion of spectroscopy and gamma-ray logs within 105.156-m of formation which is located in an interval where core data are available. The solution converges after ten iterations and 6.45 seconds of CPU time. The norm of the error between numerically simulated and measured logs after ten iterations is 0.0021 and the uncertainty in estimated mineral volumetric concentrations is an average of 4.8961e-5 percent which is depicted as error bars in Figure 3.13. Estimated and measured spectroscopy mineral logs exhibit good agreement to each other as well as core data. However, measured mineral logs do not quantify kerogen but the inversion method estimates kerogen values that correspond well with core mineralogy data.

Figure 3.14 shows measured porosity logs, matrix-corrected porosity logs, total porosity logs calculated from measured and matrix-corrected data, measured resistivity logs, computed water saturation, and matrix-sensitive logs. Core data are also included in porosity, water saturation, and matrix density logs. Quantification of kerogen is facilitated through the joint inversion of spectroscopy chemical elemental logs with

gamma-ray measurements wherein I observe a good agreement between reconstructed and measured gamma-ray logs as seen in Figure 3.14. Measured matrix density logs are greater than simulated matrix densities because measured matrix densities do not include kerogen which has a density (1.4 g/cc) significantly less than that of other minerals present in the formation. Simulated matrix densities also exhibit improved agreement to core data compared to measured log values.

Porosity logs are acquired in freshwater-saturated limestone units and I observe appreciable matrix effects in the upper section of the formation (X335 to X400-m) compared to the rest of the formation. There is also less neutron-density crossover between matrix-corrected neutron and density porosity logs in this upper interval. This behavior is due to the higher water saturation observed in the upper section since porosities are relatively constant within the examined well section. Results of total porosity calculations shown in Figure 3.14 (c) indicate that matrix effects result in matrix-corrected total porosities that are less than total porosities calculated from measured logs. The matrix-corrected total porosities exhibit improved agreement with core data compared to uncorrected total porosity estimations.

Water saturation is calculated using a formation water resistivity obtained based on a formation water salinity of 140 NaCl kppm (similar to that used in Field Cases No. 2 and 3 because this formation is also located within the Haynesville shale), deep resistivity logs (AT90), and temperature well logs. Figure 3.14 (e) shows that results of saturation calculations exhibit good agreement to core data particularly in the bottom interval of the well (X370 to X440-m).

3.6 DISCUSSION

Synthetic and field cases studied in this chapter show that joint-matrix inversion of spectroscopy elemental and matrix-sensitive logs yield accurate estimations of formation matrix lithology. The estimation method also allows for the quantification of kerogen, with neutron-capture spectroscopy logs, which is ordinarily impractical because elements associated with kerogen are typically not measured by neutron-capture spectroscopy tools. The joint inversion method is also useful in the quantification of other minerals in similar underdetermined problems. I can further improve the convergence of underdetermined inversion problems by including a reference vector with values in the neighborhood of expected mineral volumetric concentrations. The developed inversion algorithm can also be implemented in other tools that measure a higher number of elements, such as inelastic spectroscopy tools, which will enable the estimation of more formation minerals.

The assumption in our calculations that measured elemental and matrix-sensitive data are indicative of true formation properties necessitates substantial quality control on measured logs to ensure that they have been corrected of environmental effects that may influence measurements and are indicative of the properties of all significant minerals present within the formation matrix. I do not interpret any cased-hole logs in this chapter but the correction of environmental effects is particularly pertinent in cased hole wells or wells logged with LWD tools that have large measurement contributions from steel casing which can introduce significant amounts of iron or aluminum into logged data.

The extent of disparity between measured and simulated matrix-sensitive data could give insight into the presence of elements or minerals that are not considered in

measured logs or the mineralogy solution but might be significantly affecting log data. Examples of such cases observed in this chapter include an increase in measured matrix Sigma due to trace amounts of gadolinium or titanium (which have high capture cross sections) in the formation or an increase in measured matrix density due to the exclusion of kerogen (which have low densities) in measured matrix density logs.

The assumption of fixed chemical formulas or properties may be inaccurate in some formations where mineral properties vary locally or are considerably different from assumed chemical formulas and properties. These variations may introduce errors into the inversion which can be addressed by using core data available in the well or nearby wells to dynamically calibrate mineral chemical compositions or properties.

3.7 CONCLUSION

This chapter introduces a new workflow to accurately quantify matrix mineralogy, porosity, and water saturation that is applicable to conventional and unconventional formations, any spectroscopy tool type, and any well trajectory. Mineral volumetric concentrations, obtained from joint matrix inversion of spectroscopy elemental weight and lithology sensing logs, are used in the correction of matrix effects on measured porosity logs by replacing the assumed homogeneous lithology in porosity logs with detailed estimated mineralogy. Such matrix correction facilitates the diagnosis of fluid types present in the formation by unmasking previously suppressed neutron-density crossovers. In very low porosity formations with high water saturations, it is difficult to diagnose a neutron-density crossover because of the low effective volume of gas present in the formation.

Geological reports, core data, or clay typing can be used to determine the type of minerals present in the formation for the initial guess of minerals in the matrix inversion. This is a key step in initializing the inversion algorithm to avoid false representations of non-existing minerals in the formation. A major advantage of the developed joint matrix inversion method is the ability to detect individual minerals within common mineral groupings because I do not always have nor can I always rely on core data to accurately split grouped measured mineral logs into the individual minerals present in the formation.

Although root-mean-square porosity estimation methods are considered to be applicable only in conventional formations where porosities are high and volumetric concentration of shale is low, several field cases examined in this chapter show that root-mean-square methods are actually accurate in the quantification of total porosity in unconventional gas-bearing shales. I also observe that Archie's equation yields satisfactory estimations of total water saturations that generally exhibit good agreement to measured core water saturations in the field cases studied in this chapter. These methods all rely on high quality measured spectroscopy elemental, lithology sensing, porosity, and resistivity logs that have been corrected of any environmental effects that can bias the interpretation.

Table 3.1 Elemental and mineral properties assumed in the synthetic and field cases examined in this chapter.

Element name	Element Formula	Molecular weight (g/gmol)		Mineral Name	Mineral formula	Molecular weight (g/gmol)	Mineral density (g/cm^3)	Gamma-ray Constants			PEF (b/e)	Sigma (c.u.)	HI
								Th (ppm)	*U* (ppm)	*K* (%)			
Aluminum	Al	26.98		**Quartz**	SiO_2	60.09	2.65	0	0.1	0	1.806	4.551	0
Calcium	Ca	40.08		**Dolomite**	$CaMg(CO_3)_2$	184.41	2.87	0	0.9	0.1	3.142	4.697	0
Iron	Fe	55.85		**Albite**	$NaAlSi_3O_8$	262.24	2.62	0	0	0.5	2.86	4.551	0
Potassium	K	39.1		**Calcite**	$CaCO_3$	100.09	2.71	0	1.4	0	5.084	7.078	0
Magnesium	Mg	24.31		**Pyrite**	FeS_2	119.97	5.01	0	10	0	16.97	90.525	0
Sulfur	S	32.06		**Illite**	$K_{0.8}Al_{1.6}Fe_{0.2}Mg_{0.2}Si_{3.4}Al_{0.6}O_{10}O_2H_2$	396.19	2.78	12	4.8	4.5	3.03	16.735	0.127
Silicon	Si	28.09		**Montmorillonite**	$Na_{0.33}Al_{1.67}Mg_{0.33}Si_4O_{10}O_2H_2$	367.01	2.63	19	3.5	0.16	1.806	4.551	0.129
				Mg-Chlorite	$Mg_5AlSi_3AlO_{10}O_8H_8$	555.82	2.65	16	4.2	0.9	1.39	11.337	0.344
				Fe-Chlorite	$Fe_5AlSi_3AlO_{10}O_8H_8$	713.544	3.42	16	4.2	0.9	12.36	47.435	0.346
				Kaolinite	$Al_2Si_2O_5O_4H_4$	184.41	2.62	19	3.2	0.1	1.49	13.039	0.366
				K-Feldspar	$KAlSi_3O_8$	278.35	2.57	1.1	0.4	10.2	1.68	15.821	0
				Kerogen-Haynesville	$C_{102}H_{94}O_{17}$	1591.9	1.4	0	200	0	0.19	16.72	0.746
				Kerogen-Barnett	$C_{40}H_{51}O_3\ S_2N$	658	1.1	0	200	0	0.63	20.097	0.769
				Kerogen-Middle Bakken	$C_{515}H_{780}O_{72}$	7416.217	1.25				0.17	24.163	1.083
				Kerogen-Lower Bakken	$C_{350}H_{450}O_{20}$	4977.448	1.25				0.15	22.78	1.02
				Hydrocarbon-Oil	C_8H_{18}	114.23	0.82				0.12	21.269	0.954
				Hydrocarbon-Gas	CH_4	16.04	0.178				0.09549	8.896	0.401
				Water	H_2O	18.02	1				0.36	22.2	1.002

Table 3.2 Petrophysical parameters assumed in field cases examined in this chapter.

***a* (Archie's Winsauer constant)**		1						
***m* (Archie's Porosity Exponent)**		2						
***n* (Archie's Saturation Exponent)**		2						
***α* (Gamma-ray Coefficient)**		3.8						
***β* (Gamma-ray Coefficient)**		8.2						
***γ* (Gamma-ray Coefficient)**		16.5						
		Field Case No. 1		**Field Case No. 2**		**Field Case No. 3**		**Field Case No. 4**
(Gamma-ray Coefficient)	***α***	3.9563		3.1757		4		4
	β	9.89		7.5491		8		8
	γ	17.229		17.8877		16		16

Table 3.3 Layer true stratigraphic thickness (TST), migration lengths, bulk densities, elemental, mineral, and fluid compositions assumed in Synthetic Case No. 1.

Layer	Layer TST (cm)	L_m (cm)	ρ_{bulk} (g/cc)	Volumetric Concentrations (%)				
				Solids			Fluids	
				Quartz	Illite	Calcite	Hydrocarbon	Water
I	152.4	16.20	2.5198	40	30	20	9	1
II	152.4	14.21	2.4414	25	35	25	12	3
III	152.4	13.92	2.3298	45	20	15	14	6
V	152.4	12.91	2.2480	30	15	30	15	10
IV	152.4	14.86	2.4335	40	25	20	7.5	7.5
VI	152.4	16.09	2.5318	35	30	25	4	6
VII	152.4	12.24	2.2785	25	35	15	7.5	17.5
VIII	152.4	13.69	2.3568	30	20	30	4	16
IX	152.4	13.01	2.2645	40	15	20	2.5	22.5
X	152.4	14.76	2.4500	35	25	25	0	15

Table 3.4 Layer solid elemental weight compositions assumed in Synthetic Case No. 1

Layer	Formation Solid Elemental Weight Concentrations (%)					
	Magnesium	**Aluminum**	**Silicon**	**Potassium**	**Calcium**	**Iron**
I	0.4063	4.9586	27.6434	2.6131	8.6132	0.9331
II	0.4893	5.9708	22.2924	3.1466	11.1123	1.1236
III	0.2930	3.5753	29.6799	1.8842	6.9867	0.6728
IV	0.2277	2.7791	21.0034	1.4645	14.4819	0.5230
V	0.2482	2.7301	16.6983	0.9928	3.8307	0.2482
VI	0.4044	4.9351	25.0659	2.6007	10.7155	0.9287
VII	0.5243	6.3977	23.8862	3.3715	07.1440	1.2040
VIII	0.2896	3.5344	21.4556	1.8626	13.8134	0.6651
IX	0.2261	2.7588	26.3208	1.4539	9.5843	0.5192
X	0.3483	4.2499	24.5351	2.2396	11.0733	0.7998

Table 3.5 Layer true stratigraphic thickness (TST), migration lengths, bulk densities, elemental, mineral, and fluid compositions assumed in Synthetic Case No. 2.

Layer	Layer TST (cm)	L_m (cm)	ρ_{bulk} (g/cc)	Volumetric Concentrations (%)								
				Solids							Fluids	
				Quartz	Albite	Calcite	Pyrite	Kerogen	Illite	Mg-Chlorite	Hydrocarbon	Water
I	152.4	14.5	2.47	15	15	10	2	5	22.5	22.5	7.6	0.4
II	152.4	15.3	2.54	20	20	15	3	7	15	15	4.5	0.5
III	152.4	13.16	2.53	7.5	7.5	20	5	9	22	22	5.95	1.05
IV	152.4	15.51	2.62	22	22	10	6	4	15	15	4.8	1.2
V	152.4	13.97	2.57	10	10	20	6	4	20.5	20.5	6.75	2.25
VI	152.4	14.91	2.48	20	20	10	2	5	17.5	17.5	5.6	2.4
VII	152.4	13.37	2.56	10	10	15	3	7	25	25	3.25	1.75
VIII	152.4	14.64	2.52	19.5	19.5	20	5	9	10	10	4.2	2.8
IX	152.4	13.89	2.65	15	15	10	6	4	22	22	3.3	2.7
X	152.4	13.83	2.4	20.5	20.5	15	3	12	10	10	4.5	4.5

Table 3.6 Layer solid elemental weight compositions assumed in Synthetic Case No. 2

Layer	Formation Solid Elemental Weight Concentrations (%)							
	Sodium	**Magnesium**	**Aluminum**	**Silicon**	**Sulfur**	**Potassium**	**Calcium**	**Iron**
I	1.3944	5.5892	7.7710	22.3910	2.1675	1.9986	4.3917	2.6013
II	1.8113	3.6301	6.1100	22.7465	3.1675	1.2981	6.4179	3.2220
III	0.6811	5.3386	6.6590	15.4921	5.2935	1.9090	8.5804	5.2916
IV	1.9273	3.5114	6.1158	23.5899	6.1278	1.2556	4.1387	5.7849
V	0.8926	4.8899	6.4147	16.6250	6.2440	1.7485	8.4343	6.0621
VI	1.8528	4.3323	6.9295	24.3492	2.1601	1.5492	4.3768	2.4344
VII	0.8964	5.9882	7.6246	18.5765	3.1350	2.1413	6.3521	3.4948
VIII	1.7742	2.4313	4.7506	20.3169	5.3036	0.8694	8.5968	4.9291
IX	1.302	5.1043	7.1308	20.7107	6.0733	1.8252	4.1019	5.9408
X	1.9611	2.5563	5.1071	22.2281	3.3458	0.9141	6.7791	3.2401

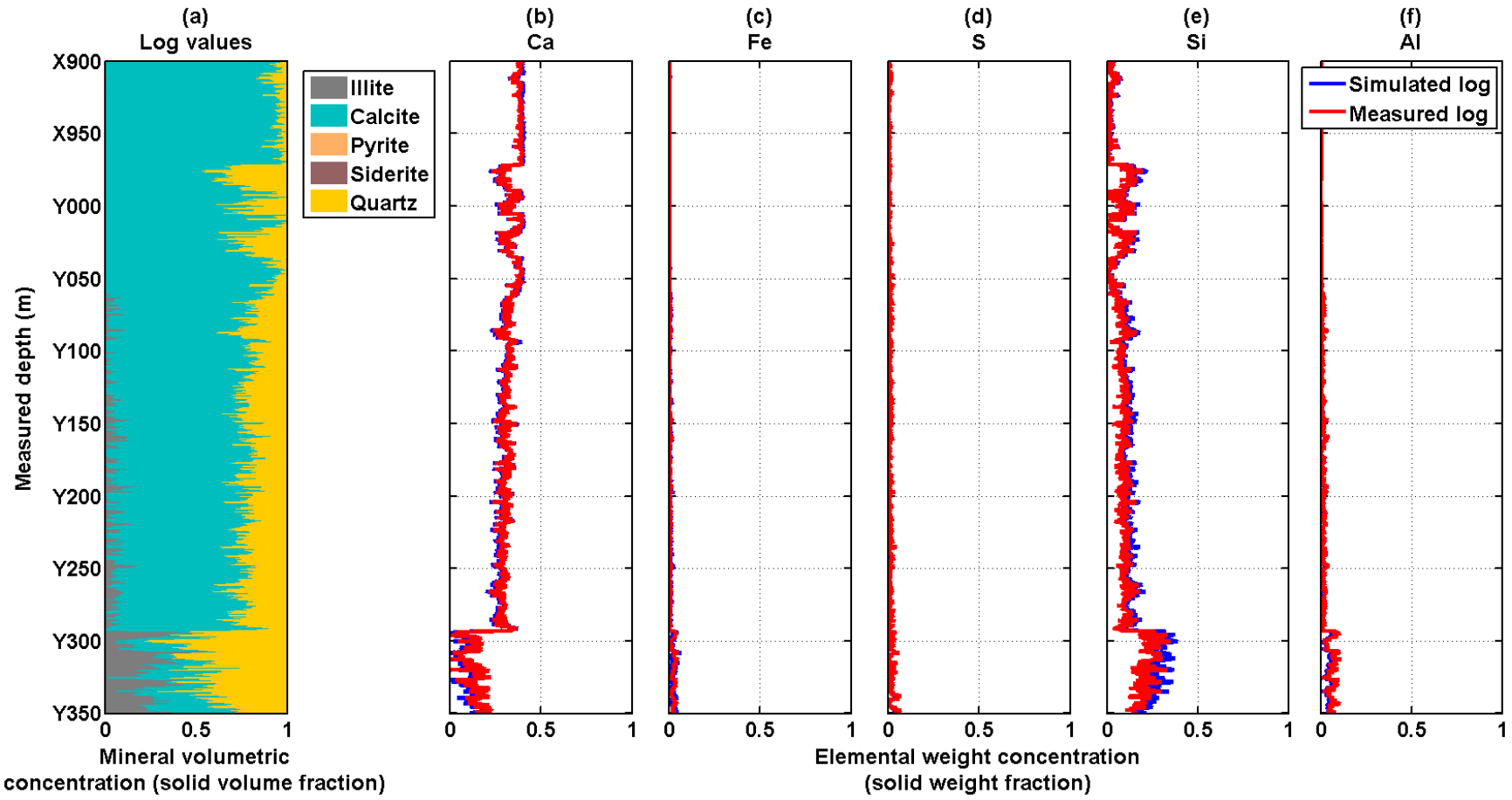

Figure 3.1: Panel (a) displays cumulative spectroscopy mineral logs; panels (b) to (f) show the comparison of measured (shown as red solid lines) to simulated (shown as blue solid lines) in a gas-bearing shale located within the Bakken formation; Ca, Fe Si, S, and Al are the elements calcium, iron, silicon, sulfur, and aluminum, respectively.

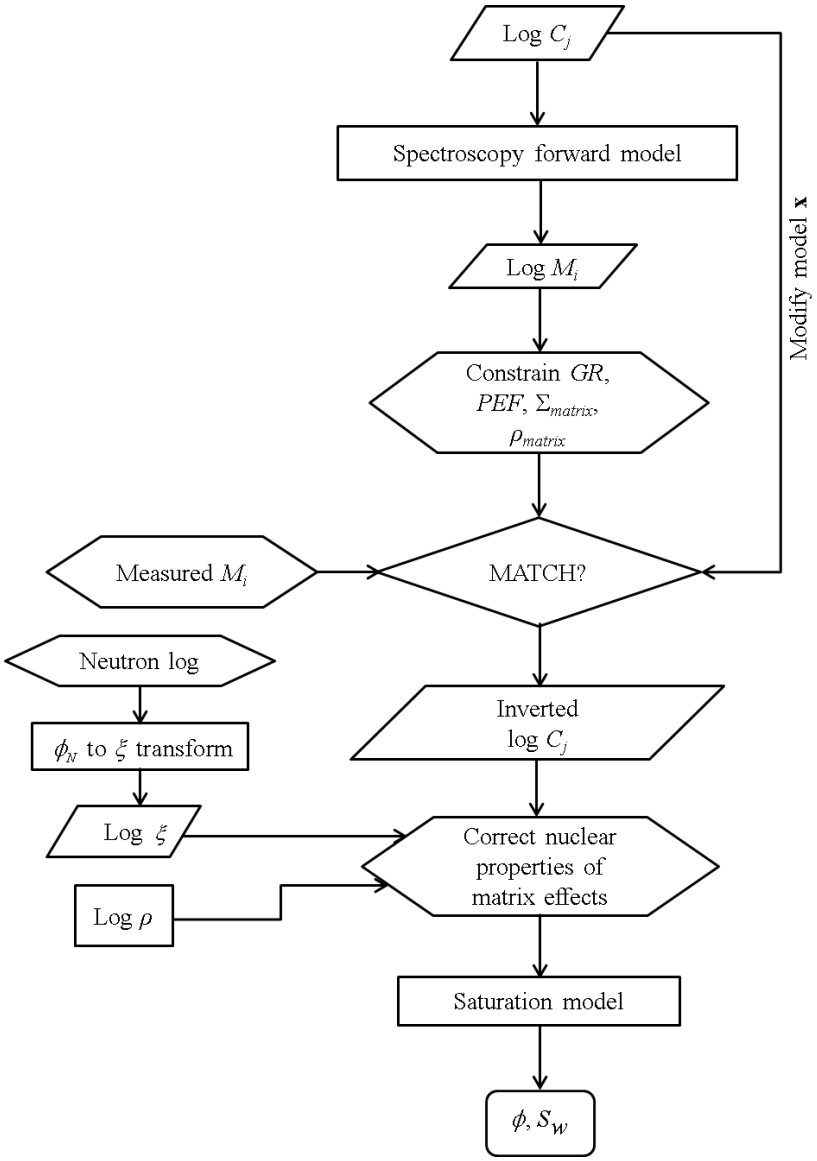

Figure 3.2: Petrophysical workflow implemented in this chapter. Workflow implemented in the estimation of layer mineral concentrations and subsequent petrophysical interpretation. The parameters ρ, ϕ, S_w, ϕ_N, M_i, C_j, **x**, and ξ represent bulk density, total porosity, total water saturation, neutron porosity, elemental weight concentration, mineral volumetric concentration, a vector of mineral volumetric concentrations, and the inverse of layer migration length, respectively. Symbols GR, PEF, ρ_{matrix}, and Σ_{matrix} are gamma ray, photoelectric factor, matrix density, and matrix Sigma layer values, respectively.

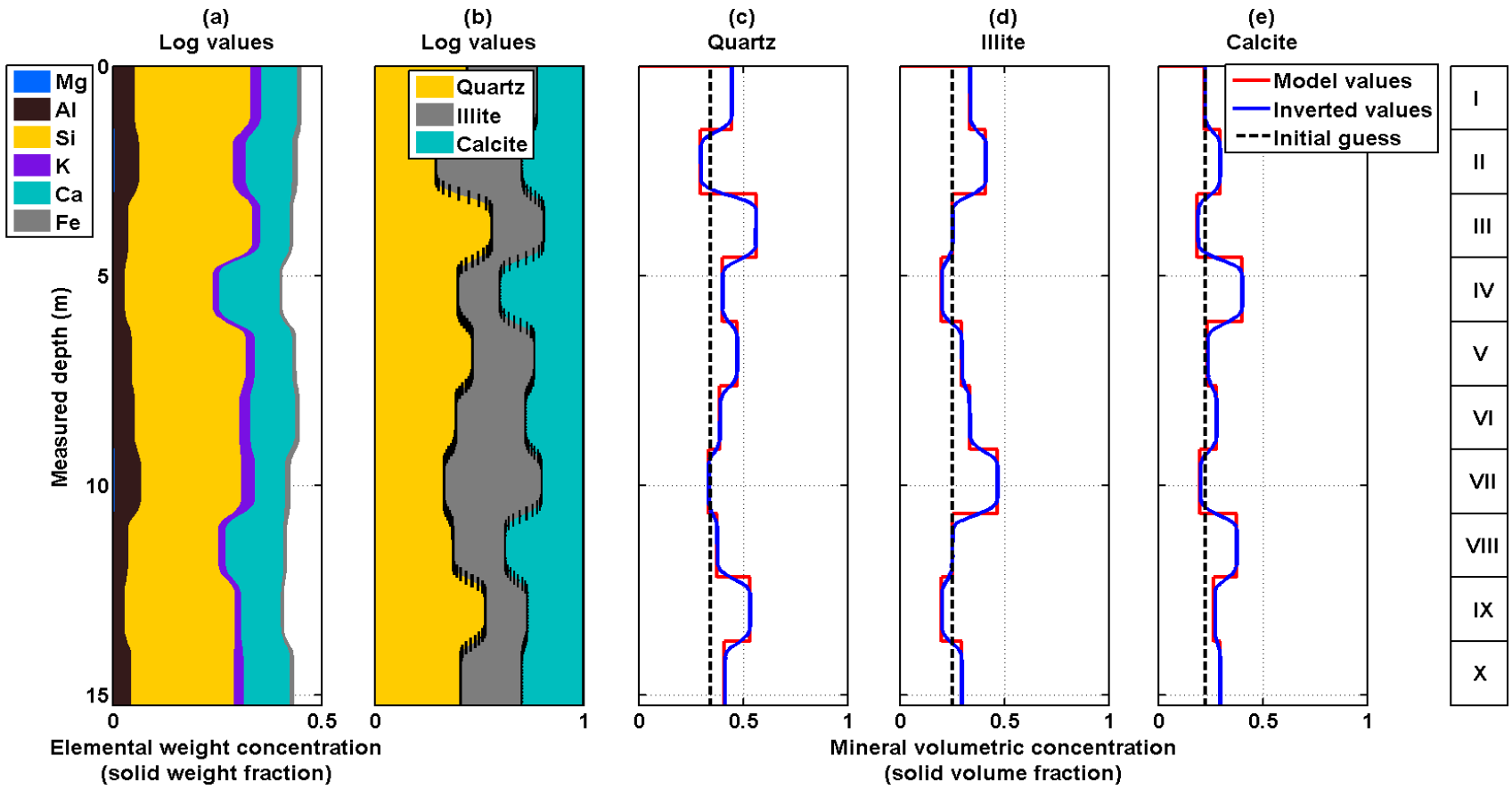

Figure 3.3: Panel (a) displays a cumulative plot of elemental weight concentrations; panel (b) shows a cumulative plot of inverted layer mineral volumetric concentrations and black uncertainty bars describe the 95% confidence interval; panels (c) to (e) exhibit inverted (shown as blue solid lines) and model layer (shown as red solid lines) mineral volumetric concentrations, for Synthetic Case No. 1. Black dashed lines describe the initial guess of the inversion; Mg, Al, Si, K, Ca, and Fe are the elements magnesium, aluminum, silicon, potassium, calcium and iron, respectively, while I to X identify distinct layers in the synthetic case.

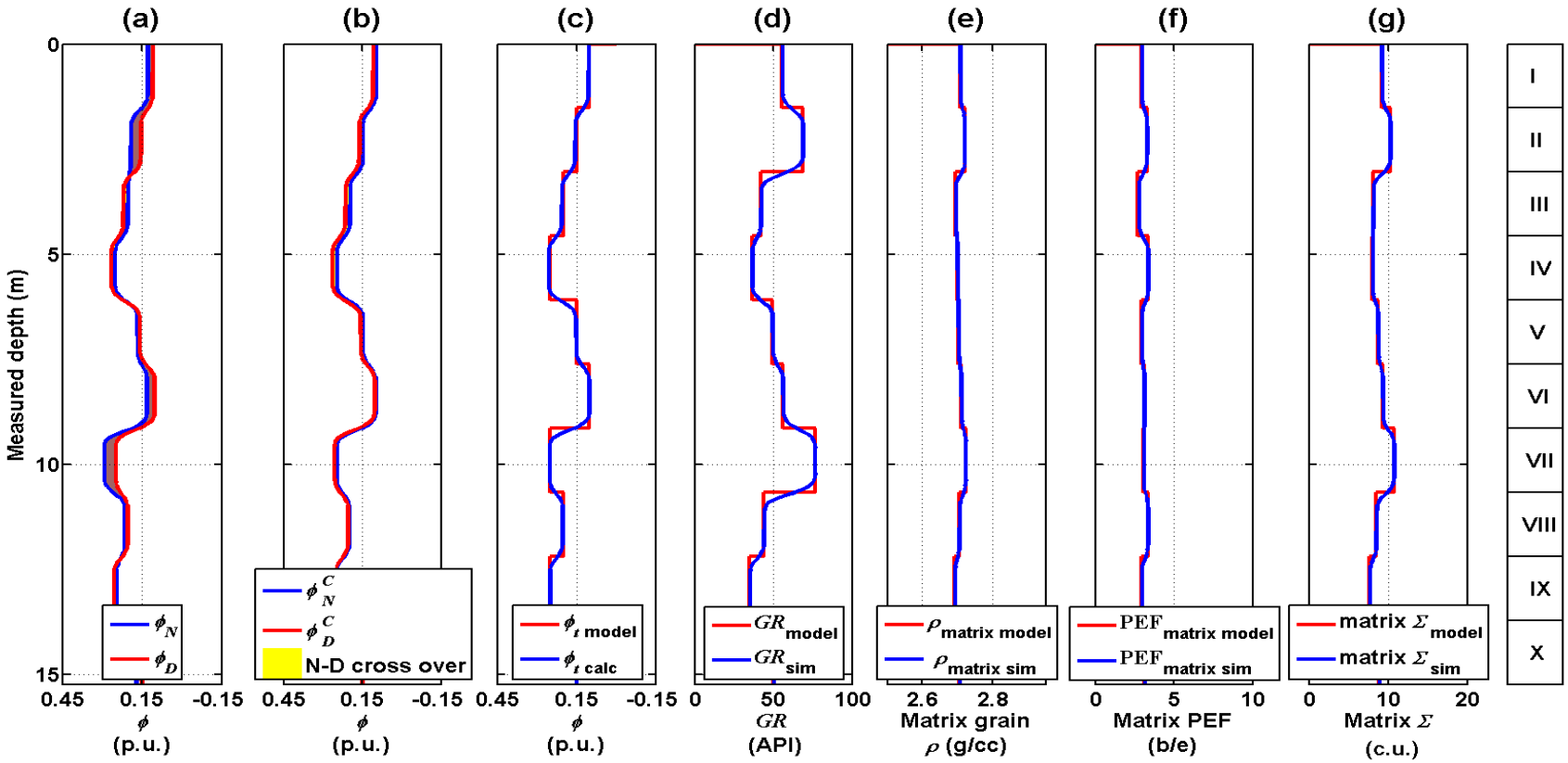

Figure 3.4: Panel (a) shows neutron-density crossover, panel (b) displays matrix-corrected neutron-density crossover where yellow and brown shading describe neutron-density crossover and matrix effects, respectively, panel (c) exhibits the comparison between model and matrix-corrected total porosity, panel (d) shows the comparison between model and simulated gamma-ray values, panel (e) describes comparison between model and simulated matrix-density values, panel (f) displays the comparison between model and simulated matrix PEF, and panel (g) shows comparison between model and simulated matrix Sigma, for Synthetic Case No. 1. Model values are shown as blocky red lines and simulated values are shown as continuous blue lines. I to X identify distinct layers in the synthetic case.

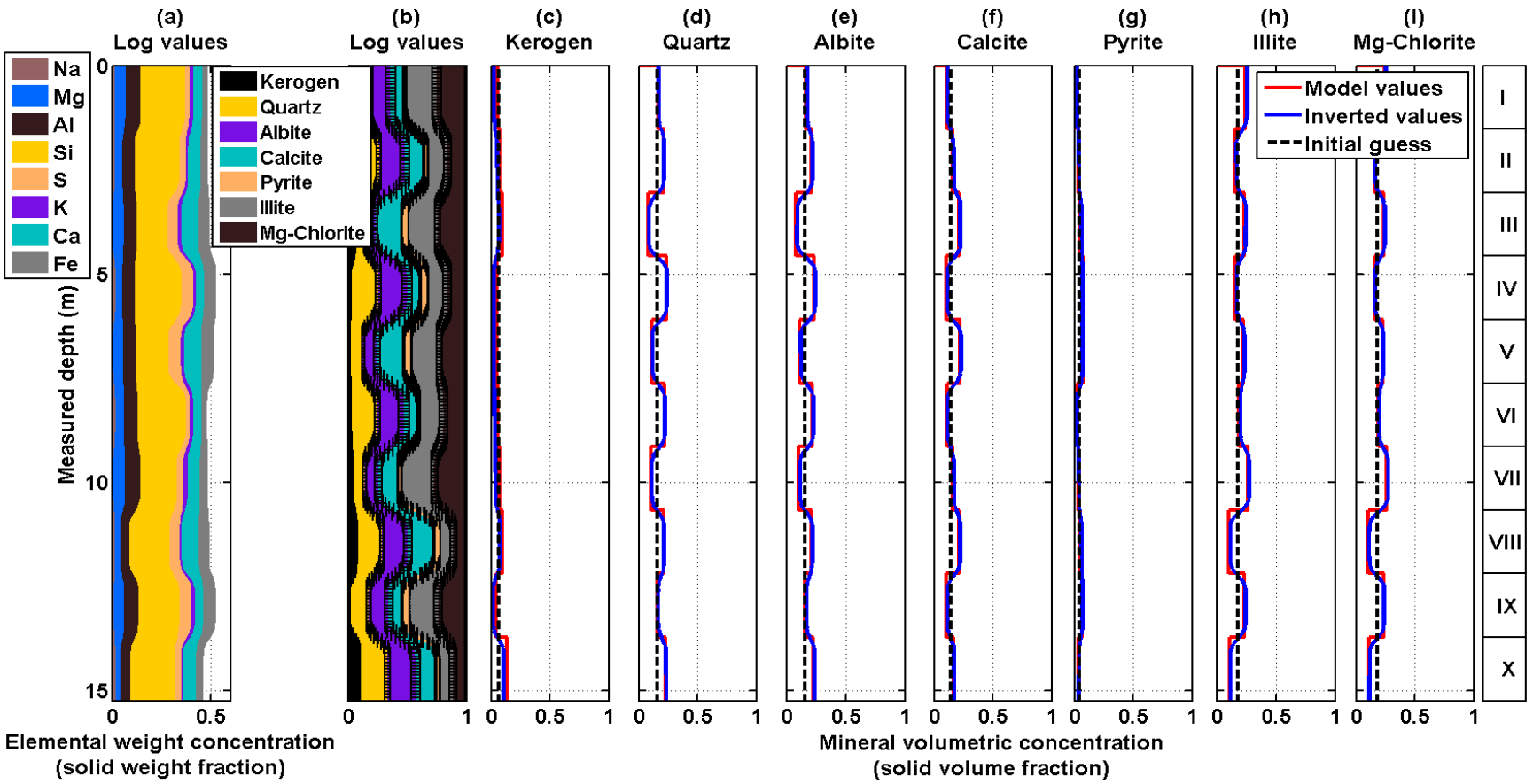

Figure 3.5: Panel (a) displays a cumulative plot of elemental weight concentrations; panel (b) shows a cumulative plot of inverted layer mineral volumetric concentrations and black uncertainty bars describe the 95% confidence interval; panels (c) to (i) exhibit inverted (shown as blue solid lines) and model layer (shown as red solid lines) mineral volumetric concentrations, for Synthetic Case No. 2. Black dashed lines describe the initial guess of the inversion; Na, Mg, Al, Si, S, K, Ca, and Fe are the elements sodium, magnesium, aluminum, silicon, sulfur, potassium, calcium and iron, respectively, while I to X identify distinct layers in the synthetic case.

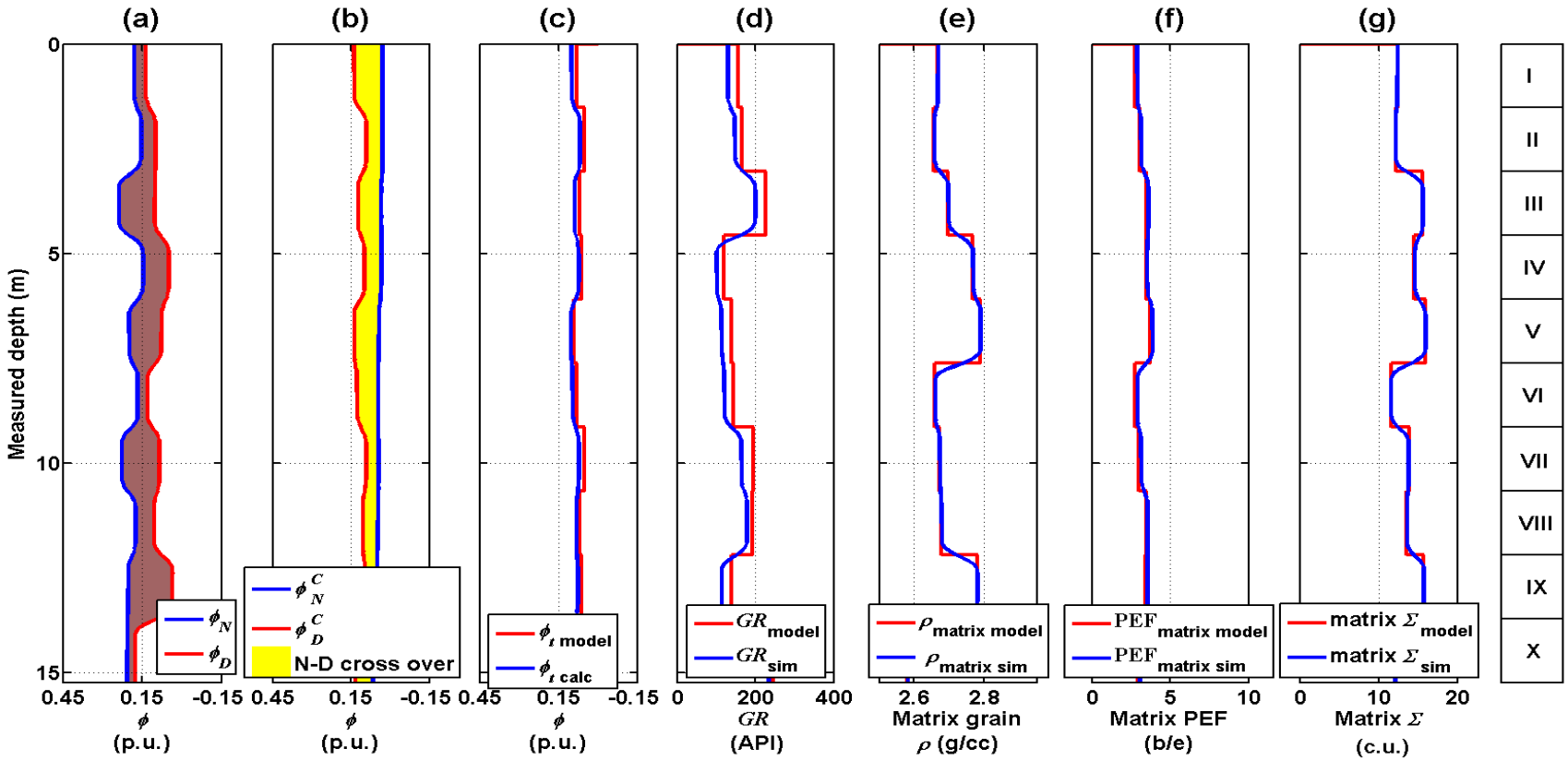

Figure 3.6: Panel (a) shows neutron-density crossover, panel (b) displays matrix-corrected neutron-density crossover where yellow and brown shading describe neutron-density crossover and matrix effects, respectively, panel (c) describes the comparison between model and matrix-corrected total porosity, panel (d) shows the comparison between model and simulated gamma-ray values, panel (e) shows the comparison between model and simulated matrix-density values, panel (f) exhibits the comparison between model and simulated matrix PEF, and panel (g) shows the comparison between model and simulated matrix Sigma, for Synthetic Case No. 2. Model values are shown as blocky red lines and simulated values are shown as continuous blue lines. I to X identify distinct layers in the synthetic case.

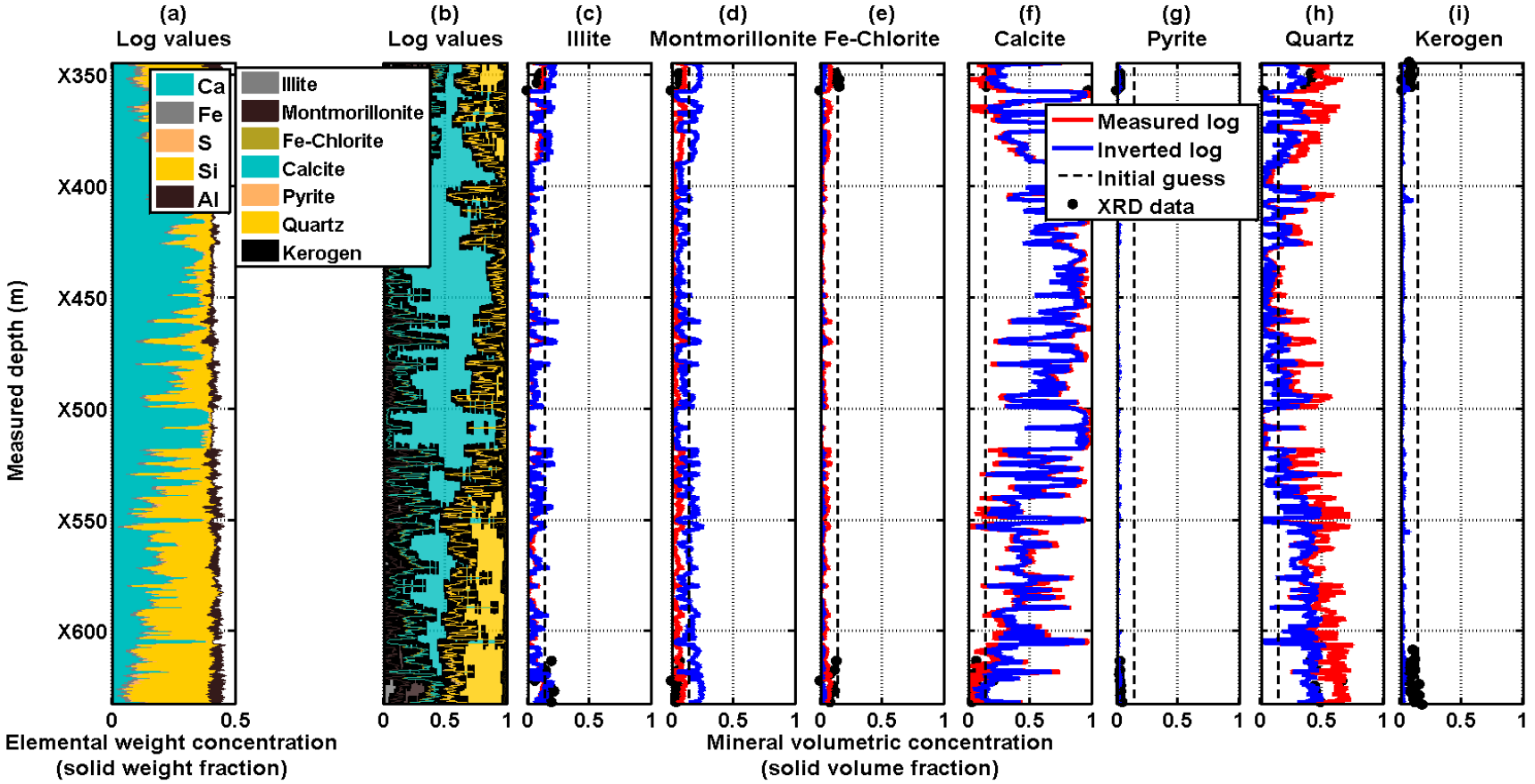

Figure 3.7: Panel (a) displays a cumulative plot of elemental weight concentrations; panel (b) shows a cumulative plot of inverted layer mineral volumetric concentrations and black uncertainty bars describe the 95% confidence interval; panels (c) to (i) describe inverted (shown as blue solid lines) and well-log (shown as red solid lines) mineral volumetric concentrations, for Field Case No. 1. Black dashed lines and black solid markers indicate the initial guess of the inversion and X-Ray Diffraction (XRD) core data, respectively; Ca, Fe, S, Si, and Al are the elements calcium, iron, sulfur, silicon, and aluminum, respectively.

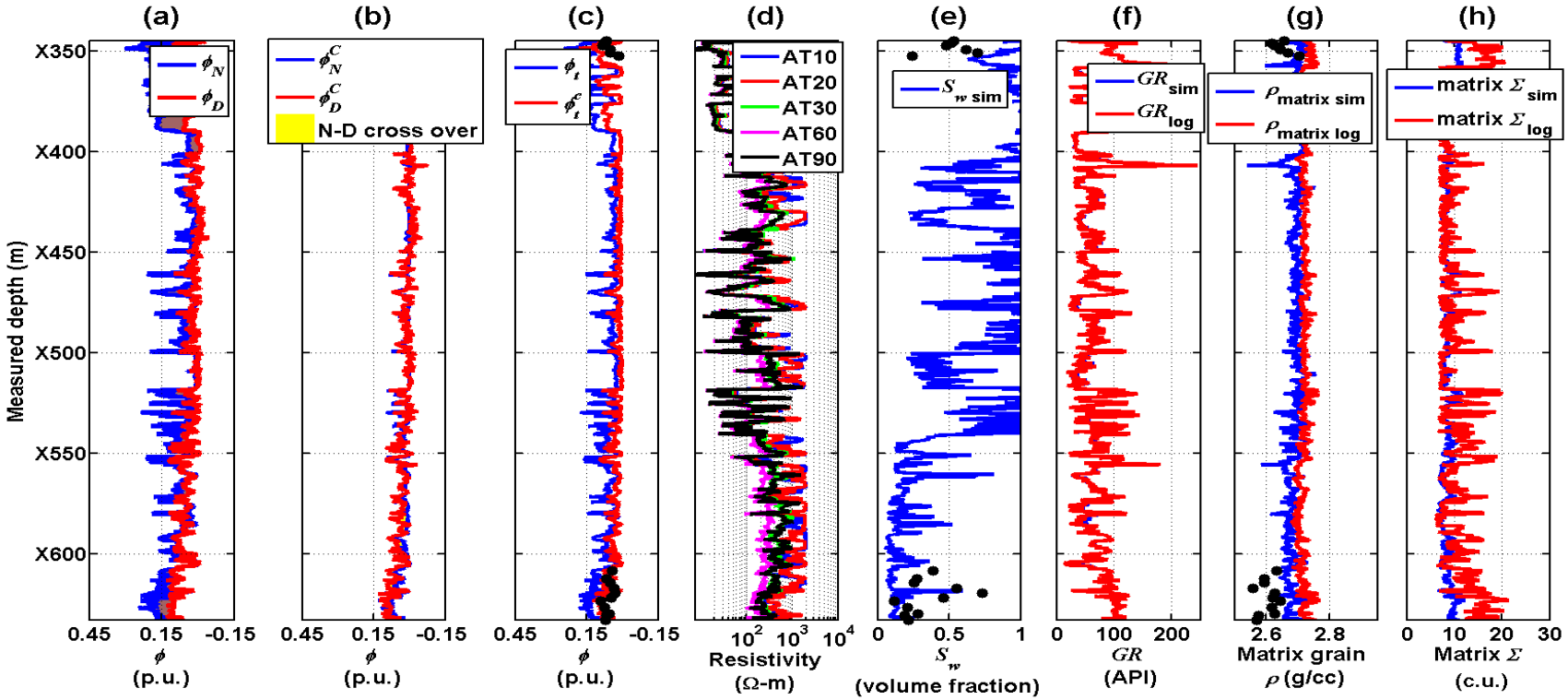

Figure 3.8 Panel (a) shows neutron-density crossover, panel (b) displays matrix-corrected neutron-density crossover where yellow and brown shading describe neutron-density crossover and matrix effects, respectively, panel (c) exhibits the comparison between well-log calculated, matrix-corrected, and core total porosities, panel (d) displays well-log resistivity measurements, panel (e) shows the comparison between calculated and core water saturation, panel (f) describes the comparison between log and simulated gamma-ray values, panel (g) shows the comparison between well-log, simulated, and core matrix-density values, and panel (h) displays the comparison between well-log and simulated matrix Sigma, for Field Case No. 1. Simulated values, log values, and core data are described by blue solid lines, red solid lines, and black solid markers, respectively; AT10, AT20, AT30, AT60, and AT90 indicate array induction two foot A10, A20, A30, A60, A90, resistivity logs, respectively.

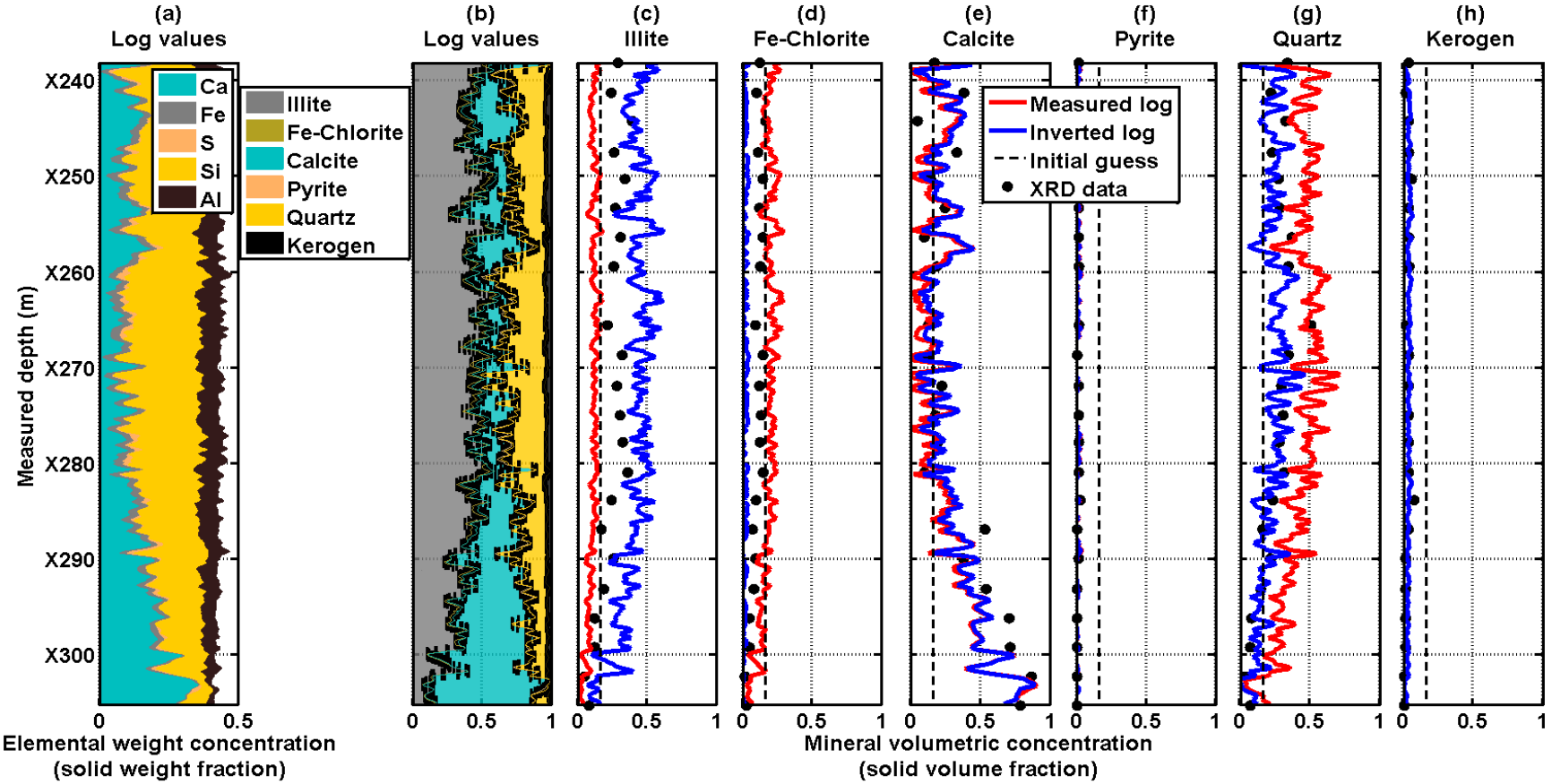

Figure 3.9: Panel (a) displays a cumulative plot of elemental weight concentrations; panel (b) shows a cumulative plot of inverted layer mineral volumetric concentrations and black uncertainty bars describe the 95% confidence interval; panels (c) to (h) describe inverted (shown as blue solid lines) and well-log (shown as red solid lines) mineral volumetric concentrations, for Field Case No. 2. Black dashed lines and black solid markers indicate the initial guess of the inversion and X-Ray Diffraction (XRD) core data, respectively; Ca, Fe, S, Si, and Al are the elements calcium, iron, sulfur, silicon, and aluminum, respectively.

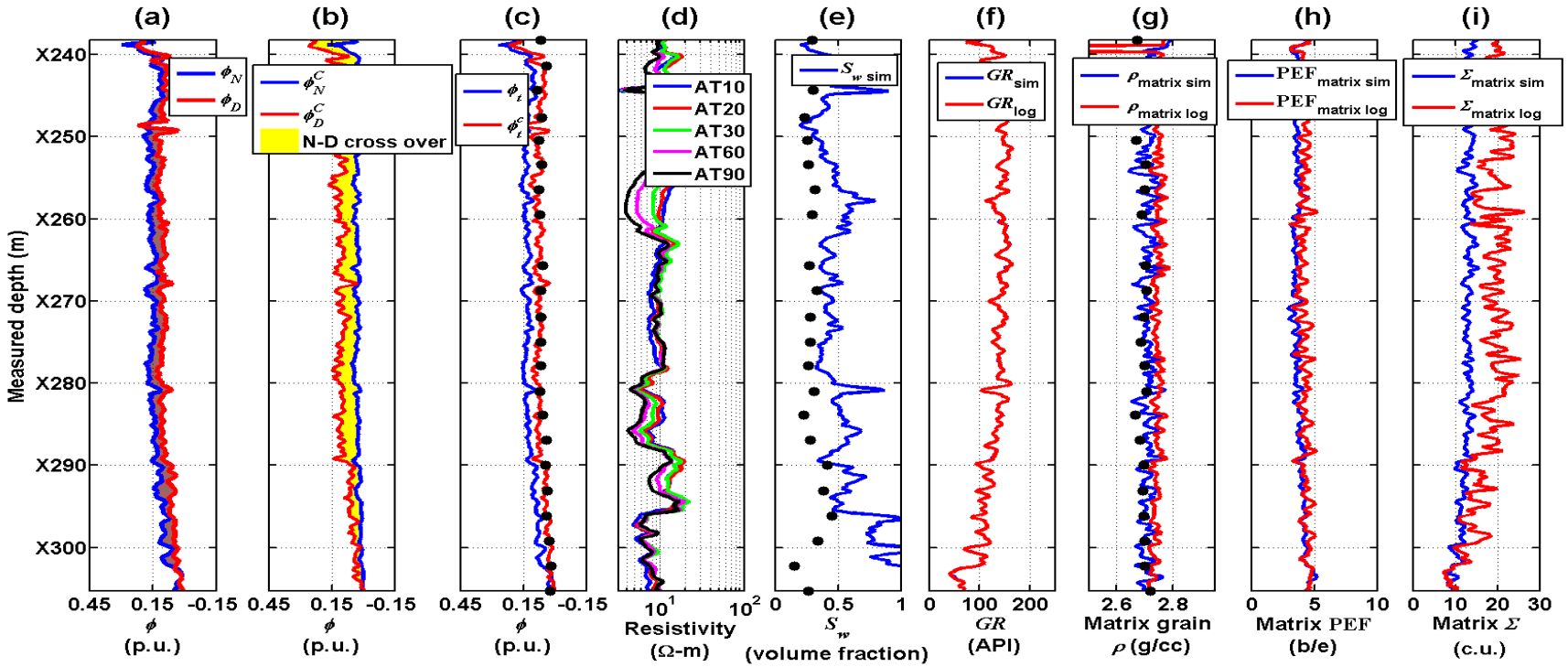

Figure 3.10: Panel (a) shows neutron-density crossover, panel (b) displays matrix-corrected neutron-density crossover where yellow and brown shading describe neutron-density crossover and matrix effects, respectively, panel (c) describes the comparison between well-log calculated, matrix-corrected, and core total porosities, panel (d) shows well-log resistivity measurements, panel (e) exhibits the comparison between calculated and core water saturation, panel (f) shows the comparison between log and simulated gamma-ray values, panel (g) displays the comparison between well-log, simulated, and core matrix-density values, panel (h) describes comparison between well-log and simulated matrix PEF, and panel (i) shows comparison between well-log and simulated matrix Sigma, for Field Case No. 2. Simulated values, log values, and core data are described by blue solid lines, red solid lines, and black solid markers, respectively; AT10, AT20, AT30, AT60, and AT90 indicate array induction two foot A10, A20, A30, A60, A90, resistivity measurements, respectively.

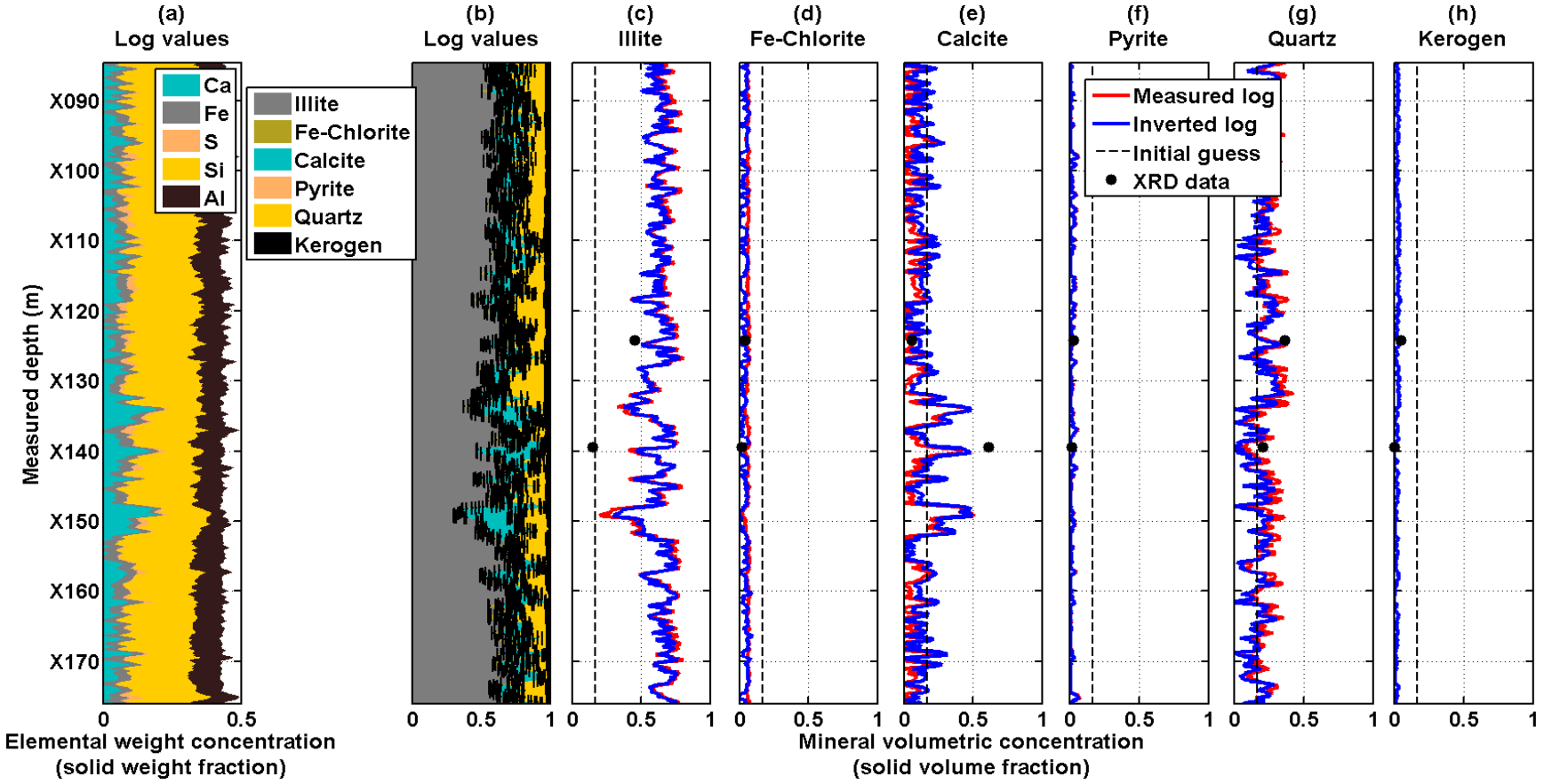

Figure 3.11: Panel (a) displays a cumulative plot of elemental weight concentrations; panel (b) shows a cumulative plot of inverted mineral volumetric concentrations and black uncertainty bars describe the 95% confidence interval; panels (c) to (h) exhibit inverted (shown as blue solid lines) and well-log (shown as red solid lines) mineral volumetric concentrations, for Field Case No. 3. Black dashed lines and black solid markers describe the initial guess of the inversion and X-Ray Diffraction (XRD) core data, respectively; Ca, Fe, S, Si, and Al are the elements calcium, iron, sulfur, silicon, and aluminum, respectively.

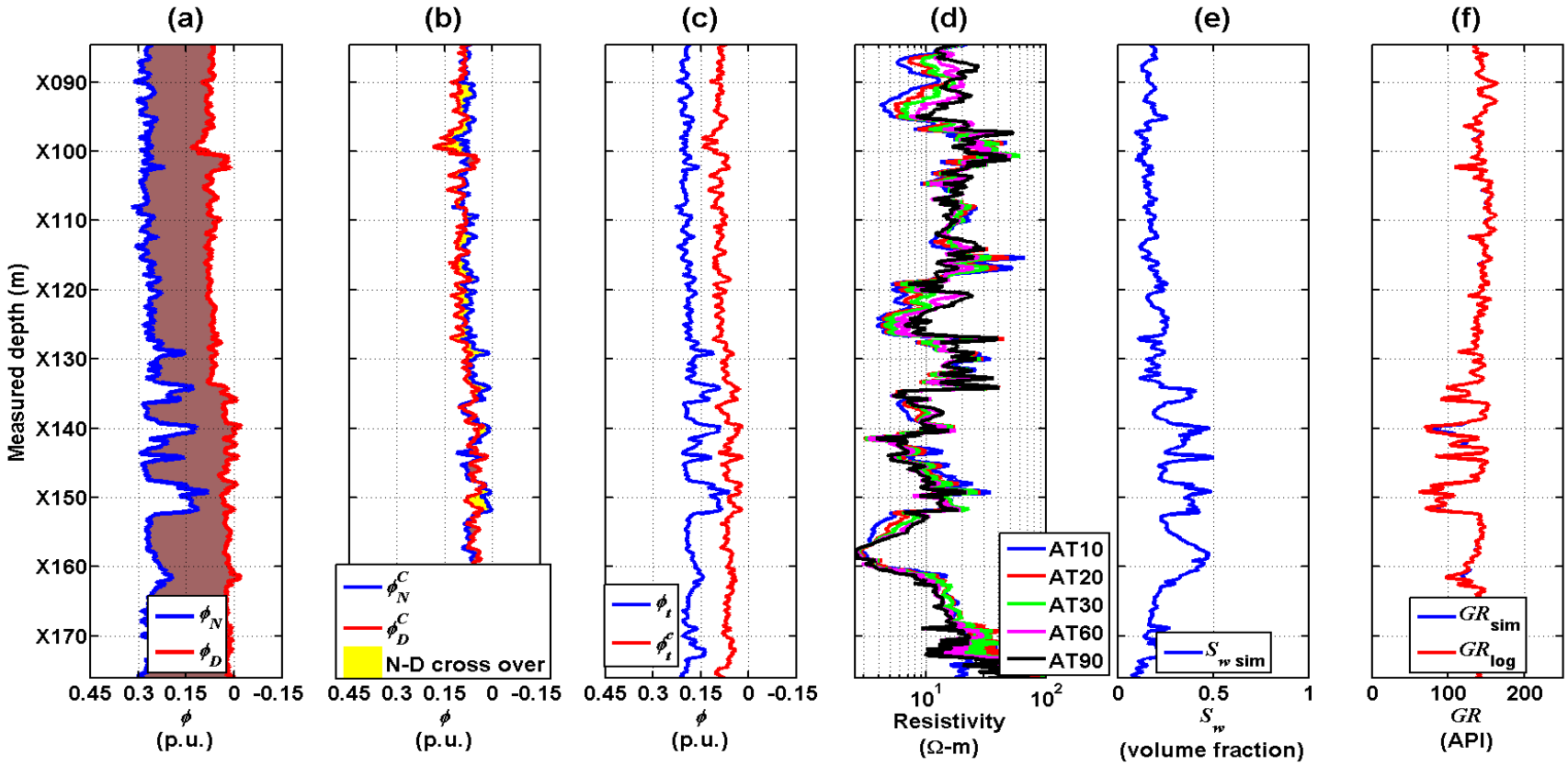

Figure 3.12: Panel (a) shows neutron-density crossover, panel (b) displays matrix-corrected neutron-density crossover where yellow and brown shading describe neutron-density crossover and matrix effects, respectively, panel (c) describes the comparison between well-log calculated and matrix-corrected total porosities, panel (d) exhibits well-log resistivity measurements, panel (e) shows the comparison between calculated water saturation, and panel (f) displays the comparison between log and simulated gamma-ray values, for Field Case No. 3. Simulated values and log values are described by blue solid lines and red solid lines, respectively; AT10, AT20, AT30, AT60, and AT90 indicate array induction two foot A10, A20, A30, A60, A90, resistivity logs, respectively.

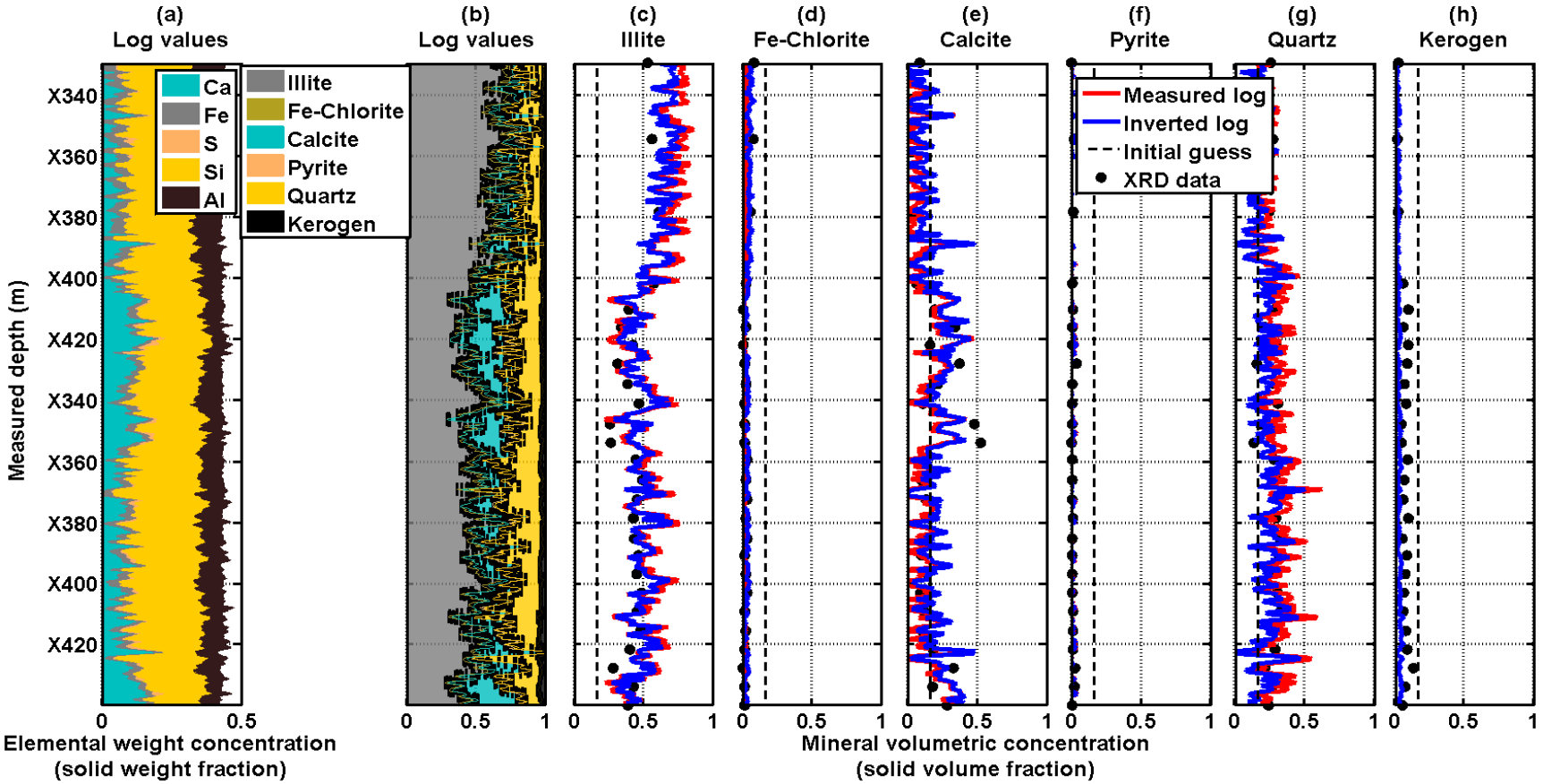

Figure 3.13: Panel (a) displays a cumulative plot of elemental weight concentrations; panel (b) shows a cumulative plot of inverted layer mineral volumetric concentrations and black uncertainty bars describe the 95% confidence interval; panels (c) to (h) describe inverted (shown as blue solid lines) and well-log (shown as red solid lines) mineral volumetric concentrations, for Field Case No. 4. Black dashed lines and black solid markers indicate the initial guess of the inversion and X-Ray Diffraction (XRD) core data, respectively; Ca, Fe, S, Si, and Al are the elements calcium, iron, sulfur, silicon, and aluminum, respectively.

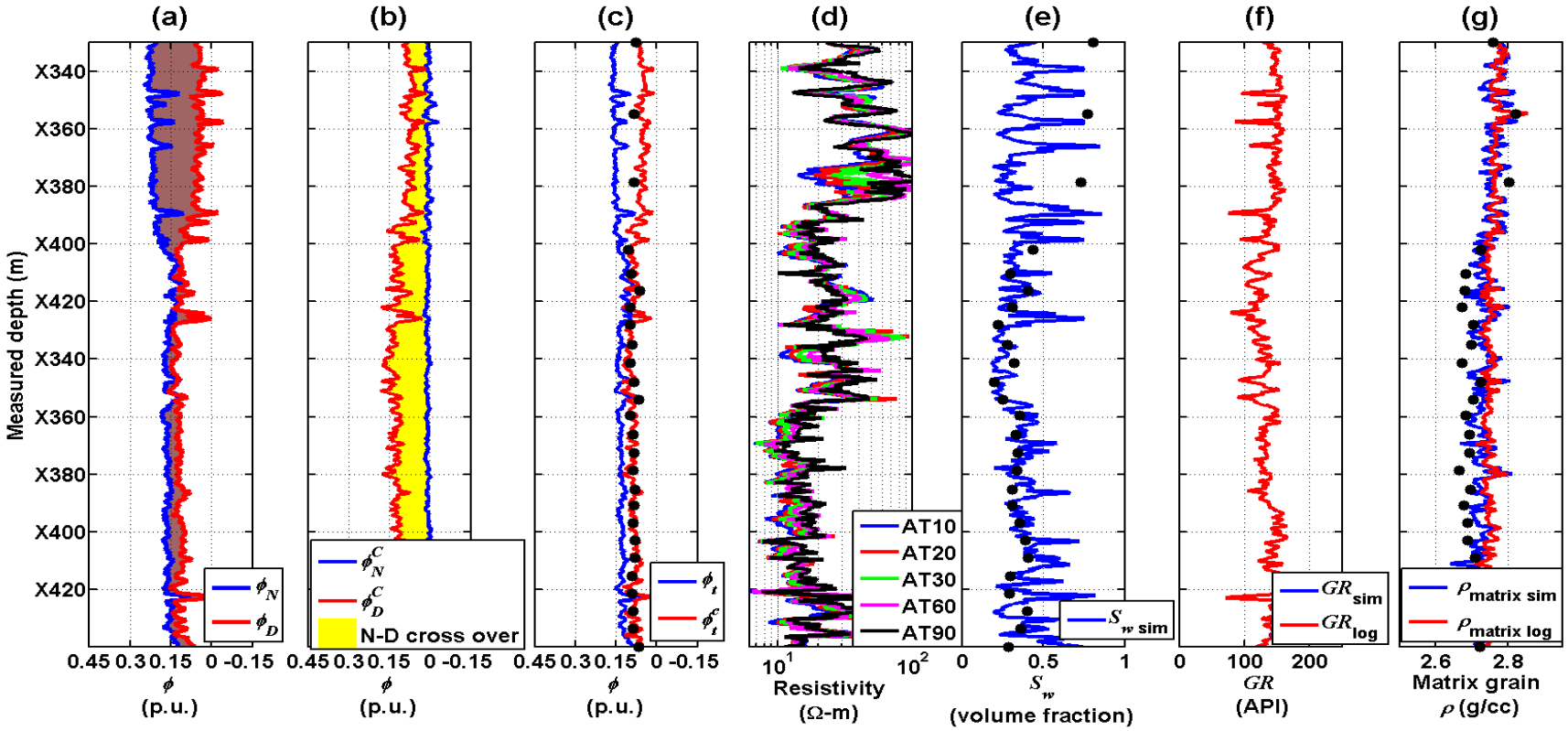

Figure 3.14: Panel (a) displays neutron-density crossover, panel (b) shows matrix-corrected neutron-density crossover where yellow and brown shading describe neutron-density crossover and matrix effects, respectively, panel (c) describes the comparison between well-log calculated, matrix-corrected, and total porosities, panel (d) exhibits well-log resistivity measurements, panel (e) shows the comparison between calculated and core water saturation, and panel (f) displays the comparison between log and simulated gamma-ray values, panel (g) describes the comparison between well-log, simulated, and core matrix-density values, for Field Case No. 4. Simulated values, log values, and core data are described by blue solid lines, red solid lines, and black solid markers, respectively; AT10, AT20, AT30, AT60, and AT90 indicate array induction two foot A10, A20, A30, A60, A90, resistivity logs, respectively.

Chapter 4: Inversion-Based Interpretation of LWD Gamma-Ray Spectroscopy Measurements

Neutron-induced spectroscopy measurements are commonly used to quantify in-situ elemental compositions of rocks from the processing of measured gamma-ray energy spectra. However, geometrical effects on measured spectroscopy logs, such as thin beds, dipping beds, and deviated well trajectories, can cause shoulder-bed averaging that compromises the assessment of true layer elemental composition. I introduce an inversion-based interpretation method to evaluate layer elemental compositions from spectroscopy measurements acquired with a commercial 14-MeV pulsed-neutron logging-while-drilling (LWD) spectroscopy tool. The algorithm is based on a new spectroscopy fast-forward simulation technique and estimates layer-by-layer elemental relative yields, weight concentrations, and their uncertainties. Calculations are performed with inelastic and capture gamma-ray spectroscopy measurements which arise from high- and low-energy neutron interactions, respectively. This strategy provides two sets of data that independently validate estimated elemental compositions and can ascertain chemical elements present in only one measurement mode. In laminated formations where layer thicknesses are appreciably below the vertical resolution of the tool, it is impossible to quantify layer properties with inversion methods. I therefore develop an additional interpretation method based on a spectroscopy mixing law to estimate elemental compositions within individual laminae. The new inversion-based interpretation methods are successfully verified with four challenging synthetic cases and implemented in two field cases with varying lithology and well trajectories. Results show that the developed methods reduce shoulder-bed averaging effects on measured spectroscopy logs by as

much as 0.4 yield fraction and 0.17 weight fraction. Estimated elemental compositions with reduced shoulder-bed averaging effects improve calculations in subsequent spectroscopy-based petrophysical interpretation.

4.1 INTRODUCTION

Spectroscopy logs measure gamma-ray counts as a function of energy. Gamma rays are emitted during high-energy inelastic neutron scattering or thermal neutron capture. Elemental relative yields and weight concentrations are obtained from measured gamma-ray spectra using weighted least-squares analysis and oxide closure models (Hertzog, 1978; Galford et al., 2009). Spectroscopy elemental logs are a more practical method of interpreting lithology (solid composition) compared to the common approach of determining lithology from a combination of well logs, such as gamma ray, bulk density, neutron porosity, and photoelectric factor (PEF) (Quirein et al., 1986), because elemental compositions are directly related to volume mineral concentrations. Elemental compositions obtained from spectroscopy logs are therefore important in accurately evaluating matrix (solid) compositions and properties (Flaum and Pirie, 1981; Herron and Herron, 1996; Herron and Herron, 2000; Herron et al., 2002). Elemental compositions are also useful in discerning the presence of minerals that may falsely affect well logs, such as sulfur from barite in drilling mud which decreases gamma-ray readings. Presence of sulfur could also be indicative of pyrite which increases electrical conductivity thereby decreasing resistivity-log values, while sulfur in anhydrite could be used to quantify the degree of sand cementation by anhydrite, for instance.

Shoulder-bed effects occur on spectroscopy measurements due to the influence of adjacent beds when two or more layers are present within the volume of investigation of

the tool. This phenomenon is commonly observed in thin beds, dipping beds, and well trajectories that traverse multiple bed boundaries, particularly in heterogeneous formations where elemental compositions change significantly from one layer to another. Shoulder-bed averaging effects lead to false representations of layer properties and have been documented in the context of several nuclear measurements such as neutron, density (Mendoza et al., 2010a, 2010b; Heidari et al., 2012), Sigma (Mimoun et al., 2011a; Ortega et al., 2014a), and spectroscopy (Ajayi et al., 2014). The degree of shoulder-bed averaging increases in highly deviated wells penetrating thin formations (Hardman and Shen, 1987). Passey et al. (2005) showed that geometrical effects in high-angle/horizontal (HA/HZ) wells can considerably affect the interpretation of well logs.

The best method to account for geometrical effects on measured logs is through the use of efficient forward modeling in conjunction with inverse estimation theory (Passey et al., 2005; Rasmus et al., 2009). Sanchez-Ramirez et al. (2009) and Heidari et al. (2012) implemented the joint inversion of nuclear and resistivity wireline logs in vertical wells to mitigate shoulder-bed effects in petrophysical interpretations. Mendoza et al. (2012) used inversion-based approaches to accurately interpret three-dimensional (3D) formation bulk density using LWD measurements acquired in high-angle/horizontal (HA/HZ) wells. Similarly, Ijasan et al. (2013) applied an inversion method to decrease geometrical effects on LWD nuclear and resistivity logs, thereby improving the petrophysical and compositional interpretation of measurements acquired in HA/HZ wells. Mimoun et al. (2011b) used inversion methods to correct shoulder-bed averaging effects on pulsed-neutron Sigma wireline measurements. Ortega (2014b) extended the 1D

Sigma inversion method introduced by Mimoun et al. (2011b) to include the effects of dipping beds and invasion in LWD measurements.

It is impossible to interpret true petrophysical layer properties in formations from measured logs and/or inversion methods when layer thicknesses are smaller than the effective vertical resolution of the tool. Bulk (macroscopic) response equations are commonly invoked to interpret such laminated formations as binary lithology systems that comprise two sequence end members in varying concentrations, e.g., sandstone and shale in laminated shaly sandstone. Examples of analysis using bulk response equations include resistivity and Sigma log interpretation methods in sandstone-shale laminated systems introduced by Poupon and Leveaux (1954) and Haley (1995), respectively. There currently exist no published works that (a) account for bed-geometry and well deviation effects on spectroscopy LWD measurements, or (b) accurately quantify spectroscopy measurements in laminations thinner than the vertical resolution of the LWD tool.

I introduce new interpretation methods to estimate layer-by-layer elemental relative yields and weight concentrations from spectroscopy measurements acquired with a 14-MeV pulsed-neutron LWD spectroscopy tool, which can also be applied to laminated formations. The tool assumed in this chapter operates commercially in the neutron capture measurement mode alone but I analyze both inelastic and capture modes to enable quantification of elements that are detectable in only one measurement mode. Furthermore, as shown in Figure 4.1, because inelastic spectroscopy measurements arise from gamma rays due to high-energy inelastic neutron scattering while capture measurements result from low-energy thermal neutron capture, flux sensitivity functions (FSFs) of inelastic and capture measurements exhibit different volumes of investigation,

where inelastic measurements have a smaller volume of investigation than capture measurements.

The inversion-based interpretation method is based on a newly developed fast-forward spectroscopy simulation algorithm summarized in Chapter 2. This rapid simulation method implements a first-order perturbation of 3D Monte Carlo-derived FSFs on layer elemental absolute yields to simulate elemental relative yield and weight logs measured at a short-spaced sodium iodide (NaI) gamma-ray detector in the LWD spectroscopy tool (Ajayi et al., 2014). Flux sensitivity functions are dependent upon formation migration lengths and are rapidly simulated as a function of perturbations in migration length; they explicitly account for borehole, tool, and formation effects on spectroscopy measurements. In the analysis of laminated formations, I introduce a mixing law to quantify elemental weight concentrations of sandstone fractions included in laminations based on a linear relationship between elemental weight concentrations and volumetric concentrations of one of two end members in the laminated system.

The following sections describe the interpretation of spectroscopy measurements using inversion and mixing law methods. Examples of application consider four synthetic and two field cases that emphasize the importance of reducing shoulder-bed effects on measured spectroscopy logs to improve the accuracy and reliability of the interpretations.

4.2 INVERSION-BASED INTERPRETATION OF SPECTROSCOPY LOGS

4.2.1 Inversion Formulation

The interpretation method introduced in this chapter is based on a spectroscopy fast-forward model outlined in Chapter 2. Inclusion of the spectroscopy forward model in the inversion–based interpretation method accounts for shoulder-bed averaging effects on simulated logs because these effects are explicitly incorporated into the forward model. The spectroscopy fast-forward model is used to numerically simulate measured elemental relative yields, **d**, as a function of layer spectroscopy properties, **x**. Layer spectroscopy properties include absolute yields, $y_{abs,i}$, and weight concentrations, M_i, of each chemical element, *i*, present in the formation. I use elemental relative yields, y_i, as the measured log property in the estimation of both layer elemental absolute yields and weight concentrations because elemental relative yields are the direct output of the spectroscopy forward model. The approach of using elemental relative yield logs in the interpretation method therefore requires no further processing of forward simulated measurements.

The nonlinearity between detector spectroscopy responses and formation migration length in the forward model (described in Chapter 2) necessitates the implementation of nonlinear inversion to minimize quadratic errors between fast-simulated and measured relative yields. To that end, I define the quadratic cost function

$$C(\mathbf{x}) = \left\| \mathbf{W}_d \cdot \left[\mathbf{g}(\mathbf{x}) - \mathbf{d}_m \right] \right\|_2^2 + \lambda^2 \left\| \mathbf{W}_x \cdot \left(\mathbf{x} - \mathbf{x}_{ref} \right) \right\|_2^2 , \qquad (4.1)$$

where λ is a regularization (stabilization) parameter, $\mathbf{x}_{ref}$ is a reference vector, **x** is a vector of layer elemental absolute yields or weight concentrations dependent upon the

desired solution, $\mathbf{W}_d$ is a data-weighting matrix, $\mathbf{W}_x$ is a model-weighting matrix, $\mathbf{d}_m$ is the vector of measured elemental relative yield logs, and $\mathbf{g}$ is the spectroscopy fast-forward model.

The regularization (stabilization) parameter, λ, in equation 4.1 enforces stability to a possibly ill-posed spectroscopy problem by improving the uniqueness and convergence of the solution in the presence of noisy and/or inadequate data by adjusting the relative weight given to the two additive terms of the quadratic cost function. In long depth intervals, λ is defined as the variance of the error between spectroscopy measurements and numerically simulated data. However, in shorter depth intervals, where there is not a significant variation in well log values, λ is obtained using Hansen's (1994) L-curve strategy which calculates a value that best minimizes the norm of the error between numerically simulated and measured logs. The impact of λ in the quadratic cost function progressively diminishes as the algorithm reaches convergence.

Additionally, the reference vector, $\mathbf{x}_{ref}$ introduced in the quadratic cost function given in equation 4.1, decreases the non-uniqueness of the problem by ensuring that the solution remains in the neighborhood of the specified reference vector and not trapped within an abnormal local minimum. This reference vector is usually defined by the bed-center values of spectroscopy elemental logs.

The data weighting matrix, $\mathbf{W}_d$ is introduced into the inversion to provide selective weighting on measured spectroscopy logs for each element; it is here defined as a diagonal matrix whose entries correspond to the statistical variance of the relative yield of each element, ∂y_i, at each depth level, and is given by

$$\partial y_i = \frac{\partial y_{abs,i}}{\sum_{i=1}^{m} y_{abs,i}}, \qquad (4.2)$$

where $\partial y_{abs,i}$ is the statistical variance for each element's energy-integrated spectrum within the energy range of the measurement (elemental absolute yield), and $\sum_{i=1}^{m} y_{abs,i}$ is the sum of energy integrated measured spectra for the *m* elements present in the formation. This approach places more emphasis on measurements acquired for elements which exhibit higher variability in measured log values. Such variability typically arises in elements that are significantly affected by shoulder-bed averaging.

There are typically few measured data points in thinly-bedded intervals, whereby it is necessary to introduce a model-weighting matrix, $\mathbf{W}_x$, which emphasizes thin bed elemental compositions in the interpretation. A strategic choice for the model-weighting matrix is a diagonal matrix with entries equal to the inverse of relative layer thickness, $1/h_f$ (where h_f designates the thickness of bed *f*), because this approach automatically emphaizes thin over thick beds.

4.2.2 Formation Geometrical Model

The formation geometrical model included in the inversion algorithm is defined by layer thicknesses, apparent dip, and apparent azimuth. Bed-boundary locations can be obtained manually based on inflection points of measurements that are sensitive to changes in layer petrophysical properties, such as density, gamma ray, PEF images, and spectroscopy logs, using a threshold variance algorithm (Uzoh et al., 2009). Alternatively, I may define bed-boundary locations using the consolidated gamma

geometrical model introduced by Ijasan et al. (2013) that also estimates apparent dip and azimuth. The consolidated gamma geometrical method uses borehole sinusoids calculated along borehole depth and azimuth to estimate formation geometrical properties via least-squares minimization (Plumb and Luthi, 1989). Sinusoids are obtained from the intersection of an initial selection of bed boundaries and based on inflection points of nuclear images and spectroscopy logs using the threshold variance algorithm (Yin et al., 2008).

4.2.3 Inversion-based Interpretation Method

The inversion-based interpretation method estimates the set of $y_{abs,i}$ and M_i that best reconstruct elemental relative yields by iteratively minimizing quadratic errors between simulated and measured elemental relative yields, as emphasized by the cost function, $C(\mathbf{x})$ in equation 4.1. Iterative nonlinear minimization of the quadratic cost function is performed using Occam's method (Aster et al., 2013):

$$\left\{\left[\mathbf{J}^T\left(\mathbf{x}^k\right)\cdot\mathbf{W}_d^T\cdot\mathbf{W}_d\cdot\mathbf{J}\left(\mathbf{x}^k\right)\right]+\lambda^2\mathbf{W}_x^T\mathbf{W}_x\right\}\mathbf{x}^{k+1}=\mathbf{J}^T\left(\mathbf{x}^k\right)\left[\left(\mathbf{W}_d{}^T\cdot\mathbf{W}_d\right)\cdot\hat{\mathbf{e}}\right]+\lambda^2\mathbf{x}_{ref}, \qquad (4.3)$$

where

$$\hat{\mathbf{e}}=\left[\mathbf{d}_m-\mathbf{g}\left(\mathbf{x}^k\right)+\mathbf{J}\left(\mathbf{x}^k\right)\mathbf{x}^k\right], \qquad (4.4)$$

and subject to $0\le x_i\le 1$, which ensures positivity of the results, where $\mathbf{x}^k$ and $\mathbf{x}^{k+1}$ indicate the vector of model properties at iteration k and the updated trial model at iteration k+1, respectively, superscript T indicates transposition, $\mathbf{x}_{ref}$ is a reference vector, $\hat{\mathbf{e}}$ is a modified vector of data misfit, and $\mathbf{J}$ is the Jacobian or sensitivity matrix.

I populate the formation geometrical model with an initial guess of elemental

relative yields or weight concentrations which is updated at every iteration in the inversion until the norm of the difference between measured and numerically simulated logs is equal to or less than 0.001 for a maximum of ten iterations. The cut-off after ten iterations is implemented because sensitivity analysis shows that convergence of the inversion algorithm is typically achieved within ten iterations.

Separate nonlinear inversion is performed in the inelastic and capture measurement domains because of the significant difference in neutron transport mechanisms between these two measurements (high-energy neutron interactions lead to inelastic gamma rays while thermal neutron interactions result in capture gamma rays). These differences result in distinct vertical resolutions (approximately 35-cm and 40-cm for inelastic and capture measurements, respectively) and depths of investigation into the formation (approximately 12-cm and 18-cm for inelastic and capture measurements, respectively) for both measurements.

In long depth segments, the formation is interpreted using "moving depth windows" that have approximately constant geometrical properties, such as well dip, azimuth, and inversion parameters including $\mathbf{W}_d$, $\mathbf{W}_x$, and λ. I limit the depth interval under study to a maximum of 45.72-m (150-ft) to avoid computational complexities due to the presence of large Jacobian matrices in the inversion algorithm.

I assume that logs are exposed to negligible invasion because the spectroscopy near gamma-ray sensor in the LWD tool under study is located close to the drill bit (Weller et al., 2005). Such an assumption is validated through the use of dry formation elemental relative yields and weight concentrations as layer spectroscopy properties because these properties are independent of invasion or fluid saturations. It follows that

formation elemental compositions and other petrophysical properties are approximately constant and isotropic within each layer. Elements present in invading or saturating fluids such as hydrogen, oxygen, and chlorine can be measurably impacted by changes in invasion, saturation, and porosity, which may introduce complexities into the interpretation, but are not actually indicative of formation solid composition, whereby they are not included in our method.

4.2.3.1 *Jacobian Matrix Calculations*

For the estimation of elemental absolute yields, entries of the Jacobian matrix, $\mathbf{J}_{y-y_{abs}}$, are defined by the derivative of elemental relative yields with respect to elemental absolute yields, where

$$\mathbf{J}_{y-y_{abs}} = \begin{bmatrix} \begin{pmatrix} \frac{\partial y_1}{\partial y_{abs,1}} & \cdots & \frac{\partial y_1}{\partial y_{abs,m}} \\ \vdots & \ddots & \vdots \\ \frac{\partial y_m}{\partial y_{abs,1}} & \cdots & \frac{\partial y_m}{\partial y_{abs,m}} \end{pmatrix}^1 & \cdots & \begin{pmatrix} \frac{\partial y_1}{\partial y_{abs,1}} & \cdots & \frac{\partial y_1}{\partial y_{abs,m}} \\ \vdots & \ddots & \vdots \\ \frac{\partial y_m}{\partial y_{abs,1}} & \cdots & \frac{\partial y_m}{\partial y_{abs,m}} \end{pmatrix}_g^1 \\ \vdots & \ddots & \vdots \\ \begin{pmatrix} \frac{\partial y_1}{\partial y_{abs,1}} & \cdots & \frac{\partial y_1}{\partial y_{abs,m}} \\ \vdots & \ddots & \vdots \\ \frac{\partial y_m}{\partial y_{abs,1}} & \cdots & \frac{\partial y_m}{\partial y_{abs,m}} \end{pmatrix}^r & \cdots & \begin{pmatrix} \frac{\partial y_1}{\partial y_{abs,1}} & \cdots & \frac{\partial y_1}{\partial y_{abs,m}} \\ \vdots & \ddots & \vdots \\ \frac{\partial y_m}{\partial y_{abs,1}} & \cdots & \frac{\partial y_m}{\partial y_{abs,m}} \end{pmatrix}_g^r \end{bmatrix}. \quad (4.5)$$

Similarly, for the estimations of elemental weight concentrations, entries of the Jacobian matrix, $\mathbf{J}_{y\text{-}M}$, are defined by the derivative of elemental relative yields with respect to elemental weight concentrations and are given by

$$\mathbf{J}_{y-M} = \begin{bmatrix} \begin{pmatrix} \frac{\partial y_1}{\partial M_1} & \cdots & \frac{\partial y_1}{\partial M_m} \\ \vdots & \ddots & \vdots \\ \frac{\partial y_m}{\partial M_1} & \cdots & \frac{\partial y_m}{\partial M_m} \end{pmatrix}_1^1 & \cdots & \begin{pmatrix} \frac{\partial y_1}{\partial M_1} & \cdots & \frac{\partial y_1}{\partial M_m} \\ \vdots & \ddots & \vdots \\ \frac{\partial y_m}{\partial M_1} & \cdots & \frac{\partial y_m}{\partial M_m} \end{pmatrix}_g^1 \\ \vdots & \ddots & \vdots \\ \begin{pmatrix} \frac{\partial y_1}{\partial M_1} & \cdots & \frac{\partial y_1}{\partial M_m} \\ \vdots & \ddots & \vdots \\ \frac{\partial y_m}{\partial M_1} & \cdots & \frac{\partial y_m}{\partial M_m} \end{pmatrix}_1^r & \cdots & \begin{pmatrix} \frac{\partial y_1}{\partial M_1} & \cdots & \frac{\partial y_1}{\partial M_m} \\ \vdots & \ddots & \vdots \\ \frac{\partial y_m}{\partial M_1} & \cdots & \frac{\partial y_m}{\partial M_m} \end{pmatrix}_g^r \end{bmatrix}, \qquad (4.6)$$

where the size of the Jacobian matrices in equations 4.5 and 4.6 is $m \times r$ rows which describe the number of elements, *m*, at *r* measurement points, and $m \times g$ columns which describe the number of elements, *m*, in *g* beds.

The Jacobian matrix can be calculated numerically by perturbing model properties and simulating corresponding elemental relative yields with the forward model. However, it is computationally expensive to invoke the forward model for first-order derivative Jacobian matrix calculations at each iteration in the inversion. A more efficient approach is to calculate the Jacobian matrix using analytical expressions of the forward model which is approximately fifteen times faster than numerical calculations of the Jacobian matrix. Analytical solutions of the Jacobian matrix are calculated through a first-order derivative of the equation that describes spectroscopy fast-forward simulation outlined in Chapter 2. At a single measurement point, this calculation is given by

$$\frac{\partial y(i)}{\partial y_{abs}(i)} = \frac{\left[\mathrm{FSF}_{jac}\left(\sum_{i=1}^{m}\mathrm{FSF}_{jac}y_{abs,i}\right)\right] - \left\{\left(\mathrm{FSF}_{jac}y_{abs,i}\right)\left[\mathrm{FSF}_{jac} + \left(\sum_{ii=1}^{m}\mathrm{FSF}_{jac}y_{abs,ii}\right)_{ii\neq i}\right]\right\}}{\left(\sum_{i=1}^{m}\mathrm{FSF}_{jac}y_{abs,i}\right)^{2}},$$

(4.7)

for the estimation of elemental absolute yields and

$$\frac{\partial y(i)}{\partial M(i)} = \frac{\left[\mathrm{FSF}_{jac}\left(\sum_{i=1}^{m}\mathrm{FSF}_{jac}Se_{i}M_{i}\right)\right] - \left\{\left(\mathrm{FSF}_{jac}Se_{i}M_{i}\right)\left[\mathrm{FSF}_{jac} + \left(\sum_{ii=1}^{m}\mathrm{FSF}_{jac}Se_{ii}M_{ii}\right)_{ii\neq i}\right]\right\}}{\left(\sum_{i=1}^{m}\mathrm{FSF}_{jac}Se_{i}M_{i}\right)^{2}},$$

(4.8)

for the estimation of elemental weight concentrations, where *Se* designates the relative detection sensitivity of each element to the production of gamma rays, and subscript *ii* designates the index for *m* elements excluding element *i*. The term FSF_{jac} designates the sensitivity at a single measurement point to the *f*-th layer and is calculated from the normalized FSF for all materials within the volume of investigation of the detector using the FSF and formation geometrical model at a single measurement point in the forward simulation.

4.2.3.2 *Processing of Estimated Parameters*

Estimated layer elemental absolute yields are converted into elemental relative yields by

$$y_i = \frac{y_{abs,i}}{\sum_{i=1}^{m} y_{abs,i}}. \qquad (4.9)$$

As an alternative to the estimation of elemental weight concentrations through the outlined inversion methods, they can be calculated from inverted elemental relative yields using an oxide closure model that assumes that the primary measured formation elements add to unity and exist as oxides or carbonates (Galford and Hertzog, 1989; Hertzog et al., 1989; Grau et al., 1990; Galford et al., 2009). The oxide closure model is described by

$$F\sum_{i=1}^{m} \frac{X_i y_i}{Se_i} = 1 , \qquad (4.10)$$

where X_i is a factor used to account for the weights of elements that are not measured but are associated with element i (such as oxygen and carbon in oxides and carbonates, respectively), and F is a depth varying normalization factor that accounts for the variability of neutron flux due to changes in environmental properties. The solid weight concentration of element i, M_i, is calculated through

$$M_i = F\frac{y_i}{Se_i}, \qquad (4.11)$$

where F is obtained from equation 4.10.

In field measurements, the spectrum of aluminum, measured by the LWD spectroscopy tool under study, is weak but strongly correlated with the spectrum of other elements, particularly iron. Aluminum is therefore not directly estimated in the inversion but modeled from other elemental weight concentrations (Herron and Herron, 1996). The aluminum modeling equation for the LWD spectroscopy tool is given by

$$M_{Aluminum} = 0.38\left(1 - 2.139M_{Silicon} - 2.497M_{Calcium} - 1.99M_{Iron}\right), \qquad (4.12)$$

where $M_{Aluminum}$, $M_{Silicon}$, $M_{Calcium}$, and M_{Iron} designate the solid weight fraction of aluminum, silicon, calcium, and iron, respectively.

4.2.3.3 *Initial Guess Generation*

Inversion-based interpretation is relatively insensitive to the initial guess of the formation geometrical model because the estimation problem is always even determined. Even determinedness arises because the number of inverted and measured elements is the same. In most cases, it therefore suffices to assume a uniform average value for the initial guess equal to the reciprocal of the number of elements in the estimation problem. When estimation problems are unstable, the initial guess can be obtained from spectroscopy elemental logs or elemental core data such as X-ray fluorescence (XRF) data.

4.2.3.4 *Assessment of Uncertainty of Inversion Results*

The 95% confidence interval in each estimated parameter is calculated through a modification to the covariance method of evaluating uncertainty bars given by (Aster et al., 2013)

$$\pm 1.96 q \sqrt{\left\| \mathbf{W}_d \cdot \mathbf{e}(\mathbf{x}) \right\|_2^2 \cdot diag\left\{ \left[\mathbf{J}^T \cdot \mathbf{W}_d^T \cdot \mathbf{W}_d \cdot \mathbf{J} \right]^{-1} \right\}} \quad , \qquad (4.13)$$

where **e** is the vector of data misfit given by $\left[\mathbf{d}_m - \mathbf{g}\left(\mathbf{x}^k\right) \right]$, *diag* describes diagonal matrix entries, and q is the number of degrees of freedom in the inversion. Confidence intervals quantify the stability of inversion results and the uncertainty in estimated elemental relative yields and weight concentrations due to perturbations in the input data.

4.2.3.5 *Assumptions made in the inversion of synthetic and field cases*

For the examples of inversion-based interpretation considered below, I assume a rock-formation model consisting of horizontal layers with constant spectroscopy properties (including elemental absolute yields, relative yields, and weight concentrations). Likewise, I assume a fixed well trajectory with constant well dip and azimuth for synthetic cases, while in field cases I interpret a 30.48-m section of the well where well dip and azimuth are approximately constant. In synthetic and field cases, inversion is performed with only one processing window for the entire depth interval (interpreted measured depths are relatively short and do not exceed 30.48-m for any of the cases examined in this chapter).

4.3 INTERPRETATION OF LAMINATED FORMATIONS

In laminated formations, where individual beds are appreciably thinner than the vertical resolution of the tool, it is impossible to resolve layer elemental compositions with the previously outlined inversion techniques. I seek to define a linear spectroscopy mixing law that estimates elemental weight concentrations in such laminated formations. The mixing law quantifies elemental weight concentrations with respect to the volumetric concentration of one end member of a binary lithology laminated sequence. This end member is usually a water-saturated unit and the mixing law estimates the elemental composition of the remaining sequence end member. A common example is laminated shaly sandstone where the volumetric concentration of water-saturated shale is used to quantify elemental compositions of a hydrocarbon-bearing sandstone matrix.

I perform numerical simulations and well-log calculations to determine the relationship between elemental weight concentrations and an end member of a binary

lithology sequence. Monte Carlo simulations using the Monte Carlo N-Particle code, MCNP (X-5 Monte Carlo Team, 2005), reported in Figure 4.2, indicate a linear relationship between simulated elemental weight concentrations and volumetric concentration of shale for the elements present in the formation [silicon (Si), aluminum (Al), potassium (K), and iron (Fe)]. Results are obtained in synthetic cases of laminated shaly sandstone with the volumetric concentration of shale (C_{sh}) varying from 0 to 1. Sandstone has an assumed porosity and hydrocarbon (oil) saturation of 20 porosity units (p.u.) and 80%, respectively. The solid volumetric composition of sandstone is defined as 10% quartz, 20% limestone, and 40% K-feldspar. Shale has an assumed solid volumetric composition of 20% quartz, 40% illite, and 40% kaolinite with 8 p.u. and 100% water saturation.

Figure 4.3 shows results obtained in a hydrocarbon-bearing section of a laminated shaly-sandstone formation for a field case. Solid elemental weight concentrations are obtained from LWD spectroscopy capture elemental weight logs and C_{sh} is estimated from the spectroscopy clay mineral log. Results indicate a linear relationship between elemental weight concentrations and C_{sh} for the elements present in the formation [iron (Fe), aluminum (Al), and silicon (Si)].

The linear relationship observed in these results is mathematically expressed as

$$\begin{aligned} M_i &= \left(M_i\right)_{end\ member\ 1} C_{end\ member\ 1} + \left(M_i\right)_{end\ member\ 2} C_{end\ member\ 2} \\ M_i &= \left(M_i\right)_{end\ member\ 1} C_{end\ member\ 1} + \left(M_i\right)_{end\ member\ 2} \left(1 - C_{end\ member\ 1}\right) \end{aligned}, \qquad (4.14)$$

where *end member* 1 and *end member* 2 represent the two end members of a binary lithology laminated system; $\left(M_i\right)_{end\ member\ 1}$ and $\left(M_i\right)_{end\ member\ 2}$ are the elemental weight

compositions of end members 1 and 2, respectively; $C_{end\ member\ 1}$ and $C_{end\ member\ 2}$ are the concentrations of end members 1 and 2, respectively. It follows that

$$\left(M_i\right)_{end\ member\ 2} = \frac{M_i - \left(M_i\right)_{end\ member\ 1} C_{end\ member\ 1}}{1 - C_{end\ member\ 1}}, \qquad (4.15)$$

where $\left(M_i\right)_{end\ member\ 1}$ is obtained from spectroscopy elemental weight logs that have been corrected for shoulder-bed averaging effects as outlined in this chapter, $C_{end\ member\ 1}$ can be calculated from $\left(M_i\right)_{end\ member\ 1}$ through matrix inversion (Ajayi et al., 2014). In laminated shaly sandstones where $C_{end\ member\ 1}$ is C_{sh}, $C_{end\ member\ 1}$ can alternatively be calculated from gamma-ray data (Ellis and Singer, 2007) by

$$C_{sh} = \frac{GR - GR_s}{GR_{sh} - GR_s}, \qquad (4.16)$$

where GR is the total gamma-ray reading, GR_s is the gamma-ray reading in clean sandstones, GR_{sh} is the gamma-ray reading in pure shales, and gamma-ray values have been corrected for geometrical averaging effects (Ijasan et al., 2013).

Elemental relative yields within hydrocarbon-bearing laminations, $\left(y_i\right)_{end\ member\ 2}$, can be calculated from $\left(M_i\right)_{end\ member\ 2}$ by

$$\left(y_i\right)_{end\ member\ 2} = \frac{Se_i \left(M_i\right)_{end\ member\ 2}}{\sum_{i=1}^{m} Se_i \left(M_i\right)_{end\ member\ 2}}. \qquad (4.17)$$

Figure 4.4 summarizes the workflow outlined in this chapter.

4.4 SYNTHETIC EXAMPLES

This section verifies the inversion-based interpretation method with four synthetic cases that include complex lithologies, thin beds, and deviated wells. A fourth synthetic laminated shaly-sandstone example in a vertical well validates the accuracy of the developed mixing law in laminated formations and describes the effect of noise on results obtained from this example. Measured elemental relative yields are obtained from MCNP simulations at a sampling rate of 7.62-cm (3-in). Each measured depth location is defined by the geometrical center and depth of investigation of FSFs (Ijasan et al., 2011) used in the spectroscopy fast-forward simulation. Table 4.1 describes the chemical properties of elements and minerals assumed in synthetic examples. Migration lengths and elemental compositions are required inputs for the spectroscopy fast-forward model, which is invoked by the inversion, and are calculated from mineral and fluid compositions using Schlumberger's Nuclear Parameter program, SNUPAR (McKeon and Scott, 1989).

The inversion algorithm in these synthetic cases is stable and converges to the same result independent of the initial guess. I therefore choose a conservative initial guess equal to the reciprocal of the number of elements to be inverted, at each measurement point, and for each element. Similarly, the inclusion of a reference vector in the estimation is not required to achieve solution convergence. Layer elemental yields and weights are obtained from the inversion of MCNP-simulated elemental relative yields. The analytical approximation of Jacobian matrices (described earlier) is implemented in the inversion method to obtain the results shown in both synthetic cases. Elemental sensitivity values used in the estimation of layer elemental compositions are listed in Table 4.2. Results of estimated elemental compositions in all synthetic cases

reconstruct elemental relative yield logs that exhibit good agreement with MCNP-simulated elemental relative yield logs.

4.4.1 Synthetic Case No. 1

This example quantifies the impact of the difference in volumes of investigation between inelastic and capture measurements on elemental relative yields and weight concentrations, estimated with inversion methods, by analyzing a synthetic case in the two measurement domains. I examine (a) capture and (b) inelastic measurement modes in an oil-bearing clean quartz-dolomite formation penetrated by a 60-degree deviated well. MCNP-simulated yield and weight logs include magnesium, silicon, and calcium.

The synthetic model consists of a 4.57-m true stratigraphic thickness (TST) formation with layer thicknesses ranging from 30.48-cm to 91.44-cm. Table 4.3 describes layer thicknesses, migration lengths, element, mineral, and fluid compositions assumed in this example. Because the measured depth interval (9.14-m) is relatively short, I do not define λ by the variance of the error between numerically simulated and MCNP-simulated logs but with Hansen's L-curve strategy. For case (a), the solution converges after ten iterations which correspond to 38.7 seconds of computer processing unit (CPU) time when the Jacobian matrix is calculated with analytical methods or 730.8 seconds when the Jacobian matrix is calculated numerically. The solution also converges after ten iterations in case (b) but CPU time consumed is 718.2 seconds when the Jacobian matrix is calculated with numerical methods and 31.9 seconds when the Jacobian matrix is calculated analytically.

Figures 4.5 to 4.8 show results of estimated layer elemental compositions for cases (a) and (b) compared to MCNP-simulated logs. I observe misrepresentations of

model values by MCNP-simulated logs particularly for silicon (Si) and calcium (Ca) measurements in layers II and V (30.48-cm). These differences are due to shoulder-bed averaging effects on MCNP-simulated logs that arise from thin-bed and well deviation effects. The discrepancies in magnesium (Mg) measurements are not as significant as those observed for silicon (Si) and calcium (Ca) because magnesium is present in low concentrations (less than 0.12 weight fraction) in the formation.

In case (a), I observe that differences between MCNP-simulated capture logs and synthetic model values are as much as 0.3 yield fraction and 0.2 weight fraction as shown in Figures 4.5 and 4.6, respectively. These averaging effects are significantly decreased by inversion and the largest differences between estimated and model values decrease to 0.066 yield fraction and 0.024 weight fraction as observed in Figures 4.5 and 4.6, respectively, for silicon in layer II.

Inelastic spectroscopy logs in case (b) are less affected by shoulder-bed averaging than capture logs due to their smaller volume of investigation. Differences between MCNP-simulated logs and model layer values for inelastic results in case (b) therefore decrease to 0.25 yield fraction and 0.15 weight fraction (as observed in Figures 4.7 and 4.8, respectively) compared to differences observed in case (a). However, differences observed between inelastic spectroscopy logs and model layer values, in case (b), are still appreciable enough to require inversion-based interpretation to further decrease averaging effects. Layer elemental relative yields and weight concentrations estimated with inelastic data and shown in Figures 4.7 and 4.8, respectively, exhibit considerable improvements from results calculated using capture logs. Similar to results obtained using capture logs, the largest differences between estimated and model values are

observed for silicon measurements in layer II but decrease to approximately 0.028 yield fraction and 0.0074 weight fraction. It should be noted that the differences between estimated and model values in both cases (a) and (b) are approximately within measurement uncertainties shown as error bars in Figures 4.5 to 4.8.

4.4.2 Synthetic Case No. 2

Unconventional hydrocarbon-bearing mudrocks are typically low porosity formations with complex lithology and consequently complex elemental composition. This leads to the presence of several formation elements in low concentrations which are significantly affected by numerical noise in MCNP simulations. The present example therefore quantifies the reliability of the developed interpretation method in the presence of such numerical noise.

The synthetic model consists of a 5.64-m TST low porosity unconventional gas-bearing shale formation penetrated by a 70-degree deviated well with layer thicknesses ranging from 21.34-cm to 91.44-cm. Similar to Synthetic Case No. 1, the measured depth interval (16.49-m) is relatively short and I therefore estimate λ using Hansen's L-curve strategy. The solution converges after ten iterations and the CPU time consumed is 7229.3 seconds or 227.5 seconds when the Jacobian matrix is calculated numerically or analytically, respectively.

Although there are nine layers with distinct petrophysical properties included in this synthetic model, Figures 4.9 and 4.10 show that measured yield and weight logs, respectively, do not exhibit significant variability except in layer VI. It is important to determine the reliability of our method to estimate layer compositions in this case where there is not significant variability in elemental relative yield or weight logs.

I examine the inelastic measurement mode in order to quantify carbon which is only detectable from inelastic measurements. Results distinguish between total organic carbon present in kerogen and inorganic carbon present in carbonates based on the ability of the forward model to separate carbon measurements by elemental isotope (Ajayi et al., 2014). Tables 4.4 and 4.5 describe layer thicknesses, migration lengths, element, mineral, and fluid compositions assumed in the synthetic model. Elemental relative yields and weight concentrations are simulated using MCNP for inelastic inorganic carbon (C), organic carbon, sodium (Na), sulfur (S), magnesium (Mg), aluminum (Al), silicon (Si), potassium (K), calcium (Ca), and iron (Fe).

Although layers II and VI are less than 30.48-cm thick, several elements are present in very low concentrations (less than 0.02 yield fraction and 0.01 weight fraction), Figures 4.9 and 4.10 show that differences between estimated elemental compositions and actual model values do not exceed 0.02 yield fraction or 0.01 weight fraction. I also observe that these differences are within the estimated 95% confidence interval shown as error bars in Figures 4.9 and 4.10. Average differences in estimated elemental compositions compared to model values are 0.0036 yield fraction and 0.002 weight fraction. It is also important to note that our method can accurately resolve distinct layer elemental compositions even though there is marginal variability in MCNP-simulated elemental relative yield and weight logs.

4.4.3 Synthetic Case No. 3

This example tests the accuracy of the developed interpretation method in the complex geometry observed in a thinly-bedded formation penetrated by a HA/HZ well. Complex well trajectories and thin-bed effects lead to averaging of several layers at each

measurement point which makes it difficult to resolve true layer properties. The synthetic model is composed of a 3.65-m TST shaly-sandstone formation penetrated by an 85-degree well, bed thicknesses vary from 15.24-cm to 52.93-cm, and the interpretation is implemented in the capture measurement mode. Formation elements present in this synthetic example include capture magnesium (Mg), aluminum (Al), silicon (Si), potassium (K), calcium (Ca), and iron (Fe). Tables 4.6 and 4.7 summarize depth-periodic compositions, TST, and migration lengths assumed in this example. This is an extreme case for the forward simulation method due to the large perturbation in migration lengths from one layer to the next (Ajayi et al., 2014), as seen in Table 4.6, which introduces errors into the Jacobian matrix. Because the measured depth interval is relatively long (41.9-m) in synthetic cases, I estimate λ as the variance of the error between numerically simulated and MCNP-simulated spectroscopy element relative yield logs.

The solution converges after ten iterations when 7817.3 or 155.3 seconds of CPU time has been consumed using numerical or analytical methods, respectively in formulating the Jacobian matrix. Figures 4.11 and 4.12 show that magnesium is present in very low concentrations (less than 0.02 yield fraction and 0.005 weight fraction), and therefore is very noisy with largest relative errors compared to model values. Despite the large perturbation in layer migration lengths, highest differences observed between model and estimated values are 0.08 yield fraction and 0.02 weight fraction but these differences are approximately within measurement uncertainties shown as error bars in Figures 4.11 and 4.12, respectively. The top and bottom layers: I and XIII (52.93-cm thick), respectively, are the thickest layers in this example and are thus least affected by shoulder-bed averaging and therefore have smallest differences compared to model

values (less than 0.0014 yield fraction and 0.0027 weight fraction). Average differences in estimated element compositions compared to model values are 0.0237 yield fraction and 0.0079 weight fraction for element relative yield and weight concentrations, respectively.

4.4.4 Synthetic Case No. 4

This fourth synthetic case is designed to evaluate the reliability and accuracy of the spectroscopy mixing law developed for laminated formations. The model is a 3.35-m laminated shaly-sandstone formation penetrated by a vertical well. Bed thicknesses range from 30.48-cm to 91.44-cm, and the interpretation is implemented in the conventional LWD spectroscopy capture mode. The 30.48-cm beds (layers II and IV) include laminations that are below the vertical resolution of the LWD spectroscopy tool. Tables 4.8 and 4.9 describe layer thicknesses, migration lengths, volumetric concentration of shale (C_{sh}), elemental, mineral, and fluid compositions assumed in this example. Chemical elements present in the assumed formation lithology include magnesium (Mg), aluminum (Al), silicon (Si), sulfur (S), potassium (K), calcium (Ca), and iron (Fe). Table 4.1 describes the properties of elements and minerals assumed in this example.

The measured depth interval is relatively short (3.35-m) and I therefore calculate the regularization parameter, λ, using Hansen's L-curve strategy. Layer elemental yields and weights are obtained from the inversion of MCNP-simulated elemental relative yields. Inversion convergence is achieved after ten iterations within 2086.3 or 129.7 seconds when the Jacobian matrix is estimated via numerical or analytical methods, respectively. Figures 4.13 and 4.14 show that estimated elemental compositions in thick layers (layers I, III, and V), where laminations are not present, exhibit a good fit to model

values, with average differences less than 0.007 yield fraction and 0.02 weight fraction. However, in laminated layers II and IV, there are discrepancies between estimated and model values even though Figure 4.13 shows a good agreement between reconstructed and MCNP-simulated elemental relative yield logs. Results in Figure 4.13 and 4.14 show that inversion cannot resolve elemental compositions of laminations within layers II and IV and solutions converge to a value approximately equal to that of the bed-center spectroscopy log. This behavior underlines the importance of evaluating sufficient geological and well-log information to detect the presence of laminations before performing the interpretation; I note that accurate reconstruction of elemental relative yield logs is not a reliable indicator of accuracy in estimated elemental compositions for laminated formations.

Due to the differences between model and estimated values observed in results within laminations, I use the mixing law in equation 4.15 to resolve elemental compositions in sandstone laminations. Tables 4.8 and 4.9 list C_{sh} values and elemental compositions of pure shale: $(M_i)_{pure\ shale}$ used in the calculations ($(M_i)_{pure\ shale}$ can also be estimated from the previous inversion step). Volumetric concentrations of shale are calculated as the effective volumetric concentration of shale within the volume of investigation of the tool. Results obtained from this method are shown in Figure 4.14 and validate the developed algorithm as reliable in the estimation of elemental compositions in laminated formations because I observe good agreement between estimated and model values of sandstone matrix elemental weight concentrations (maximum difference of 0.0044).

4.4.4.1 *Effect of noise on Synthetic Case No. 4*

Elemental relative yields can be significantly affected by noise which compromises the estimation of elemental weight concentrations as well as any subsequent petrophysical interpretation. I perform a study on Synthetic Case No. 4 where I analyze the effect of noise on elemental relative yields in Layer I. Layer I is one of the thickest layers (91.44-cm) in the synthetic case and is not affected by shoulder-bed averaging. I can therefore assert that discrepancies between inverted and model elemental compositions are due to presence of noise. Accordingly, I introduce 5 to 100 percent random Gaussian and log-normal noise to MCNP-simulated elemental relative yields and estimate layer elemental relative yields through inversion. A base case comprising true layer elemental relative yields is also examined to serve as reference for results obtained when noise is added to MCNP-simulated elemental relative yields.

Figure 4.15 shows the inverted elemental compositions in layer I when random Gaussian noise is introduced into MCNP-simulated elemental relative yields. Estimated layer elemental yields tend to remain approximately constant at true layer values but there is some deviation at higher percentages of noise (mainly above 50% Gaussian noise). In aluminum, there is an approximately linear increase in layer elemental relative yields with respect to the percentage of added random Gaussian noise. These results indicate that the effect of Gaussian noise in MCNP-simulated elemental relative yields on inverted elemental relative yields is fairly predictable and not significant except at very high percentages of noise.

Figure 4.16 displays the impact of random log-normal noise in MCNP-simulated elemental relative yields on estimated layer elemental relative yields. Estimated

elemental yields do not exhibit predictable variations with respect to the percent of log-normal noise such as that observed with added Gaussian noise. There is also more appreciable deviation of inverted elemental yields from true layer values for log-normal noise above 10 percent. Presence of log-normal noise in elemental relative yields will therefore significantly affect the estimation of layer elemental yields compared to Gaussian noise and this effect will manifest itself in a more random manner. Because noise in field logs is hardly ever Gaussian in nature, one can expect that field spectroscopy elemental logs with percent noise approximately above 10 percent will yield substantial errors in estimated elemental compositions and calculations based on these elemental compositions.

4.5 FIELD EXAMPLES

The developed inversion-based interpretation methods are benchmarked with two different laminated, offshore high-angle (HA) field cases. To stabilize the inversion and enhance solution convergence in the field cases studied in this chapter, I introduce an initial guess and reference vector equal to bed-center measured elemental weight log values. Initial guesses of elemental absolute yields are estimated from elemental weight logs via the relationship

$$y_{abs,\,i} = Se_i M_i\,, \qquad (4.18)$$

and corresponding elemental relative yields are calculated according to equation 4.9. Table 4.2 lists elemental sensitivities implemented in equation 4.18.

Measured elemental relative yield logs are acquired in the capture spectroscopy mode alone because the LWD tool under study does not acquire inelastic measurements.

Measured elemental yield and weight logs used in the interpretation have been corrected for environmental effects and are therefore indicative of formation elemental compositions. Layer elemental yields and weights are estimated from the inversion of elemental relative yield logs. An analytical approximation of Jacobian matrices, described earlier (equation 4.5), is implemented in the inversion method to obtain the results for both field cases. Results of inverted elemental compositions in all field cases reconstruct elemental relative yield logs that exhibit good agreement with measured elemental relative yield logs. Interpretation in the two field cases includes inversion in conjunction with the use of the developed spectroscopy mixing law due to the presence of several beds that are thinner than the vertical resolution of the LWD spectroscopy tool.

Layer migration lengths used in the spectroscopy fast-forward model are obtained from inversion-based interpretation of neutron porosity logs (Ijasan et al., 2013). Table 4.1 describes the chemical properties of elements assumed in the field examples while Table 4.10 lists layer thicknesses assumed in the field examples. The formation geometrical model, including bed-boundary locations and well dip, are obtained from calculations of a consolidated gamma model, outlined in this chapter, using nuclear gamma-ray, density, and PEF images, and spectroscopy logs.

4.5.1 Field Case No. 1

The section of the well under study penetrates a sequence of 30.48-m thinly-bedded formations (including formations 1-C, 12-A1, 12-A2, and 12-A3) in an offshore well (2-26-G well) with a deviated trajectory, as shown in Figure 4.17. Geological reports, spectroscopy logs, nuclear and resistivity borehole images indicate that the formation consists of alternating laminations of calcite-cemented feldspathic siltstones

and hydrocarbon-bearing argillaceous uncemented feldspathic siltstones that were deposited in the middle- to outer-shelf environment. Silstones are composed mainly of quartz and feldspar, and are classified as subarkosic to arkosic. Reservoir quality is degraded by detrital clay matrix and calcite cement but the geological correlation between individual calcite cemented and non-cemented layers indicates spatial continuity of the reservoir.

The parameter $C_{end\ member\ 1}$ is thus defined by the volumetric concentration of calcite-cemented feldspathic siltstones while $C_{end\ member\ 2}$ is the volumetric concentration of hydrocarbon-bearing argillaceous uncemented feldspathic siltstones. This behavior is in contrast to typical laminated formations that have alternating layers of sandstone and shale. Therefore, the example is intended to validate the flexibility of developed inversion-based methods because it includes a lithology which is different from typical laminated formations.

Chemical elemental logs include capture relative yields and weight concentrations for calcium (Ca), iron (Fe), silicon (Si), sulfur (S), and aluminum (Al). These spectroscopy logs are significantly affected by shoulder-bed averaging due to the presence of several layers thinner than 30.48-cm TST and well deviation effects resulting from the large relative angle between the well axis and the formation dip plane (approximately 60 degrees).

The nonlinear inversion converges after ten iterations which correspond to 1394.2 seconds of CPU time when the Jacobian matrix is calculated numerically, or 113.3 seconds of CPU time for analytical Jacobian matrices estimations. Comparison between estimated elemental compositions and field spectroscopy logs in Figures 4.18 and 4.19

for elemental relative yields and weight concentrations, respectively, confirm the efficacy of inversion-based methods in LWD HA spectroscopy log interpretation across thin beds for reducing shoulder-bed effects. Reductions of shoulder-bed averaging effects on spectroscopy logs of up to 0.2 yield fraction are observed in layer XXI, for silicon, and 0.1 weight fraction, for calcium. Larger uncertainty bars are associated with thin beds, particularly layers VII and XXI.

In some of the thin layers (layers VI, IX, XI, XVII, XXII, and XXIII) I observe that estimated elemental compositions are approximately equal to bed-center spectroscopy log values. This outcome is due to the inability of inversion methods to resolve true elemental compositions within very thin beds. I therefore implement a secondary interpretation method using the developed spectroscopy mixing law to quantify elemental weights in hydrocarbon-bearing calcite uncemented layers. Results, shown in Figure 4.20, indicate that the elemental composition of hydrocarbon-bearing laminations do not include significant concentrations of calcium (less than 0.05 weight fraction). The absence of appreciable amounts of calcium, which is a major constituent of calcite, confirms that the hydrocarbon-bearing laminations in this formation are not cemented by calcite.

4.5.2 Field Case No. 2

Field Case No. 2 is a typical laminated shaly-sandstone formation where sandstone layers are hydrocarbon bearing and shale layers are water saturated. The formation consists of a thinly-bedded siliciclastic sequence in an offshore deviated well (approximately 73 degrees) and the formation lithology includes sandstone, clay, pyrite, and feldspars. Figure 4.21 shows the well trajectory and emphasizes the 30.48-m thick

zone of interest which is located within the hydrocarbon-bearing interval of the well. Nuclear and resistivity image logs as well as the construction of a Thomas-Stieber diagram (shown in Figure 4.22 and constructed using apparent porosity and gamma-ray logs to calculate total porosity and C_{sh}, respectively) diagnose the formation as laminated. This field case verifies the ability of the inversion and mixing-law methods to account for shoulder-bed and well deviation effects on spectroscopy elemental logs in laminated sandstone-shale systems. Spectroscopy logs include capture elemental relative yields and weight concentrations of calcium iron (Fe), silicon (Si), sulfur (S), and aluminum (Al).

The nonlinear inversion converges after ten iterations within 907.9 seconds of CPU time if the Jacobian matrix is calculated numerically or in 81.8 seconds when the Jacobian matrix is estimated through analytical methods. Figures 4.23 and 4.24 show estimated elemental relative yields and weight concentrations, respectively, and measured spectroscopy logs. Results indicate significant reductions of shoulder-bed averaging effects on measured well logs of up to 0.2 yield fraction (layer X) and 0.14 weight fraction (layer XVI) for silicon. Estimated uncertainties, shown as error bars, in Figures 4.23 and 4.24 are strongly inversely correlated to the thickness of each bed. Similar to Field Case No. 1, I observe that estimated elemental compositions in some layers (Layers I, IV, VI, VII, and XII) are equal to bed-center spectroscopy log values which are attributed to the inability of the inversion method to resolve true layer values in thin beds. This situation calls for further interpretation with the developed spectroscopy mixing law.

Figure 4.25 shows results obtained from the implementation of the mixing law which quantifies elemental compositions within hydrocarbon-bearing sandstone laminations. Results do not include iron and sulfur, which are the main constituents of

clay and pyrite, respectively, in all layers. The absence of elements associated with clay and pyrite within sandstone laminations suggests that the sandstone matrix is composed primarily of quartz and feldspars.

4.6 DISCUSSION

Implementation of inversion and mixing-law interpretation methods leads to appreciable corrections of geometrical effects on measured elemental logs and can therefore improve the combined petrophysical interpretation of estimated elemental compositions with other well logs. In synthetic cases, estimations of elemental weight concentrations agreed better with model values than elemental relative yields. This behavior indicates that elemental weight concentrations could be more reliable than elemental relative yields as an input for joint petrophysical interpretation with other well logs.

Environmental conditions that may influence spectroscopy logs include presence of barite in the mud which can falsely decrease the sulfur content in elemental compositions. There can also be a large contribution from iron present in steel-cased wells or from logging tools which alter iron relative yields and weight concentrations. Proper quality control must therefore be performed on measured spectroscopy logs to ensure that the latter are not influenced by such environmental effects.

Large variations in migration lengths pose an extreme case for the spectroscopy fast-forward model embedded in the inversion, and can therefore introduce inaccuracies into the entries of the Jacobian matrix used in the inversion-based interpretation. This condition affects the accuracy of estimated elemental compositions, but I did not observe differences between estimated and model values that exceeded 0.08 yield fraction or

0.024 weight fraction in any of the synthetic cases studied even though there were perturbations in migration length of up to 6-cm.

Spectroscopy interpretation methods advanced in this chapter are best suited for the reduction of shoulder-bed averaging effects in the estimation of solid rock elemental compositions in thinly-bedded formations. Although the spectroscopy forward model can accurately simulate elemental compositions in the presence of invasion (Ajayi et al., 2014), I do not include invasion effects in this chapter because invasion does not significantly affect rock solid composition.

The approach outlined in this chapter can be modified to include fluid-sensitive elements such as hydrogen, carbon, and oxygen. However, the inversion-based interpretation methods developed in this chapter can be implemented with spectroscopy tools that include inelastic measurements to enable the quantification of carbon or oxygen because these elements are only discernable in the inelastic measurement mode. To quantify fluid saturations, more conventional approaches can be implemented such as the use of resistivity logs in a saturation model. However, the developed methods can be implemented with spectroscopy tools that include inelastic measurements to enable the quantification of carbon, oxygen, and consequently fluid saturations. In this latter case, it becomes necessary to quantify invasion because the tool senses all carbon and oxygen within its volume of investigation, including that present in invading and virgin fluids.

Synthetic Case No. 2 showed that although measured spectroscopy logs did not exhibit significant variability, there could be a number of layers within the formation with distinct petrophysical properties. A choice of bed boundaries based on the lack of variability in spectroscopy logs may lead to an incorrect assumption of fewer layers than

are actually present in the formation. Inaccurate selection of bed boundaries will lead to an erroneous solution of elemental compositions or other petrophysical properties, especially across thin beds. Such errors in estimated petrophysical properties can ultimately lead to bypassing hydrocarbon bearing layers. It is therefore important to accurately define bed-boundary locations using a consolidated approach that includes other well logs, such as density images, which often respond conspicuously to changes in layer petrophysical properties. This approach is particularly useful when spectroscopy logs are relatively constant due to non-varying lithology while porosity and fluid saturations are widely varying.

Interpretation methods commonly place an arbitrary cut-off in the thickness of layers that can be examined (Passey et al., 2004), but the interpretation methods advanced in this chapter facilitate the evaluation of such thin hydrocarbon-bearing layers. It is practical to evaluate petrophysical properties of these thin beds because current LWD technology in HA/HZ wells increases the spatial exposure and effective resolution of thin hydrocarbon-bearing layers.

Due to the presence of numerical noise in synthetic cases and logging tool noise in field cases, the norm of the error between numerically simulated and measured/ MCNP-simulated logs did not fall below 0.001 for any of the cases considered above. Inversion stops after the mandatory cut off of ten iterations but typically converges after five iterations. However, we still observe a good agreement between reconstructed and measured/MCNP-simulated logs as well as a good agreement between estimated and model values in synthetic cases.

The spectroscopy mixing law used to determine elemental compositions within thin laminations is based on the assumption that the interpreter can independently estimate elemental weight concentrations of one pure end-member lithology in a binary lithology system but this is not always the case. Likewise, the method assumes that the pure end-member lithology and the interval of interest are located within similar petrophysical zones such that the elemental compositions of the pure end-member lithologies are constant within the interval of interest. To validate this assumption, one must ensure that different petrophysical zones are not erroneously combined in the interpretation. Similarly, in the inversion algorithm, one should analyze each petrophysical zone separately because of the implicit assumption of constant geometrical and inversion parameters within each inversion depth window under analysis.

4.7 CONCLUSION

I developed a nonlinear inversion-based method and mixing law to account for shoulder-bed effects on measured elemental relative yields and weight concentrations in both inelastic and capture measurement modes. Four synthetic and two field cases showed that the new interpretation methods were reliable in the estimation of layer elemental compositions across formations with varying layer thicknesses, lithologies, and well trajectories.

The inversion-based interpretation method becomes unreliable when layer thicknesses are considerably below the vertical resolution of the tool, whereby it cannot resolve true elemental compositions of such thin layers. Circumventing this limitation necessitated the introduction of a spectroscopy mixing law to quantify elemental compositions in laminated formations.

Absence of numerical noise in the forward model embedded in the inversion method may introduce biases into estimated elemental compositions because spectroscopy measurements can be significantly affected by noise. However in Synthetic Case No. 2, which was the most affected by numerical noise in MCNP, I did not observe errors between estimated and model elemental compositions that exceeded 0.02 yield fraction or 0.01 weight fraction.

Results from synthetic cases showed that inelastic measurements exhibited certain advantages over capture measurements including improved measurement resolution due to a smaller volume of investigation, and the ability to detect elements such as carbon and oxygen that are not discernable from capture elemental data. In order to extend the observed improvements to field cases, acquisition of inelastic measurements can be used to complement the inversion-based interpretation.

Conventional inversion methods are best suited for the estimation of layer elemental compositions when bed thicknesses are above the vertical resolution of the tool. However, when bed thicknesses are thinner than the vertical resolution of the tool, the mixing law method must be used to accurately resolve layer elemental compositions. The methods established in this chapter are useful in the estimation of elemental compositions in thinly-bedded formations, where I observe reductions of shoulder-bed averaging effects on spectroscopy logs as high as 0.3 yield and 0.27 weight fraction, respectively, through the use of a combination of inversion and mixing-law methods.

Table 4.1: Elemental and mineral properties assumed in synthetic and field cases examined in this chapter

Element Name	Element Formula	Molecular Weight (g/gmol)		Mineral Name	Mineral Formula	Molecular Weight (g/gmol)	Mineral Density (g/cm^3)
Aluminum	Al	26.98		**Quartz**	SiO_2	60.09	2.65
Carbon	C	12.01		**Dolomite**	$CaMg(CO_3)_2$	184.41	2.87
Calcium	Ca	40.08		**Albite**	$NaAlSi_3O_8$	262.24	2.62
Iron	Fe	55.85		**Calcite**	$CaCO_3$	100.09	2.71
Potassium	K	39.1		**Pyrite**	FeS_2	119.97	5.01
Magnesium	Mg	24.31		**Illite**	$K_{0.8}Al_{1.6}Fe_{0.2}Mg_{0.2}Si_{3.4}Al_{0.6}O_{10}O_2H_2$	396.19	2.78
Sulfur	S	32.06		**Montmorillonite**	$Na_{0.33}Al_{1.67}Mg_{0.33}Si_4O_{10}O_2H_2$	367.01	2.63
Silicon	Si	28.09		**Mg-Chlorite**	$Mg_5AlSi_3AlO_{10}O_8H_8$	555.82	2.65
				Kaolinite	$Al_2Si_2O_5O_4H_4$	184.41	2.62
				K-Feldspar	$KAlSi_3O_8$	278.35	2.57
				Kerogen	$C_{102}H_{94}O_{17}$	1591.9	1.4
				Hydrocarbon-Oil	C_8H_{18}	114.23	0.82
				Hydrocarbon-Gas	CH_4	16.04	0.178
				Water	H_2O	18.02	1

Table 4.2: Calculated elemental inelastic and capture sensitivities. Hyphens indicate negligible values.

Element Name	Element	Calculated Inelastic Sensitivity	Calculated Capture Sensitivity
Aluminum	Al	1.08	1.21
Carbon	C	0.60	-
Calcium	Ca	0.76	1.65
Chlorine	Cl	-	104.93
Iron	Fe	0.72	6.48
Gadolinium	Gd	-	28,364
Hydrogen	H	-	13.10
Potassium	K	0.51	6.03
Magnesium	Mg	0.77	0.40
Oxygen	O	0.75	-
Sulfur	S	0.77	2.54
Silicon	Si	1	1
Titanium	Ti	0.84	17.98

Table 4.3: Layer true stratigraphic thickness (TST), migration lengths, layer elemental, mineral, and fluid compositions assumed in Synthetic Case No. 1.

Layer	Layer TST (cm)	L_m (cm)	Volumetric Concentrations (%)				Formation Solid Elemental Weight Concentrations (%)		
			Solids		Fluids				
			Quartz	Dolomite	Hydrocarbon-Oil	Water	Magnesium	Silicon	Calcium
I	91.44	16.25	65	10	15	10	1.7	36.07	2.79
II	30.48	14.51	10	60	15	15	10.05	5.48	16.56
III	60.96	15.33	20	55	10	15	8.89	10.59	14.66
IV	91.44	21.12	80	10	3	7	1.51	39.62	2.49
V	30.48	17.07	70	15	3	12	11.77	2.47	19.39
VI	60.96	15.12	10	65	2.5	22.5	10.35	5.21	17.06
VII	91.44	17.06	60	20	0	20	3.2	31.44	5.28

Table 4.4: Layer true stratigraphic thickness (TST), migration lengths, mineral, and fluid compositions assumed in Synthetic Case No. 2.

Layer	Layer TST (cm)	L_m (cm)	Volumetric Concentrations (%)								
			Solids							Fluids	
			Quartz	Albite	Calcite	Pyrite	Kerogen	Illite	Mg-Chlorite	Hydrocarbon-Gas	Water
I	91.44	19.59	7.72	2.14	66.69	1.21	4.09	9.14	2.02	4.76	2.23
II	24.38	20.51	6.26	1.59	73.04	0.65	3.64	6.9	1.32	5.01	1.59
III	91.44	19.03	7.01	2.62	66.61	1.49	6.45	8.17	1.08	4.67	1.91
IV	30.48	19.21	10.17	3.96	61.05	1.32	5.46	11.1	1.15	3.53	2.26
V	91.44	18.93	11.93	4.94	59.85	1.21	5.87	8.47	0.94	3.49	3.49
VI	21.34	23.38	37.83	3.96	47.67	0.77	1.06	1.54	3.67	1.91	1.59
VII	91.44	23.15	10.78	2.65	76.97	0.76	1.13	1.3	0.96	4.13	1.31
VIII	30.48	24.13	14	1.81	75.99	0.38	0.57	1.1	1.37	3.8	0. 98
IX	91.44	23.71	7.25	1.62	82.9	0.29	1.14	1.54	0.66	3.62	0.98

Table 4.5: Layer elemental compositions assumed in Synthetic Case No. 2.

Layer	Formation Solid Elemental Weight Concentrations (%)									
	Formation Carbon	**Kerogen Carbon**	**Sodium**	**Sulfur**	**Magnesium**	**Aluminum**	**Silicon**	**Potassium**	**Calcium**	**Iron**
I	10.43	0.48	0.14	0.15	0.17	0.48	4.50	0.13	34.81	0.30
II	9.57	0.24	0.16	0.20	0.32	0.50	7.80	0.09	31.92	0.38
III	9.75	0.48	0.24	0.39	0.24	0.59	6.56	0.11	32.54	0.73
IV	5.96	0.44	0.35	0.40	0.84	1.02	20.26	0.13	19.89	0.74
V	7.80	2.54	0.46	0.65	0.33	2.05	10.02	0.75	26.04	1.40
VI	7.88	2.34	0.36	0.70	0.41	2.37	9.46	0.97	26.28	1.57
VII	8.71	2.79	0.24	0.80	0.36	1.76	6.75	0.72	29.06	1.66
VIII	9.45	1.56	0.15	0.35	0.40	1.45	5.67	0.60	31.54	0.82
IX	8.65	1.76	0.20	0.65	0.59	1.96	7.30	0.80	28.86	1.41

Table 4.6: Layer true stratigraphic thickness (TST), migration lengths, mineral, and fluid compositions assumed in Synthetic Case No. 3.

Layer	Layer TST (cm)	L_m (cm)	Volumetric Concentrations (%)					
			Solids				Fluids	
			Calcite	Illite	Kaolinite	Quartz	Hydrocarbon-Oil	Water
I	52.93	18.17	38	40	10	10	0	2
II	30.48	12.44	5	5	54	6	29	1
III	15.24	14.15	30	10	45	5	5	5
IV	30.48	18.17	38	40	10	10	0	2
V	15.24	12.44	5	5	54	6	29	1
VI	30.48	14.15	30	10	45	5	5	5
VII	15.24	18.17	38	40	10	10	0	2
VIII	30.48	12.44	5	5	54	6	29	1
IX	15.24	14.15	30	10	45	5	5	5
X	30.48	18.17	38	40	10	10	0	2
XI	15.24	12.44	5	5	54	6	29	1
XII	30.48	14.15	30	10	45	5	5	5
XIII	52.93	18.17	38	40	10	10	0	2

Table 4.7: Layer elemental compositions assumed in Synthetic Case No. 3.

Layer	Formation Solid Elemental Weight Concentrations (%)					
	Magnesium	**Aluminum**	**Silicon**	**Potassium**	**Calcium**	**Iron**
I	0.51	8.23	16.69	3.26	15.33	1.17
II	0.14	11.54	15.45	0.88	13.04	0.31
III	0.08	15.1	19.83	0.52	02.59	0.19
IV	0.51	8.23	16.69	3.26	15.33	1.17
V	0.14	11.54	15.45	0.88	13.04	0.31
VI	0.08	15.1	19.83	0.52	2.59	0.19
VII	0.51	8.23	16.69	3.26	15.33	1.17
VIII	0.14	11.54	15.45	0.88	13.04	0.31
IX	0.08	15.1	19.83	0.52	2.59	0.19
X	0.51	8.23	16.69	3.26	15.33	1.17
XI	0.14	11.54	15.45	0.88	13.04	0.31
XII	0.08	15.1	19.83	0.52	2.59	0.19
XIII	0.51	8.23	16.69	3.26	15.33	1.17

Table 4.8: Layer true stratigraphic thickness (TST), migration lengths, volumetric composition of shale, mineral, and fluid compositions assumed in Synthetic Case No. 4.

Layer		Layer TST (cm)	L_m (cm)	Volumetric Concentrations (%)								C_{sh} (volume fraction)
				Solids						Fluids		
				Mg-Chlorite	Illite	K-Feldspar	Quartz	Pyrite	Dolomite	Hydro Carbon-Oil	Water	
I		91.44	16.98	0	0	6.88	68.82	1.72	2.58	12	8	0
II	IIA	6.1	14.86	20	53	8	9	0	0	0	10	0.43
	IIB	9.14	15.78	0	0	12.1	56.45	2.42	4.03	12.5	12.5	
	IIC	6.1	14.86	20	53	8	9	0	0	0	10	
	IID	9.14	15.78	0	0	12.1	56.45	2.42	4.03	12.5	12.5	
III		91.44	14.86	20	53	8	9	0	0	0	10	1
IV	IVA	6.1	16.45	0	0	5.14	64.29	1.71	6.86	8.8	13.2	0.57
	IVB	9.14	14.86	20	53	8	9	0	0	0	10	
	IVC	6.1	16.45	0	0	5.14	64.29	1.71	6.86	8.8	13.2	
	IVD	9.14	14.86	20	53	8	9	0	0	0	10	
V		91.44	15.04	0	0	10	50	2	8	9	21	0

Table 4.9: Layer elemental compositions assumed in Synthetic Case No. 4.

Layer		Formation Solid Elemental Weight Concentrations (%)						
		Magnesium	**Aluminum**	**Silicon**	**Sulfur**	**Potassium**	**Calcium**	**Iron**
I		0.42	0.73	38.73	1.97	1.06	0.69	1.72
II	**IIA**	5.26	11.47	23.92	0	5.7	0	1.63
	IIB	0.67	1.34	34.93	2.85	1.92	1.11	2.48
	IIC	5.26	11.47	23.92	0	5.7	0	1.63
	IID	0.67	1.33	34.93	2.85	1.92	1.11	2.48
III		5.26	11.47	23.92	0	5.7	0	1.63
IV	**IVA**	1.12	0.55	36.01	1.98	0.8	1.84	1.72
	IVB	5.26	11.47	23.92	0	5.7	0	1.63
	IVC	1.12	0.55	36.01	1.98	0.8	1.84	1.72
	IVD	5.26	11.47	23.92	0	5.7	0	1.63
V		1.38	1.13	31.75	2.44	1.64	2.27	2.12

Table 4.10: Layer true stratigraphic thickness (TST) assumed in the field cases examined in this chapter.

Layer	Field Case No. 1 Bed Thickness (cm)		Field Case No. 2 Bed Thickness (cm)
I	9.02		17.87
II	56.01		35.73
III	32.52		17.87
IV	107.12		26.8
V	39.33		17.87
VI	37.18		17.87
VII	22.14		17.87
VIII	79.914		17.87
IX	33.54		26.8
X	34.2		17.87
XI	37.21		13.4
XII	60.29		17.87
XIII	37.87		17.87
XIV	63.74		40.2
XV	50.23		26.8
XVI	33.6		17.87
XVII	44.96		17.87
XVIII	48.52		17.87
XIX	28.74		17.87
XX	70.95		45.94
XXI	25.16		55.67
XXII	32.08		44.19
XXIII	40.51		51.03
XXIV	48.05		74.74
XXV	80.02		100.35
XXVI	36.1		65.48
XXVII	7.5		53.93

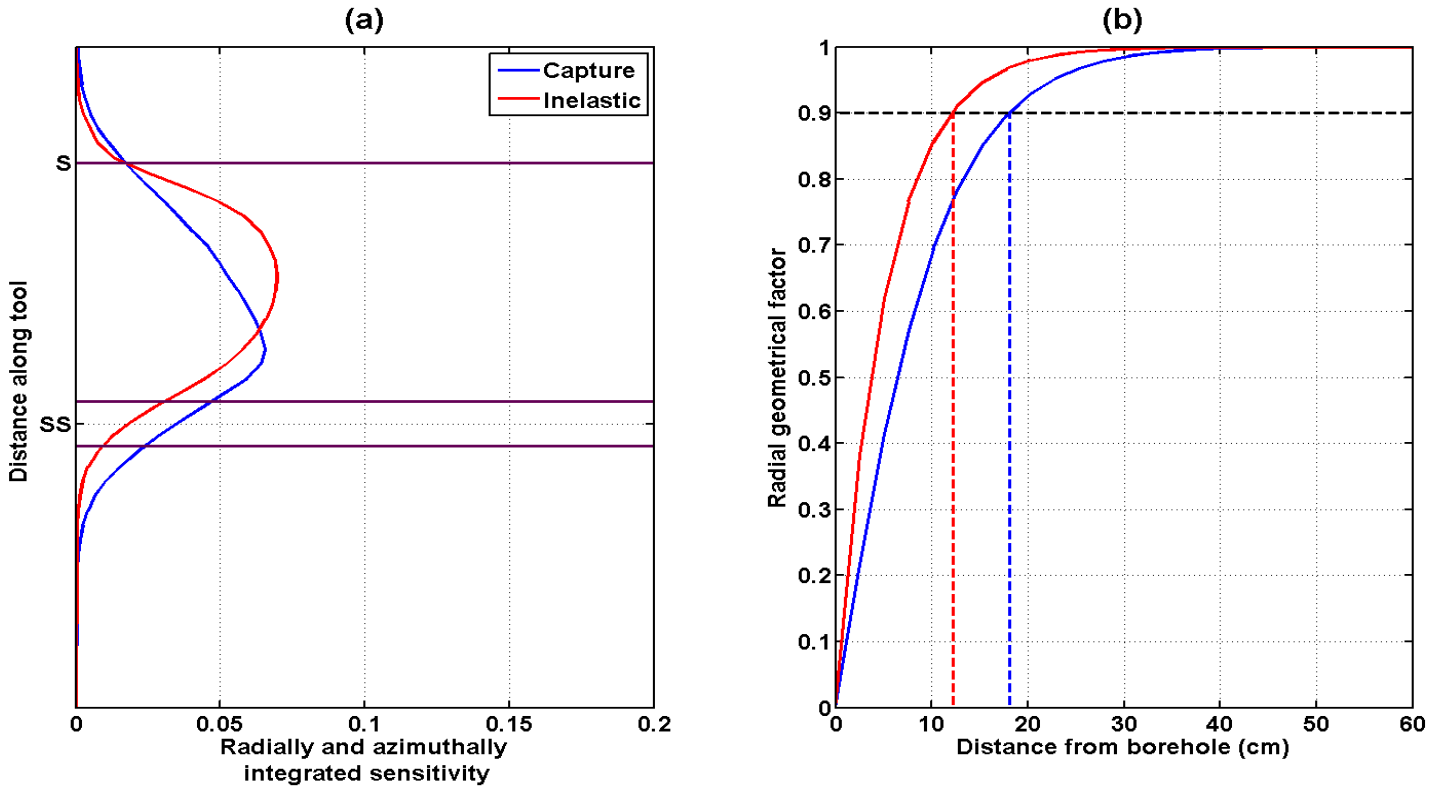

Figure 4.1: Comparison of (a) vertical resolution and (b) radial length of investigation between inelastic and capture measurements in a 25 p.u. freshwater-saturated sandstone formation. Panel (a) shows radially and azimuthally integrated inelastic and capture neutron FSFs along the tool, where purple lines at S and SS identify the pulsed-neutron source and short-spaced detector positions along the tool, respectively; panel (b) shows the cumulative vertically integrated FSF (radial geometrical factor). The depth of investigation of the tool is defined by 90% of the radial geometrical factor and is shown in panel (b) as dashed blue and red lines for capture and inelastic measurements, respectively. Note: the vertical axis on panel (a) is not shown because the location of the neutron source and short-spaced gamma-ray detector of the commercial tool under study are confidential.

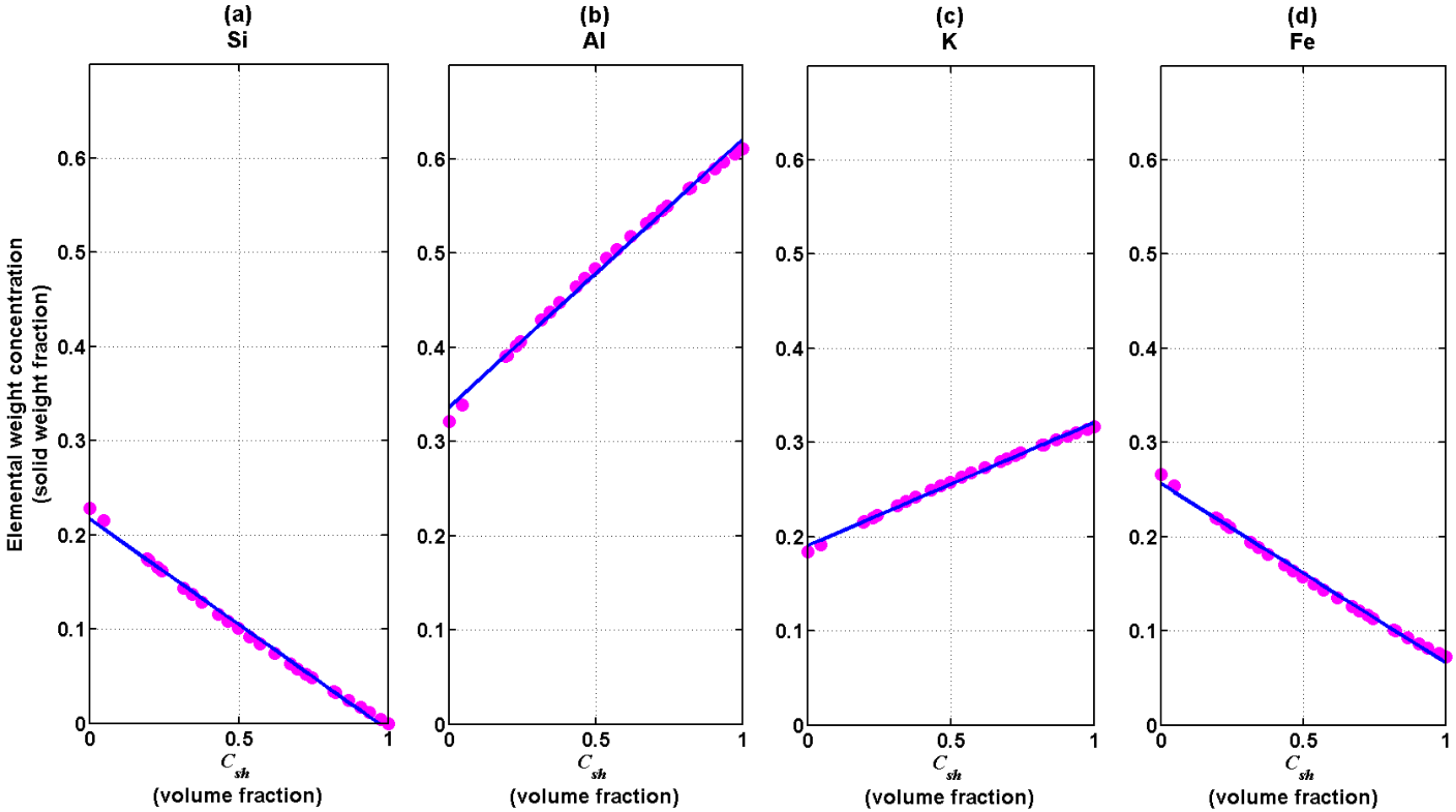

Figure 4.2: Linear relationship between elemental weight concentrations and volumetric concentration of shale (C_{sh}) in a synthetic case. Panels (a), (b), (c), and (d) describe the linear relationship for silicon (Si), aluminum (Al), potassium (K), and iron (Fe), respectively.

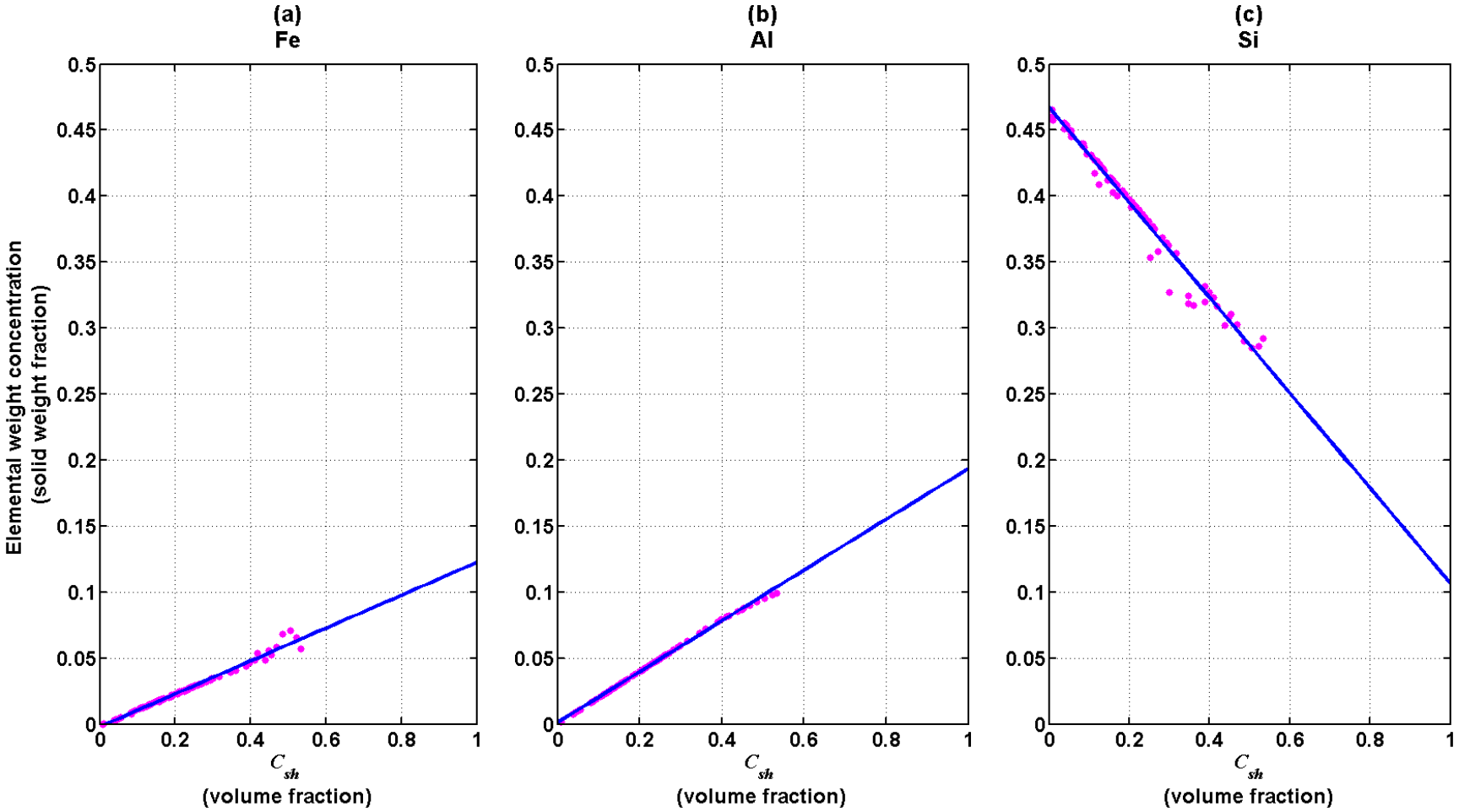

Figure 4.3: Linear relationship between elemental weight concentrations and volumetric concentration of shale (C_{sh}) in a field case. Panels (a), (b), and (c) describe the linear relationship for iron (Fe), aluminum (Al), and silicon (Si), respectively.

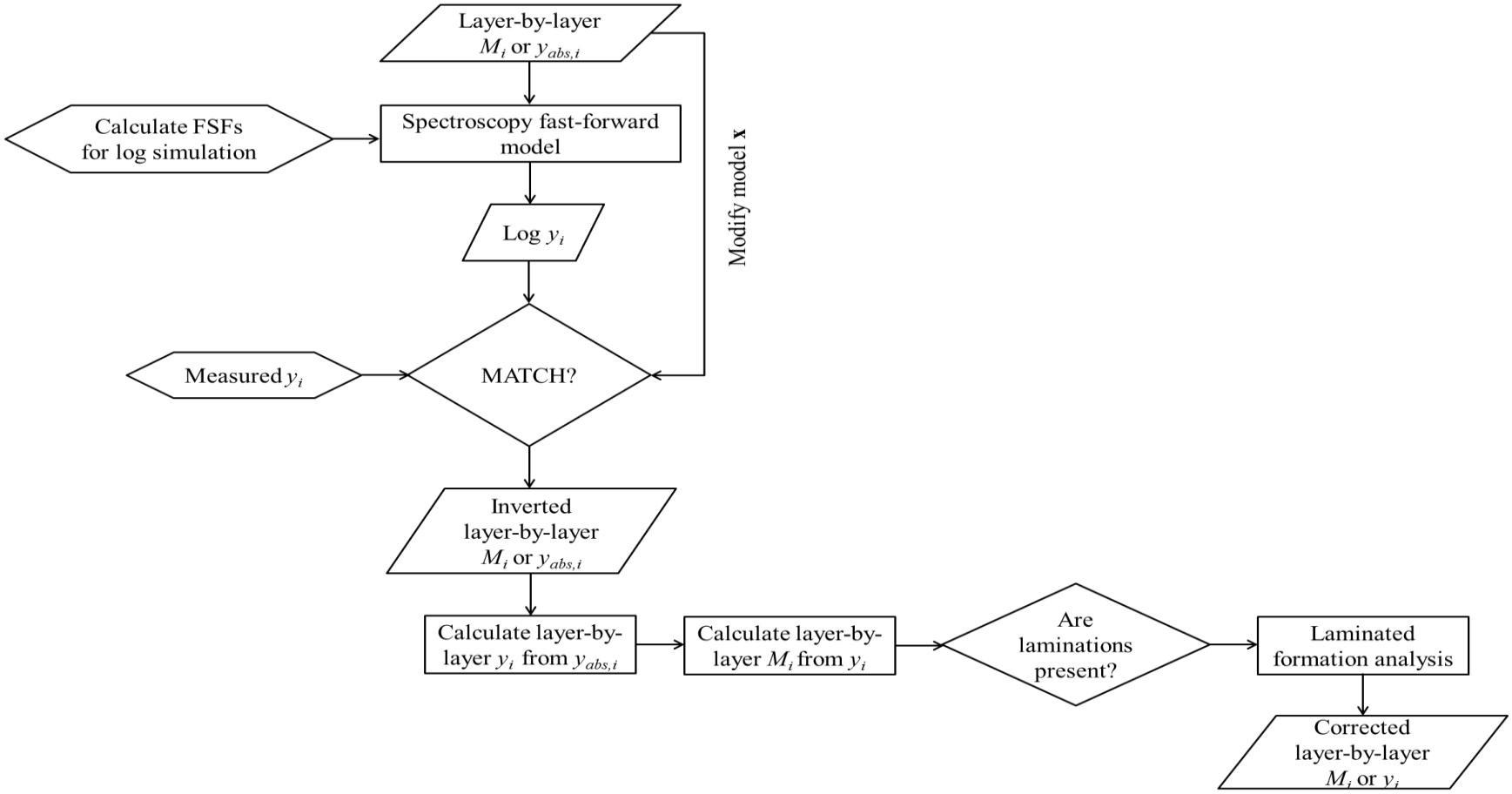

Figure 4.4: Workflow adopted in this chapter for the interpretation of layer elemental relative yields and weight concentrations. The parameters $y_{abs,\,i}$, M_i, y_i, and **x** represent layer elemental absolute yields, layer elemental weight concentrations, layer elemental relative yields, and a vector of layer spectroscopy properties, respectively.

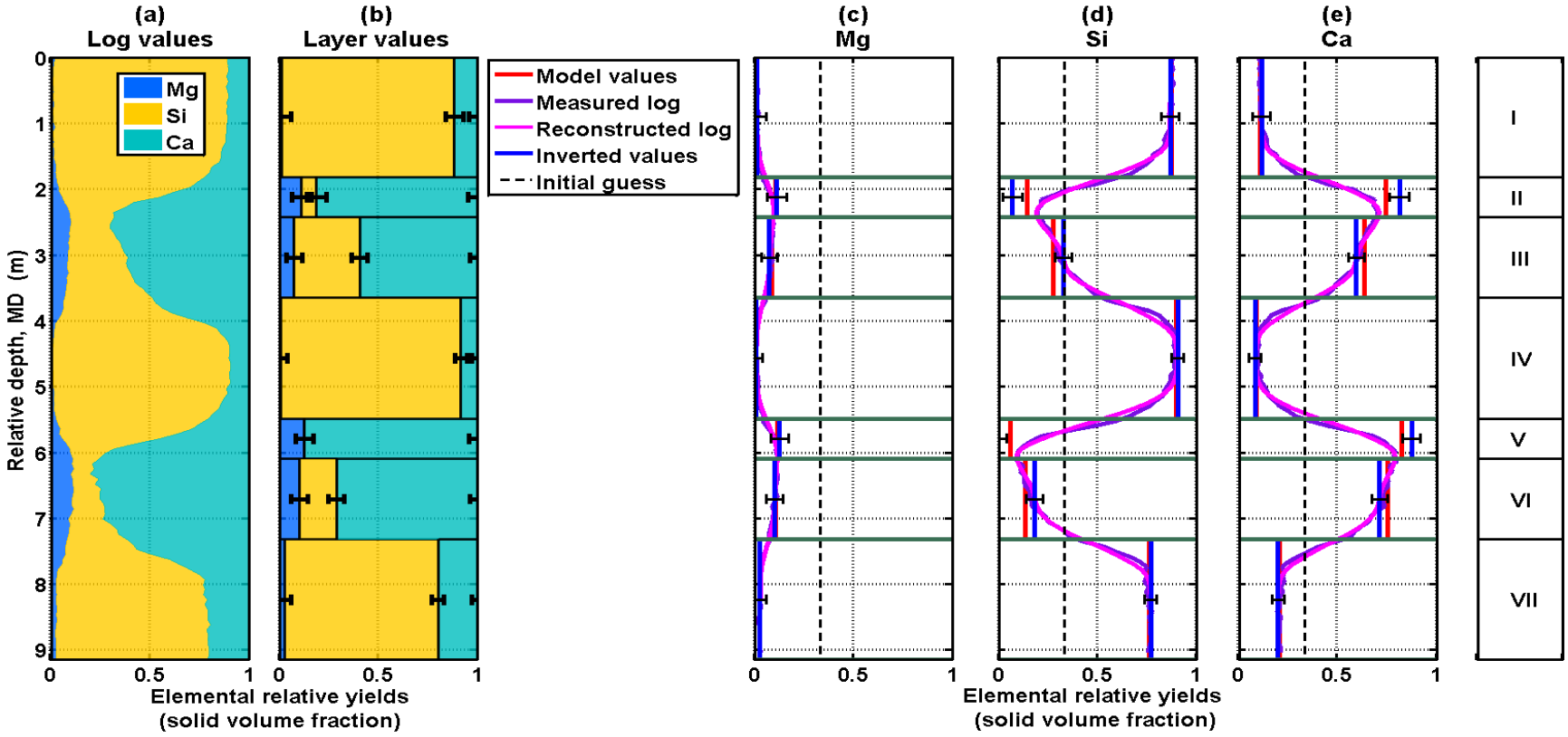

Figure 4.5: Comparison of inverted layer elemental relative yields (blue solid lines) to model values (red solid lines) for Synthetic Case No. 1(a). Panel (a) displays a cumulative plot of MCNP-simulated capture elemental relative yields shown as purple solid lines in panels (c) to (e). Panel (b) exhibits a cumulative plot of inverted elemental relative yields shown as blue solid lines in panels (c) to (e). Black dashed lines, black uncertainty bars, purple solid lines, and magenta solid lines describe the initial guess of the inversion, 95% confidence interval, MCNP-simulated, and reconstructed elemental relative yields, respectively; Mg, Si, and Ca are the elements magnesium, silicon, and calcium, respectively, while I to VII identify distinct layers in the synthetic case.

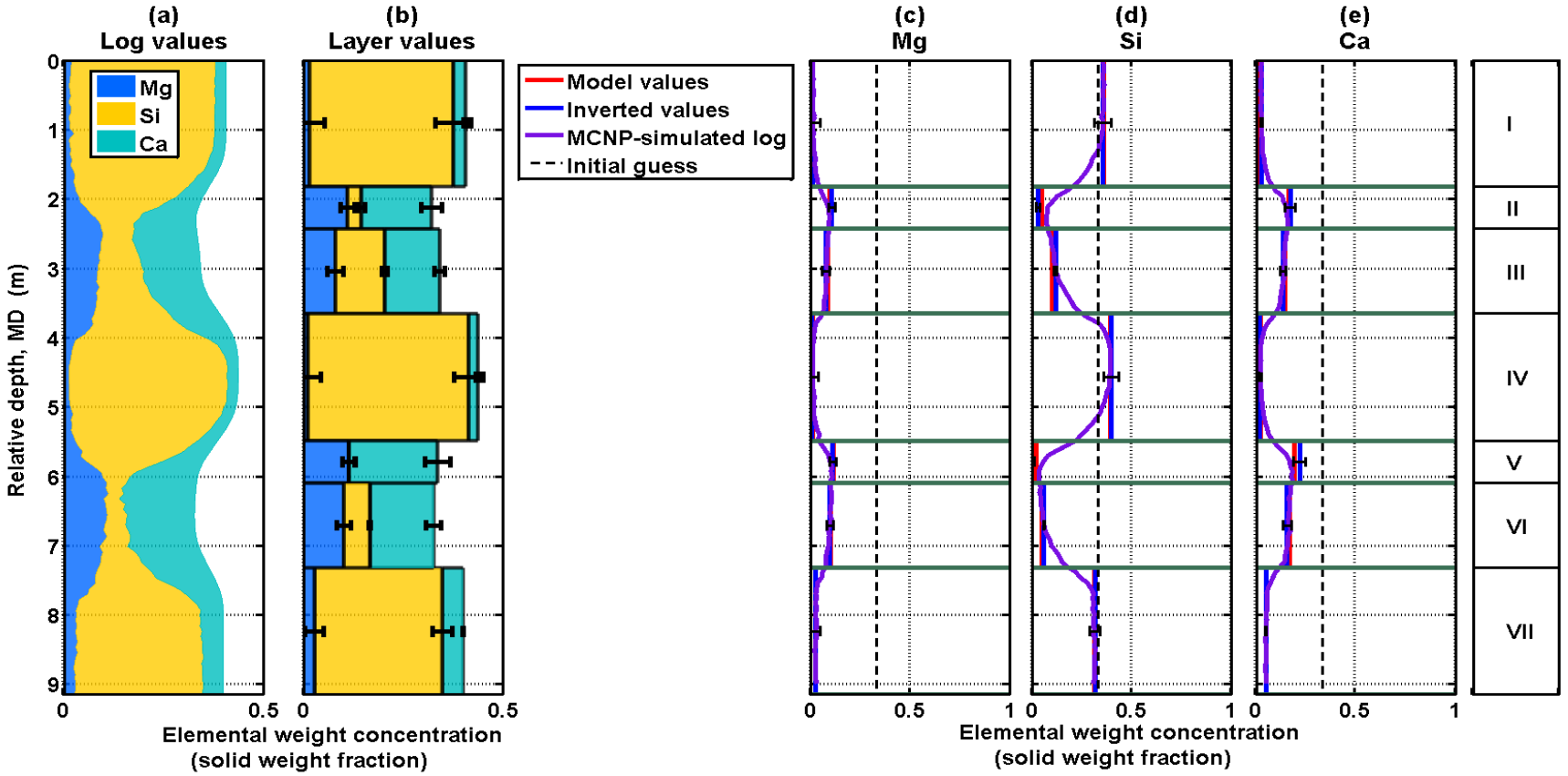

Figure 4.6: Comparison of inverted layer elemental weight concentrations (blue solid lines) to model values (red solid lines) for Synthetic Case No. 1(a). Panel (a) displays a cumulative plot of MCNP-simulated capture elemental weight concentrations shown as purple solid lines in panels (c) to (e). Panel (b) exhibits a cumulative plot of inverted elemental weight concentrations shown as blue solid lines in panels (c) to (e). Black dashed lines, black uncertainty bars, and purple solid lines describe the initial guess of the inversion, 95% confidence interval, and MCNP-simulated elemental weight concentrations, respectively; Mg, Si, and Ca are the elements magnesium, silicon, and calcium, respectively, while I to VII identify distinct layers in the synthetic case.

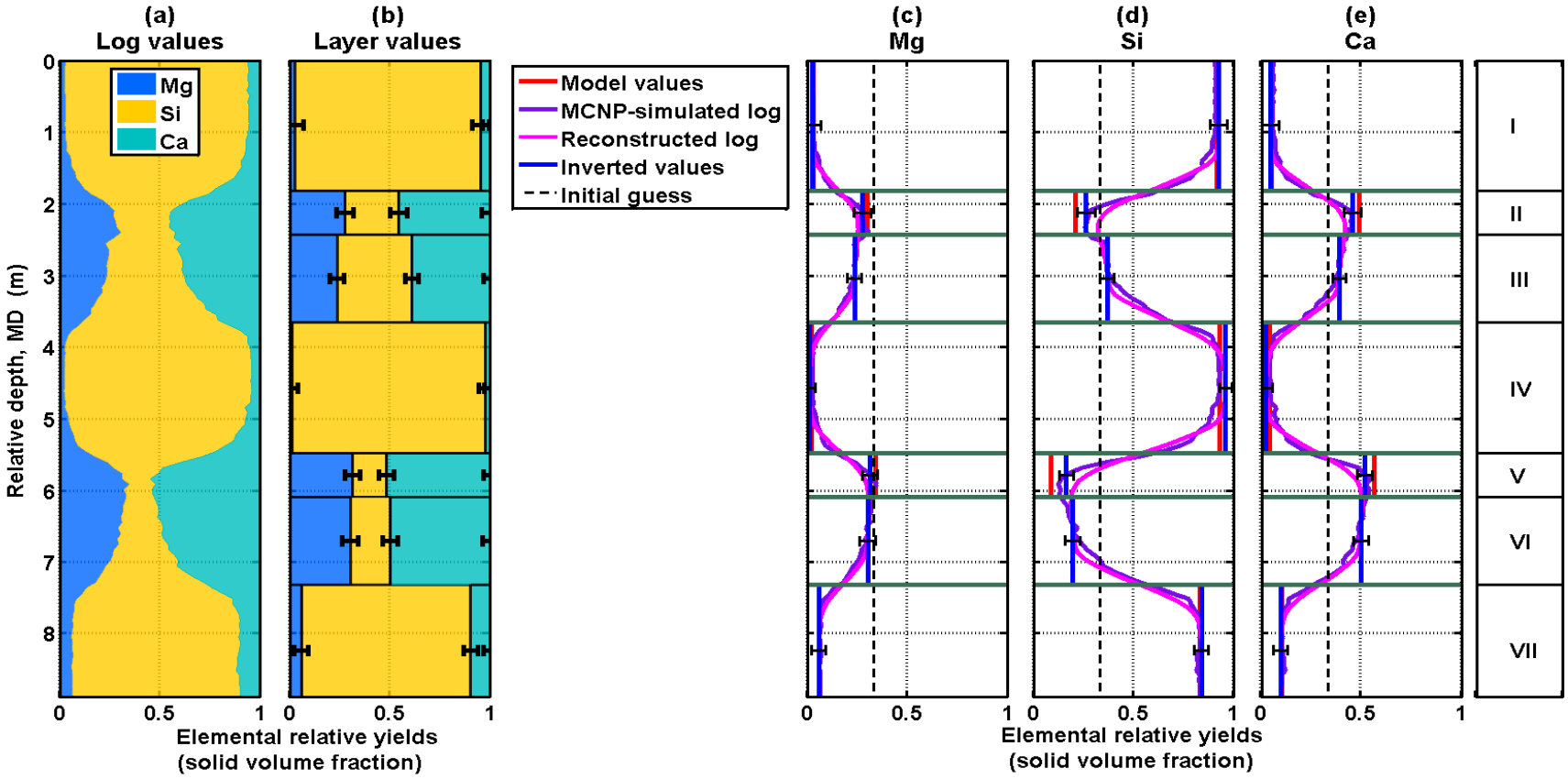

Figure 4.7: Comparison of inverted layer elemental relative yields (blue solid lines) to model values (red solid lines) for Synthetic Case No. 1(b). Panel (a) displays a cumulative plot of MCNP-simulated inelastic elemental relative yields shown as purple solid lines in panels (c) to (e). Panel (b) exhibits a cumulative plot of inverted elemental relative yields shown as blue solid lines in panels (c) to (e). Black dashed lines, black uncertainty bars, purple solid lines, and magenta solid lines describe the initial guess of the inversion, 95% confidence interval, MCNP-simulated, and reconstructed elemental relative yields, respectively; Mg, Si, and Ca are the elements magnesium, silicon, and calcium, respectively, while I to VII identify distinct layers in the synthetic case.

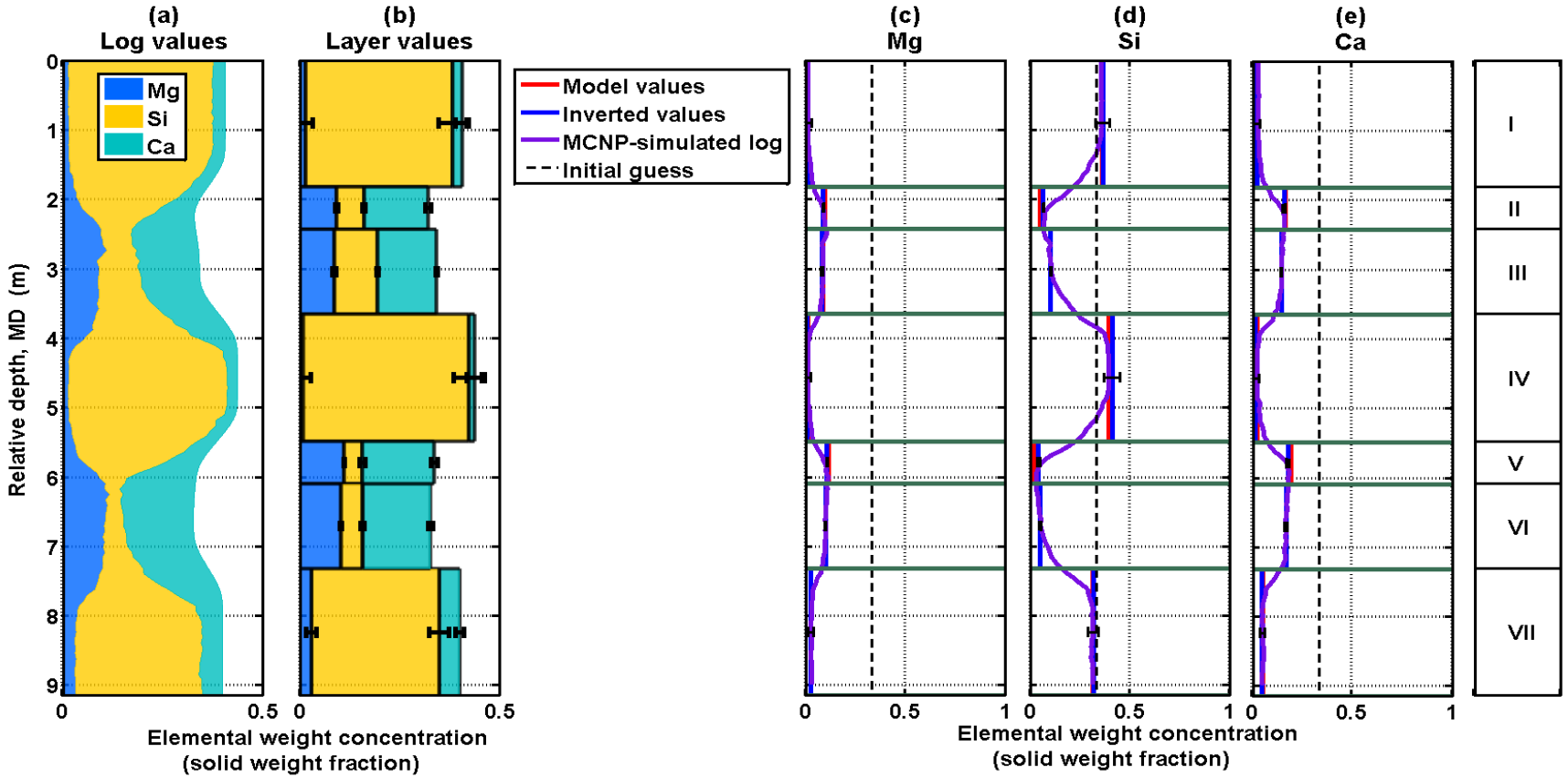

Figure 4.8: Comparison of inverted layer elemental weight concentrations (blue solid lines) to model values (red solid lines) for Synthetic Case No. 1(b). Panel (a) displays a cumulative plot of MCNP-simulated inelastic elemental weight concentrations shown as purple solid lines in panels (c) to (e). Panel (b) exhibits a cumulative plot of inverted elemental weight concentrations shown as blue solid lines in panels (c) to (e). Black dashed lines, black uncertainty bars, and purple solid lines describe the initial guess of the inversion, 95% confidence interval, and MCNP-simulated elemental weight concentrations, respectively; Mg, Si, and Ca are the elements magnesium, silicon, and calcium, respectively, while I to VII identify distinct layers in the synthetic case.

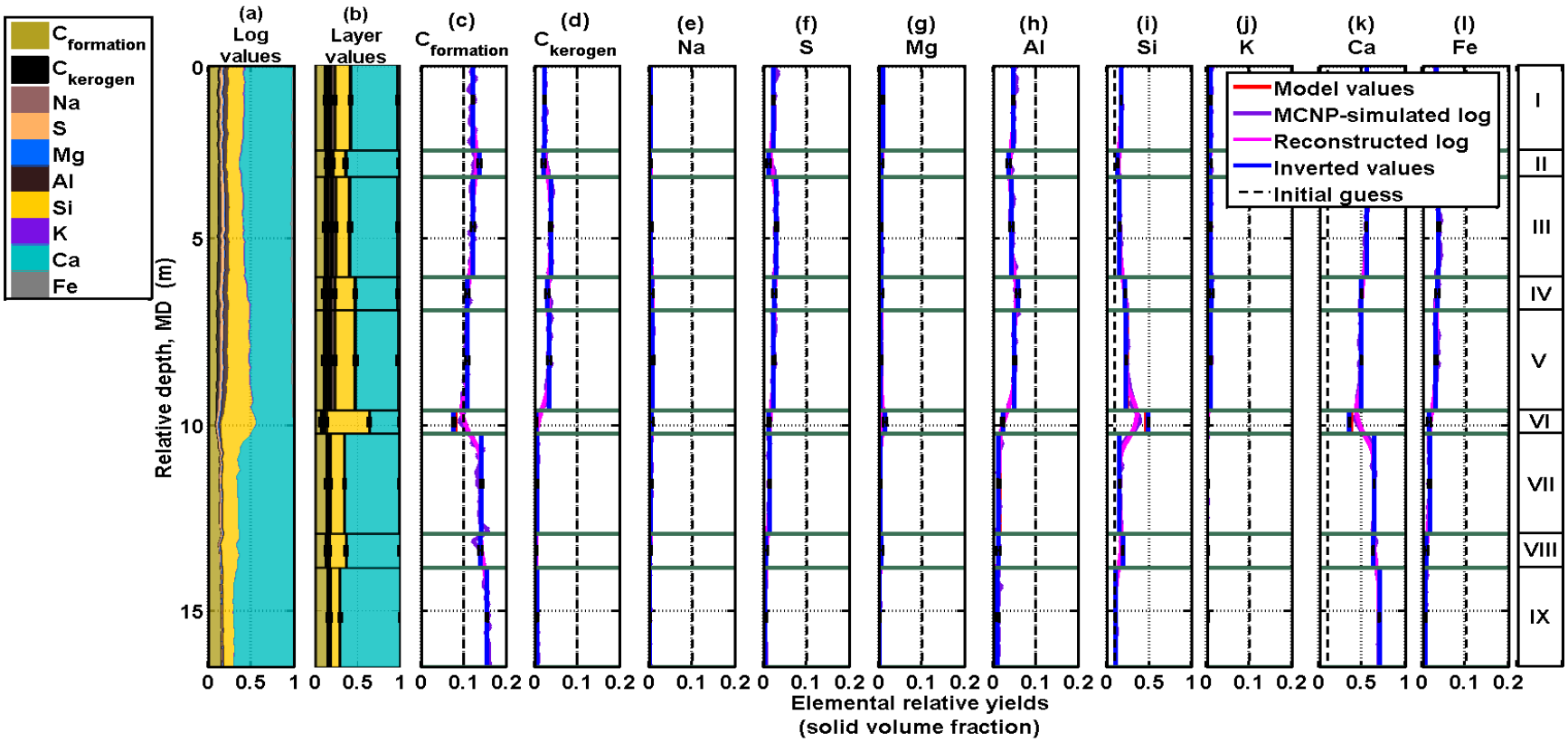

Figure 4.9: Comparison of inverted layer elemental relative yields (blue solid lines) to model values (red solid lines) for Synthetic Case No. 2. Panel (a) displays a cumulative plot of MCNP-simulated inelastic elemental relative yields shown as purple solid lines in panels (c) to (l). Panel (b) exhibits a cumulative plot of inverted elemental relative yields shown as blue solid lines in panels (c) to (l). Black dashed lines, black uncertainty bars, purple solid lines, and magenta solid lines describe the initial guess of the inversion, 95% confidence interval, MCNP-simulated, and reconstructed elemental relative yields, respectively; $C_{formation}$, $C_{kerogen}$, Na, S, Mg, Al, Si, K, Ca, and Fe represent carbon present in the formation, carbon present in kerogen, sodium, sulfur, magnesium, aluminum, silicon, potassium, calcium, and iron respectively, while I to IX identify distinct layers in the synthetic case.

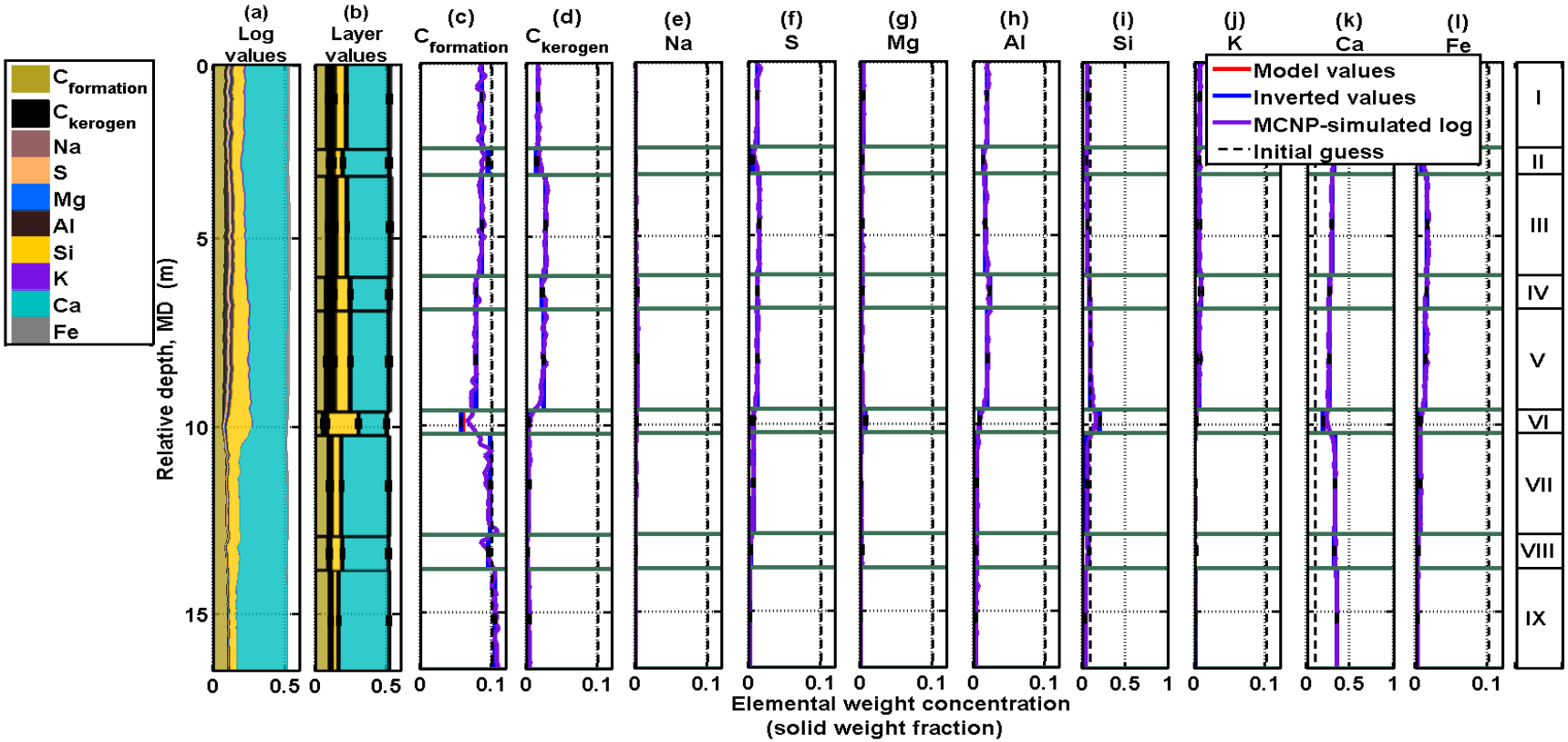

Figure 4.10: Comparison of inverted layer elemental weight concentrations (blue solid lines) to model values (red solid lines) for Synthetic Case No. 2. Panel (a) displays a cumulative plot of MCNP-simulated inelastic elemental weight concentrations shown as purple solid lines in panels (c) to (l). Panel (b) exhibits a cumulative plot of inverted elemental weight concentrations shown as blue solid lines in panels (c) to (l). Black dashed lines, black uncertainty bars, and purple solid lines describe the initial guess of the inversion, 95% confidence interval, and MCNP-simulated elemental weight concentrations, respectively; $C_{formation}$, $C_{kerogen}$, Na, S, Mg, Al, Si, K, Ca, and Fe represent carbon present in the formation, carbon present in kerogen, sodium, sulfur, magnesium, aluminum, silicon, potassium, calcium, and iron, respectively, while I to IX identify distinct layers in the synthetic case.

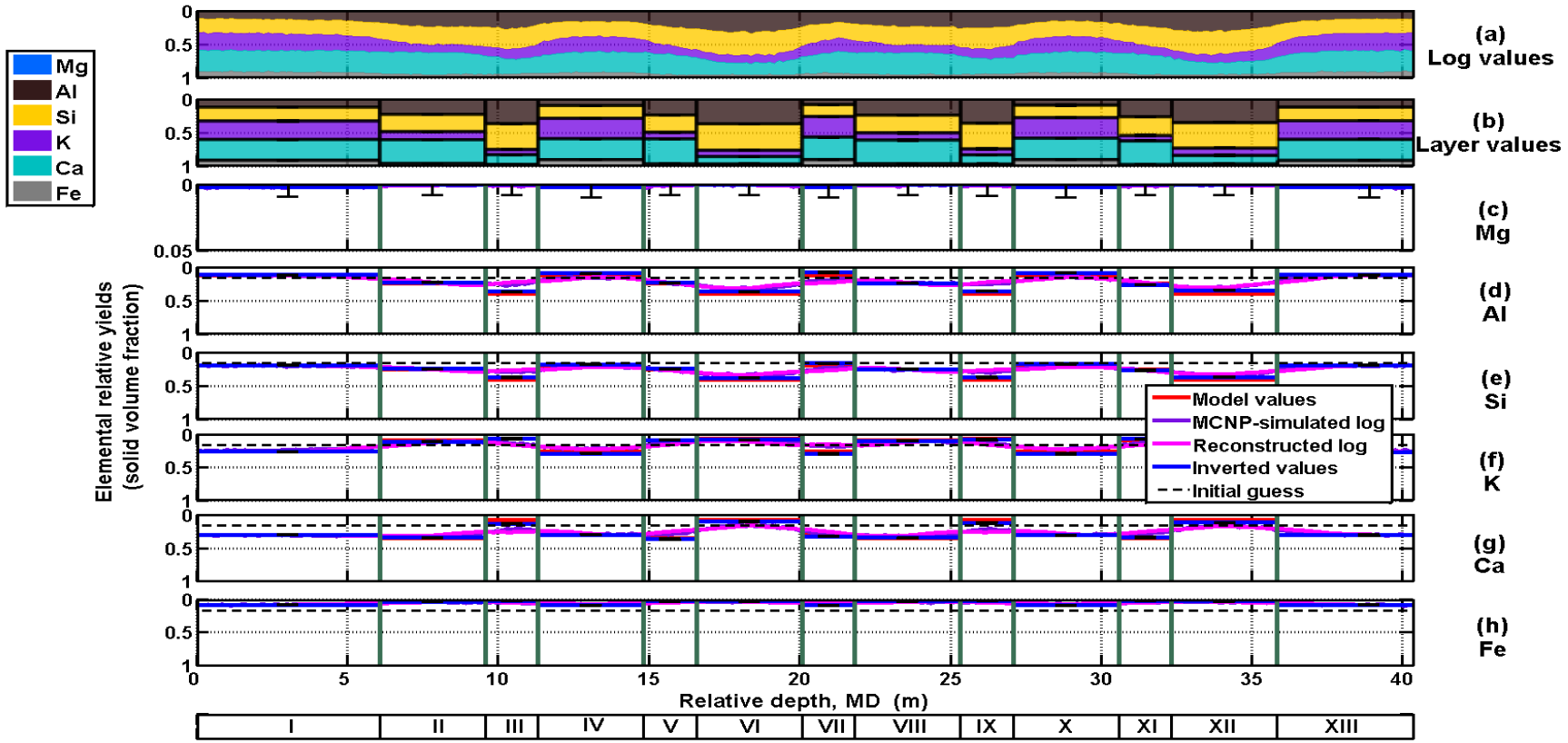

Figure 4.11: Comparison of inverted layer elemental relative yields (blue solid lines) to model values (red solid lines) for Synthetic Case No. 3. Panel (a) displays a cumulative plot of MCNP-simulated capture elemental relative yields shown as purple solid lines in panels (c) to (h). Panel (b) exhibits a cumulative plot of inverted elemental relative yields shown as blue solid lines in panels (c) to (h). Black dashed lines, black uncertainty bars, purple solid lines, and magenta solid lines describe the initial guess of the inversion, 95% confidence interval, MCNP-simulated, and reconstructed elemental relative yields, respectively; Mg, Al, Si, K, Ca, and Fe represent magnesium, aluminum, silicon, potassium, calcium, and iron respectively, while I to IX identify distinct layers in the synthetic case.

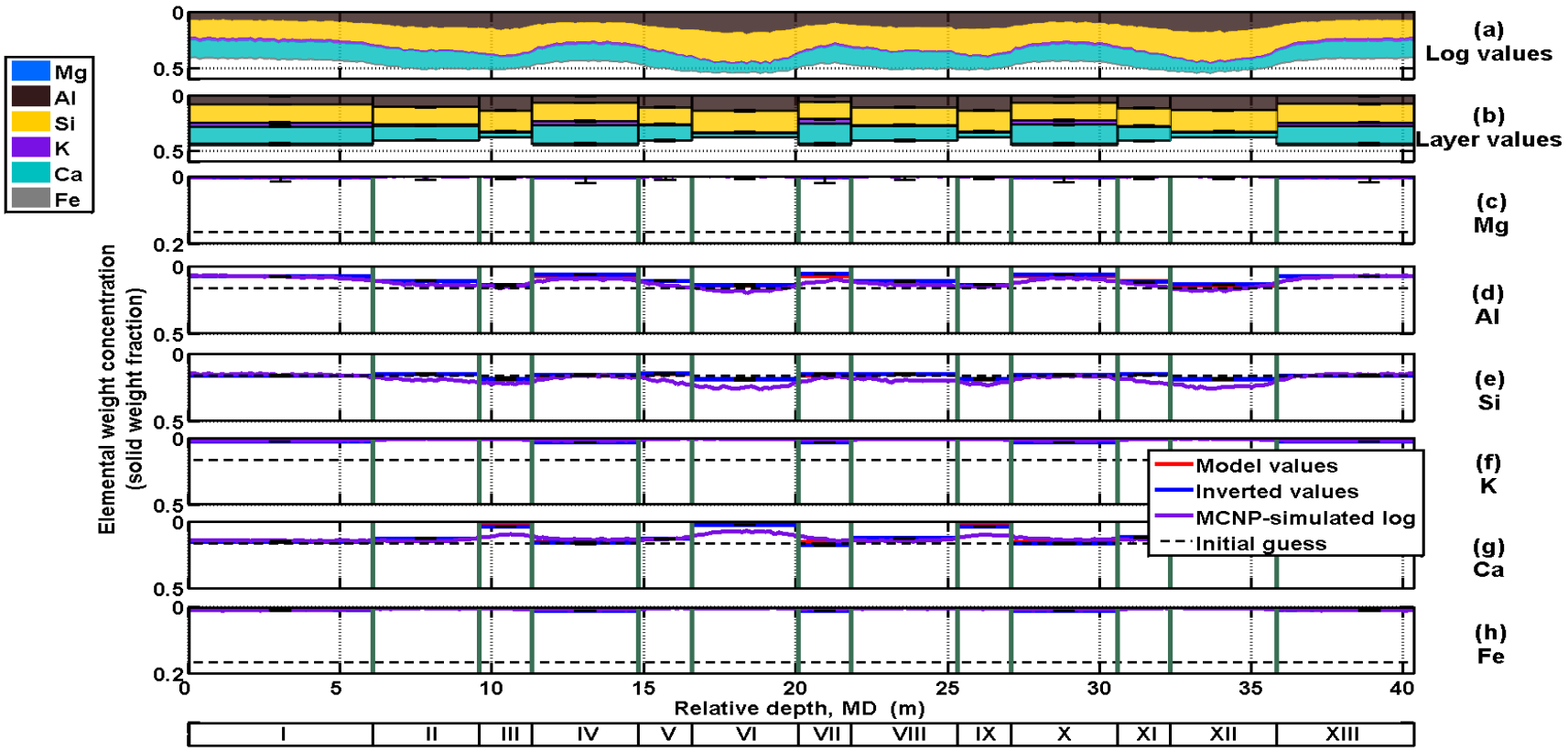

Figure 4.12: Comparison of inverted layer elemental weight concentrations (blue solid lines) to model values (red solid lines) for Synthetic Case No. 3. Panel (a) displays a cumulative plot of MCNP-simulated inelastic elemental weight concentrations shown as purple solid lines in panels (c) to (h). Panel (b) exhibits a cumulative plot of inverted elemental weight concentrations shown as blue solid lines in panels (c) to (h). Black dashed lines, black uncertainty bars, and purple solid lines describe the initial guess of the inversion, 95% confidence interval, and MCNP-simulated elemental weight concentrations, respectively; Mg, Al, Si, K, Ca, and Fe represent magnesium, aluminum, silicon, potassium, calcium, and iron, respectively, while I to IX identify distinct layers in the synthetic case.

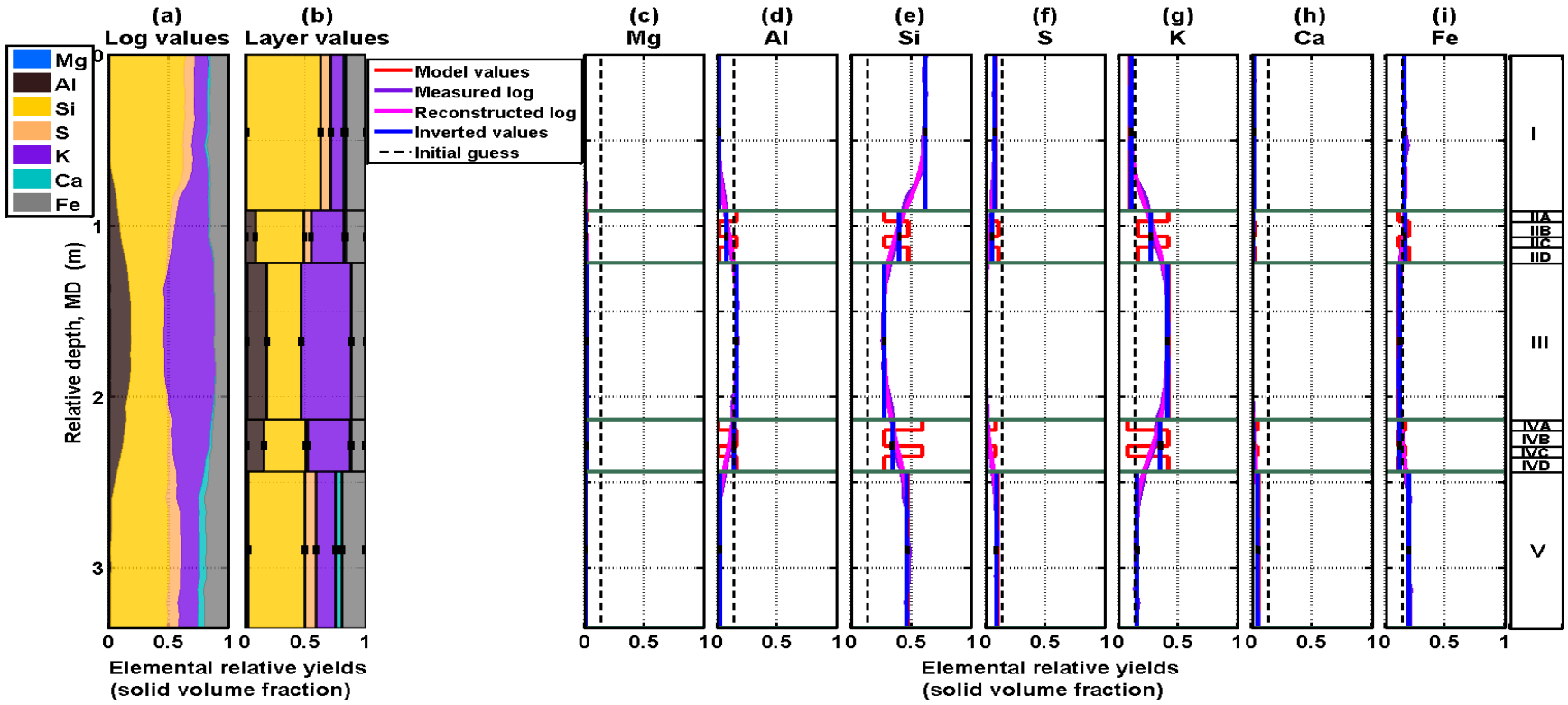

Figure 4.13: Comparison of inverted layer elemental relative yields (blue solid lines) to model values (red solid lines) for Synthetic Case No. 4. Panel (a) displays a cumulative plot of MCNP-simulated capture elemental relative yields shown as purple solid lines in panels (c) to (i). Panel (b) exhibits a cumulative plot of inverted elemental relative yields shown as blue solid lines in panels (c) to (i). Black dashed lines, black uncertainty bars, purple solid lines, and magenta solid lines describe the initial guess of the inversion, 95% confidence interval, MCNP-simulated, and reconstructed elemental relative yields, respectively; Mg, Al, Si, S, K, Ca, and Fe are the elements magnesium, aluminum, silicon, sulfur, potassium, calcium, and iron, respectively; I to V identify distinct layers in the synthetic case, while A to D identify laminations within layers.

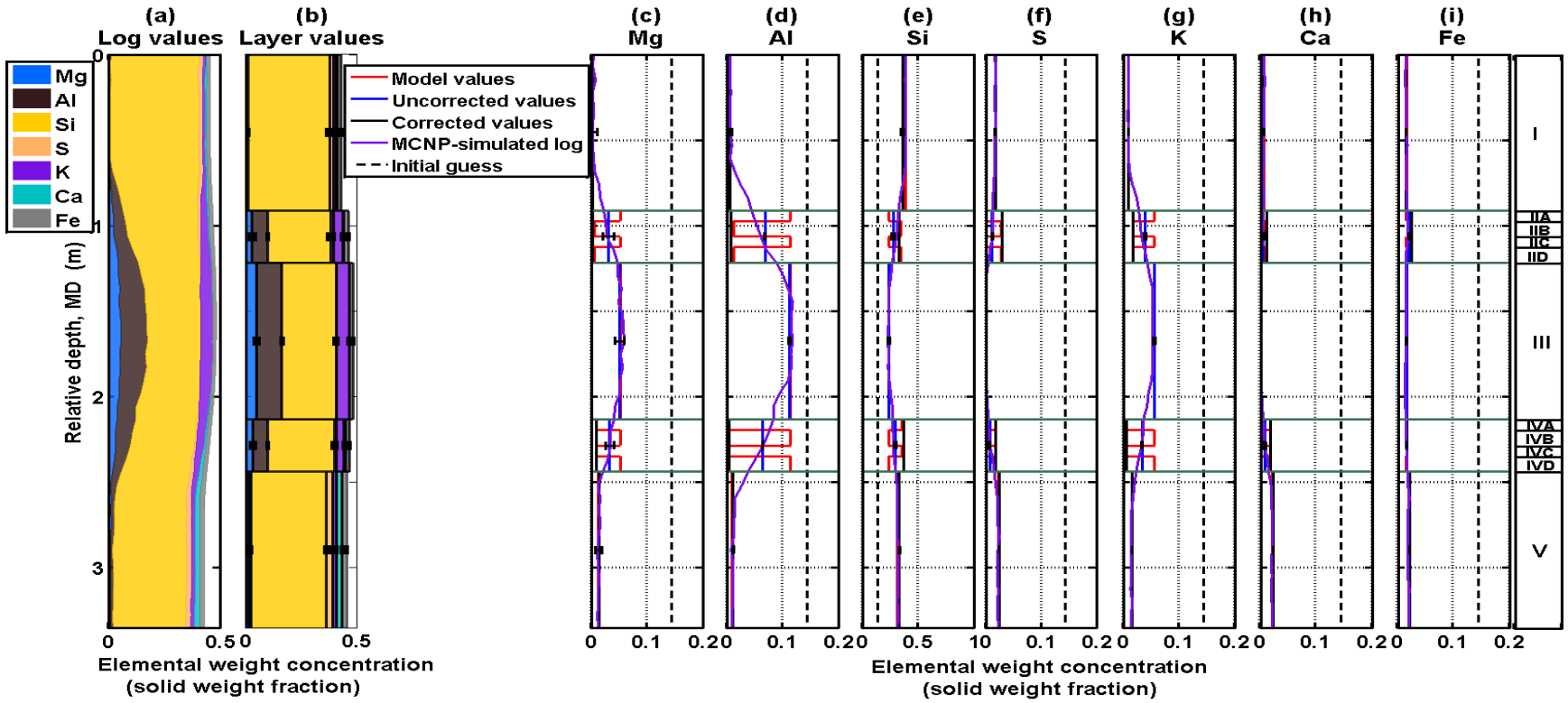

Figure 4.14: Panel (a) displays a cumulative plot of MCNP-simulated capture elemental weight concentrations shown as purple solid lines in panels (c) to (i). Panel (b) exhibits a cumulative plot of inverted elemental weight concentrations shown as blue solid lines in panels (c) to (i). Panels (c) to (i) describes the comparison of estimated layer elemental weight concentrations (blue solid lines) to model values (red solid lines) for Synthetic Case No. 4. Black dashed lines, black uncertainty bars, purple solid lines, and black solid lines indicate the initial guess of the inversion, 95% confidence interval, MCNP-simulated, and corrected elemental weight concentrations in the sandstone matrix, respectively; Mg, Al, Si, S, K, Ca, and Fe are the elements magnesium, aluminum, silicon, sulfur, potassium, calcium, and iron, respectively; I to V identify distinct layers in the synthetic case, while A to D identify laminations within layers.

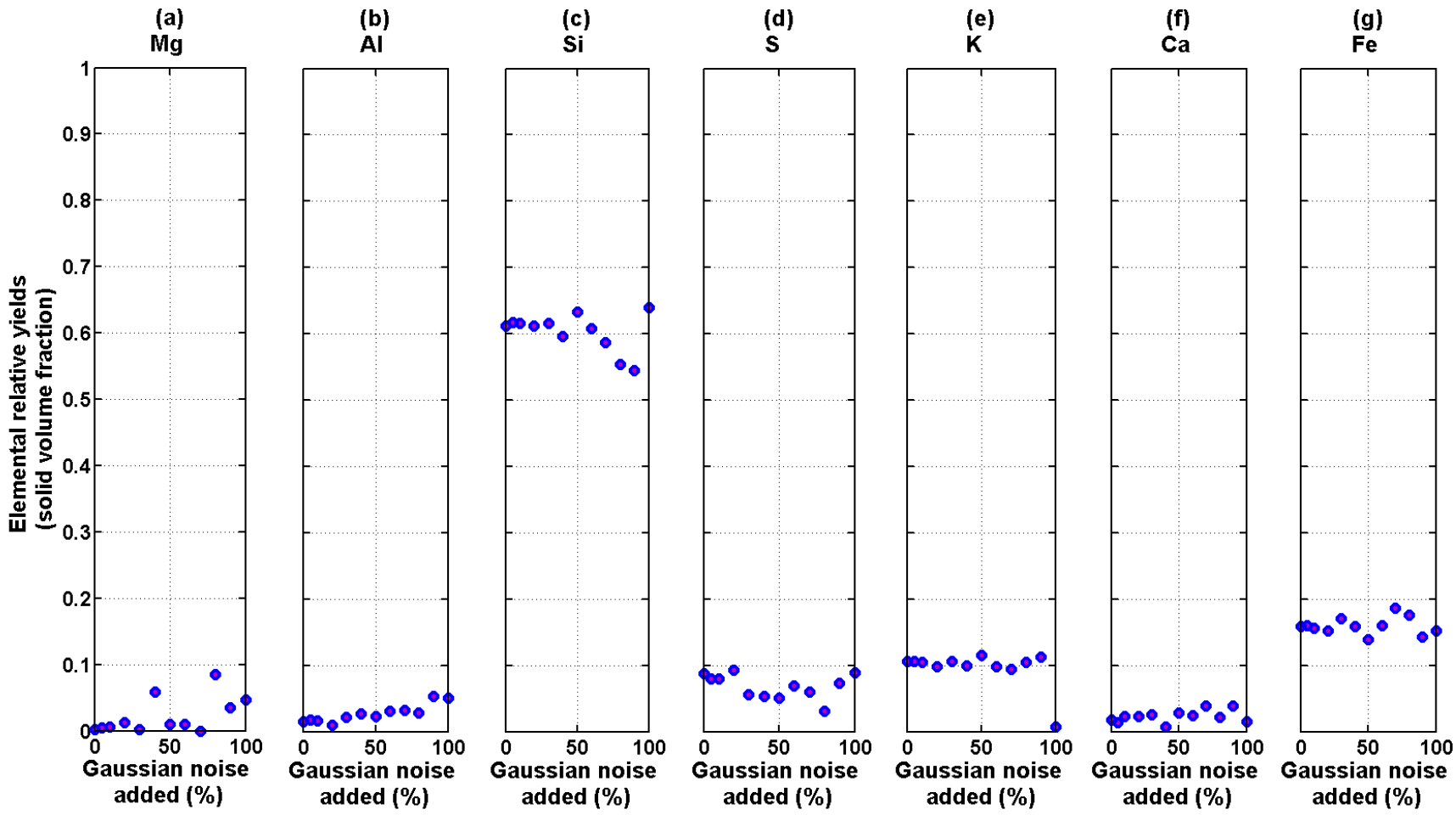

Figure 4.15: Effect of random Gaussian noise on elemental relative yields for layer I in Synthetic Case No. 4. Mg, Al, Si, S, K, Ca, and Fe are the elements magnesium, aluminum, silicon, sulfur, potassium, calcium, and iron, respectively.

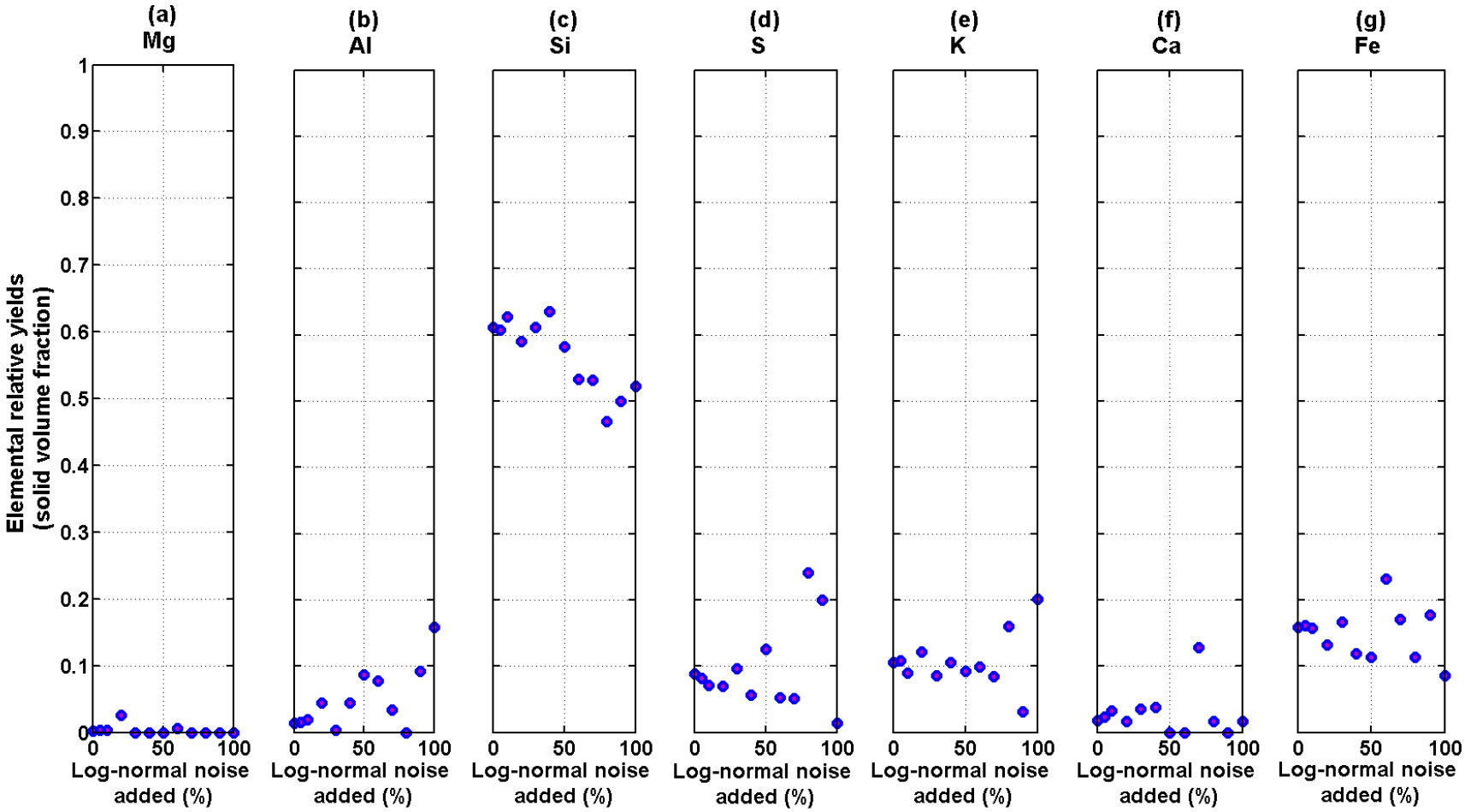

Figure 4.16: Effect of random log-normal noise on elemental relative yields for layer I in Synthetic Case No. 4. Mg, Al, Si, S, K, Ca, and Fe are the elements magnesium, aluminum, silicon, sulfur, potassium, calcium, and iron, respectively.

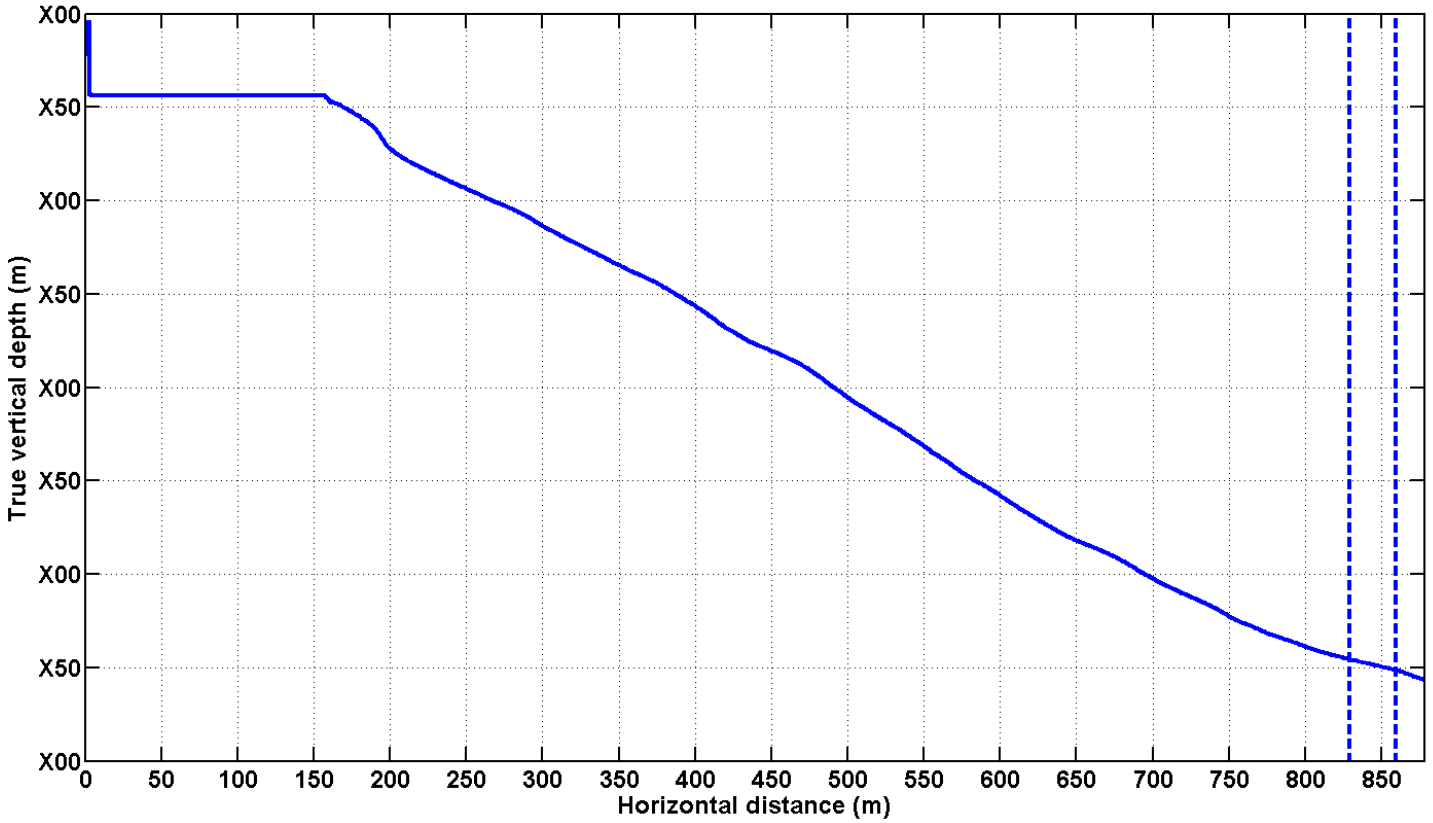

Figure 4.17: Well 2-26-G trajectory in Field Case No. 1 (2D projection of 3D well trajectory); dashed lines bracket the zone of interest in this chapter which is located within formations 1-C, 12-A1, 12-A2, and 12-A3.

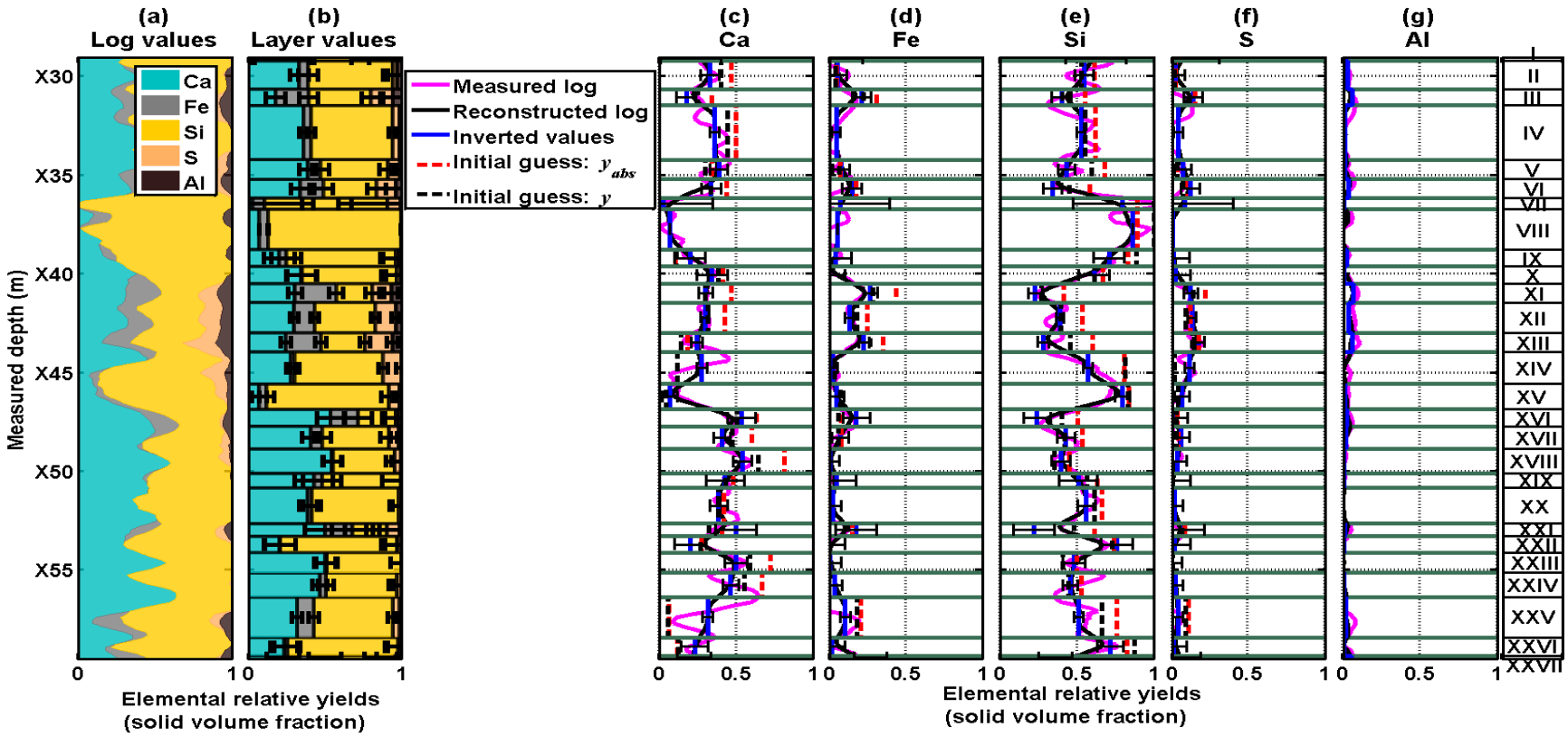

Figure 4.18: Panel (a) displays cumulative measured capture elemental relative yield logs shown as magenta lines in panels (c) to (g); panel (b) shows cumulative inverted layer elemental relative yields shown as blue solid lines in panels (c) to (g) for Field Case No. 1. Panels (c) to (g) exhibit the inverted layer values (blue solid lines), measured elemental relative yield logs (magenta solid lines), and reconstructed elemental yield logs (black solid lines). Black dashed lines describe the initial guess of absolute yields value, $y_{abs,i}$, and red dashed lines are the corresponding elemental relative yield values, y_i. Black uncertainty bars describe the 95% confidence interval; Ca, Fe Si, S, and Al are the elements calcium, iron, silicon, sulfur, and aluminum, respectively, while I to XXVII identify distinct layers in the field case.

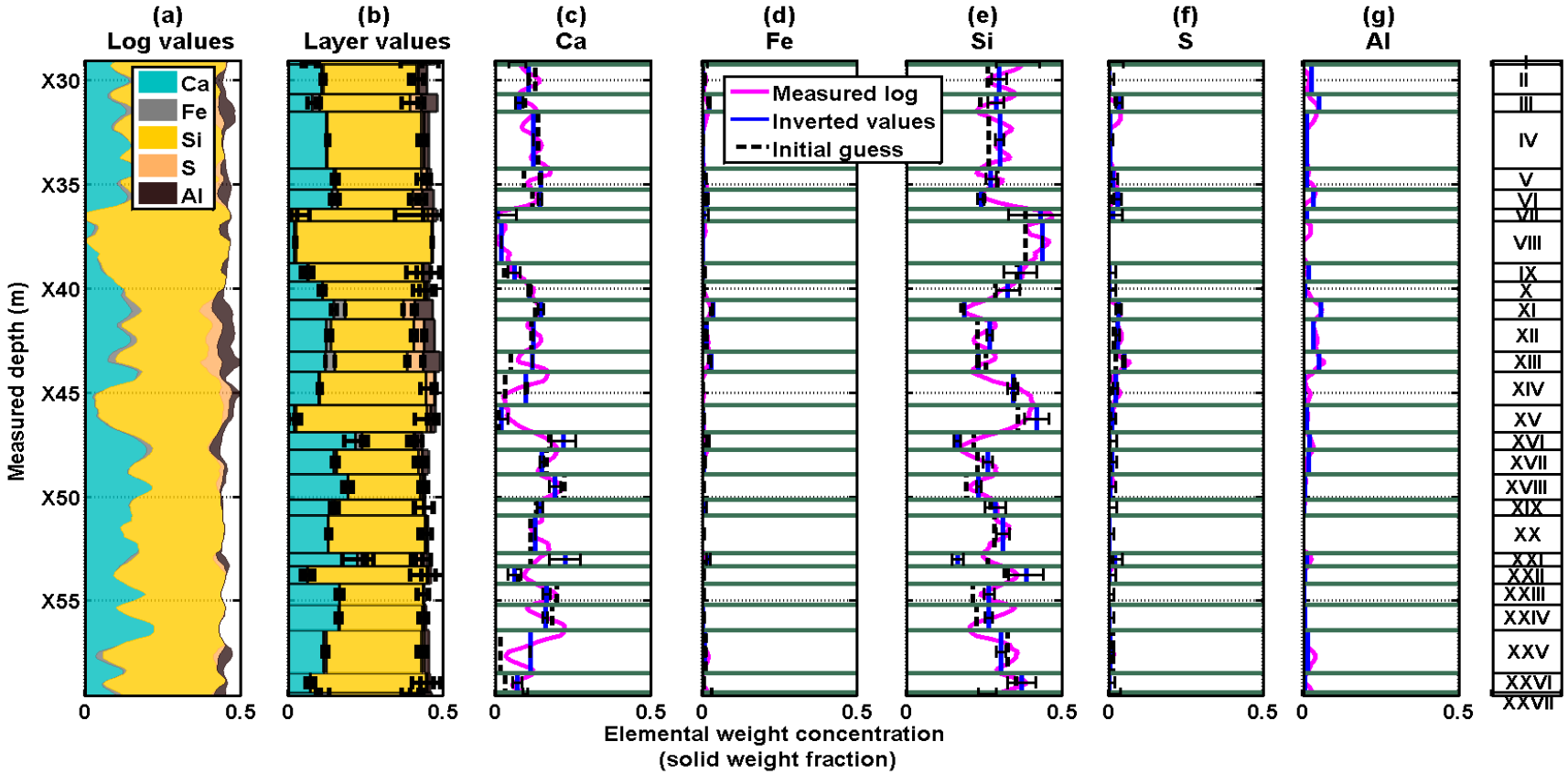

Figure 4.19: Panel (a) displays cumulative measured capture elemental weight logs shown as magenta solid lines in panels (c) to (g); panel (b) exhibits cumulative inverted layer elemental weight concentrations shown as blue solid lines in panels (c) to (g) for Field Case No. 1. Panels (c) to (g) show the inverted layer elemental weight values (blue solid lines) and elemental weight logs (magenta solid lines). Black dashed lines and black uncertainty bars describe the initial guess and 95% confidence interval, respectively; Ca, Fe Si, S, and Al are the elements calcium, iron, silicon, sulfur, and aluminum, respectively, while I to XXVII identify distinct layers in the field case.

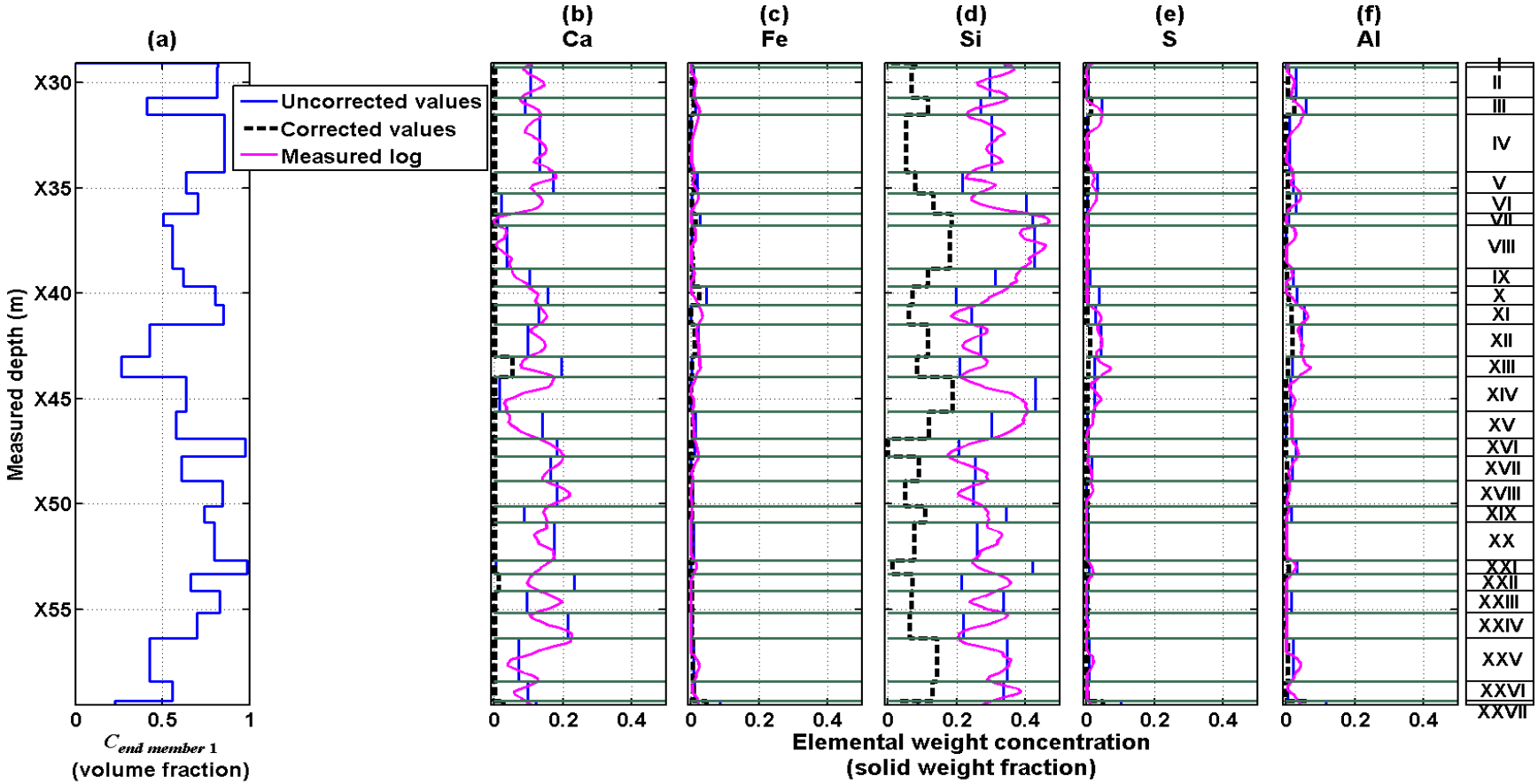

Figure 4.20: Panel (a) displays the volumetric concentration of *end member* 1: calcite-cemented feldspathic siltstones. Panels (b) to (f) show the comparison between corrected (hydrocarbon-bearing argillaceous uncemented siltstones) layer elemental weight concentrations (black dashed lines) and uncorrected (inverted) values (blue solid lines) for Field Case No. 2. Magenta solid lines describe measured elemental weight concentration logs; Ca, Fe Si, S, and Al are the elements calcium, iron, silicon, sulfur, and aluminum, respectively, while I to XXVII identify distinct layers in the field case.

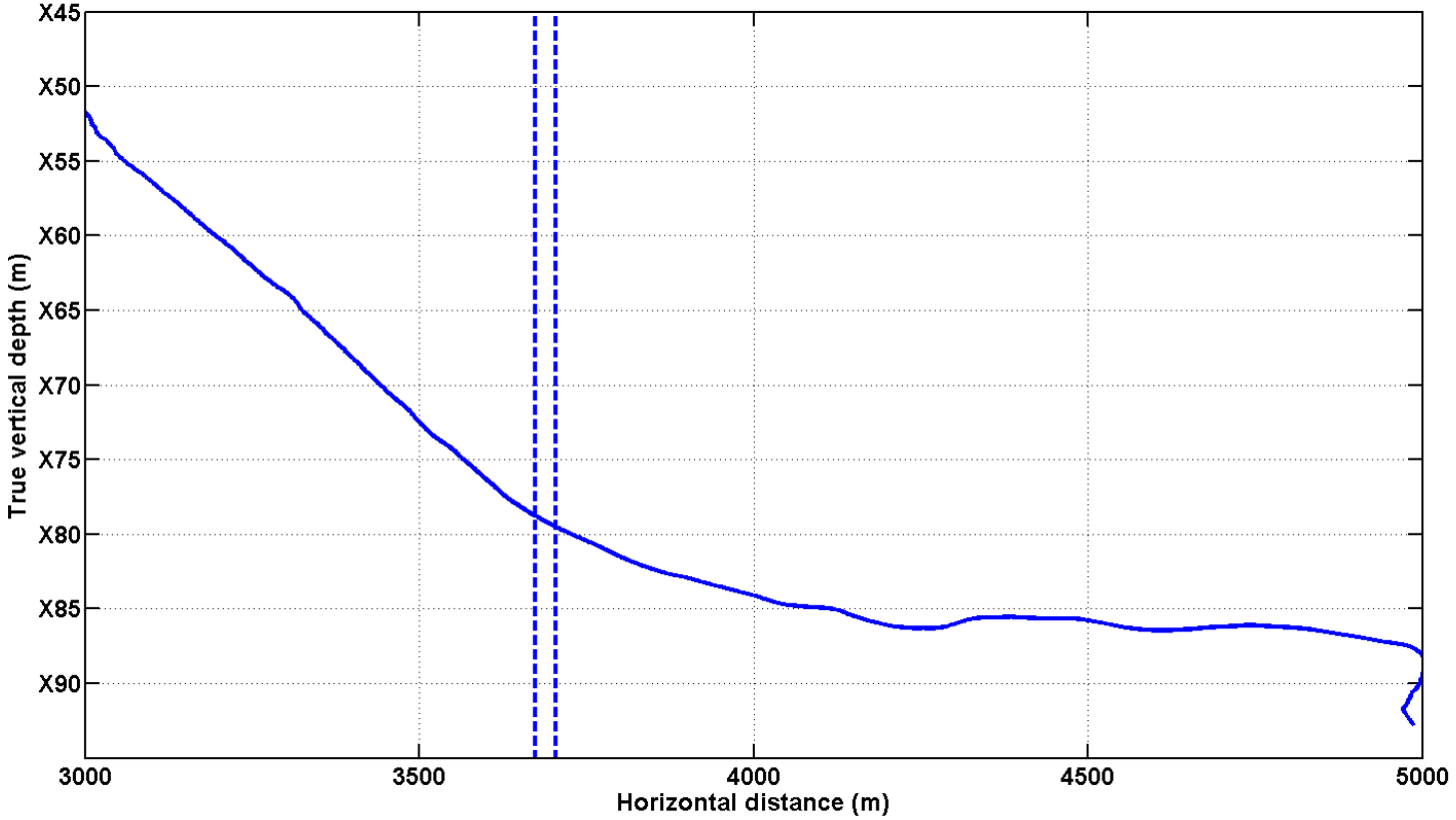

Figure 4.21: Well trajectory in Field Case No. 2 (2D projection of 3D well trajectory); dashed lines bracket the zone of interest analyzed in this chapter.

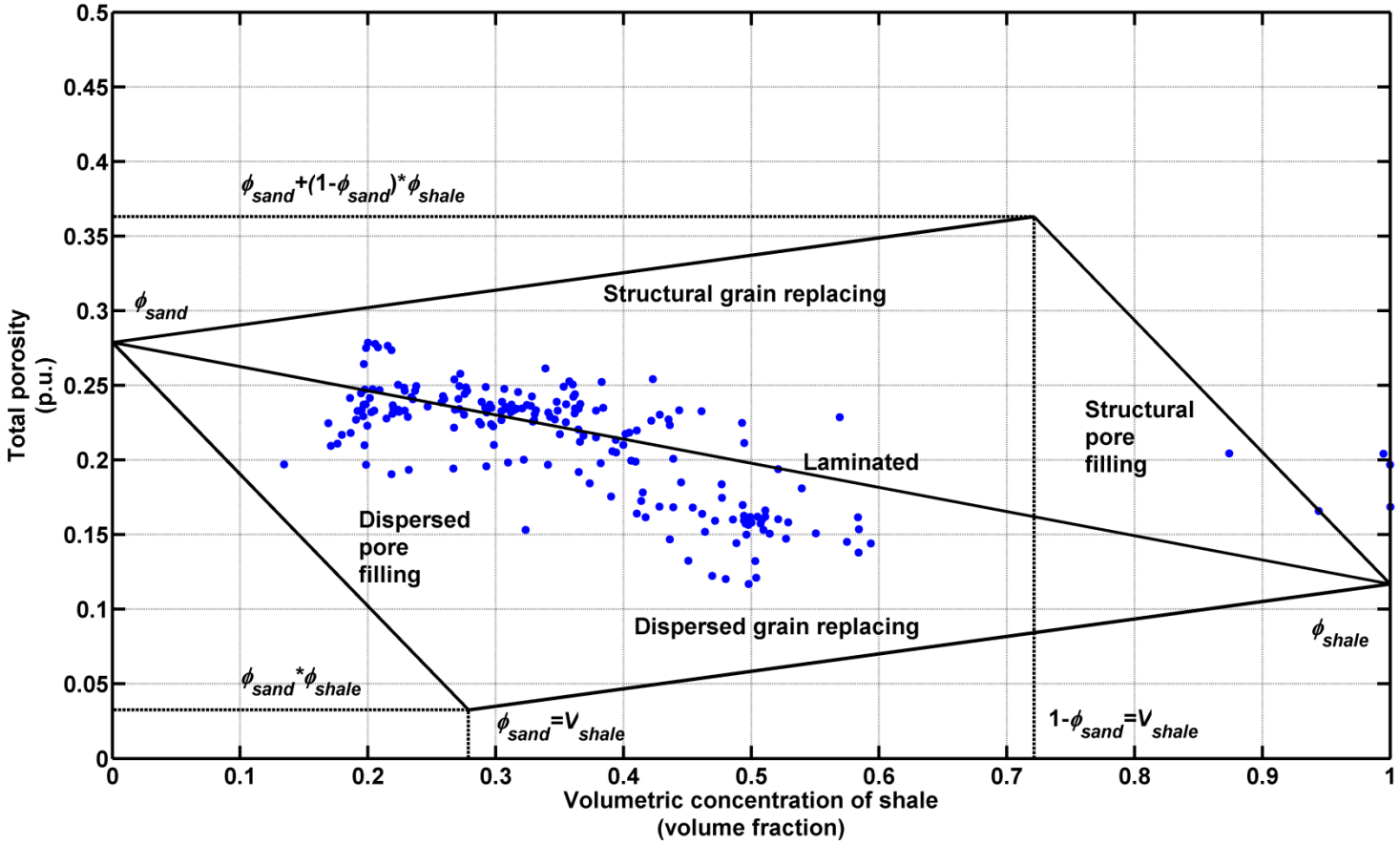

Figure 4.22: Thomas-Stieber diagram indicating a laminated formation in Field Case No. 2.

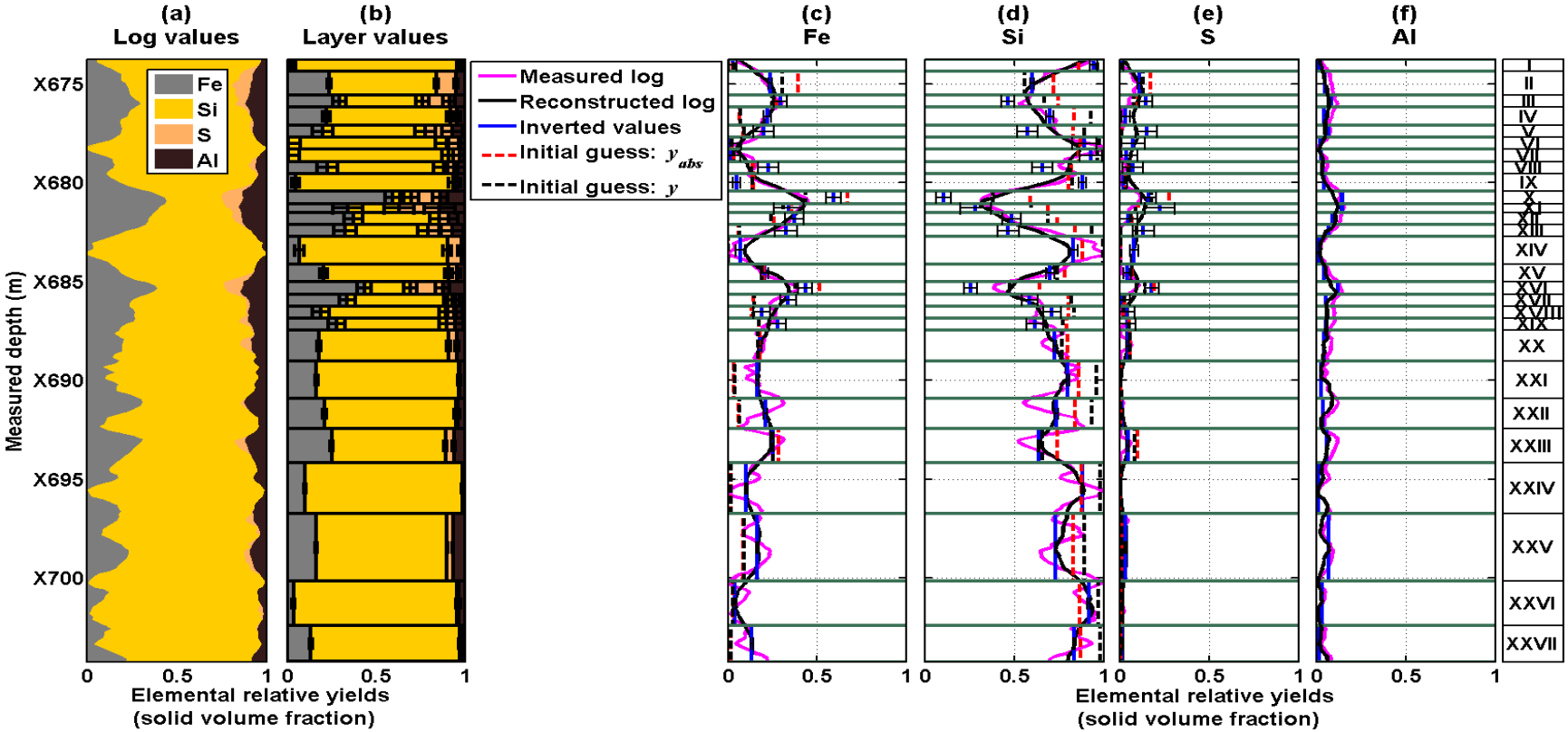

Figure 4.23: Panel (a) displays cumulative measured capture elemental relative yield logs shown as magenta lines in panels (c) to (f); panel (b) exhibits cumulative inverted layer elemental relative yields shown as blue solid lines in panels (c) to (f) for Field Case No. 2. Panels (c) to (f) show the inverted layer values (blue solid lines), measured elemental relative yield logs (magenta solid lines), and reconstructed elemental yield logs (black solid lines). Black dashed lines describe the initial guess of absolute yields value, $y_{abs,i}$, and red dashed lines are the corresponding elemental relative yield values, y_i. Black uncertainty bars describe the 95% confidence interval; Fe, Si, S, and Al are the elements iron, silicon, sulfur, and aluminum, respectively, while I to XXVII identify distinct layers in the field case.

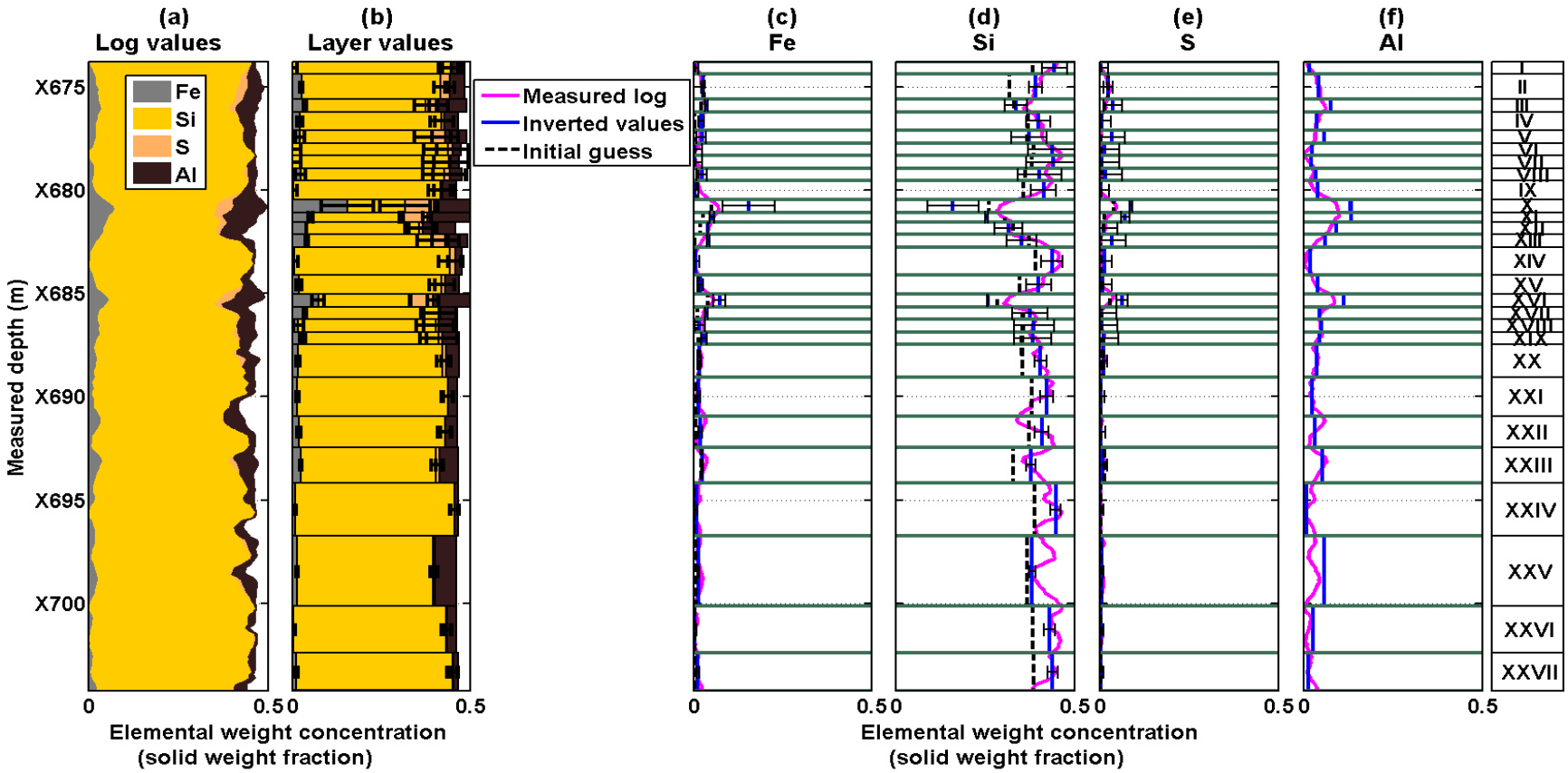

Figure 4.24. Panel (a) displays cumulative measured capture elemental weight logs shown as magenta solid lines in panels (c) to (f); panel (b) exhibits cumulative inverted layer elemental weight concentrations shown as blue solid lines in panels (c) to (f) for Field Case No. 1. Panels (c) to (f) show the inverted layer elemental weight values (blue solid lines) and elemental weight logs (magenta solid lines). Black dashed lines and black uncertainty bars describe the initial guess and 95% confidence interval, respectively; Fe Si, S, and Al are the elements iron, silicon, sulfur, and aluminum, respectively, while I to XXVII identify distinct layers in the field case.

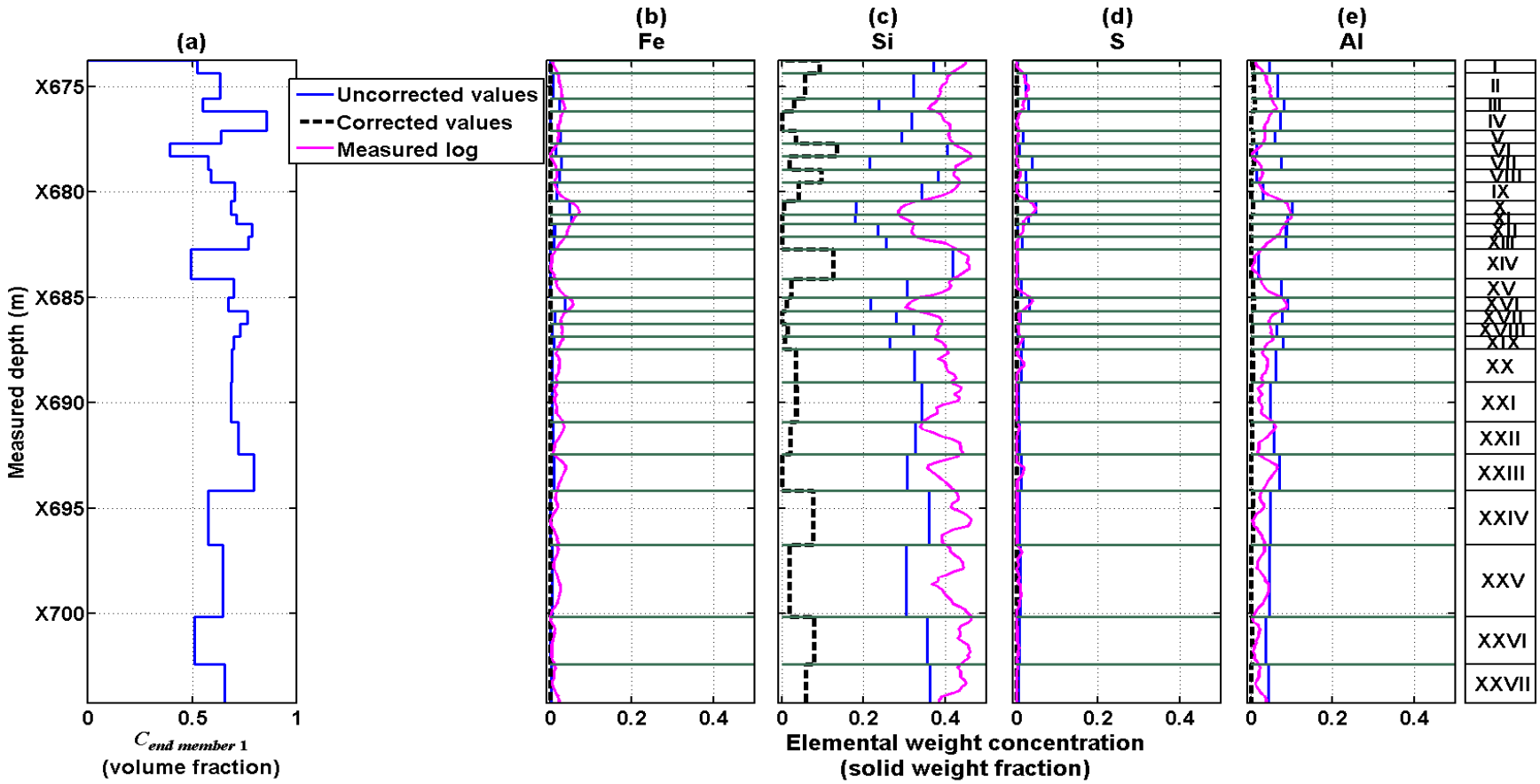

Figure 4.25. Panel (a) displays the volumetric concentration of *end member* 1: shale. Panels (b) to (e) show the comparison between corrected (sand) layer elemental weight concentrations (black dashed lines) and uncorrected (inverted) values (blue solid lines) for Field Case No. 2. Magenta solid lines describe measured elemental weight concentration logs; Fe, Si, S, and Al are the elements iron, silicon, sulfur, and aluminum, respectively, while I to XXVII identify distinct layers in the field case.

[2]Chapter 5: Inversion-Based Petrophysical Interpretation of LWD Gamma-Ray Spectroscopy Measurements

Geometrical effects on spectroscopy logs, such as those arising from shoulder beds and well deviation, lead to an averaging of true layer properties which can significantly compromise log-based petrophysical interpretation. I introduce a workflow, based on spectroscopy logs that have been corrected for geometrical effects, to quantify true layer matrix composition, porosity, and hydrocarbon saturation. Geometrical effects are corrected through nonlinear matrix inversion of elemental relative yields primarily based on a spectroscopy fast-forward model in a commercial logging-while-drilling (LWD) tool with a 14-MeV pulsed neutron source. The spectroscopy forward model facilitates the elimination of geometrical effects in the inversion method through the reproduction of tool physics, geometrical, and environmental effects on measurements. The inversion method is adapted, based on linear mixing-law techniques, to quantify layer petrophysical properties in thin hydrocarbon-bearing layers where conventional inversion methods fail because bed thicknesses are below the vertical resolution of the LWD spectroscopy tool. Petrophysical consistency in estimated mineralogy is achieved by ensuring that matrix-sensitive nuclear properties, such as gamma ray, matrix density, matrix Sigma, and photoelectric factor (PEF), simulated with inverted mineral volumetric concentrations correspond to measured well-log values. Estimated mineral compositions are used to correct

[2] The information within this chapter has been published in Petrophysics journal as "Ajayi, O., C. Torres-Verdín, and W. E. Preeg, 2015, Petrophysical Interpretation of LWD, Neutron-Induced Gamma-Ray Spectroscopy Measurements: An inversion-based approach: Petrophysics: Petrophysics, **56**, No. 4, 358-378". Co-authors Torres-Verdín and Preeg supervised the research presented in this publication.

matrix effects on neutron and density porosity logs, calculate matrix-corrected total porosity, and quantify hydrocarbon saturation through joint interpretation with fluid-sensitive logs. The developed workflow is implemented in four synthetic and two field cases to validate the accuracy and flexibility of the developed methods in different well trajectories and lithologies.

5.1 INTRODUCTION

Quantifying in-situ lithology is of primary interest to formation evaluation specialists because matrix compositions evaluate rock mechanical and petrophysical properties. Core analysis is a common approach to interpret formation lithology but it is neither economical nor practical to core every well. Lithology evaluation using well logs is a viable alternative that is typically employed when core data are not available. However, most methods of estimating mineralogy using well logs do not consider geometrical effects on measurements.

Early lithology evaluation methods based on well logs include correlation charts of two nuclear measurements such as density-sonic, density-PEF, neutron-sonic, and neutron-density (Clavier and Rust, 1976; Schlumberger, 2009). Such methods are only applicable in quantifying basic lithology types and are not robust enough to handle prevalent complex heterogeneous lithologies. Numerical methods used in diagnosing and quantifying lithofacies such as artificial neural networks, fuzzy logic, and neuro-fuzzy models also tend to fail in complex mineralogy (Gonçalves et al., 1995; Cuddy, 2000). Other numerical techniques include linear inversion of well logs, which is commonly implemented in commercial mineral solvers, to calculate both mineral and fluid compositions (Mayer and Sibbit, 1980; Doveton, 1994). However, linear inversion methods sometimes incorrectly assume linearity between certain well logs, such as thermal neutron porosity and resistivity, and volumetric rock mineral and fluid compositions.

Additional numerical approaches that estimate mineral and fluid volumetric compositions include statistical and probabilistic methods introduced by Quirein et al., 1986 and Busch et al., 1987, respectively. However, none of these methods typically include spectroscopy logs even though elemental concentrations have the most straightforward relationship to minerals because they directly indicate mineral compositions.

Spectroscopy-based lithology quantification approaches include a probabilistic method introduced by Galford et al. (2009) where spectroscopy elemental wireline logs are used in conjunction with nuclear logs to ascertain mineral and fluid compositions. Eslinger and Boyle (2013) also advanced a probabilistic clustering procedure to convert spectroscopy elements into minerals. Other approaches include the use of spectroscopy elemental-based correlation parameters to assess mineral compositions and matrix nuclear properties in wireline tools (Herron and Herron, 1996, Herron et al., 2002). However, none of these methods account for the existence of axial resolution limitations in thin beds which can lead to errors in the estimation of mineral and fluid compositions.

Recently, nonlinear inversion methods have been developed that correct geometrical effects on both wireline and LWD tool measurements, as well as estimate mineral and fluid compositions particularly in thinly-bedded formations. Joint nonlinear inversion of well logs including resistivity, gamma ray, PEF, neutron, and density logs acquired with wireline tools has been implemented to improve petrophysical assessment in thinly-bedded siliciclastic and carbonate formations (Liu et al., 2007; Sanchez-Ramirez et al., 2009; Heidari et al., 2012). Ijasan et al. (2013) introduced a joint nonlinear inversion method to calculate volumetric mineral and fluid compositions in an LWD tool using nuclear and resistivity measurements that have been

corrected for geometrical and environmental effects. Ortega (2014) applied a similar approach but replaced resistivity with Sigma measurements in the joint nonlinear inversion algorithm.

The missing part in these studies, which I introduce in this chapter, is the use of spectroscopy elemental logs to quantify lithology for a more accurate representation of the solid matrix composition of the formation. In the following sections, I describe the development of a petrophysical interpretation workflow that begins with a nonlinear matrix inversion of inelastic and capture spectroscopy elemental logs wherein I ensure petrophysical consistency between estimated mineral compositions and matrix-sensing logs. Matrix inversion is followed by the integration of estimated mineral volumetric compositions with nuclear and resistivity logs to obtain porosity and fluid saturations. Nuclear and resistivity logs are also acquired with the LWD tool under study and corrected for geometrical and environmental effects through inversion algorithms introduced by Ijasan et al. (2013). In laminated formations where layer thicknesses are below the vertical resolution of the tool, I implement an additional inversion method based on a spectroscopy mixing law and shaly-sand saturation model to quantify petrophysical properties within laminations.

5.2 NONLINEAR MATRIX INVERSION OF SPECTROSCOPY LOGS

LWD spectroscopy logs can be acquired in both inelastic and capture gamma-ray measurement modes which arise from inelastic scattering and thermal neutron capture, respectively, of formation neutrons with 14-MeV source neutrons. Due to this difference in nuclear physics, elements have distinct sensitivities to the detection of gamma rays, *Se*, in inelastic and capture measurement modes. Table 5.1 lists the sensitivities of common rock-forming elements in the inelastic and capture measurement modes. The LWD spectroscopy tool

under study operates only in the capture mode (Weller et al., 2005) but, in synthetic cases, I also perform analysis using inelastic data because this enables quantification of elements and associated minerals that can be detected only in the inelastic measurement mode. Inelastic spectroscopy data also exhibit a smaller volume of investigation than capture measurements, as seen in Figure 5.1, due to the high neutron energies that exist in inelastic nuclear interactions and are therefore less affected by environmental effects and yield better estimations of mineralogy (Ajayi et al., 2014). I hence perform separate nonlinear matrix inversion in both inelastic and capture measurement domains.

Measured logs are exposed to negligible invasion in the LWD spectroscopy tool under study because the tool has all measurements located close to the drill bit (Weller et al., 2005). Additionally, the solid matrix composition is independent of fluid effects such as porosity, saturation, and invasion. I therefore assume that estimated mineralogy data are approximately constant and isotropic within each layer.

5.2.1 Formulation

The nonlinear inversion method used in the estimation of mineral compositions is based on the fast-forward spectroscopy simulation procedure, outlined in Chapter 2, which includes geometrical and physical effects of the tool, borehole, and the formation through the use of FSFs. The estimation method thereby explicitly accounts for shoulder-bed averaging effects on spectroscopy measurements. The spectroscopy forward model numerically simulates an output, **d** as a function of layer properties, **x**, where **x** is a vector of layer mineral volumetric compositions, C_j, and **d** is a vector elemental relative yields, y_i, where subscript i represents the index for m elements present in the formation, and subscript j represents the index for n minerals present in

the formation. Outputs of the forward model also include elemental weight concentrations, M_i, but elemental relative yields are preferred in this interpretation because they are direct outputs of the model and minimize the processing of forward-simulated spectroscopy logs.

Error minimization between elemental relative yields simulated via the spectroscopy forward model and measured elemental relative yields is achieved with a damped least squares problem of the form

$$C(\mathbf{x}) = \left\| \mathbf{W}_d \cdot \left[\mathbf{g}(\mathbf{x}) - \mathbf{d}_m \right] \right\|_2^2 + \lambda^2 \left\| \mathbf{W}_x \cdot \left(\mathbf{x} - \mathbf{x}_{ref} \right) \right\|_2^2 , \qquad (5.1)$$

where λ is a regularization parameter that lends stability by improving the uniqueness and convergence of the solutions to ill-posed spectroscopy problems, $\mathbf{d}_m$ is a vector of measured elemental relative yields or weight concentrations, $\mathbf{W}_d$ is a data-weighting matrix, $\mathbf{W}_x$ is a model-weighting matrix, $\mathbf{x}_{ref}$ is the reference vector, and $\mathbf{g}$ is the spectroscopy fast-forward model. I introduce constraints that ensure mineral volumetric concentrations are positive and sum up to one by subjecting inversion results at each iteration to $0 \le x_j \le 1$ and $\sum_{j=1}^{n} \mathbf{x}_j = 1$, respectively.

I also ensure that matrix-sensitive nuclear properties such as matrix density, gamma ray, matrix PEF, and matrix Sigma, simulated with estimated mineral volumetric concentrations correspond to matrix-sensitive nuclear log values. This is achieved by implementing linear mixing laws for matrix-sensitive nuclear measurements at each iteration. The mixing laws are given by

$$GR_{matrix,\,log} = \sum_{j=1}^{n} C_j \times GR_j,$$

$$\text{where } GR_j = \alpha U_j + \beta Th_j + \gamma K_j,$$

$$\text{PEF}_{matrix,\,log} = \sum_{j=1}^{n} C_j \times \text{PEF}_j, \qquad (5.2)$$

$$\rho_{matrix,\,log} = \sum_{j=1}^{n} C_j \times \rho_j,$$

$$\Sigma_{matrix,\,log} = \sum_{j=1}^{n} C_j \times \Sigma_j,$$

where GR_j, PEF_j, ρ_j, and Σ_j are gamma-ray, PEF, density, and Sigma values, respectively, associated with each mineral *j*; $GR_{matrix,\,log}$, $\text{PEF}_{matrix,\,log}$, $\rho_{matrix,\,log}$, and $\Sigma_{matrix,\,log}$, are gamma-ray, PEF, matrix density, and Sigma log values, respectively. The parameter U_j is the mass concentration in ppm of uranium for mineral *j*, Th_j is the mass concentration in ppm of thorium for mineral *j*, and K_j is the mass concentration in % of potassium for mineral *j*; the coefficients α, β, and γ depend on the detector and tool design details (Ellis and Singer, 2007). Equation 5.2 is implemented only when it has been established that lithology-sensing logs are affected solely by the formation matrix as opposed to spurious effects on measured logs such as the presence of barite in drilling mud which falsely decreases gamma-ray values. The use of equation 5.2 in the interpretation decreases non-uniqueness in estimated results particularly in underdetermined cases where the number of measured elements is less than the number of minerals present in the formation.

Within long depth segments, the formation is interpreted in short intervals that have approximately constant geometrical properties (including well dip and azimuth) and inversion parameters (including $\mathbf{W}_d$, $\mathbf{W}_x$, $\mathbf{x}_{ref}$, and λ). I limit the analyzed depth interval to a maximum of

45.72-m (150-ft) to avoid large matrices in the inversion which can introduce complexities into the algorithm.

Bed-boundary locations in the formation geometrical model, included in the interpretation method, can be obtained manually based on inflection points of well logs, such as density, gamma ray, PEF images, spectroscopy logs, or other measurements, that are sensitive to changes in layer petrophysical properties using a threshold variance algorithm (Uzoh et al., 2009). Alternatively, I can define bed-boundary locations using a consolidated gamma geometrical model introduced by Ijasan et al. (2013) that also estimates the apparent dip and azimuth along the well trajectory. Calculations are performed through least-squares minimization of borehole sinusoids along borehole depth and azimuth (Plumb and Luthi, 1989) where sinusoids are obtained using the intersection of an initial selection of bed boundaries with a circular borehole (Yin et al., 2008). An initial selection of bed boundaries is obtained from inflection points of nuclear borehole images and spectroscopy logs using the threshold variance algorithm.

5.2.2 Inversion Method

The estimation of mineral volumetric concentrations is achieved through iterative nonlinear minimization of the quadratic cost function, $C(\mathbf{x})$ expressed in equation 5.1 via a modification of Occam's method that includes a data-weighting matrix, a model-weighting matrix, and a reference vector (Aster et al., 2013) and is given by

$$\left\{\left[\mathbf{J}^T\left(\mathbf{x}^k\right)\cdot\mathbf{W}_d^T\cdot\mathbf{W}_d\cdot\mathbf{J}\left(\mathbf{x}^k\right)\right]+\lambda^2\mathbf{W}_x^T\mathbf{W}_x\right\}\mathbf{x}^{k+1}=\mathbf{J}^T\left(\mathbf{x}^k\right)\left[\left(\mathbf{W}_d{}^T\cdot\mathbf{W}_d\right)\cdot\hat{\mathbf{e}}\right]+\lambda^2\mathbf{x}_{ref}, \quad (5.3)$$

where

$$\hat{\mathbf{e}} = \left[\mathbf{d}_m - \mathbf{g}\left(\mathbf{x}^k\right) + \mathbf{J}\left(\mathbf{x}^k\right)\mathbf{x}^k \right], \qquad (5.4)$$

where $\mathbf{x}^k$ and $\mathbf{x}^{k+1}$ indicate the vector of mineral volumetric concentrations at iteration k and the updated trial model at iteration $k+1$, respectively, superscript T indicates transposition, $\hat{\mathbf{e}}$ is the modified vector of data misfit, and $\mathbf{J}$ is the Jacobian or sensitivity matrix. The inclusion of a data-weighting matrix, a model-weighting matrix, and a reference vector can significantly improve solution convergence and stabilization.

The regularization parameter can be obtained using Hansen's (1994) L-curve strategy which calculates a value that best minimizes the norm of the error between numerically simulated and measured logs. In longer depth intervals, where there is more likely to be an appreciable variability in spectroscopy logs, another choice of λ that can optimally minimize the norm of the error between numerically simulated and measured logs is the variance of the error between measured and numerically simulated logs. Both strategies for choosing λ ensure that the impact of λ progressively diminishes from the quadratic cost function as the algorithm reaches convergence.

Entries of the Jacobian matrix, $\mathbf{J}_{y\text{-}C}$, are the derivatives of elemental relative yields with respect to mineral volumetric concentrations whereby

$$\mathbf{J}_{y-C} = \begin{bmatrix} \begin{pmatrix} \frac{\partial y_1}{\partial C_1} & \cdots & \frac{\partial y_1}{\partial C_n} \\ \vdots & \ddots & \vdots \\ \frac{\partial y_m}{\partial C_1} & \cdots & \frac{\partial y_m}{\partial C_n} \end{pmatrix}_1^1 & \cdots & \begin{pmatrix} \frac{\partial y_1}{\partial C_1} & \cdots & \frac{\partial y_1}{\partial C_n} \\ \vdots & \ddots & \vdots \\ \frac{\partial y_m}{\partial C_1} & \cdots & \frac{\partial y_m}{\partial C_n} \end{pmatrix}_g^1 \\ \vdots & \ddots & \vdots \\ \begin{pmatrix} \frac{\partial y_1}{\partial C_1} & \cdots & \frac{\partial y_1}{\partial C_n} \\ \vdots & \ddots & \vdots \\ \frac{\partial y_m}{\partial C_1} & \cdots & \frac{\partial y_m}{\partial C_n} \end{pmatrix}_1^r & \cdots & \begin{pmatrix} \frac{\partial y_1}{\partial C_1} & \cdots & \frac{\partial y_1}{\partial C_n} \\ \vdots & \ddots & \vdots \\ \frac{\partial y_m}{\partial C_1} & \cdots & \frac{\partial y_m}{\partial C_n} \end{pmatrix}_g^r \end{bmatrix}, \qquad (5.5)$$

for solutions of mineral volumetric concentrations using elemental relative yield data. Entries of the Jacobian matrix, $\mathbf{J}_{M\text{-}C}$, are the derivatives of elemental weight concentrations with respect to mineral volumetric concentrations whereby

$$\mathbf{J}_{M-C} = \begin{bmatrix} \begin{pmatrix} \frac{\partial M_1}{\partial C_1} & \cdots & \frac{\partial M_1}{\partial C_n} \\ \vdots & \ddots & \vdots \\ \frac{\partial M_m}{\partial C_1} & \cdots & \frac{\partial M_m}{\partial C_n} \end{pmatrix}_1^1 & \cdots & \begin{pmatrix} \frac{\partial M_1}{\partial C_1} & \cdots & \frac{\partial M_1}{\partial C_n} \\ \vdots & \ddots & \vdots \\ \frac{\partial M_m}{\partial C_1} & \cdots & \frac{\partial M_m}{\partial C_n} \end{pmatrix}_g^1 \\ \vdots & \ddots & \vdots \\ \begin{pmatrix} \frac{\partial M_1}{\partial C_1} & \cdots & \frac{\partial M_1}{\partial C_n} \\ \vdots & \ddots & \vdots \\ \frac{\partial M_m}{\partial C_1} & \cdots & \frac{\partial M_m}{\partial C_n} \end{pmatrix}_1^r & \cdots & \begin{pmatrix} \frac{\partial M_1}{\partial C_1} & \cdots & \frac{\partial M_1}{\partial C_n} \\ \vdots & \ddots & \vdots \\ \frac{\partial M_m}{\partial C_1} & \cdots & \frac{\partial M_m}{\partial C_n} \end{pmatrix}_g^r \end{bmatrix}. \qquad (5.6$$

)

for solutions of mineral volumetric concentrations using elemental weight concentration data. The size of the Jacobian matrices in equations 5.5 and 5.6 is $m \times r$ rows which is the number of elements, *m*, at *r* measurement points and $n \times g$ columns which is the number of minerals, *n*, in *g* beds. The Jacobian matrix can be calculated numerically by perturbing model parameters and simulating corresponding elemental relative yields or weight concentrations using the forward model. However, it is computationally expensive to invoke the forward model for first-order derivative Jacobian matrix calculations at each iteration in the inversion. A more efficient approach, which is approximately fifteen times faster than numerical calculations of the Jacobian matrix, is to compute the Jacobian matrix using analytical expressions of the forward model developed in Chapter 2.

There are two different approaches to estimate layer mineral volumetric concentrations from spectroscopy elemental logs:

(a) Matrix inversion of spectroscopy elemental relative yield or weight logs, or

(b) Matrix inversion of layer elemental relative yields or weight concentrations.

5.2.2.1 *Matrix Inversion of Spectroscopy Elemental Relative Yield or Weight Logs*

Mineral volumetric concentrations can be estimated through the inversion of elemental relative yield or weight logs. Analytical entries of the Jacobian matrix are defined by the first-order derivative of elemental relative yields or weight concentrations with respect to mineral volumetric concentrations as expressed by equations B-1 to B-4 in Appendix B.

The data-weighting matrix included in the inversion is a diagonal matrix with entries for each spectroscopy element defined by the statistical variance of the element which is given by

$$\partial y_i = \frac{\partial y_{abs,i}}{\sum_{i=1}^{m} y_{abs,i}}, \quad (5.7)$$

where $\partial y_{abs,i}$ is the statistical variance in each element's energy integrated measured spectrum within the energy measurement range of the tool (elemental absolute yield), and $\sum_{i=1}^{m} y_{abs,i}$ is the sum of energy integrated measured spectra for the *m* elements present in the formation within the energy measurement range of the tool. This technique emphasizes measured spectroscopy elements that exhibit greater variability in their responses in the inversion method.

In thinly-bedded intervals, a model-weighting matrix, $\mathbf{W}_x$, is introduced with diagonal entries inversely proportional to relative layer thicknesses, h_f, of each layer, *f*. This technique enhances the significance of thin beds in the solution by assigning model-weighting values that increase with decreasing layer thicknesses.

5.2.2.2 *Matrix Inversion of Layer Elemental Relative Yields or Weight Concentrations*

Mineral volumetric concentrations can also be estimated through nonlinear matrix inversion of layer elemental relative yields or weight concentrations. Layer elemental relative yields or weight concentrations are obtained through nonlinear inversion of elemental relative yield logs which corrects shoulder-bed averaging effects on measured elemental logs based on the spectroscopy fast-forward model, described in Chapter 2 (Ajayi et al., 2014).

Matrix inversion of layer elemental relative yields or weight concentrations is based on the forward relationship between elemental relative yields or weight concentrations and mineral volumetric concentrations which is given by

$$y_i = \frac{\sum_{j=1}^{n} \frac{Se_i \rho_j C_j N_{ij} MM_i}{MM_j}}{\sum_{i=1}^{m} \sum_{j=1}^{n} \frac{Se_i \rho_j C_j N_{ij} MM_i}{MM_j}}, \quad (5.8)$$

in the estimation of mineral volumetric concentrations using elemental relative yields or

$$M_i = \frac{\sum_{j=1}^{n} \frac{\rho_j C_j N_{ij} MM_i}{MM_j}}{\sum_{i=1}^{m} \sum_{j=1}^{n} \frac{\rho_j C_j N_{ij} MM_i}{MM_j}}, \quad (5.9)$$

in the estimation of mineral volumetric concentrations using elemental weight concentrations, where MM_i is the molar mass of element *i*, MM_j is the molar mass of mineral *j*, and N_{ij} is the number of atoms of the *i-th* element in the *j-th* mineral which is obtained from mineral chemical formulas.

In this method, I observe through sensitivity analysis that the optimum value for the data weighting matrix which best minimizes the error between simulated and measured spectroscopy logs is approximately 0.05. Jacobian matrix entries are defined by the first-order derivative of equations 5.8 and 5.9 and are listed in the Appendix B.

5.2.3 Initial Guess Generation

In underdetermined inversion cases, where the number of measured elements in the estimation is less than the number of minerals, the initial guess is typically obtained from bed-center values of spectroscopy mineral logs and a reference vector of the same value is included in the estimation to stabilize the convergence of the solution. In other cases, such as evendetermined inversion problems, the solution is relatively insensitive to the initial guess and

it usually suffices to assume a uniform average value for the initial guess. Careful consideration is given to the choice of minerals in the solution by reviewing geological information, core mineral data, or performing sensitivity analysis to determine the set of minerals that optimize solution convergence. This strategy prevents false representations of non-existing minerals in the solution. The initial guess is updated at every iteration until the norm of the differences between measured and numerically simulated logs are equal to or less than 0.001 up to a maximum of ten iterations. After ten iterations, studies show that a well-posed inversion problem will have converged to a unique and stable solution.

5.2.4 Assessment of Uncertainty in Inversion Results

The 95% confidence interval is obtained through a modification to the covariance approach of evaluating uncertainty bars in nonlinear inverse problems (Aster et al., 2013) and is defined by

$$\pm 1.96 q^{-\frac{1}{4}} \sqrt{\left\| \mathbf{W}_d \cdot \mathbf{e}(\mathbf{x}) \right\|_2^2 \cdot diag\left\{ \left[\mathbf{J}^T \cdot \mathbf{W}_d^T \cdot \mathbf{W}_d \cdot \mathbf{J} \right]^{-1} \right\}}, \qquad (5.10)$$

where $\mathbf{e}$ is the vector of data misfit given by $\left[\mathbf{d}_m - \mathbf{g}\left(\mathbf{x}^k\right) \right]$, *diag* describes diagonal matrix entries, and q is the number of degrees of freedom in the inversion problem. Confidence intervals quantify the stability and uncertainty in estimated mineral volumetric concentrations due to perturbations in the input elemental relative yields and weight concentrations. Mineral weight concentrations, $C_{w,j}$, can be estimated from results of mineral volumetric compositions through

$$C_{w,j} = \frac{\rho_j C_j}{\sum_{j=1}^{n} \rho_j C_j}. \qquad (5.11)$$

5.3 PETROPHYSICAL INTERPRETATION

In this section, I describe a nuclear solver that estimates porosities and water saturations based on spectroscopy mineral logs that have been corrected for shoulder-bed averaging and well deviation effects. Estimated layer mineral volumetric compositions are used to correct neutron and density porosities from matrix effects in order to accurately quantify porosity and fluid saturations.

5.3.1 Nuclear Solver

5.3.1.1 *Porosity Calculations*

Density porosities are calculated through

$$\phi_D = \frac{\rho_{bulk} - \rho_{matrix}}{\rho_{fluid} - \rho_{matrix}}, \qquad (5.12)$$

where ϕ_D is the density porosity, ρ_{bulk} is the measured layer bulk density, ρ_{matrix} is the layer matrix density, and ρ_{fluid} is the formation fluid density.

Measured density porosity logs are typically based on the assumption of a freshwater-saturated formation with a lithology of limestone or sandstone. To correct the lithology assumption, ρ_{matrix} is replaced by a value calculated using the inverted mineralogy but the assumption of freshwater saturation is retained which corresponds to a fluid density of one. I

obtain model layer bulk densities through an interpretation method advanced by Ijasan et al. (2013) that eliminates geometrical and environmental effects on density logs.

I exploit the approximate linear relationship between neutron porosity and the inverse of migration length, ξ, to correct neutron porosities of matrix effects. Similar to density porosity logs, neutron porosity logs are acquired based on the assumption of a freshwater-saturated formation and a lithology of limestone or sandstone. Model layer ξ values are obtained using an interpretation method, similar to that used to estimate layer bulk densities, advanced by Ijasan et al. (2013) which corrects geometrical and environmental effects on neutron porosity logs. The lithology assumed in measured neutron porosity logs is replaced with the inverted mineralogy using Schlumberger's Nuclear Parameter program, SNUPAR (McKeon and Scott., 1989) whereby I calculate ξ values based on the assumption of freshwater-saturated porosity and dynamically adjust porosity values until calculated ξ values match model layer ξ values. Porosities that yield ξ values consistent with model layer ξ values are the matrix-corrected neutron porosities.

Total porosity values are calculated from matrix corrected neutron and density porosity according to the root-mean-square method proposed by Gaymard and Poupon, 1968 which is given by

$$\phi_t^C \approx \sqrt{\frac{\left(\phi_D^C\right)^2 + \left(\phi_N^C\right)^2}{2}}, \qquad (5.13)$$

where ϕ_t is the matrix-corrected total porosity, ϕ_D^C is the matrix-corrected density porosity, and ϕ_N^C is the matrix-corrected neutron porosity. In water-saturated formations, matrix-corrected

neutron, density, and total porosities are equal but in hydrocarbon-bearing formations, matrix-corrected neutron and density porosities differ due to fluid effects. Equation 5.13 provides an approximation for total porosity in such cases where matrix-corrected neutron and density vary.

5.3.1.2 *Saturation Calculations*

Water saturation is calculated according to saturation balance equations given by

$$S_w = \frac{\rho_{fluid} - \rho_h}{\rho_w - \rho_h}, \qquad (5.14)$$

where

$$\rho_{fluid} = \frac{\rho_{bulk} - (1 - \phi_t)\rho_{matrix}}{\phi_t}, \qquad (5.15)$$

ρ_h is the density of hydrocarbons in the formation, ρ_w is the density of formation water, and S_w is the water saturation. I compute hydrocarbon density using a flash calculation simulator based on Peng-Robinson's equation of state (Abdollah-Pour, 2011) that ensures hydrocarbon composition, volume, temperature, and pressure is thermodynamically consistent. The density of formation water is calculated using SNUPAR which accounts for the salinity of formation water.

5.4 INTERPRETATION OF LAMINATED FORMATIONS

5.4.1 Spectroscopy Mixing Law

In thinly-bedded formations, conventional matrix inversion methods fail because layer thicknesses are below the vertical resolution of the spectroscopy tool. I use a linear mixing law that estimates elemental weight concentrations within laminations to calculate mineral volumetric concentrations in thin beds.

The mixing law estimates elemental weight concentrations of one end member, typically hydrocarbon bearing, in a binary-lithology sequence, $(M_i)_{end\ member\ 2}$, based on the linear relationship given by

$$\begin{aligned} M_i &= (M_i)_{end\ member\ 1} C_{end\ member\ 1} + (M_i)_{end\ member\ 2} C_{end\ member\ 2} \\ M_i &= (M_i)_{end\ member\ 1} C_{end\ member\ 1} + (M_i)_{end\ member\ 2} (1 - C_{end\ member\ 1}) \end{aligned}, \qquad (5.16)$$

whereby

$$(M_i)_{end\ member\ 2} = \frac{M_i - (M_i)_{end\ member\ 1} C_{end\ member\ 1}}{1 - C_{end\ member\ 1}}, \qquad (5.17)$$

where $(M_i)_{end\ member\ 1}$ is the layer weight concentration of element *i* in *end member* 1, and $C_{end\ member\ 1}$ is the layer volumetric concentration of *end member* 1. The parameter $(M_i)_{end\ member\ 1}$ is obtained from spectroscopy elemental weight logs that have been corrected for shoulder-bed averaging effects (Ajayi et al., 2014), $C_{end\ member\ 1}$ can be calculated from $(M_i)_{end\ member\ 1}$ through layer matrix inversion (described in the matrix inversion of layer elemental relative yields or weight concentrations section). Mineral volumetric concentrations of *end member* 2, $C_{end\ member\ 2}$, can also be estimated from $(M_i)_{end\ member\ 2}$ through layer matrix inversion.

In laminated shaly-sands where $C_{end\ member\ 1}$ is the volumetric concentration of shale, C_{sh}, $C_{end\ member\ 1}$ may alternatively be calculated from gamma-ray data (Ellis and Singer, 2007) through

$$C_{sh} = \frac{GR - GR_s}{GR_{sh} - GR_s}, \quad (5.18)$$

where GR is the total gamma-ray reading, GR_s is the gamma-ray reading in clean sands, GR_{sh} is the gamma-ray reading in pure shales, and gamma-ray values have been corrected for geometrical effects (Ijasan et al., 2013).

5.4.2 Petrophysical Interpretation

I use laminated shaly-sand saturation models (Poupon et al., 1954), the relationship between total and sand (non-shale) porosity, and Archie's equation (Archie, 1942) to compute water saturation within sand laminations through

$$\frac{1}{R_t} = \frac{\left(1 - C_{sh}\right)}{R_s} + \frac{C_{sh}}{R_{sh}}, \quad (5.19)$$

where

$$\phi_t = \phi_s \left(1 - C_{sh}\right) + \phi_{sh} C_{sh}, \quad (5.20)$$

$$R_s = \frac{aR_w}{\phi_s^{\,m} S_{w,s}^{\,n}}, \quad (5.21)$$

R_t is the total resistivity, R_s is sand (non-shale) resistivity, R_{sh} is the resistivity of pure shale, R_w is the resistivity of formation water, a is Archie's Winsauer constant, m is Archie's porosity exponent, n is Archie's saturation exponent, ϕ_t is the total porosity, ϕ_s is sand (non-shale) porosity, ϕ_{sh} is shale porosity, and $S_{w,s}$ is the water saturation within the sand (non-shale) lamination. Formation water resistivity, R_w is calculated by

$$R_w \approx \left[0.0123 + \frac{3647.5}{\left(NaCl_{ppm}\right)^{0.955}}\right] \cdot \frac{81.77}{\mathrm{T} + 6.77} \quad \text{(Schlumberger, 2009).} \quad (5.22)$$

where $NaCl_{ppm}$ is the formation water salinity, T is the formation temperature, and both parameters are obtained from well-log information.

The workflow adopted in this chapter is outlined in Figure 5.2.

5.5 SYNTHETIC EXAMPLES

Synthetic cases benchmark the reliability and flexibility of the developed workflow through its implementation in four synthetic cases which include different well trajectories and lithologies. The fourth synthetic case describes the application of the interpretation methods, particularly those based on the spectroscopy mixing law, in a laminated formation. Layer mineral volumetric compositions are obtained through the inversion of elemental relative yield logs simulated with Monte Carlo N-Particle code, MCNP (X-5 Monte Carlo Team, 2005) at a sampling rate of 7.62-cm (3-in). Analytical approximation of Jacobian matrices, (described earlier), is implemented in the inversion method for results shown in synthetic cases. Synthetic mineral logs are obtained through matrix inversion of MCNP-simulated elemental relative yield logs based on the forward model described by equation 5.8.

Table 5.2 shows elemental, mineral, chemical, and nuclear properties assumed in synthetic examples. Inverse of layer migration length, ξ values, and elemental compositions used in the fast-forward spectroscopy simulation method are calculated from synthetic mineral and fluid compositions using SNUPAR. Measured depth locations are defined by the geometrical center and depth of investigation of FSFs (Ijasan et al., 2011) used in the spectroscopy forward simulation. Neutron and density porosity layer values are calculated in limestone units assuming a freshwater-saturated formation. Apparent neutron porosity in limestone units is obtained using

a SNUPAR-derived calibration between apparent freshwater-saturated neutron porosity in limestone units and ξ values.

Data-weighting matrices employed in the inversion algorithm have diagonal entries corresponding to the statistical variance of each element which is calculated using equation 5.7. Model-weighting matrices, with diagonal entries equal to the inverse of relative layer thicknesses, are introduced to emphasize the estimation of mineralogy in thin beds present in synthetic cases. I observe, in all of the synthetic cases studied, that the inversion is stable and converges to the same result independent of the initial guess value. The initial guess is therefore chosen to be a constant value equal to the reciprocal of the number of minerals in the estimation, in each layer, and for each mineral.

Because slight perturbations in matrix density and porosity significantly affect estimations of water saturation calculated through saturation balance equations shown in equations 5.14 and 5.15, I only use this method to calculate water saturations in Synthetic Cases Nos. 3 and 4, where I have the most accurate estimations of matrix density and porosity.

5.5.1 Synthetic Case No. 1

This synthetic case includes (a) capture and (b) inelastic MCNP simulations in a hydrocarbon-bearing 4.57-m true stratigraphic thickness (TST) formation composed of quartz and dolomite, and penetrated by a 60-degree deviated well. Analysis of both inelastic and capture spectra allows one to quantify the impact of differences in volume of investigations and elemental sensitivities between inelastic and capture measurements on results. I introduce another carbonate mineral, calcite, into the interpretation to characterize the ability of the

inversion to detect the absence of calcite in the synthetic model and properly allocate all the calcium present in the formation to dolomite. The inclusion of calcite into the solution does not result in an underdetermined inversion problem because silicon, magnesium, calcium, and matrix-sensitive nuclear data are present to quantify quartz, calcite, and dolomite. Table 5.3 lists layer elemental, mineral, fluid compositions, thicknesses, bulk densities, and migration lengths assumed in this example. Regularization parameter, λ, values used in the estimation method for cases (a) and (b) are calculated using Hansen's (1994) L-curve method which computes a value of λ that best minimizes the error between numerically and MCNP-simulated elemental relative yield logs.

The solution for case (a) converges after ten iterations, when a computer processing unit (CPU) time of 738.96 seconds has elapsed, if the Jacobian matrix is calculated numerically or after 40.01 seconds when the Jacobian matrix is calculated analytically. Estimated mineral volumetric compositions for case (a) show that the solution allocates some of the MCNP-simulated calcium elemental relative yields to calcite (average 0.02 mineral volume fraction of calcite) particularly in layers II and V, which are the layers most affected by shoulder-bed averaging as seen in Figure 5.3. Average differences between model and estimated mineralogy are 0.0097 mineral volume fraction (excluding calcite because it is not actually present in the formation) and are all approximately within uncertainty bounds shown as error bars on estimated mineralogy.

In case (b), the solution converges after 746.91 seconds of CPU time, if the Jacobian matrix is calculated numerically, or after 32.3 seconds, when the Jacobian matrix is calculated analytically, on the tenth inversion iteration. Figure 5.4 shows that mineralogy estimated using

inelastic spectroscopy yield logs in case (b) exhibit improved agreement with model values, in thin layers II and V, compared to results from case (a). This is because inelastic measurements have a smaller volume of investigation than capture measurements. The inversion does not estimate any appreciable amount of calcium to calcite (less than 0.0023 mineral volume fraction of calcite) and thus properly quantifies dolomite. This behavior is due to increased sensitivity of inelastic measurements to magnesium (Pemper et al., 2006) which, in this example, is a unique component of dolomite and thereby improves dolomite characterization. Similar to case (a), differences between model and estimated mineralogy values [average 0.0012 mineral volume fraction (excluding calcite)] are within uncertainty bounds shown as error bars on estimated mineral volumetric concentrations.

I observe significant reduction of shoulder-bed effects observed in mineral logs particularly in the thin layers II and V (as much as 0.3 mineral volume fraction). Calculations of matrix nuclear properties: gamma ray, matrix density, matrix Sigma, and matrix PEF obtained using results from case (b) exhibit good agreement with model layer values (differences less than 0.3 API, 0.01g/cc, 0.005 c.u., and 0.06 b/e for gamma ray, matrix density, matrix Sigma, and matrix PEF, respectively) as seen in Figure 5.5. I also observe that gamma-ray values are insignificant (less than 8 API) because Synthetic Case No. 1 comprises a clean, shale-free formation.

Figure 5.5 also shows that neutron and density porosities are influenced by the assumption of a limestone matrix whereby apparent neutron porosities are greater than density porosities in all layers, particularly in layers with high dolomite content because dolomite has nuclear properties significantly different from limestone. Estimated mineral volumetric

concentrations are used to correct layer neutron and density porosities for these matrix effects such that crossovers between neutron and density porosities become indicative of fluid properties. Due to the assumption of a freshwater-saturated formation, neutron and density porosities overlap in the presence of water. In the presence of hydrocarbons, migration lengths increase which cause a decrease in neutron porosities such that I can observe neutron-density crossovers. Neutron-density crossovers are only appreciable when there is gas or a light hydrocarbon in the formation and are typically negligible in the presence of oil or water. This behavior occurs because oil-saturated formations have migration lengths and densities similar to freshwater-saturated formations but gas-saturated formations have significantly larger migration lengths.

Total porosities are computed via root-mean-square methods and exhibit good agreement with model values. The model exhibits a continuous increase in water saturation, from 0.4 in layer I to 1 in layer VII, and I therefore observe in the water-saturated layer VII that neutron matrix-corrected neutron and density values overlap. Neutron and density porosities also tend to overlap in oil-saturated layers I to VI, because oil has nuclear properties similar to water, but slight neutron-density crossovers are observed in layers I and II due to the lower water saturations and high porosities in these two layers.

5.5.2 Synthetic Case No. 2

Quantifying kerogen in gas-bearing shale reservoirs is impractical using capture spectroscopy logs alone because capture logs do not measure any of the elements typically associated with kerogen. In this example, I use inelastic MCNP-simulated carbon logs in conjunction with joint interpretation of spectroscopy elemental logs and matrix-sensitive nuclear

logs to facilitate the estimation of kerogen. This example is also important in quantifying the errors in calculating total porosity, with root-mean-square methods, in the presence of gas and low porosities that are prevalent in gas-bearing shales. The model consists of a 5.64-m TST gas-bearing shale formation penetrated by a 70-degree deviated well with porosities ranging from 3.5 to 7 porosity units (p.u.). Tables 5.4 and 5.5 list layer elemental, mineral, fluid compositions, thicknesses, bulk densities, and migration lengths assumed in this example.

There are ten measured elemental isotopes (formation inorganic carbon, formation organic carbon, sodium, sulfur, magnesium, aluminum, silicon, potassium, calcium, and iron) in this synthetic case which cause many elements (with the exception of formation inorganic carbon, calcium, and silicon) to occur in less than 5% elemental weight concentration. The low concentration of most elements leads to a high degree of numerical noise in MCNP-simulated inelastic relative yield logs for these elements. Nevertheless, Figure 5.6 indicates good agreement between estimated and model mineralogy which includes quartz, albite, kerogen, pyrite, calcite, illite, and mg-chlorite. I observe reductions of shoulder-bed effects on mineral logs, particularly for quartz and calcite in thin layer VI (up to 0.15 mineral volume fraction). The solution converges after ten iterations and 7208.4 seconds if the Jacobian matrix is calculated numerically or 218.3 seconds when the Jacobian matrix is calculated analytically. Regularization parameter values are obtained using Hansen's L-curve technique which calculates values that optimize error minimization between numerically and MCNP-simulated logs. I accurately estimate kerogen present in the synthetic model with differences less than 9e-4 mineral volume fraction compared to model values. Differences between model and estimated values do not exceed 0.01 mineral volume fraction and are within the uncertainty bounds shown as error bars

in Figure 5.6. Figure 5.7 exhibits the good agreement between reconstructed and model gamma ray, matrix grain density, matrix Sigma, and PEF values.

Neutron and density porosities also shown in Figure 5.7 indicate that matrix effects mask the presence of hydrocarbons mainly due to the presence of hydroxyls in shales that decrease migration lengths and thereby increase apparent neutron porosities. Estimated mineral volumetric concentrations are used to correct neutron and density porosities for matrix effects; whereupon significant neutron-density crossovers are revealed especially in layers I, II, III, and IV, due to the presence of gas and low water saturations (approximately 0.2 volume fraction water saturation) in these layers. I observe an overestimation of total porosity in layers VI to IX due to the difficulty of root mean square methods in accurately resolving total porosity in low porosity formations.

5.5.3 Synthetic Case No. 3

This synthetic model is designed to address challenges in petrophysical interpretation due to highly deviated well trajectories. I present an 85-degree deviated well penetrating a 3.65-m TST thinly-bedded oil-bearing shaly sand with depth periodic petrophysical properties. Additional complexities in the interpretation arise due to high shale content (up to 0.59 mineral volume fraction) and large variations in porosities and water saturations from one layer to the next (from 2 to 30 p.u. and 100% to 3.3% water saturation). High shale content significantly alters neutron and density porosities while the large variation in layer petrophysical properties coupled with well deviation effects lead to shoulder-bed averaging considerably higher than that observed in the other synthetic cases. Tables 5.6 and 5.7 list layer thicknesses, compositions, and nuclear properties assumed in this synthetic example. Measured elements include capture

magnesium, aluminum, silicon, potassium, calcium, and iron and the minerals present in the formation are calcite, illite, kaolinite, and quartz.

The solution converges after ten iterations in 7703.2 seconds when the Jacobian matrix is computed numerically or in 149.8 seconds if the Jacobian matrix is calculated analytically. Regularization parameters are specified as the variance of the error between numerically and MCNP-simulated elemental relative yields because the depth interval in this example (41.9-m) is long enough to exhibit significant variability in measured data. This approach ensures λ progressively diminishes from the cost function until the solution converges and optimally minimizes differences between numerically and MCNP-simulated logs. Figure 5.8 shows that layer mineral volumetric concentrations estimated using capture elemental relative yield logs exhibit good agreement with respect to model values (less than an average difference of 1.36e-19 mineral volume fraction). The severity of previously unaccounted shoulder-bed effects facilitates significant corrections of shoulder-bed averaging on mineral logs in all layers. Largest corrections in shoulder-bed averaging are 0.36 mineral volume fraction which is seen in layer VII for kaolinite. The accuracy of estimated mineralogy is also exhibited by the small uncertainty bars on estimated mineral volumetric concentrations as seen in Figure 5.8. Furthermore, results in Figure 5.9 indicate a good agreement between matrix-sensitive nuclear properties reconstructed using the estimated mineralogy and corresponding model values.

Because of the high clay content in the formation, Figure 5.10 shows that there are significant matrix effects on porosity logs which are eliminated by using the inverted mineralogy to correct the assumption of a limestone matrix. Matrix-corrected neutron and density porosities are approximately equal except in the 96.67% oil-saturated layers II, V, VIII, and XI where

neutron porosities are slightly less than densities. This behavior is due to fluid effects of hydrocarbons in these layers where hydrocarbons have a higher migration length and lower density than that of the assumed saturating fluid, water. Estimations of porosity and water saturation, obtained through equations 5.13 to 5.15, exhibit good agreement to model values with differences less than 0.0068 p.u. and 0.012 volume fraction water saturation, respectively.

5.5.4 Synthetic Case No. 4

This example shows the application of the developed interpretation methods in a 3.35-m TST laminated shaly-sand formation penetrated by a vertical well wherein I acquire capture spectroscopy well logs. Laminations include alternating thin layers of sand and shale within the 30.48-cm thick layers II and IV. Tables 5.8 and 5.9 list layer thicknesses, migration lengths, bulk densities, C_{sh}, elemental, mineral, and fluid compositions assumed in this example. Measured elements include capture magnesium, aluminum, silicon, sulfur, potassium, calcium, and iron while minerals in the synthetic model are mg-chlorite, illite, K-feldspar, quartz, pyrite, and dolomite. Table 5.2 describes the chemical properties of elements and minerals assumed in this example. Measured elemental relative yields are obtained from MCNP simulations at a sampling rate of 7.62-cm (3-in). Each measured depth location is defined by the geometrical center and depth of investigation of FSFs used in the spectroscopy fast-forward simulation.

I perform an initial inversion step to quantify layer elemental weight concentrations (Ajayi et al., 2014) and mineralogy through the inversion of MCNP-simulated elemental relative yields. Layer elemental yields and weights are obtained from the inversion of MCNP-simulated elemental relative yields. The estimation takes 2068 or 115.1 seconds of CPU time when the Jacobian matrix is calculated analytically or numerically, respectively, and ten iterations to

converge to the final solution. Results shown in Figures 5.11 and 5.12 demonstrate that conventional inversion methods do not resolve elemental and mineral compositions within laminations but converge at bed-center elemental and mineral log values. This procedure cannot resolve properties of laminations within layers II and IV because these laminations are below the vertical resolution of the LWD spectroscopy tool. Estimated elemental and mineral compositions exhibit good agreement to model values in thicker layers I, III, and V (average differences of 0.003 elemental weight fraction and 0.02 mineral volume fraction) where bed thicknesses, at 91.44-cm, are above the vertical resolution of the LWD spectroscopy tool.

In order to quantify elemental and mineral concentrations within laminations, I use the mixing law described by equation 5.17 to obtain elemental weight concentrations within sand laminations where elemental weight concentrations of pure shale can be obtained from the initial inversion step or Table 5.9; and C_{sh} (listed in Table 5.8) is calculated as the effective volumetric concentration of shale within the volume of investigation of the tool. Corrected layer elemental weight concentrations are used to obtain mineral compositions within sand laminations through layer matrix inversion which converges after ten iterations in 0.06 seconds. This estimation is considerably faster than the initial inversion step because inputs of layer elemental weight concentrations have already been corrected for shoulder-bed averaging effects such that the Jacobian matrix can be rapidly calculated as the derivative of equation 5.9. Results of elemental and mineral concentrations obtained from laminated analysis are shown in Figures 5.11 and 5.12 and exhibit good agreement to model values of sand matrix compositions within thin beds (average differences are less than 0.0027 elemental weight fraction and 0.00765 mineral volume fraction).

Figure 5.13 shows the impact of inaccurate layer mineral compositions, obtained using conventional inversion methods alone, on calculations of matrix-sensitive nuclear properties wherein the solution averages model values within laminations. However, solutions that include the spectroscopy mixing law accurately reproduce matrix-sensitive nuclear properties within laminations.

Figure 5.14 shows that total porosity and water-saturation calculations,, for layers II and IV average true lamination properties such that I underestimate porosity and hydrocarbon saturations in sand laminations. These averaging effects also lead to the erroneous conclusion of higher hydrocarbon saturation in layer IV compared to layer II whereas the hydrocarbon saturation in layer II is actually higher than that in layer IV. Results show a good correlation to model values in thicker layers that are not affected by averaging of lamination model properties.

Porosities and water saturations, obtained via equations 5.13 to 5.15, within sand laminations shown in Figure 5.15 are calculated with neutron and density porosities that have been corrected for matrix effects using mineralogy estimated through laminated analysis. Results accurately resolve petrophysical properties within laminations present in layers II and IV as well as in thicker layers I, III, and V. Shale layers within laminations, IIA, IIC, IVB, and IVD are water-saturated and therefore neutron and density porosities overlap but I observe neutron-density crossovers in hydrocarbon-bearing sand layers. The crossover between neutron and density porosities, where neutron porosities are less than density porosities, is larger in sand laminations within layer II than in sand laminations within layer IV. This behavior is consistent with the higher hydrocarbon saturation within sand laminations in layer II compared to layer IV.

5.6 FIELD EXAMPLES

Developed petrophysical interpretation methods are implemented in two laminated offshore high-angle (HA) field cases. Formation geometrical model parameters including bed-boundary locations, apparent dip, and azimuth are calculated using the consolidated geometrical model approach described earlier. Table 5.11 shows bed thicknesses obtained from consolidated geometrical model calculations; Table 5.2 shows elemental, mineral, chemical, and nuclear properties assumed in field examples; Table 5.10 shows petrophysical properties assumed in calculations. Measured elemental relative yield logs are acquired in the capture spectroscopy mode alone because the LWD tool under study does not quantify inelastic measurements. Measured elemental yield and weight logs used in the interpretation have been corrected for environmental effects and are therefore indicative of formation elemental compositions. Estimations of layer mineral volumetric compositions are estimated through the inversion of measured elemental relative yield logs. Analytical approximation of Jacobian matrices, described earlier, is implemented in the inversion method for results shown in both field cases.

Due to the long depth interval in the two field cases studied (30.48-cm), there is significant variability in measured logs and λ is calculated as the variance of the error between numerically and MCNP-simulated elemental relative yield logs. Data-weighting matrices are defined by a diagonal matrix with diagonal entries equal to the statistical variance of each element according to equation 5.7. This approach places more importance, in the inversion algorithm, on elements with higher statistical variance. The presence of several thin beds in the field examples necessitates the use of a model-weighting matrix with diagonal entries equal to the inverse of the relative thickness of each layer in order to emphasize thin beds in the

interpretation. Initial guesses and the reference vector of mineral volumetric concentrations, included in the inversion for both field cases, are obtained from bed-center spectroscopy mineral logs for optimal solution convergence.

Neutron and density porosity logs are acquired in limestone units assuming a freshwater-saturated formation. Layer ξ and bulk densities used in correcting matrix effects on neutron and density porosities are obtained using interpretation methods that eliminate shoulder-bed averaging effects on measured porosity logs (Ijasan et al., 2013). Phase shift resistivity, P40H, resistivity logs (40 inch spacing at 2 MHz and environmentally corrected) are used for saturation calculations in equation 5.19 and R_w is calculated with equation 5.22.

5.6.1 Field Case No. 1

This field case includes thinly-bedded formation (comprising formations 1-C, 12-A1, 12-A2, and 12-A3) penetrated by an approximately 60-degree deviated well (well 2-26-G). The entire well trajectory highlighting the 30.48-m measured depth (MD) interval under study, which is in the hydrocarbon-bearing section of the well, is shown in Figure 5.16. The formation includes alternating laminations of calcite-cemented feldspathic siltstones and hydrocarbon-bearing argillaceous uncemented siltstones. Measured capture elemental logs include calcium, iron, silicon, sulfur, and aluminum and geological reports indicate that formation lithology consists of several minerals including illite, montmorillonite, kaolinite, calcite, pyrite, quartz, and K-feldspar. This situation results in an underdetermined inversion problem, but constraining simulated matrix-sensitive logs (gamma ray, matrix density, matrix Sigma, and matrix PEF) to match corresponding well-log values, decreases the non-uniqueness of the problem. I detect the

formation is laminated through geological reports and laminations observed in nuclear and resistivity borehole images.

The solution converges after ten iterations when 1388.2 or 110.4 seconds have elapsed if the Jacobian matrix is calculated numerically or analytically, respectively. Figure 5.17 shows the comparison between measured grouped mineral logs, such as clays and quartz-feldspar-mica (QFM), and estimated individual mineral (clay minerals: illite, montmorillonite, kaolinite, QFM minerals: quartz, and K-feldspar) layer compositions because I do not know the proportion of each mineral within predefined mineral groups in the measured field data. I can therefore only comment on reduction of shoulder-bed averaging effects on measured minerals that are not grouped such as calcite (calcite is the only mineral present within the carbonate mineral group in field logs) or pyrite. Since pyrite is present in less than 0.012 mineral volume fraction in the formation, largest reductions of shoulder-bed averaging on mineral logs are achieved for calcite (0.33 and 0.23 calcite mineral volume fraction in layers XVI and XXI, respectively). K-feldspar needs to be introduced into silicate composition to achieve solution convergence and stability as well as reconstruct gamma-ray logs that are comparable to measured data as seen in Figure 5.18. This presence of K-feldspar is consistent with the formation lithology of feldspathic siltstones suggested by geological reports. Measured matrix Sigma logs exhibit higher values than simulated layer matrix Sigmas particularly in layers XIII and XXIII. I attribute these differences to the presence of trace elements, such as gadolinium and titanium, with high capture cross sections that can significantly increase measured matrix Sigma log values. The matrix Sigma logs is therefore not included in the joint interpretation of spectroscopy and matrix-sensitive logs for the results shown in this chapter.

Results shown in Figure 5.19 indicate that matrix effects arising from the assumption of a limestone matrix mask the presence of hydrocarbons in the formation by suppressing neutron-density crossovers on measured porosity logs. I correct these matrix effects by replacing the assumed limestone matrix in neutron and density porosity logs with the estimated detailed mineralogy. The overlay between matrix-corrected layer neutron and density porosities, in Figure 5.19 (e), demonstrates the presence of hydrocarbons.

Estimated mineralogy, shown in Figure 5.17, does not resolve compositions within laminations because several layer thicknesses are below the vertical resolution of the spectroscopy tool such that I need to perform additional petrophysical interpretation to account for the laminations. The previous initial matrix inversion step is used to obtain $C_{end\ member\ 1}$: the mineral volumetric concentrations of calcite-cemented feldspathic siltstones which is required to estimate layer elemental weights within hydrocarbon-bearing argillaceous uncemented siltstone laminations, $(M_i)_{end\ member\ 2}$, using the spectroscopy mixing law given by equation 5.17. Layer elemental weight concentrations, M_i, are also required for this solution and are obtained using a spectroscopy interpretation method that corrects shoulder-bed averaging on elemental weight logs (Ajayi et al., 2014). Figure 5.20 shows results of the mixing law for layer elemental weight concentrations within hydrocarbon-bearing argillaceous uncemented siltstones. Results indicate that hydrocarbon-bearing argillaceous uncemented siltstone laminations do not include significant amounts of calcium (less than 0.05 weight fraction), which is consistent with the lack of calcite cementation observed in these laminations.

Figure 5.21 shows results of matrix compositions, calculated through layer matrix inversion of corrected elemental weight concentrations (the inversion algorithm implemented in

the calculation converges after two iterations in 0.03 seconds), and water saturations, computed using Poupon and Archie saturation models as described earlier. I observe that water saturations within laminations are less than total water saturations computed without accounting for laminations. This highlights the importance of implementing appropriate petrophysical interpretation methods in laminated formations to avoid bypassing hydrocarbon-bearing laminations.

5.6.2 Field Case No. 2

I examine a thinly-bedded shaly-sand formation penetrated by a highly-deviated well at an approximately 73-degree angle. The depth interval under study is 30.48-m MD and is located within the hydrocarbon-bearing section of the formation as shown in Figure 5.22. Nuclear, resistivity borehole images, and the construction of a Thomas-Stieber diagram indicate the presence of laminations within in the formation. The Thomas-Stieber diagram is shown in Figure 5.23 where total porosities are calculated from matrix-corrected neutron and density porosity logs (with equation 5.13) and C_{sh} is obtained from the gamma-ray log (with equation 5.18). Due to the presence of laminations in the formation, I implement the mixing law based petrophysical interpretation methods specifically adapted for laminated formations. Measured capture spectroscopy elemental logs include iron, silicon, sulfur, and aluminum and measured spectroscopy mineral logs are pyrite, QFM, and clay.

Initial estimations of mineralogy through conventional inversion methods consume 897.7 seconds of CPU time, when the Jacobian matrix is calculated numerically, or 75.2 seconds, when the Jacobian matrix is computer analytically, within ten iterations. I observe that solution convergence and stability is optimized when I assume a formation composition of illite, quartz,

pyrite, and K-feldspar. Similar to Field Case No. 1, a comparison is made between the measured log of the mineral group, QFM, and estimated layer quartz or K-feldspar, because I do not know the compositions of quartz or K-feldspar within measured QFM logs. I therefore cannot quantify corrections on measured QFM mineral logs by inverted quartz or K-feldspar layer values. Figure 5.24 shows results of estimated mineralogy wherein I observe largest reductions in shoulder-bed averaging on illite mineral logs up to 0.34 mineral volume fraction. There are also reductions of shoulder-bed averaging effects in pyrite but these corrections do not exceed 0.08 mineral volume fraction as pyrite is present in less than 0.018 mineral volume fraction in the formation.

Figure 5.25 shows the agreement between reconstructed and measured matrix-sensing logs. There are some discrepancies between reconstructed and measured matrix Sigma where measured matrix Sigma values are higher than simulated layer values particularly in layers XVI and XXIII. Similar to Field Case No. 1, I attribute these differences to the presence of trace elements, with high capture cross sections, in the formation such as gadolinium and titanium and therefore do not include matrix Sigma in the joint interpretation method for results shown in Figure 5.25 in this chapter. Figure 5.26 shows that matrix-corrected neutron and density porosities adjust the assumption of a limestone matrix in measured porosity logs and indicate the presence of hydrocarbon (by the crossover between matrix-corrected neutron and density porosities). This crossover was previously suppressed, particularly between X680-m to X688-m, due to matrix effects.

In order to resolve mineralogy within sand laminations, I use equation 5.17 where layer elemental weight concentrations that have been corrected for shoulder-bed averaging but not the effects of laminations, M_i, are obtained from spectroscopy weight logs through interpretation

methods advanced by Ajayi et al. (2014). The parameter $C_{end\ member\ 1}$ is interpreted as C_{sh} and is calculated from gamma-ray logs that have also been corrected for shoulder-bed averaging effects (Ijasan et al., 2013). Results shown in Figure 5.27 indicate the absence of iron and sulfur in the formation which suggests that the sandstone matrix does not include pyrite or illite. Mineralogy estimated through matrix inversion of corrected elemental weights (the inversion algorithm converges after three iterations in 0.04 seconds), shown in Figure 5.27, reveal that sand laminations indeed do not contain pyrite and illite but consist of only quartz and K-feldspar. If I do not employ petrophysical interpretation specifically adapted for laminated sands, averaging of water saturations between laminated hydrocarbon-bearing sands and water-saturated shales result in total water saturations that are higher than actual water saturations within hydrocarbon-bearing sand laminations as seen in Figure 5.28. I therefore observe that water saturations estimated within sand laminations, using Poupon and Archie shaly-sand saturation models, are less than total water saturations that do no not account for laminations.

5.7 DISCUSSION

The choice of minerals included in the initial guess for the estimation of mineral compositions should be as accurate as possible to avoid false representations of non-existing minerals. The inclusion of such non-existing minerals also tends to create an underdetermined estimation problem which increases the non-uniqueness of the solution. Core mineralogy data and geological studies are useful guides in determining the type of minerals present in the formation. Clay typing can also be performed using correlation charts of spectral gamma-ray logs, when such information is available, to improve the choice of the initial guess of minerals.

Minerals that are in very low concentrations may be excluded from the estimation if their existence in the solution decrease its stability and their estimation are not crucial to further petrophysical interpretation. This approach is validated by the fact that substantial reductions of shoulder-bed averaging effects cannot be observed in trace minerals because they are already present in low concentrations. However, minerals associated with trace elements such as gadolinium and titanium can significantly affect interpretation because they have high capture cross sections. It can therefore become necessary to include such minerals in the interpretation even though they may be present in very low concentrations.

I observe in field cases that the grouping of mineral logs in the LWD spectroscopy tool under study inhibits quantitative comparison between grouped mineral logs and individual estimated minerals. A practical alternative to benchmarking estimated mineralogy is through comparison with core mineral data, if available.

The solution of mineral volumetric concentrations in most of the synthetic and field cases studied concludes after ten inversion iterations which is the maximum cut-off imposed in the solution. However, in these cases, the solution actually converges typically after five iterations but continues up to ten iterations because the other cut-off criteria, where the norm of the error between numerically and MCNP-simulated logs must fall below 0.001, is not met. This behavior is due to the presence of noise in MCNP-simulated and field logs. Nevertheless, in synthetic cases, I observe good agreement between model and estimated mineral concentrations and, in all cases, there is a good match between reconstructed and lithology-sensing nuclear logs.

The inclusion of lithology-sensing nuclear logs, such as gamma ray, matrix PEF, matrix density, and matrix Sigma, in joint mineral interpretation enables the quantification of minerals

with no associated elements present in measured logs such as kerogen in gas-bearing shales when inelastic carbon logs are not available. This approach is an important consideration for the LWD spectroscopy tool because it only acquires logs in the capture measurement mode. Due to the difference in volume of investigation and elemental sensitivity between inelastic and capture measurement modes, it may be preferable to use inelastic over capture measured data in logging tools that acquire inelastic data.

Spurious effects on measured logs can affect the stability and convergence of the solution of formation mineralogy. Such effects include barite in drilling mud that can decrease gamma-ray log values and the sulfur content in elemental spectroscopy logs. Iron in the tool housing or steel casing, in cased wells, can also falsely increase spectroscopy iron log values. In the joint interpretation of spectroscopy and lithology-sensing logs, it is therefore important to perform extensive quality control on measured logs to ensure that they are indicative of formation matrix properties alone.

Petrophysical interpretation methods should be implemented with caution in low porosity gas-bearing shales due to the difficulty in resolving total porosities in these formation types. Such erroneous values of porosity will invariably propagate into water saturation calculations using any saturation model. Core porosity and saturation data can be used to validate estimated porosities and water saturations where such information is present.

Additional petrophysical interpretation methods that account for laminations in thinly-bedded formations can prevent the bypassing of thin hydrocarbon-bearing layers whereas conventional interpretation methods tend to underestimate porosity and hydrocarbon saturation. Errors in conventional calculations typically occur due to the averaging of petrophysical

properties of several thin high porosity hydrocarbon and low porosity water bearing layers. Petrophysical interpretation of thin beds is practical in the LWD spectroscopy tool because the tool has the capability to log horizontal wells thereby increasing the exposure of thin beds which maximizes hydrocarbon production potential.

5.8 CONCLUSION

Developed interpretation methods quantify formation mineralogy, porosity, and water saturation in a wide range of well trajectories, formation lithologies, and laminated formations. Interpretation includes the use of matrix inversion methods to quantify detailed layer mineral compositions through the use of spatial flux sensitivity functions, FSFs, in inelastic and capture measurement modes. This results in the elimination of shoulder-bed averaging effects on measured mineral logs. However, it is important to note that the estimation method assumes fixed elemental and mineral chemical properties which may vary considerably from one formation to another. This assumption can be adapted such that mineral chemical properties are more representative of a specific geological region through benchmarking of mineral properties with available measured core elemental and mineral data.

Matrix effects, due to the assumption of an inaccurate matrix, in the acquisition of neutron and density porosity logs, commonly mask the presence of hydrocarbons in the formation by suppressing neutron-density crossovers. Detailed mineral quantification allows for matrix correction on porosity logs which enables the diagnosis of fluid types and saturations in the formation. Low porosity formations can cause a low effective volume of hydrocarbon which can still suppress the extent of a neutron-density crossover in hydrocarbon-bearing formations even after correction of matrix effects on porosity logs.

In order to resolve petrophysical properties within laminations, I introduce an adapted petrophysical workflow based on a spectroscopy mixing law and a laminated shaly-sand model. The methods assume that elemental, nuclear, and resistivity properties are known within a pure shale section and do not vary within the section under study. Results from this application indicate that laminated analysis is essential to accurately quantify petrophysical properties within hydrocarbon-bearing laminations.

Table 5.1: Calculated elemental inelastic and capture sensitivities. Hyphens indicate negligible values.

Element Name	Element Formula	Calculated Inelastic Sensitivity	Calculated Capture Sensitivity
Aluminum	Al	1.08	1.21
Carbon	C	0.60	-
Calcium	Ca	0.76	1.65
Chlorine	Cl	-	104.93
Iron	Fe	0.72	6.48
Gadolinium	Gd	-	28,364
Hydrogen	H	-	13.10
Potassium	K	0.51	6.03
Magnesium	Mg	0.77	0.40
Oxygen	O	0.75	-
Sulfur	S	0.77	2.54
Silicon	Si	1	1
Titanium	Ti	0.84	17.98

Table 5.2: Elemental and mineral properties assumed in the synthetic and field cases examined in this chapter.

Element Name	Element Symbol	Molecular Weight (g/gmol)		Mineral Name	Mineral Formula	Molecular Weight (g/gmol)	Mineral Density (g/cm^3)	Gamma-ray Constants			PEF (b/e)	Sigma (c.u.)	HI
								Th (ppm)	*U* (ppm)	*K* (%)			
Aluminum	Al	26.98		**Quartz**	SiO_2	60.09	2.65	0	0.1	0	1.806	4.551	0
Carbon	C	12.01		**Dolomite**	$CaMg(CO_3)_2$	184.41	2.87	0	0.9	0.1	3.142	4.697	0
Calcium	Ca	40.08		**Albite**	$NaAlSi_3O_8$	262.24	2.62	0	0	0.5	2.86	4.551	0
Iron	Fe	55.85		**Calcite**	$CaCO_3$	100.09	2.71	0	1.4	0	5.084	7.078	0
Potassium	K	39.1		**Pyrite**	FeS_2	119.97	5.01	0	10	0	16.97	90.525	0
Magnesium	Mg	24.31		**Illite**	$K_{0.8}Al_{1.6}Fe_{0.2}Mg_{0.2}Si_{3.4}Al_{0.6}O_{10}O_2H_2$	396.19	2.78	12	4.8	4.5	3.03	16.735	0.127
Sulfur	S	32.06		**Montmorillonite**	$Na_{0.33}Al_{1.67}Mg_{0.33}Si_4O_{10}O_2H_2$	367.01	2.63	19	3.5	0.16	1.806	4.551	0.129
Silicon	Si	28.09		**Mg-Chlorite**	$Mg_5AlSi_3AlO_{10}O_8H_8$	555.82	2.65	16	4.2	0.9	1.39	11.337	0.344
				Fe-Chlorite	$Fe_5AlSi_3AlO_{10}O_8H_8$	713.544	3.42	16	4.2	0.9	12.36	47.435	0.346
				Kaolinite	$Al_2Si_2O_5O_4H_4$	184.41	2.62	19	3.2	0.1	1.49	13.039	0.366
				K-Feldspar	$KAlSi_3O_8$	278.35	2.57	1.1	0.4	10.2	1.68	15.821	
				Kerogen	$C_{102}H_{94}O_{17}$	1591.9	1.4	0	200	0	1.49	13.039	0.746
				Hydrocarbon-Oil	C_8H_{18}	114.23	0.82						0.954
				Hydrocarbon-Gas	CH_4	16.04	0.178						0.401
				Water	H_2O	18.02	1						1.002

Table 5.3: Layer true stratigraphic thickness (TST), migration lengths, bulk densities, element, mineral, and fluid compositions, assumed in Synthetic Case No. 1.

Layer	Layer TST (cm)	L_m (cm)	ρ_{bulk} (g/cc)	Volumetric Concentrations (%)				Formation Solid Elemental Weight Concentrations (%)		
				Solids		Fluids				
				Quartz	Dolomite	Hydrocarbon-Oil	Water	Magnesium	Silicon	Calcium
I	91.44	16.25	2.23	65	10	15	10	1.7	36.07	2.79
II	30.48	14.51	2.26	10	60	15	15	10.05	5.48	16.56
III	60.96	15.33	2.34	20	55	10	15	8.89	10.59	14.66
IV	91.44	21.12	2.5	80	10	3	7	1.51	39.62	2.49
V	30.48	17.07	2.57	70	15	3	12	11.77	2.47	19.39
VI	60.96	15.12	2.38	10	65	2.5	22.5	10.35	5.21	17.06
VII	91.44	17.06	2.36	60	20	0	20	3.2	31.44	5.28

Table 5.4: Layer true stratigraphic thickness (TST), migration lengths, bulk densities, mineral, and fluid compositions assumed in Synthetic Case No. 2.

Layer	Layer TST (cm)	L_m (cm)	ρ_{bulk} (g/cc)	Volumetric Concentrations (%)								
				Solids							Fluids	
				Quartz	Albite	Calcite	Pyrite	Kerogen	Illite	Mg-Chlorite	Hydrocarbon-Oil	Water
I	91.44	19.59	2.52	7.72	2.14	66.69	1.21	4.09	9.14	2.02	4.76	2.23
II	24.38	20.51	2.52	6.26	1.59	73.04	0.65	3.64	6.9	1.32	5.01	1.59
III	91.44	19.03	2.51	7.01	2.62	66.61	1.49	6.45	8.17	1.08	4.67	1.91
IV	30.48	19.21	2.54	10.17	3.96	61.05	1.32	5.46	11.1	1.15	3.53	2.26
V	91.44	18.93	2.51	11.93	4.94	59.85	1.21	5.87	8.47	0.94	3.49	3.49
VI	21.34	23.38	2.61	37.83	3.96	47.67	0.77	1.06	1.54	3.67	1.91	1.59
VII	91.44	23.15	2.58	10.78	2.65	76.97	0.76	1.13	1.3	0.96	4.13	1.31
VIII	30.48	24.13	2.59	14	1.81	75.99	0.38	0.57	1.1	1.37	3.8	0. 98
IX	91.44	23.71	2.59	7.25	1.62	82.9	0.29	1.14	1.54	0.66	3.62	0.98

Table 5.5: Layer elemental compositions assumed in Synthetic Case No. 2.

Layer	Formation Solid Elemental Weight Concentrations (%)									
	Formation carbon	**Kerogen carbon**	**Sodium**	**Sulfur**	**Magnesium**	**Aluminum**	**Silicon**	**Potassium**	**Calcium**	**Iron**
I	10.43	0.48	0.14	0.15	0.17	0.48	4.50	0.13	34.81	0.30
II	9.57	0.24	0.16	0.20	0.32	0.50	7.80	0.09	31.92	0.38
III	9.75	0.48	0.24	0.39	0.24	0.59	6.56	0.11	32.54	0.73
IV	5.96	0.44	0.35	0.40	0.84	1.02	20.26	0.13	19.89	0.74
V	7.80	2.54	0.46	0.65	0.33	2.05	10.02	0.75	26.04	1.40
VI	7.88	2.34	0.36	0.70	0.41	2.37	9.46	0.97	26.28	1.57
VII	8.71	2.79	0.24	0.80	0.36	1.76	6.75	0.72	29.06	1.66
VIII	9.45	1.56	0.15	0.35	0.40	1.45	5.67	0.60	31.54	0.82
IX	8.65	1.76	0.20	0.65	0.59	1.96	7.30	0.80	28.86	1.41

Table 5.6: Layer true stratigraphic thickness (TST), migration lengths, bulk densities, mineral, and fluid compositions assumed in Synthetic Case No. 3.

Layer	Layer TST (cm)	L_m (cm)	ρ_{bulk} (g/cc)	Volumetric Concentrations (%)					
				Solids				Fluids	
				Calcite	Illite	Kaolinite	Quartz	Hydrocarbon-Oil	Water
I	52.93	18.17	2.69	38	40	10	10	0	2
II	30.48	12.44	2.1	5	5	54	6	29	1
III	15.24	14.15	2.5	30	10	45	5	5	5
IV	30.48	18.17	2.69	38	40	10	10	0	2
V	15.24	12.44	2.1	5	5	54	6	29	1
VI	30.48	14.15	2.5	30	10	45	5	5	5
VII	15.24	18.17	2.69	38	40	10	10	0	2
VIII	30.48	12.44	2.1	5	5	54	6	29	1
IX	15.24	14.15	2.5	30	10	45	5	5	5
X	30.48	18.17	2.69	38	40	10	10	0	2
XI	15.24	12.44	2.1	5	5	54	6	29	1
XII	30.48	14.15	2.5	30	10	45	5	5	5
XIII	52.93	18.17	2.69	38	40	10	10	0	2

Table 5.7: Layer elemental compositions assumed in Synthetic Case No. 3.

Layer	Formation Solid Elemental Weight Concentrations (%)					
	Magnesium	**Aluminum**	**Silicon**	**Potassium**	**Calcium**	**Iron**
I	0.51	8.23	16.69	3.26	15.33	1.17
II	0.14	11.54	15.45	0.88	13.04	0.31
III	0.08	15.1	19.83	0.52	02.59	0.19
IV	0.51	8.23	16.69	3.26	15.33	1.17
V	0.14	11.54	15.45	0.88	13.04	0.31
VI	0.08	15.1	19.83	0.52	2.59	0.19
VII	0.51	8.23	16.69	3.26	15.33	1.17
VIII	0.14	11.54	15.45	0.88	13.04	0.31
IX	0.08	15.1	19.83	0.52	2.59	0.19
X	0.51	8.23	16.69	3.26	15.33	1.17
XI	0.14	11.54	15.45	0.88	13.04	0.31
XII	0.08	15.1	19.83	0.52	2.59	0.19
XIII	0.51	8.23	16.69	3.26	15.33	1.17

Table 5.8: Layer true stratigraphic thickness (TST), migration lengths, bulk densities, volumetric composition of shale, mineral, and fluid compositions assumed in Synthetic Case No. 4.

Layer		Layer TST (cm)	L_m (cm)	ρ_{bulk} (g/cc)	Volumetric Concentrations (%)								ϕ_t (p.u.)	C_{sh} (volume fraction)
					Solids						Fluids			
					Mg-Chlorite	Illite	K-Feldspar	Quartz	Pyrite	Dolomite	Hydro Carbon-Oil	Water		
I		91.44	16.98	2.34	0	0	6.88	68.82	1.72	2.58	12	8	0.20	0
II	IIA	6.1	14.86	2.55	20	53	8	9	0	0	0	10	0.1855	0.43
	IIB	9.14	15.78	2.27	0	0	12.1	56.45	2.42	4.03	12.5	12.5		
	IIC	6.1	14.86	2.55	20	53	8	9	0	0	0	10		
	IID	9.14	15.78	2.27	0	0	12.1	56.45	2.42	4.03	12.5	12.5		
III		91.44	14.86	2.55	20	53	8	9	0	0	0	10	10	1
IV	IVA	6.1	16.45	2.32	0	0	5.14	64.29	1.71	6.86	8.8	13.2	0.1516	0.57
	IVB	9.14	14.86	2.55	20	53	8	9	0	0	0	10		
	IVC	6.1	16.45	2.32	0	0	5.14	64.29	1.71	6.86	8.8	13.2		
	IVD	9.14	14.86	2.55	20	53	8	9	0	0	0	10		
V		91.44	15.04	2.2	0	0	10	50	2	8	9	21	0.30	0

Table 5.9: Layer elemental compositions assumed in Synthetic Case No. 4.

Layer		Formation Solid Elemental Weight Concentrations (%)						
		Magnesium	**Aluminum**	**Silicon**	**Sulfur**	**Potassium**	**Calcium**	**Iron**
I		0.42	0.73	38.73	1.97	1.06	0.69	1.72
II	**IIA**	5.26	11.47	23.92	0	5.7	0	1.63
	IIB	0.67	1.34	34.93	2.85	1.92	1.11	2.48
	IIC	5.26	11.47	23.92	0	5.7	0	1.63
	IID	0.67	1.33	34.93	2.85	1.92	1.11	2.48
III		5.26	11.47	23.92	0	5.7	0	1.63
IV	**IVA**	1.12	0.55	36.01	1.98	0.8	1.84	1.72
	IVB	5.26	11.47	23.92	0	5.7	0	1.63
	IVC	1.12	0.55	36.01	1.98	0.8	1.84	1.72
	IVD	5.26	11.47	23.92	0	5.7	0	1.63
V		1.38	1.13	31.75	2.44	1.64	2.27	2.12

Table 5.10: Petrophysical parameters assumed in field cases.

***a* (Archie's Winsauer constant)**			1
***m* (Archie's Porosity Exponent)**			1.5
***n* (Archie's Saturation Exponent)**			2
***α* (Gamma-ray Coefficient)**			3.8
***β* (Gamma-ray Coefficient)**			8.2
***γ* (Gamma-ray Coefficient)**			16.5
Field Case No. 1			**Field Case No. 2**
C_w (NaCl ppm)	160, 000		140, 000
R_{sh} (Ω-m)	0.3614		3.8
ϕ_{sh} (p.u.)	8.27		8.76

Table 5.11: Layer true stratigraphic thickness (TST) assumed in field cases examined in this chapter.

Layer	Field Case No. 1 Bed Thickness (cm)		Field Case No. 2 Bed Thickness (cm)
I	9.02		17.87
II	56.01		35.73
III	32.52		17.87
IV	107.12		26.8
V	39.33		17.87
VI	37.18		17.87
VII	22.14		17.87
VIII	79.914		17.87
IX	33.54		26.8
X	34.2		17.87
XI	37.21		13.4
XII	60.29		17.87
XIII	37.87		17.87
XIV	63.74		40.2
XV	50.23		26.8
XVI	33.6		17.87
XVII	44.96		17.87
XVIII	48.52		17.87
XIX	28.74		17.87
XX	70.95		45.94
XXI	25.16		55.67
XXII	32.08		44.19
XXIII	40.51		51.03
XXIV	48.05		74.74
XXV	80.02		100.35
XXVI	36.1		65.48
XXVII	7.5		53.93

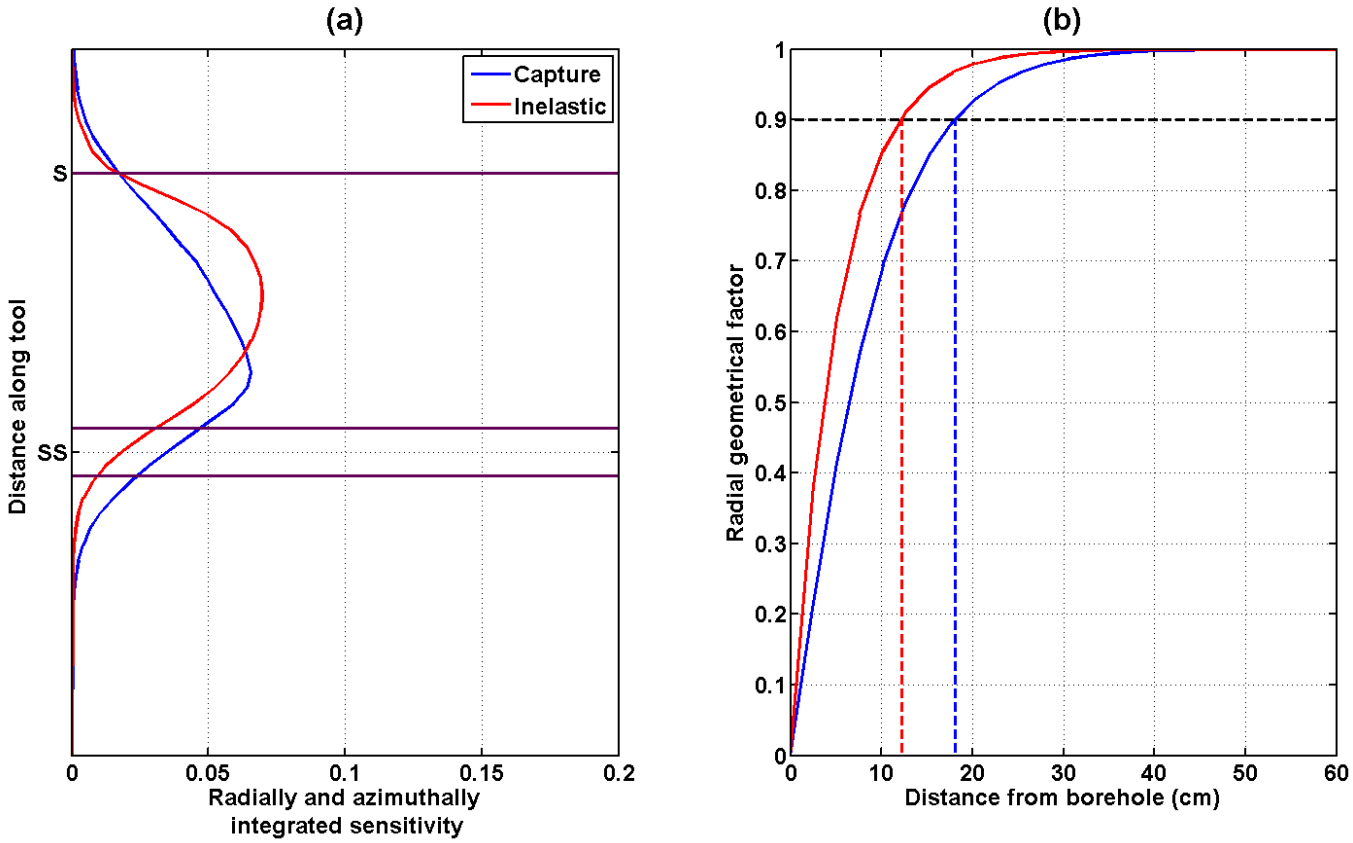

Figure 5.1: Comparison of (a) vertical resolution and (b) radial length of investigation between inelastic and capture measurements in a 25 p.u. freshwater-saturated sandstone formation. Panel (a) shows radially and azimuthally integrated inelastic and capture neutron FSFs along the tool, where purple lines at S and SS identify the pulsed-neutron source and short-spaced detector positions along the tool, respectively; panel (b) shows the cumulative vertically integrated FSF (radial geometrical factor). The depth of investigation of the tool is defined by 90% of the radial geometrical factor and is shown in panel (b) as dashed blue and red lines for capture and inelastic measurements, respectively. Note: the vertical axis on panel (a) is not shown because the location of the neutron source and short-spaced gamma-ray detector of the commercial tool under study are confidential.

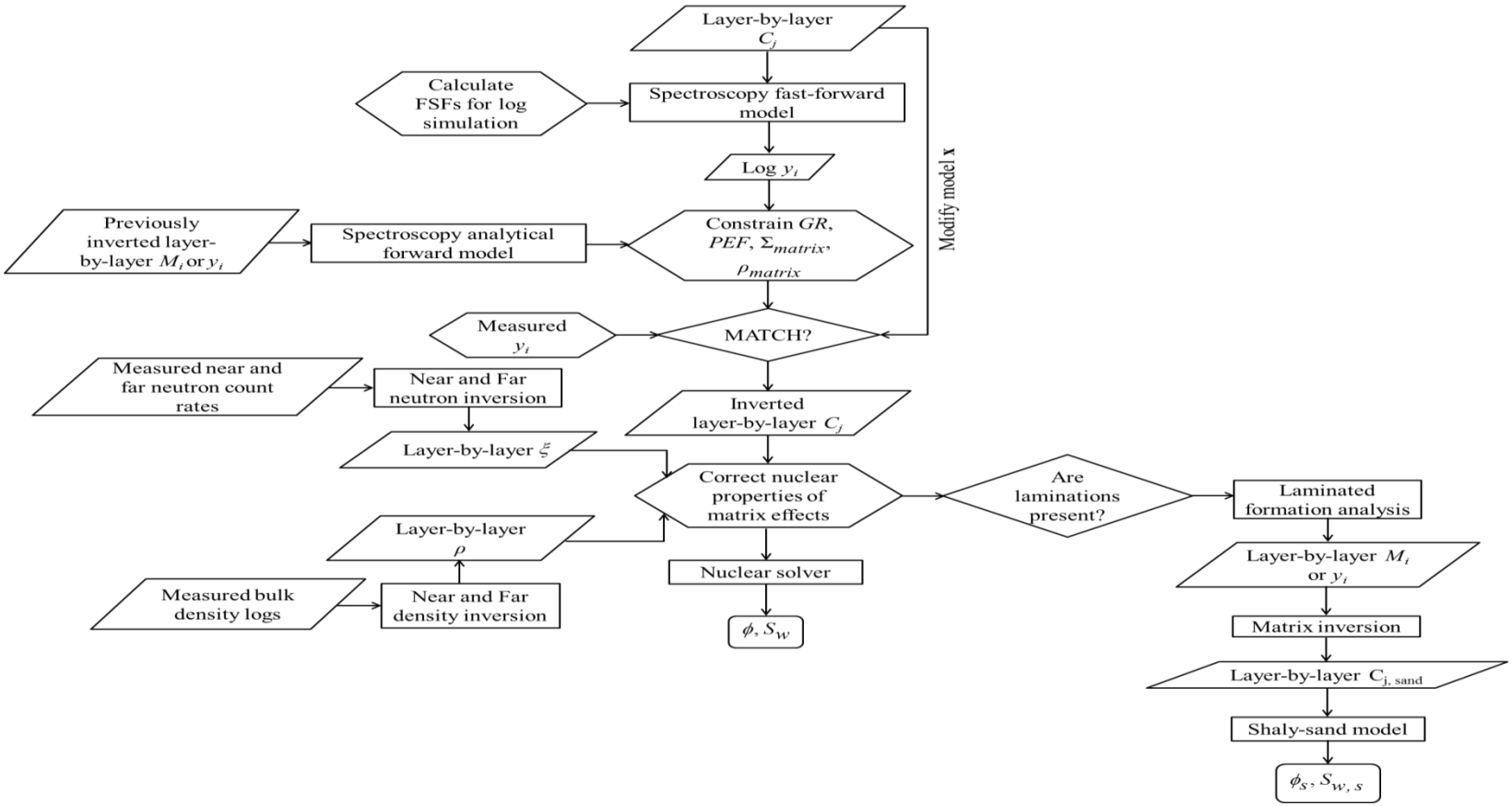

Figure 5.2: Workflow implemented in the estimation of layer mineral concentrations and subsequent petrophysical interpretation. The parameters ρ, ϕ, S_w, ϕ_s, $S_{w,s}$, M_i, y_i, C_j, , **x**, and ξ represent layer bulk density, total porosity, total water saturation, sand porosity, sand water saturation, elemental weight concentration, elemental relative yield, mineral volumetric concentration, a vector of layer mineral volumetric concentrations, and the inverse of layer migration length, respectively. Symbols GR, PEF, ρ_{matrix}, and Σ_{matrix} are gamma ray, photoelectric factor, matrix density, and matrix Sigma layer values, respectively.

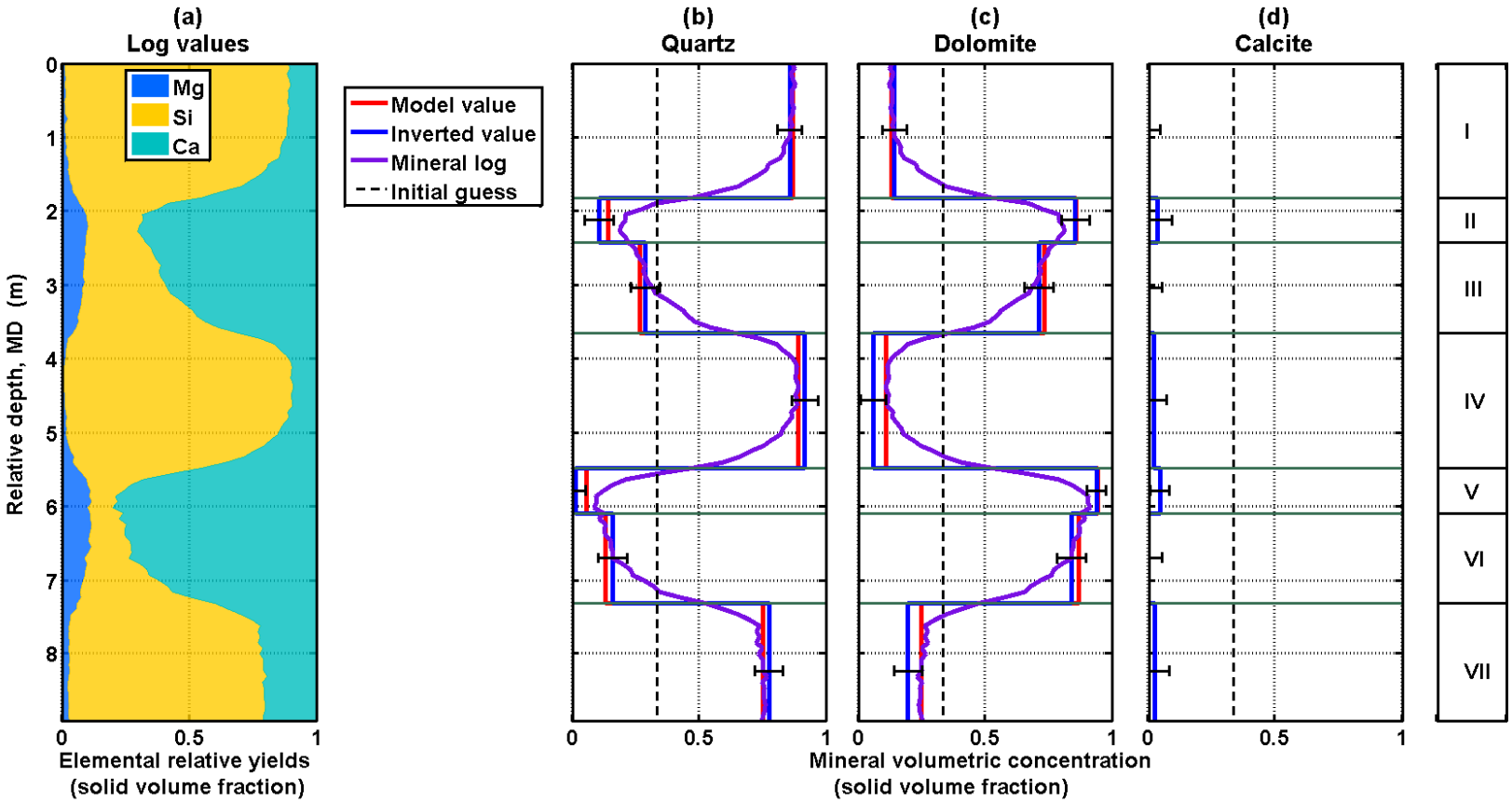

Figure 5.3: Panel (a) displays a cumulative plot of MCNP-simulated capture elemental relative yields for Synthetic Case No. 1(a); panels (b) to (d) exhibit inverted layer mineral volumetric concentrations (blue solid lines), model layer mineral volumetric concentrations (shown as red solid lines), and mineral logs (shown as purple solid lines). Black dashed lines and black uncertainty bars describe the initial guess of the inversion and the 95% confidence interval, respectively; Mg, Si, and Ca are the elements magnesium, silicon, and calcium, respectively, while I to VII identify distinct layers in the synthetic case.

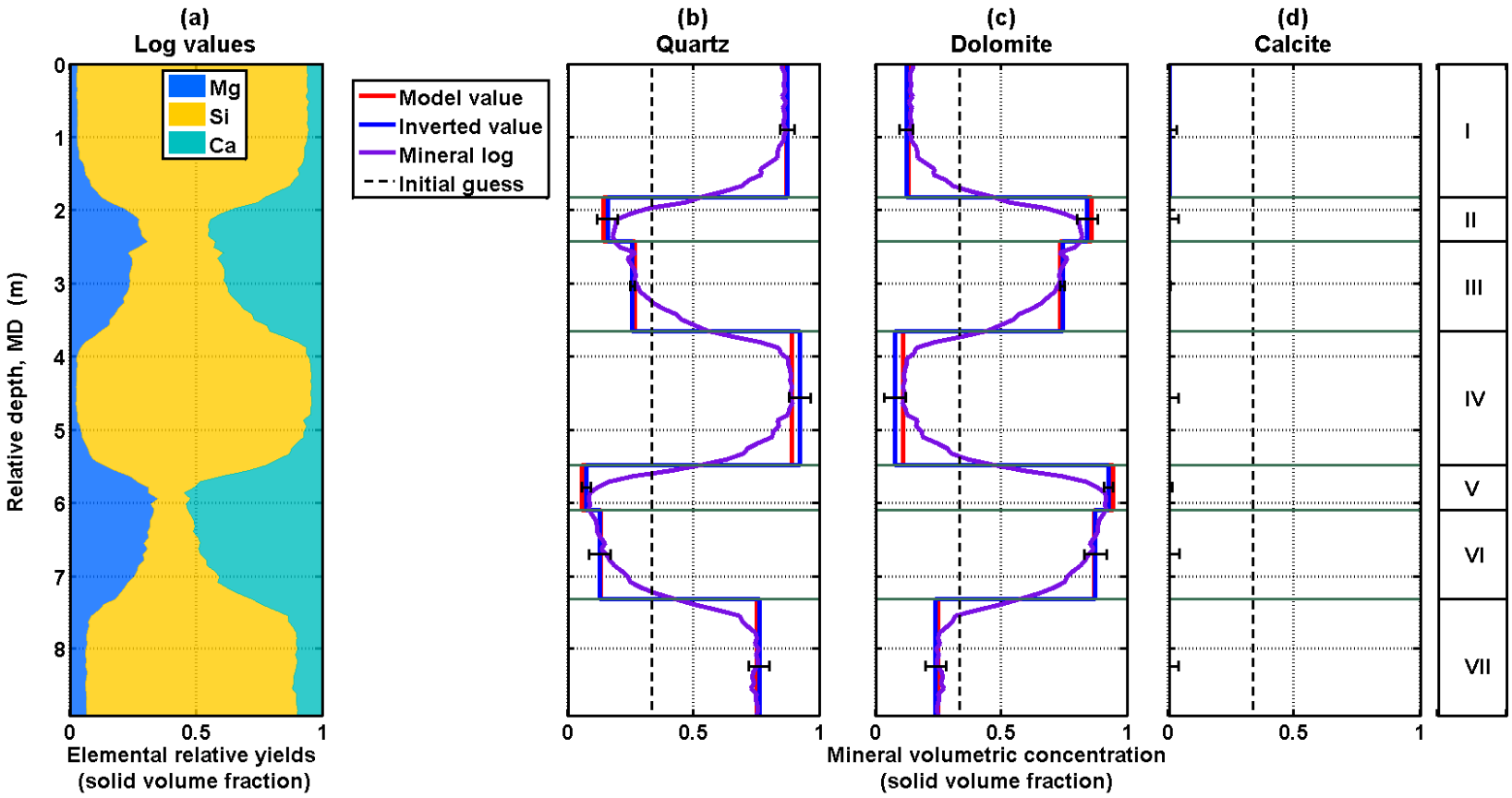

Figure 5.4: Panel (a) displays a cumulative plot of MCNP-simulated inelastic elemental relative yields for Synthetic Case No. 1(b); panels (b) to (d) exhibit inverted layer mineral volumetric concentrations (shown as blue solid lines), model layer mineral volumetric concentrations (shown as red solid lines), and mineral logs (shown as purple solid lines). Black dashed lines and black uncertainty bars describe the initial guess of the inversion and the 95% confidence interval, respectively; Mg, Si, and Ca are the elements magnesium, silicon, and calcium, respectively, while I to VII identify distinct layers in the synthetic case.

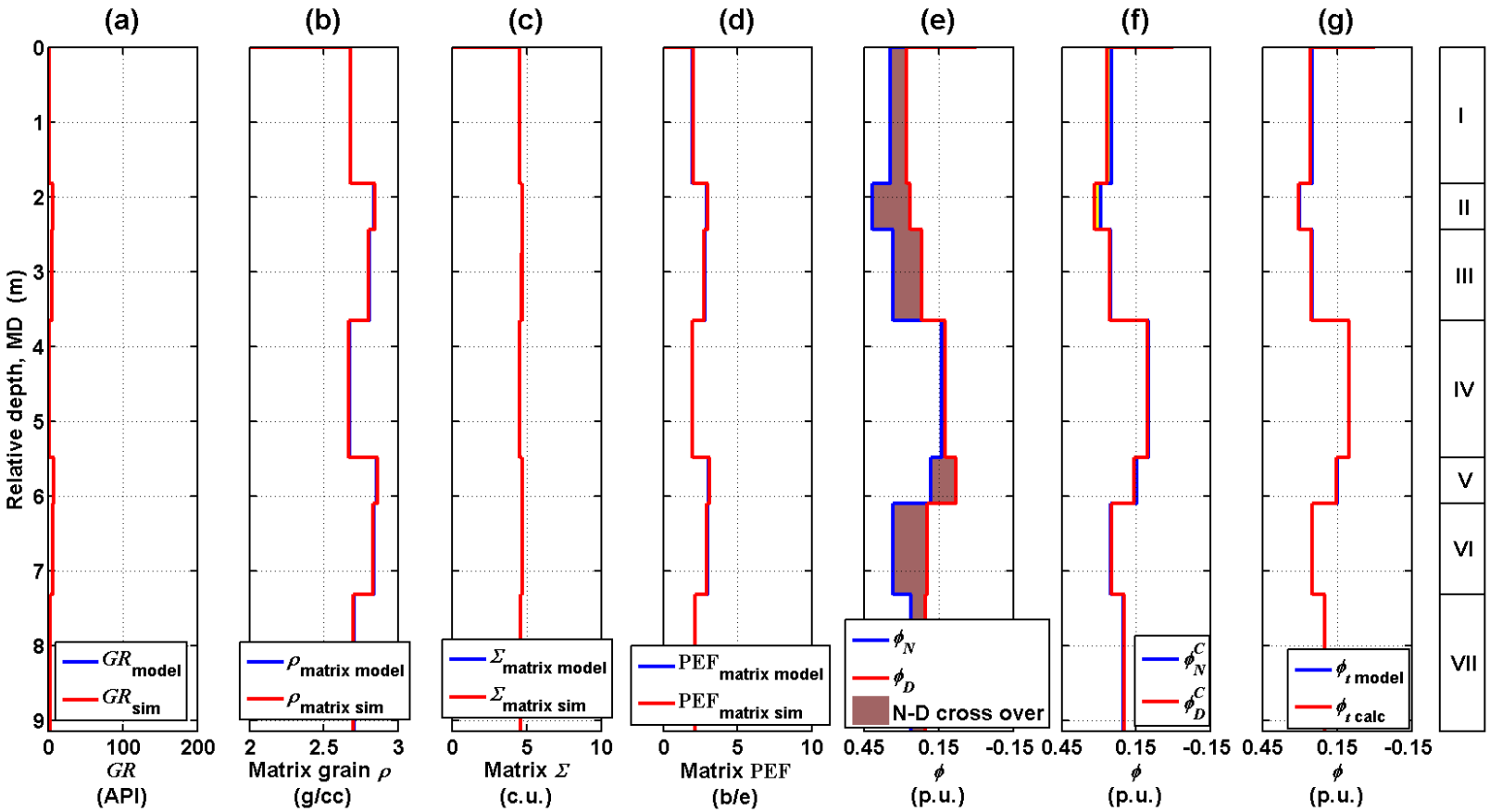

Figure 5.5 Panel (a) displays the comparison between model and simulated gamma ray, panel (b) exhibits the comparison between model and simulated matrix density, panel (c) shows the comparison between model and simulated matrix Sigma, and panel (d) displays the comparison between model and simulated matrix PEF. Model values are shown as blue solid lines and simulated values are shown as red solid lines. Panel (e) shows neutron-density crossover, panel (f) shows matrix-corrected neutron-density crossover, and panel (g) shows comparison between model (blue solid line) and calculated (red solid line) total porosity for Synthetic Case No. 1(b). I to VII identify distinct layers in the synthetic case.

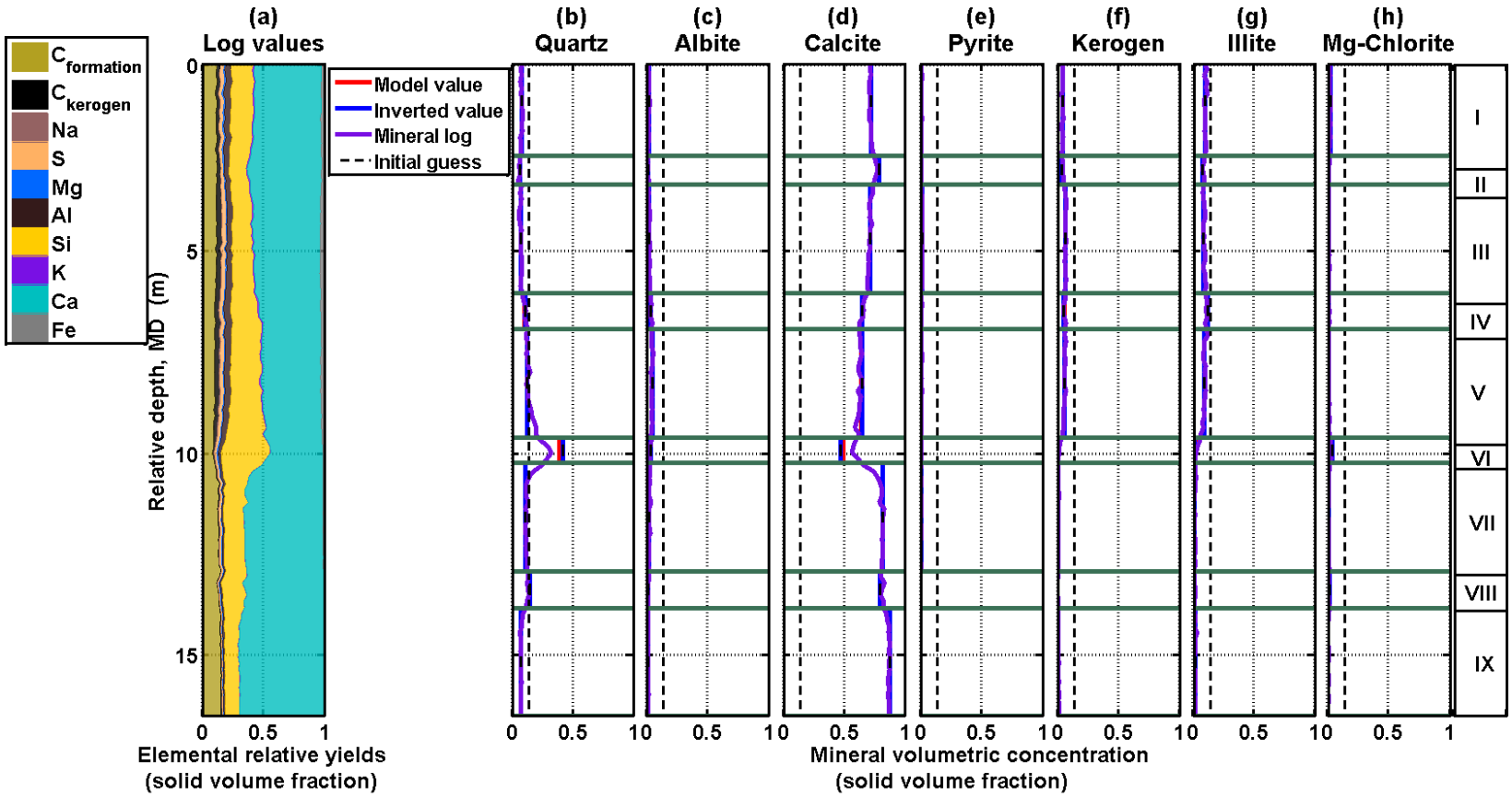

Figure 5.6: Panel (a) displays a cumulative plot of MCNP-simulated inelastic elemental relative yields for Synthetic Case No. 2; panels (b) to (h) show inverted layer mineral volumetric concentrations (shown as blue solid lines), model layer mineral volumetric concentrations (shown as red solid lines), and mineral logs (shown as purple solid lines). Black dashed lines and black uncertainty bars describe the initial guess of the inversion and the 95% confidence interval, respectively; $C_{formation}$, $C_{kerogen}$, Na, S, Mg, Al, Si, K, Ca, and Fe represent carbon present in the formation, carbon present in kerogen, sodium, sulfur, magnesium, aluminum, silicon, potassium, calcium, and iron, respectively, while I to IX identify distinct layers in the synthetic case.

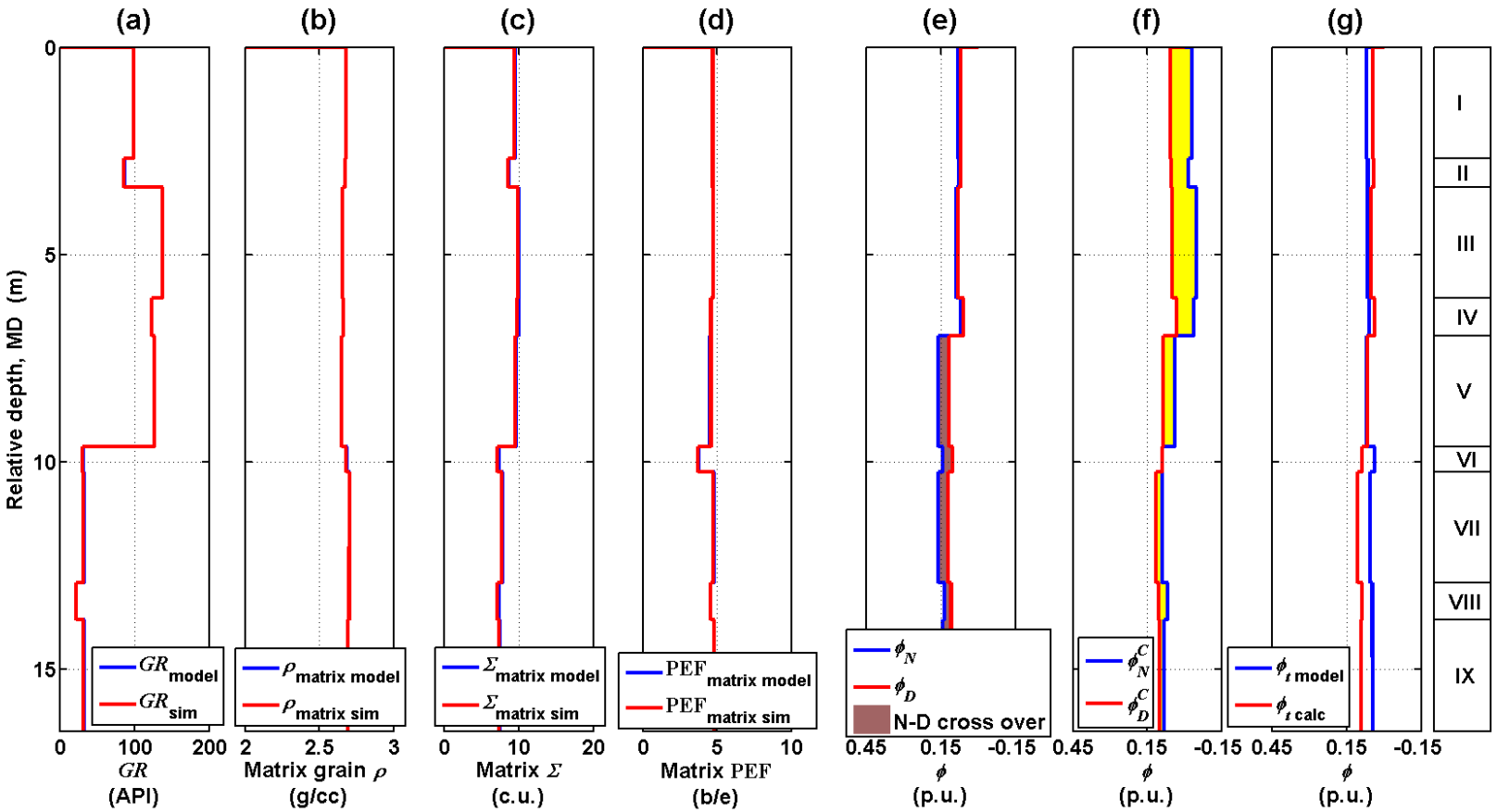

Figure 5.7: Panel (a) shows the comparison between model and simulated gamma ray, panel (b) displays the comparison between model and simulated matrix density, panel (c) exhibits the comparison between model and simulated matrix Sigma, panel (d) shows the comparison between model and simulated matrix PEF. Model values are shown as blue solid lines and simulated values are indicated by red solid lines. Panel (e) shows neutron-density crossover, panel (f) describes matrix-corrected neutron-density crossover, and panel (g) describes the comparison between model (blue solid line) and calculated (red solid line) total porosity for Synthetic Case No. 2. I to IX identify distinct layers in the synthetic case.

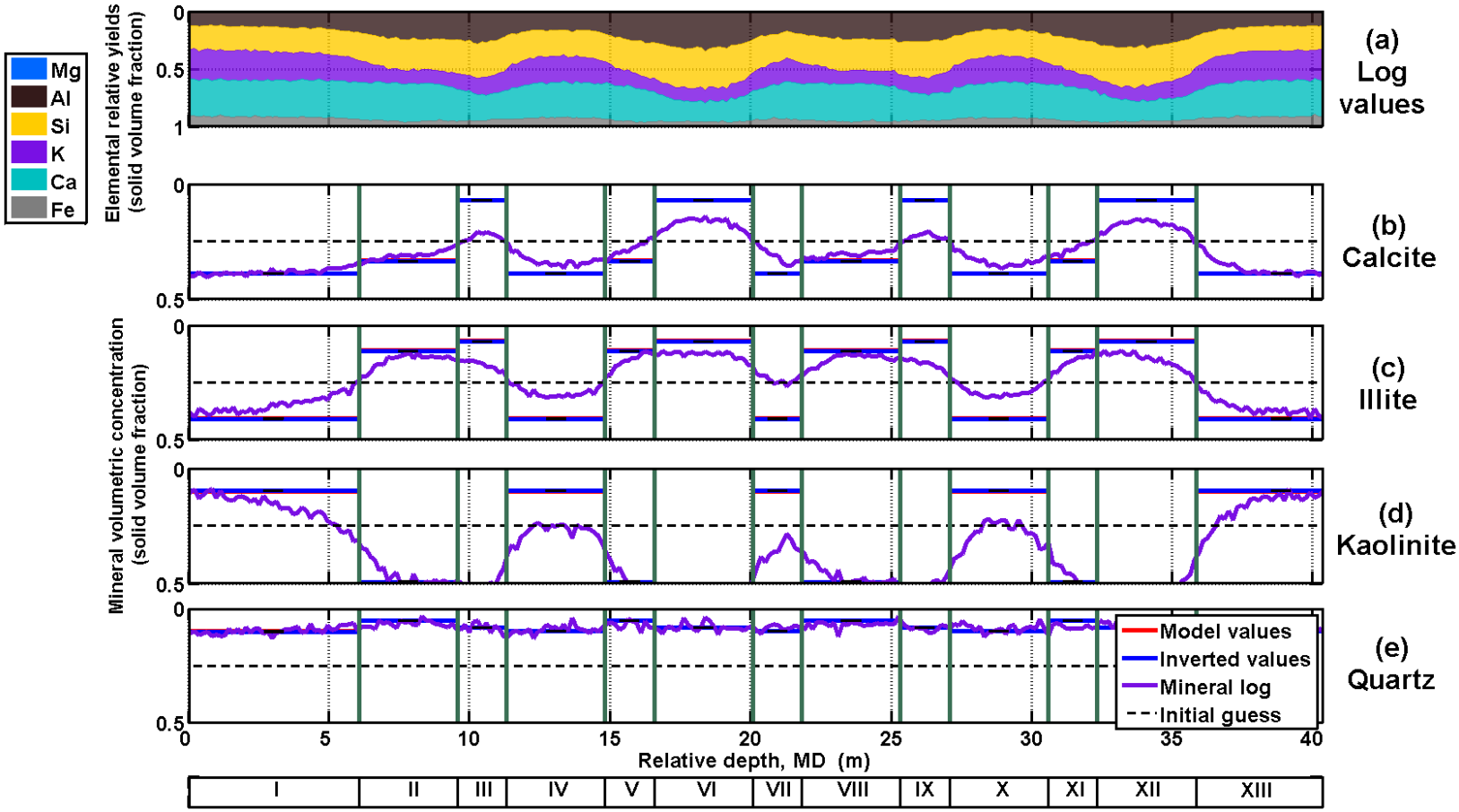

Figure 5.8: Panel (a) displays a cumulative plot of MCNP-simulated capture element relative yields for Synthetic Case No. 3; panels (b) to (e) display inverted layer mineral volumetric concentrations (shown as blue solid lines), model layer mineral volumetric concentrations (shown as red solid lines), and mineral logs (shown as purple solid lines). Black dashed lines and black uncertainty bars describe the initial guess of the inversion and the 95% confidence interval, respectively. Mg, Al, Si, K, Ca, and Fe are elements magnesium, aluminum, silicon, potassium, calcium, and iron, respectively; I to XIII identify distinct layers in the synthetic case.

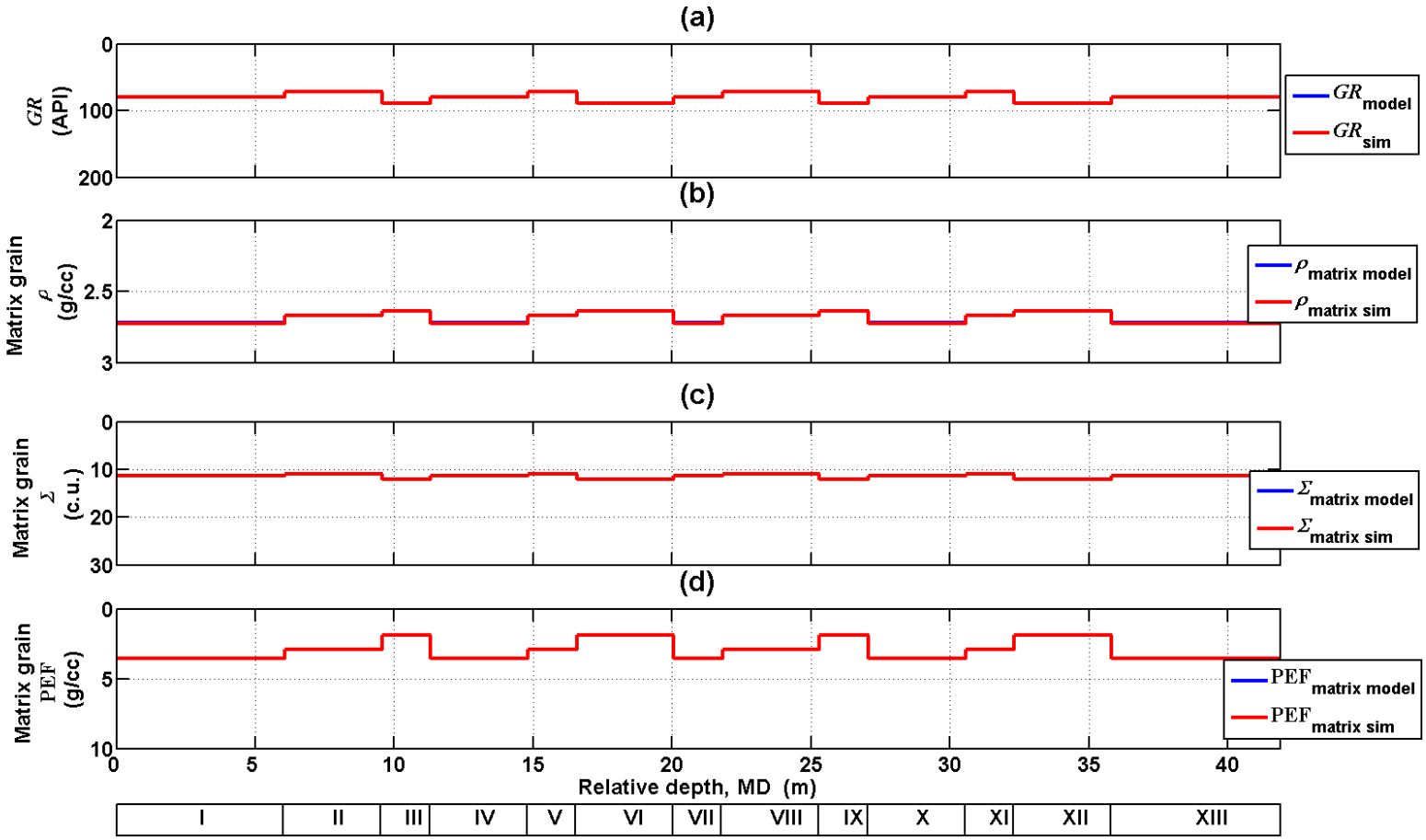

Figure 5.9: Panel (a) shows comparison between model and simulated gamma ray, panel (b) shows comparison between model and calculated matrix density, panel (c) shows comparison between model and simulated matrix Sigma, and panel (d) shows comparison between model and simulated matrix PEF for Synthetic Case No. 3. Model values are shown as solid blue lines and simulated values are shown as solid red lines. I to XIII identify distinct layers in the synthetic case.

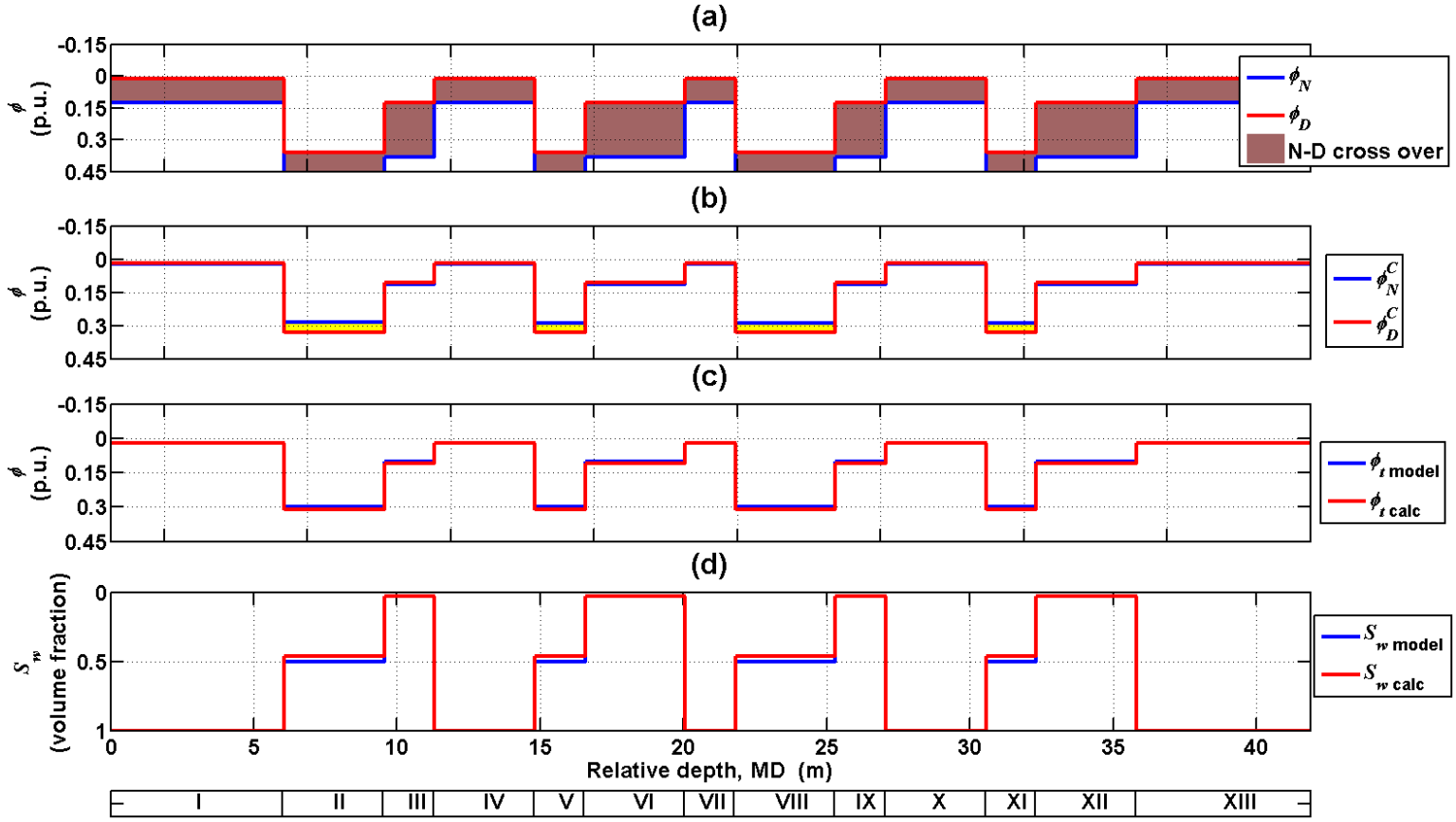

Figure 5.10: Panel (a) shows neutron-density crossover, panel (b) shows matrix-corrected neutron density, panel (c) shows comparison between model (shown as solid blue lines) and calculated total porosity (shown as solid red lines), and panel (d) shows comparison between model (shown as solid blue lines) and calculated water saturation (shown as solid red lines) for Synthetic Case No. 3. I to XIII identify distinct layers in the synthetic case.

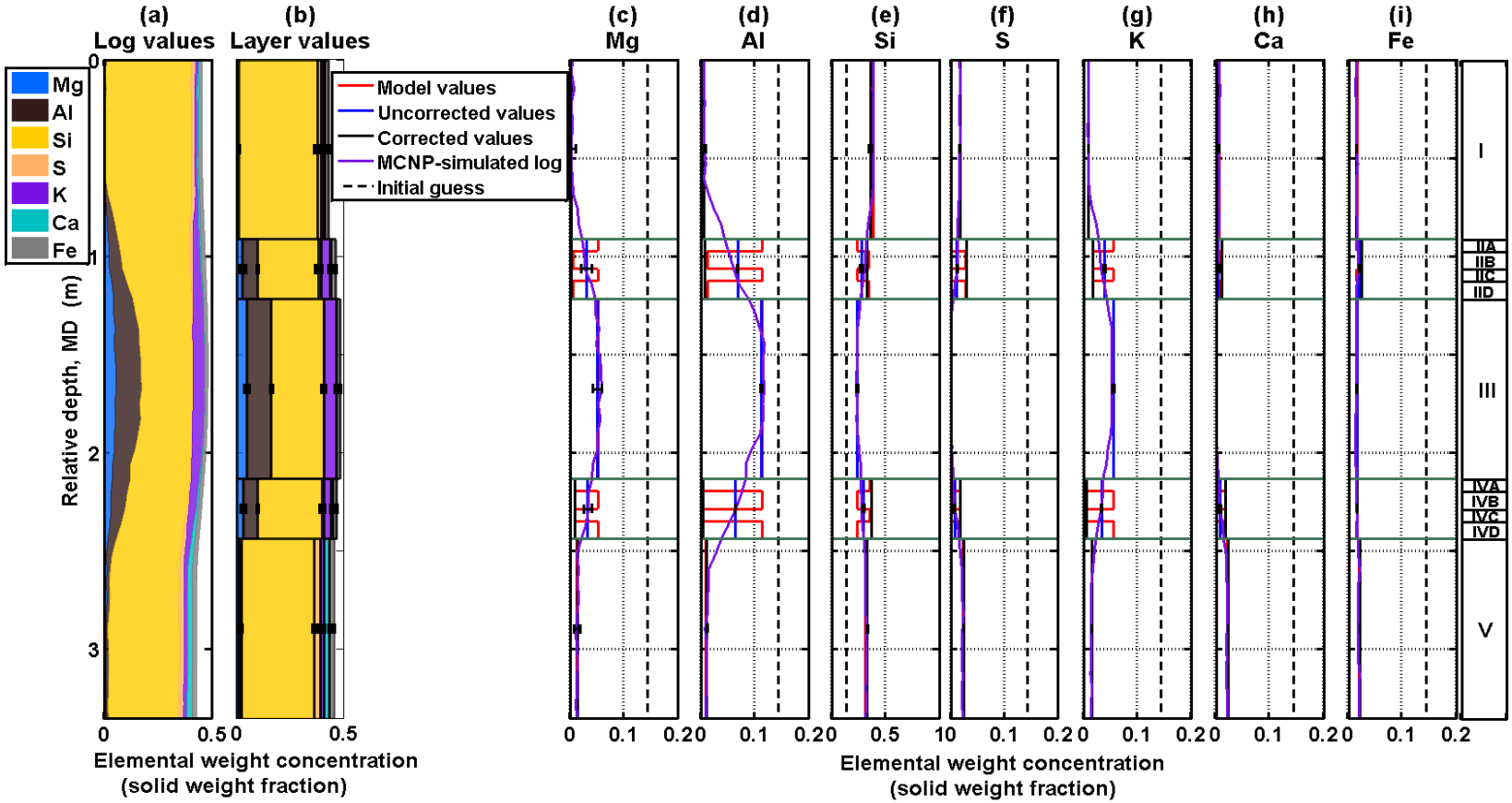

Figure 5.11: Panel (a) displays a cumulative plot of MCNP-simulated capture elemental weight concentrations shown as purple solid lines in panels (c) to (i). Panel (b) exhibits a cumulative plot of inverted elemental weight concentrations shown as blue solid lines in panels (c) to (i). Panels (c) to (i) describes the comparison of estimated layer elemental weight concentrations (blue solid lines) to model values (red solid lines) for Synthetic Case No. 4. Black dashed lines, black uncertainty bars, purple solid lines, and black solid lines indicate the initial guess of the inversion, 95% confidence interval, MCNP-simulated, and corrected elemental weight concentrations in the sandstone matrix, respectively. Mg, Al, Si, S, K, Ca, and Fe are the elements magnesium, aluminum, silicon, sulfur, potassium, calcium, and iron, respectively; I to V identify distinct layers in the synthetic case, while A to D identify laminations within layers.

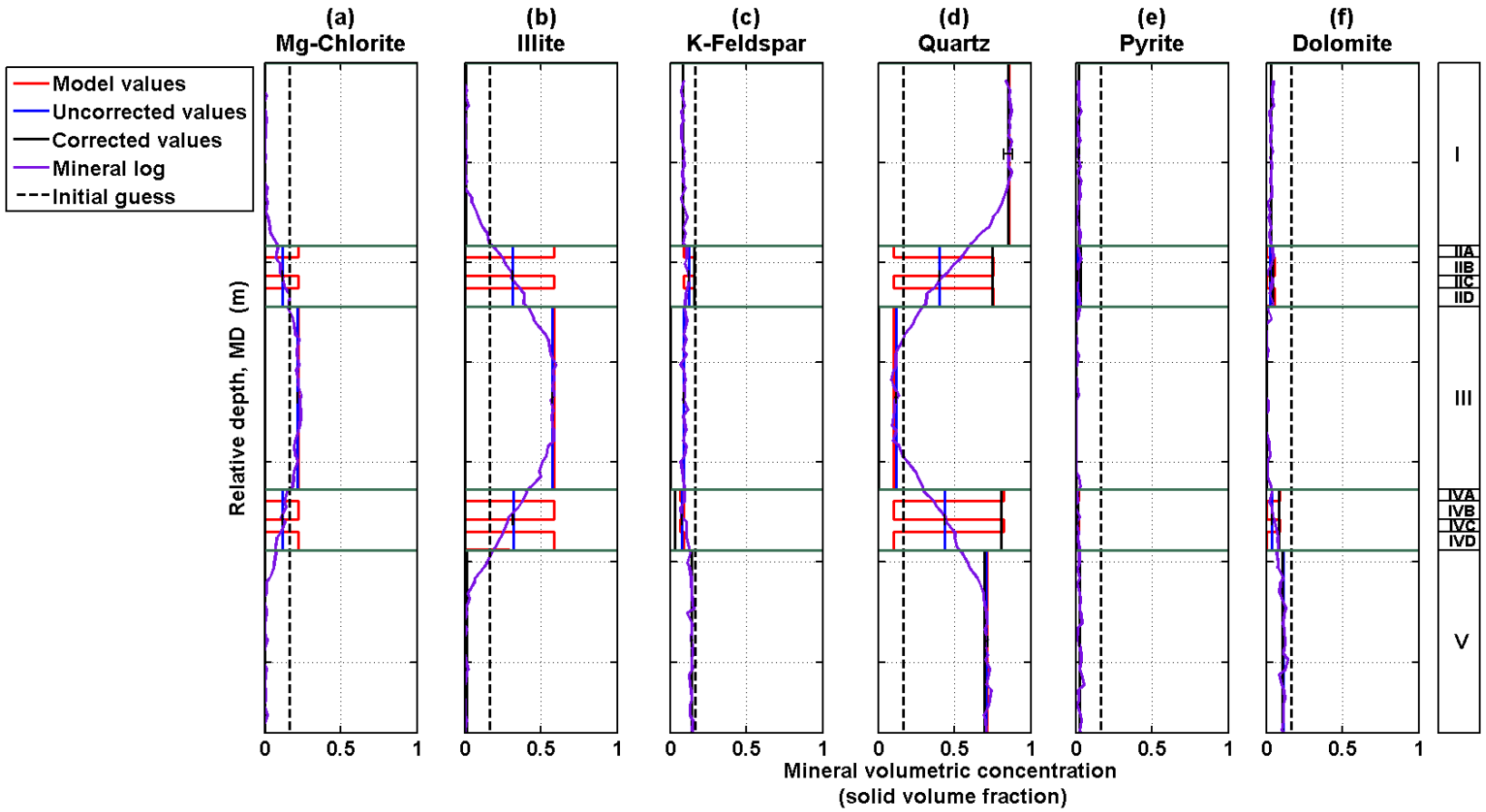

Figure 5.12: Panels (a) to (f) display uncorrected (inverted) layer mineral volumetric concentrations (shown as blue solid lines), corrected (sandstone) layer mineral volumetric concentrations (shown as black solid lines), model layer mineral volumetric concentrations (indicated by red solid lines), and MCNP-simulated mineral logs (displayed as purple solid lines) for Synthetic Case No. 4. Black dashed lines and black uncertainty bars describe the initial guess of the inversion and the 95% confidence interval, respectively. I to V identify distinct layers in the synthetic case, while A to D identify laminations within layers.

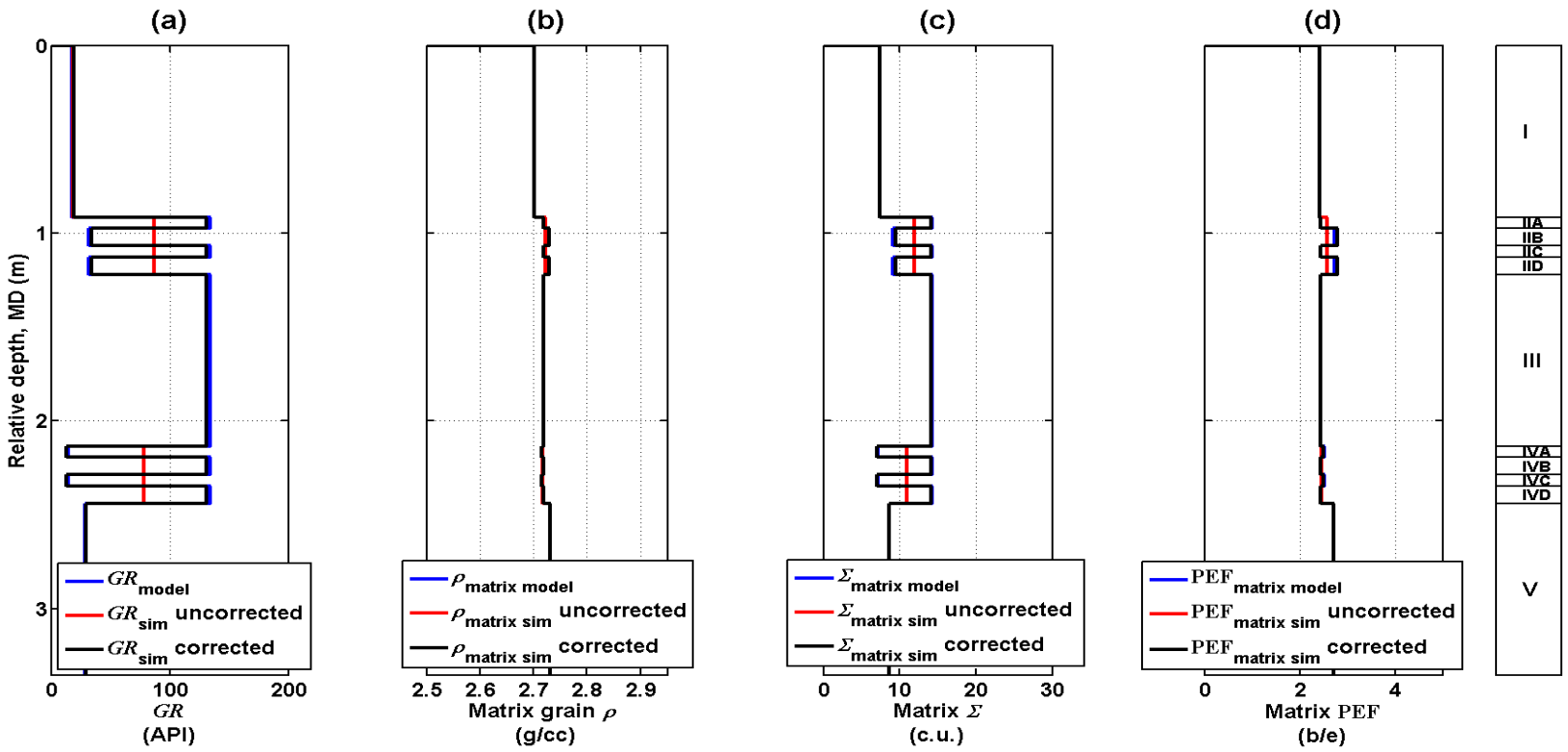

Figure 5.13: Panel (a) shows the comparison between model, simulated gamma ray using uncorrected (inverted) mineralogy, and simulated gamma ray using corrected (sandstone) mineralogy, panel (b) displays the comparison between model, simulated matrix density using uncorrected (inverted) mineralogy, and simulated matrix density using corrected (sandstone) mineralogy, panel (c) exhibits the comparison between model, simulated matrix Sigma using uncorrected (inverted) mineralogy, and simulated matrix Sigma using corrected (sandstone) mineralogy, and panel (d) describes the comparison between model, simulated matrix PEF using uncorrected (inverted) mineralogy, and simulated matrix PEF using corrected (sandstone) mineralogy for Synthetic Case No. 4. Model values, simulated values using uncorrected (inverted) mineralogy, and simulated values using corrected (sandstone) mineralogy are shown as blue, red and black solid lines, respectively. I to V identify distinct layers in the synthetic case, while A to D identify laminations within layers.

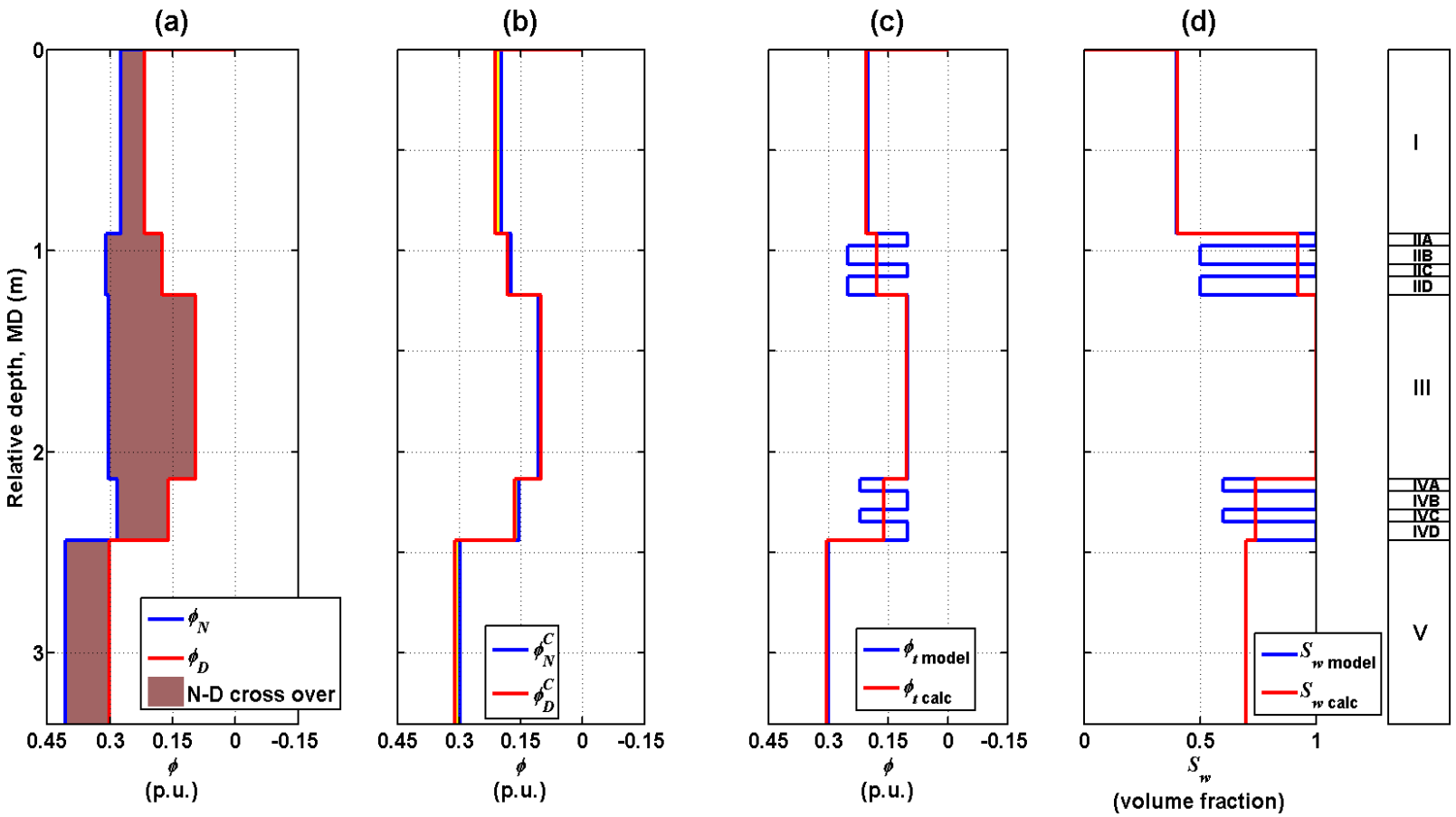

Figure 5.14: Panel (a) shows neutron-density crossover, panel (b) displays matrix-corrected neutron density where yellow and brown shadings describe neutron-density crossover and matrix effects, respectively, panel (c) describes the comparison between model (shown as blue solid lines) and calculated total porosity (shown as red solid lines), and panel (d) exhibits the comparison between model (shown as blue solid lines) and calculated water saturation (shown as red solid lines) for Synthetic Case No. 4. Calculations are based on calculations uncorrected (inverted) mineralogy and do not account for laminations below the vertical resolution of the tool. I to V identify distinct layers in the synthetic case, while A to D identify laminations within layers.

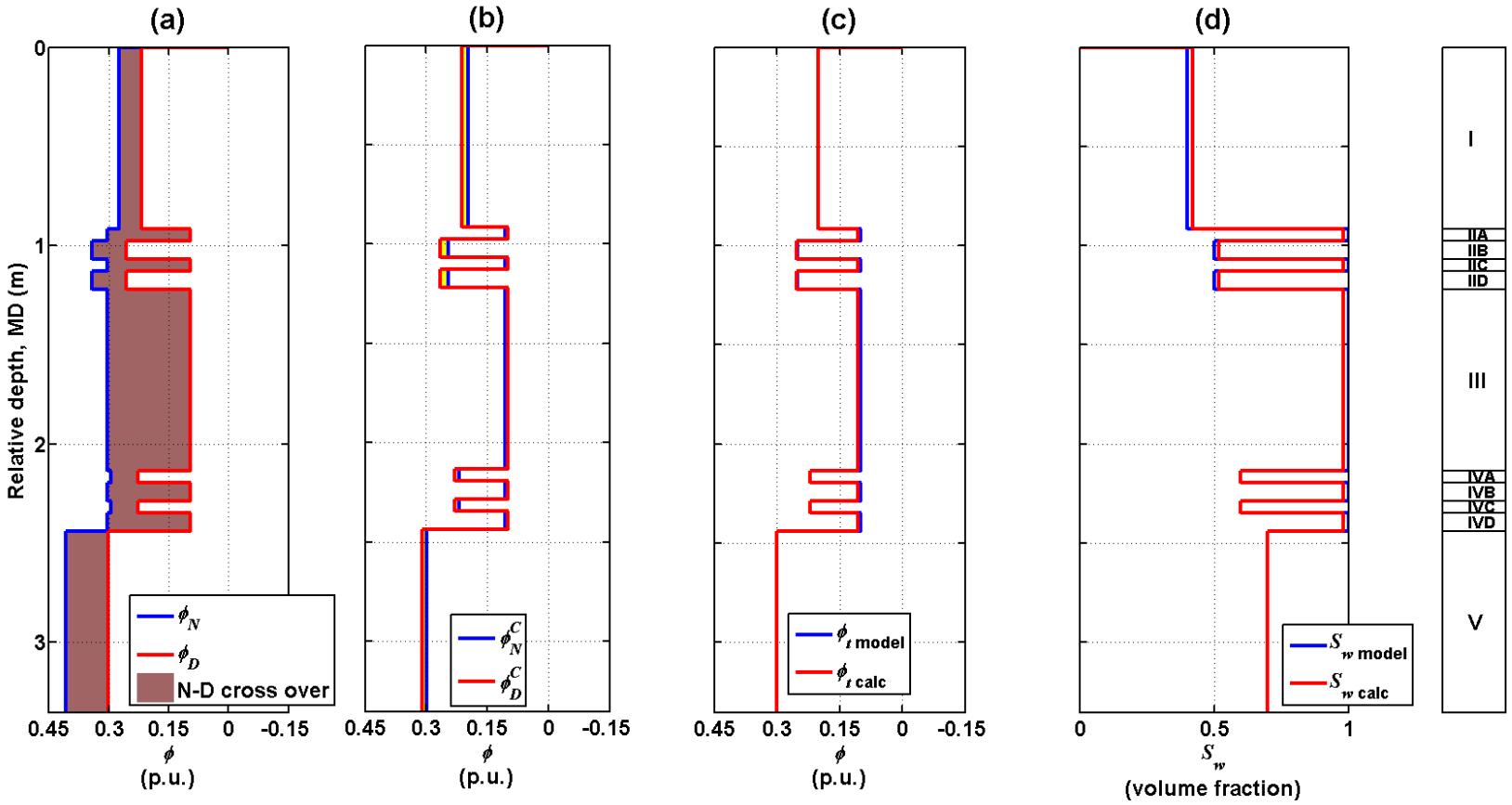

Figure 5.15: Panel (a) shows neutron-density crossover, panel (b) displays matrix-corrected neutron density where yellow and brown shadings describe neutron-density crossover and matrix effects, respectively, panel (c) describes the comparison between model (shown as blue solid lines) and calculated total porosity (shown as red solid lines), and panel (d) exhibits the comparison between model (shown as blue solid lines) and calculated water saturation (shown as red solid lines) for Synthetic Case No. 4. Calculations are based on corrected (sand) mineralogy and account for laminations below the vertical resolution of the tool. I to V identify distinct layers in the synthetic case, while A to D identify laminations within layers.

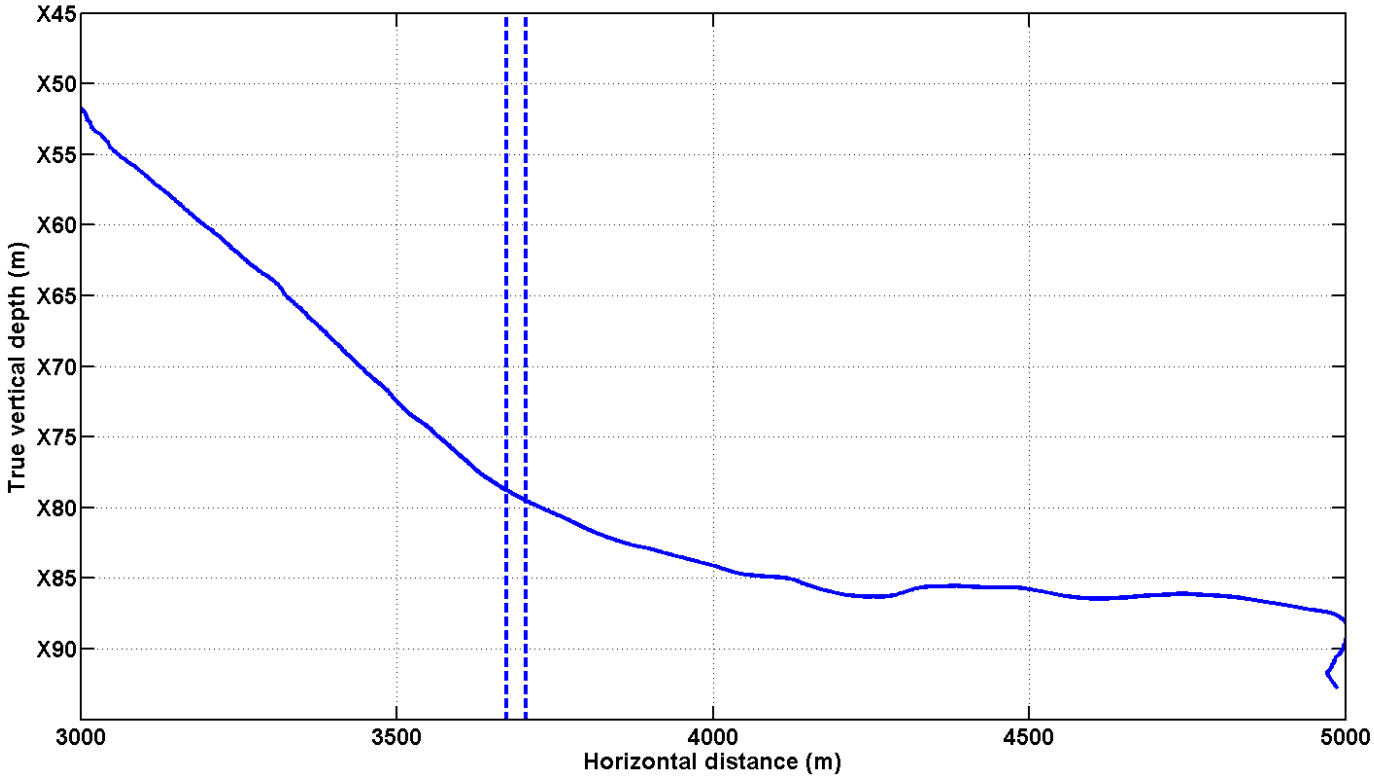

Figure 5.16: Well 2-26-G trajectory in Field Case No. 1 (2D projection of 3D well trajectory), dashed lines represent the zone of interest in this chapter which is located in formations 1-C, 12-A1, 12-A2, and 12-A3.

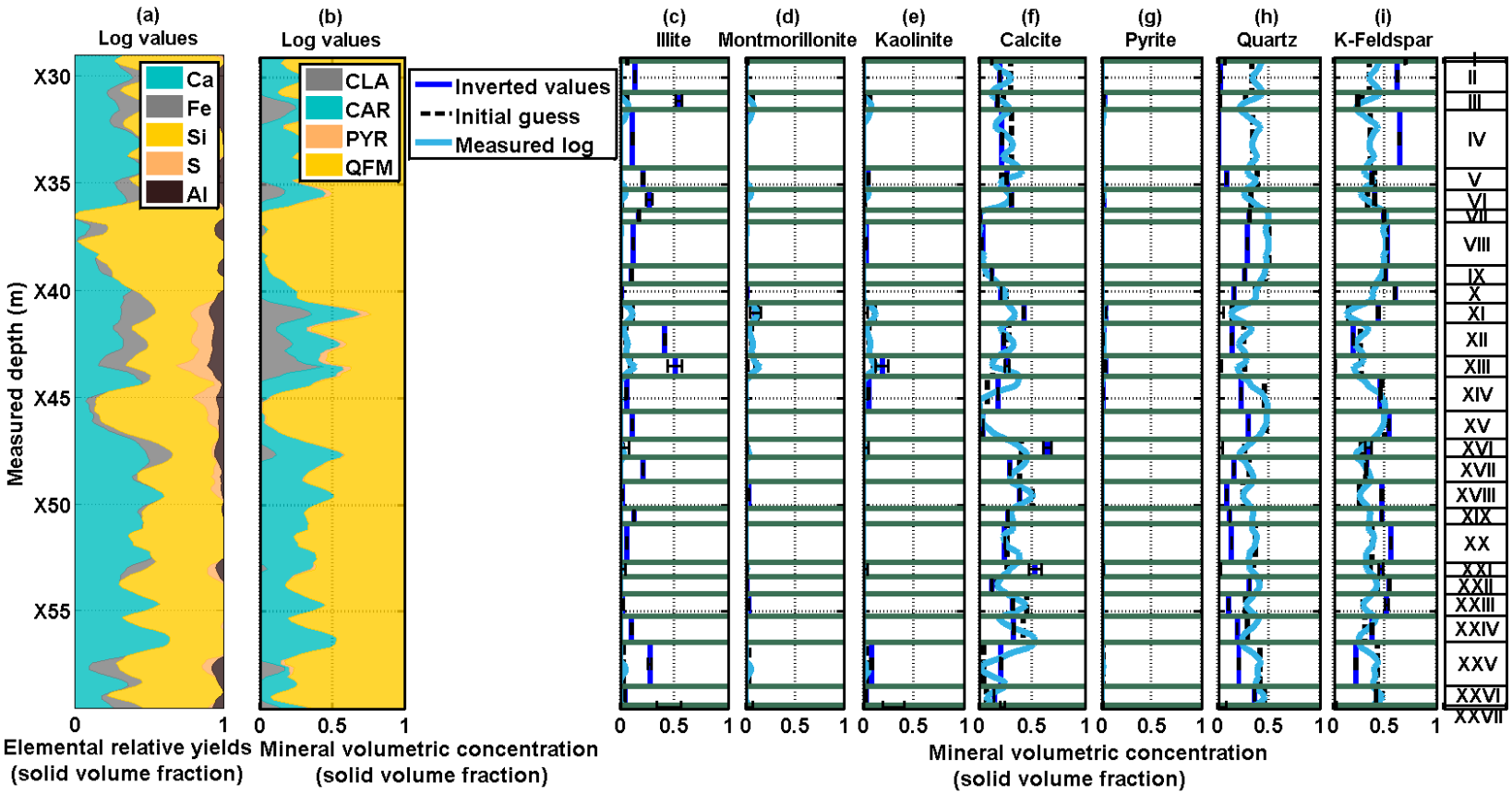

Figure 5.17: Panel (a) displays a cumulative plot of measured capture elemental relative yields; panel (b) describes a cumulative plot of spectroscopy mineral volumetric concentration logs; panels (c) to (i) show the inverted layer values (shown as blue solid lines) and spectroscopy mineral well logs (shown as light blue solid lines) for Field Case No. 1. Black dashed lines and black uncertainty bars describe the initial guess and 95% confidence interval, respectively; Ca, Fe Si, S, and Al are the elements calcium, iron, silicon, sulfur, and aluminum, respectively. CLA, CAR, PYR, and QFM refer to clay, carbonate, pyrite, and quartz-feldspar-mica group, respectively, while I to XXVII identify distinct layers in the field case.

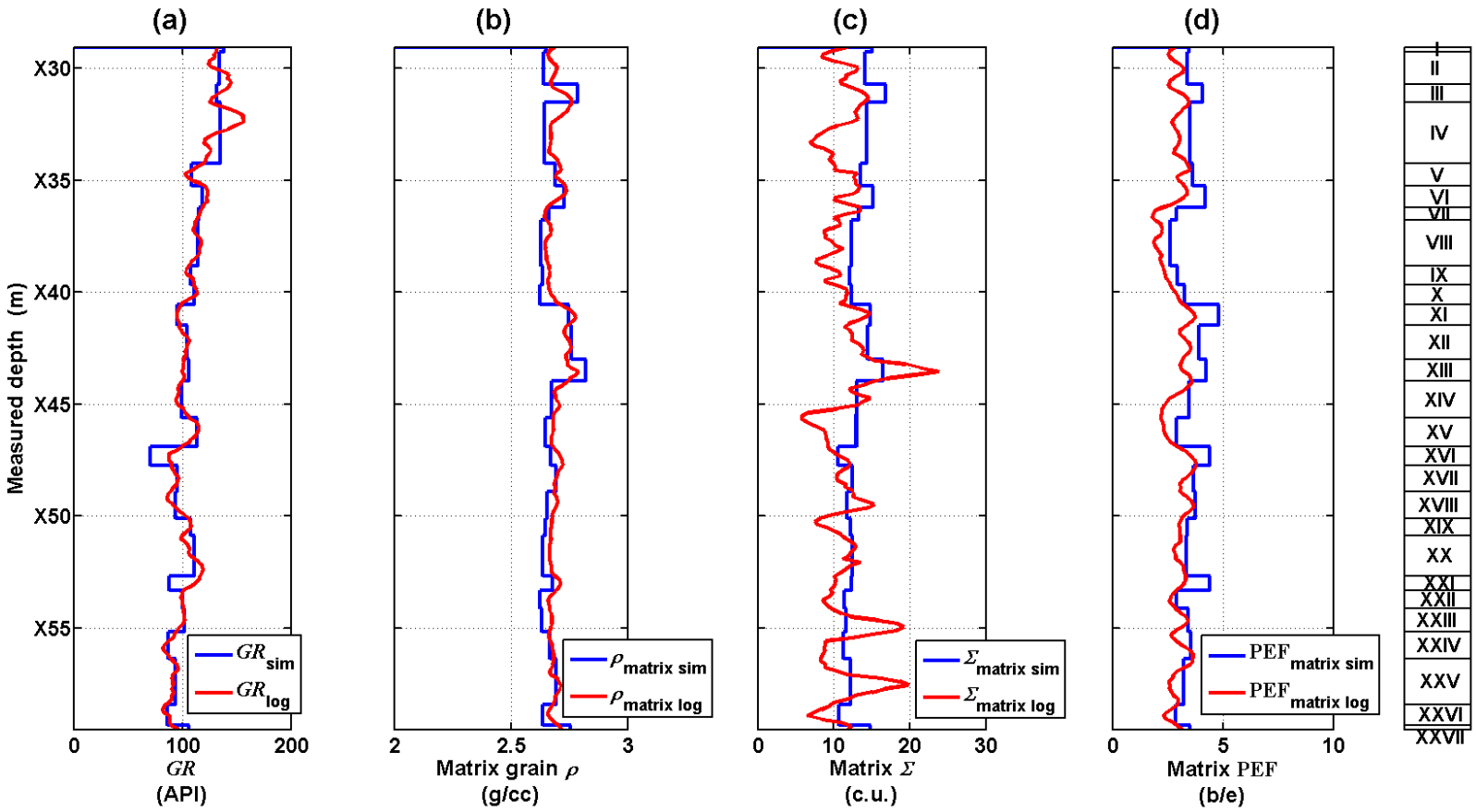

Figure 5.18: Panel (a) shows the comparison between model and simulated gamma ray, panel (b) displays the comparison between model and simulated matrix density, panel (c) exhibits the comparison between model and simulated matrix Sigma, and panel (d) describes the comparison between model and simulated matrix PEF for Field Case No. 1. Simulated and log values are shown as blue and red solid lines, respectively. I to XXVII identify distinct layers in the field case.

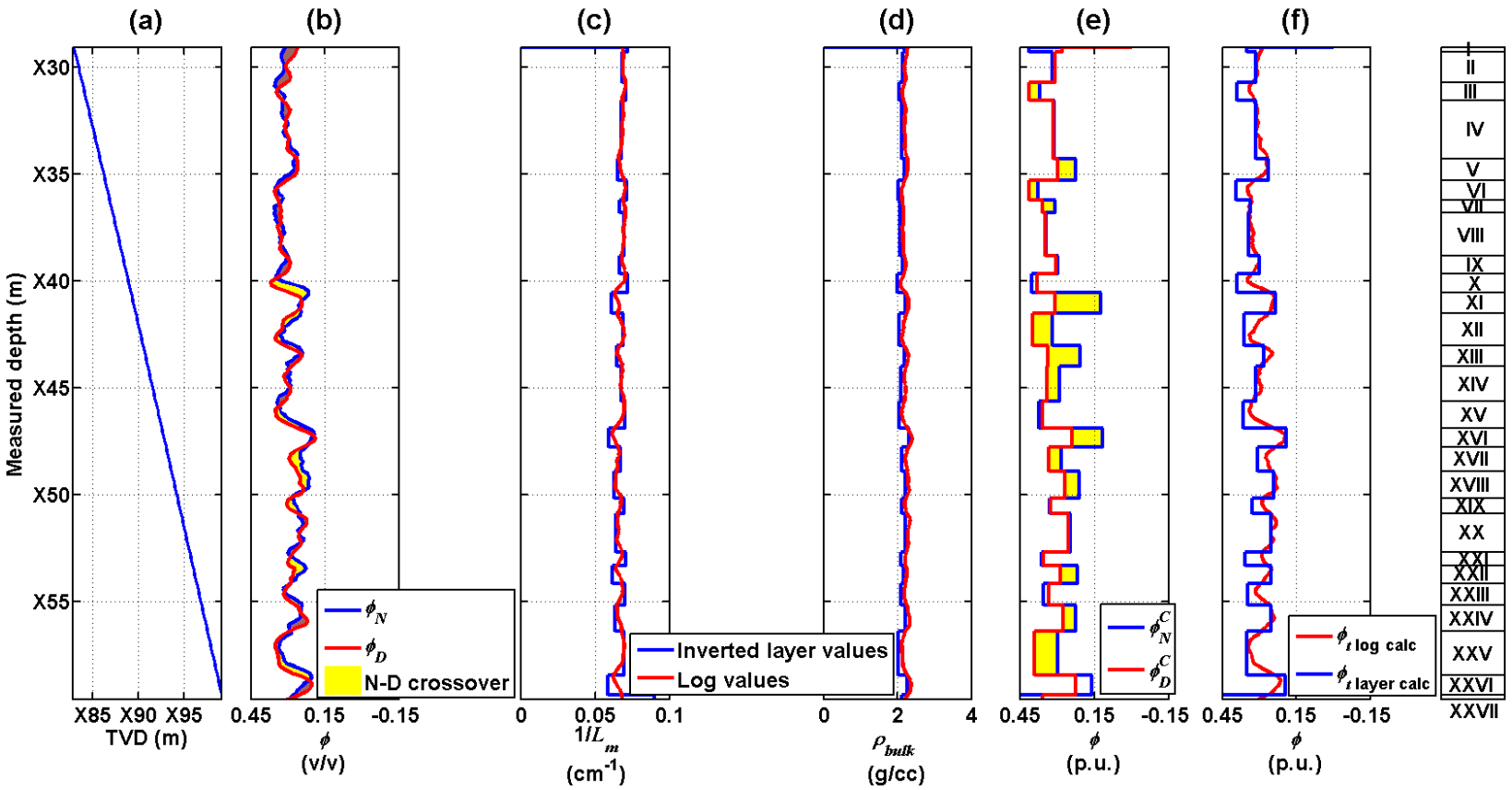

Figure 5.19: Panel (a) describes an inverted well curtain section, panel (b) shows measured neutron and density porosity logs where crossover is indicated by yellow shading and the brown shading describes matrix effects on measured porosity logs, panel (c) displays inverted layer (blue solid line) and log-derived (red solid line) inverse of migration length values, panel (d) shows inverted layer (blue solid line) and log-derived (red solid line) bulk density layer values, panel (e) exhibits matrix-corrected neutron-density crossover, and panel (f) displays calculated total porosity for Field Case No. 1. I to XXVII identify distinct layers in the field case.

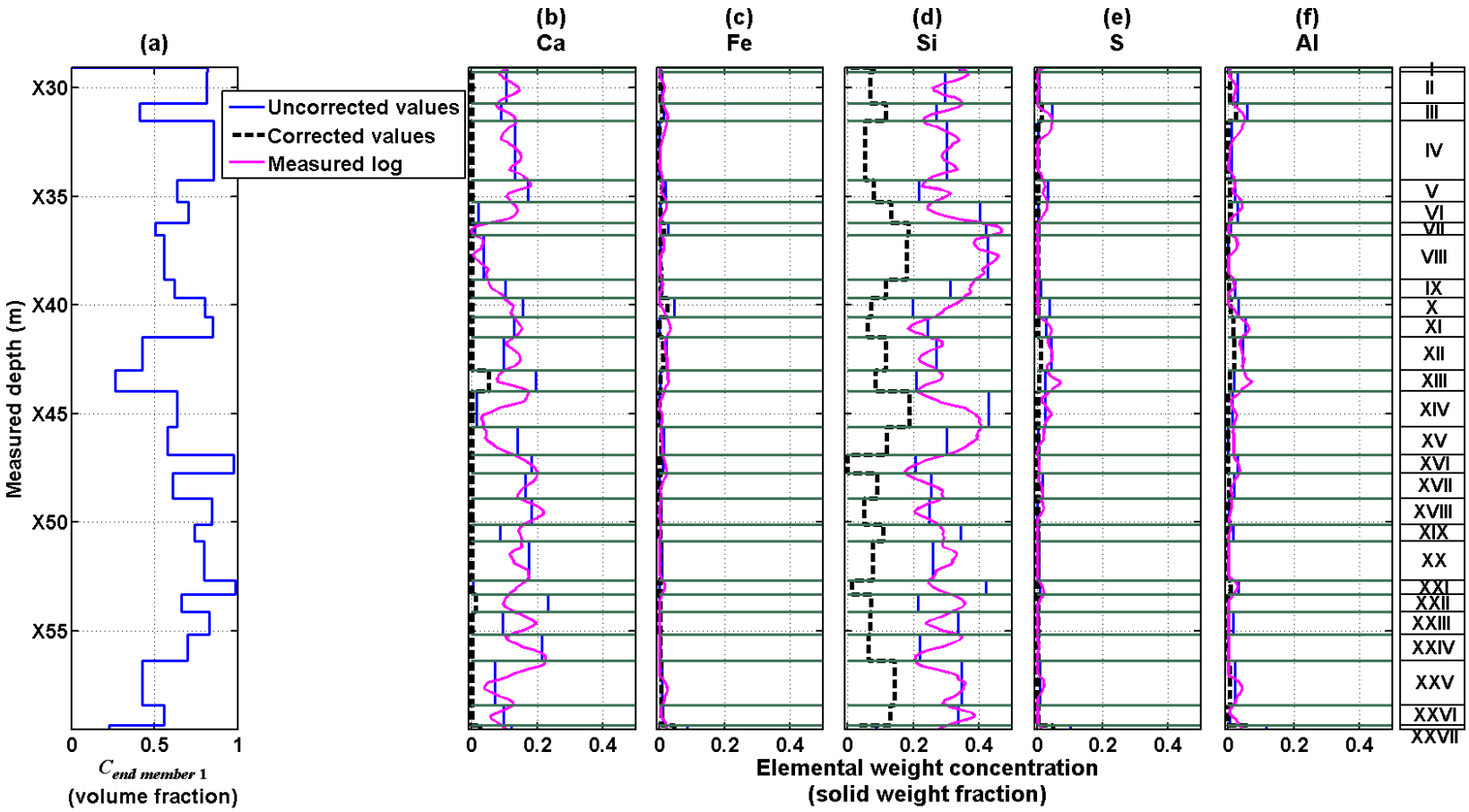

Figure 5.20: Panel (a) displays the volumetric concentration of *end member* 1: calcite-cemented feldspathic siltstones. Panels (b) to (f) show the comparison between corrected (hydrocarbon-bearing argillaceous uncemented siltstones) layer elemental weight concentrations (black solid lines) and uncorrected (inverted) values (blue solid lines) for Field Case No. 2. Magenta solid lines describe measured elemental weight concentration logs; Ca, Fe Si, S, and Al are the elements calcium, iron, silicon, sulfur, and aluminum, respectively, while I to XXVII identify distinct layers in the field case.

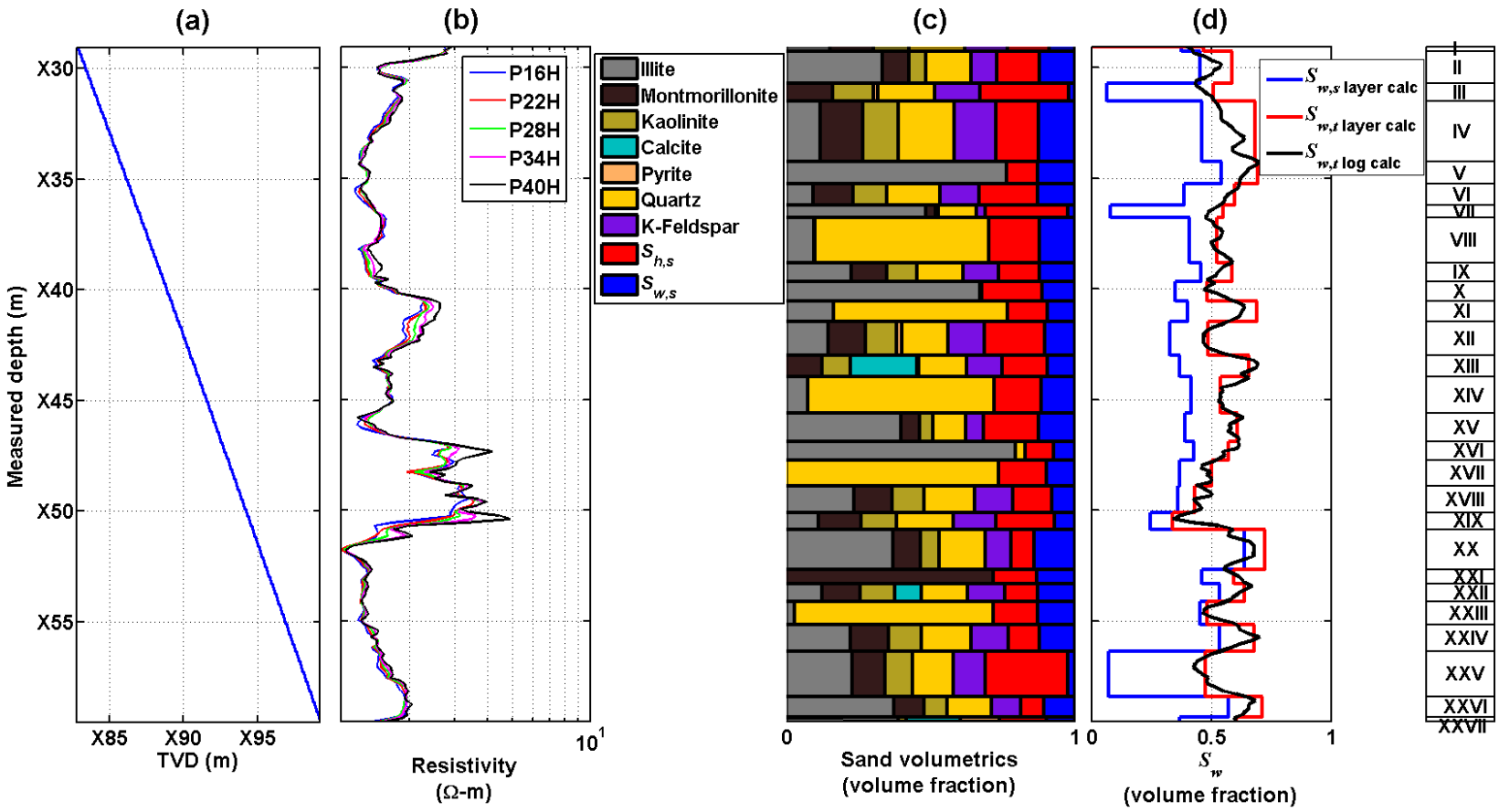

Figure 5.21: Panel (a) describes an inverted well curtain section, panel (b) displays measured resistivity values, panel (c) shows volumetric compositions in calcite uncemented laminations, and panel (d) exhibits calculated water saturation in calcite uncemented laminations (blue solid lines) and total water saturation (red solid lines) for Field Case No. 1. I to XXVII identify distinct layers in the field case.

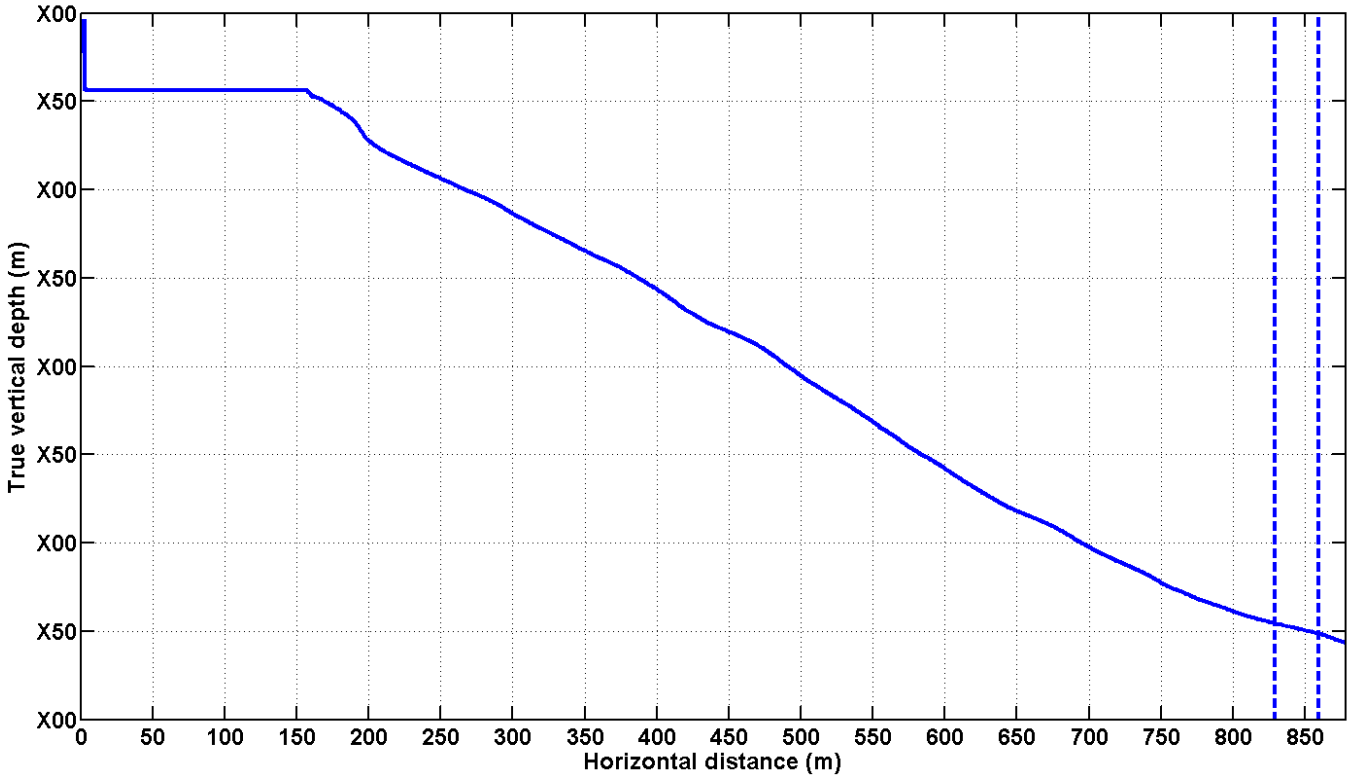

Figure 5.22: Well trajectory in Field Case No. 2 (2D projection of 3D well trajectory), dashed lines represent the zone of interest analyzed in this chapter.

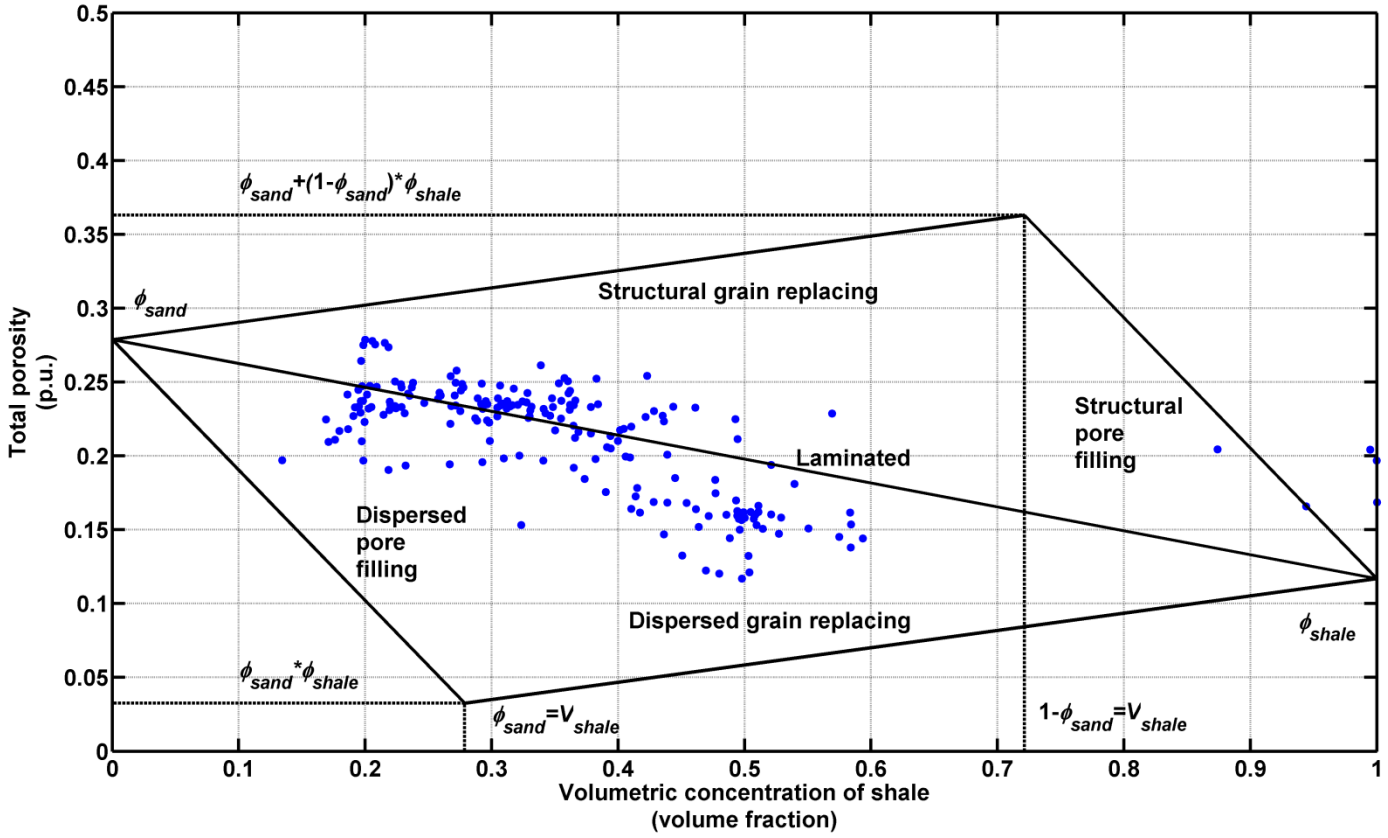

Figure 5.23: Thomas-Stieber diagram indicating a laminated formation in Field Case No. 2.

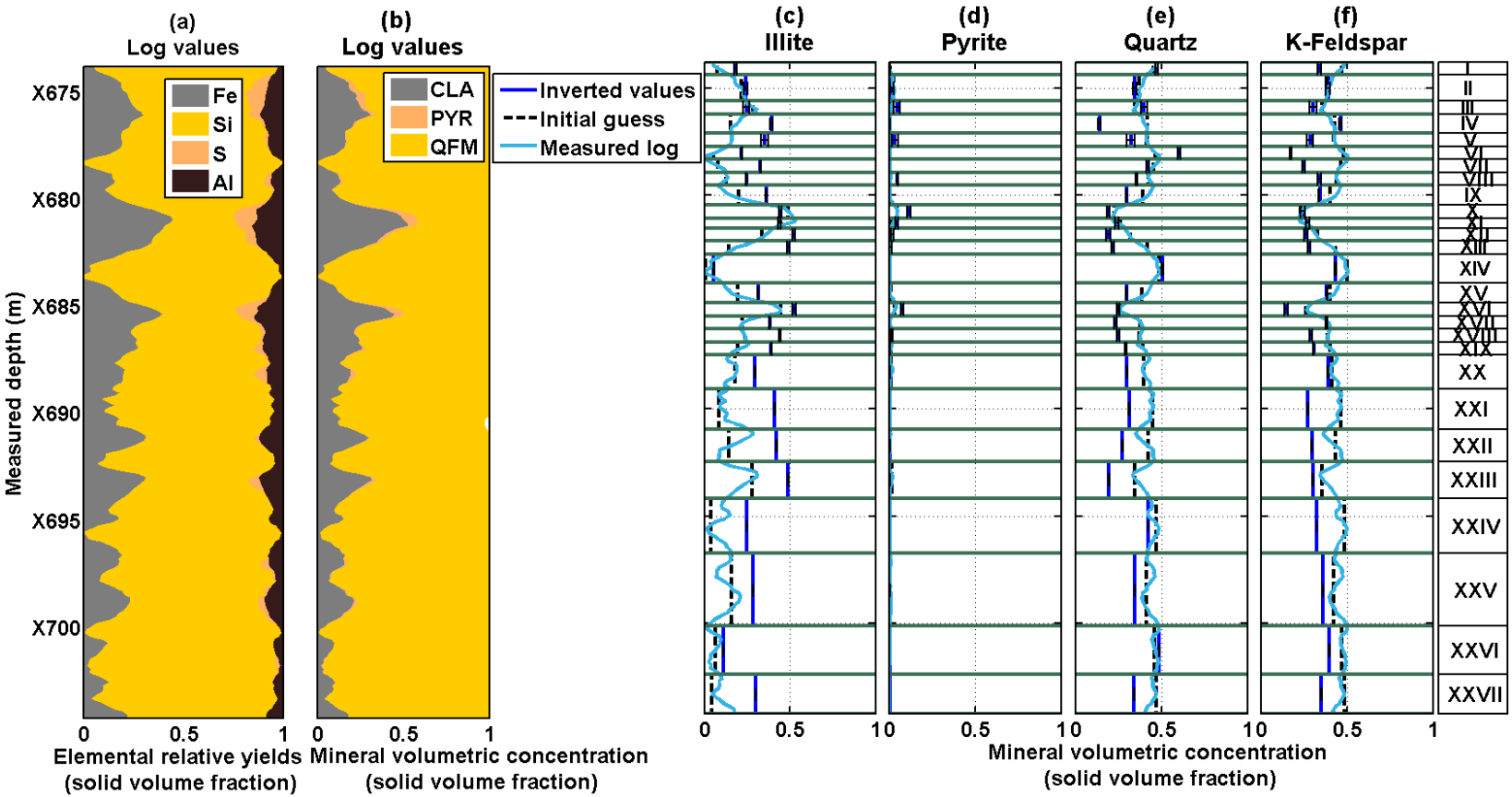

Figure 5.24: Panel (a) displays a cumulative plot of measured capture elemental relative yields; panel (b) describes a cumulative plot of spectroscopy mineral volumetric concentration logs; panels (c) to (i) show the inverted layer values (shown as blue solid lines) and spectroscopy mineral well logs (shown as light blue solid lines) for Field Case No. 2. Black dashed lines and black uncertainty bars describe the initial guess and 95% confidence interval respectively; Fe Si, S, and Al are the elements iron, silicon, sulfur, and aluminum, respectively. CLA, PYR, and QFM refer to clay, pyrite, and quartz-feldspar-mica group, respectively, while I to XXVII identify distinct layers in the field case.

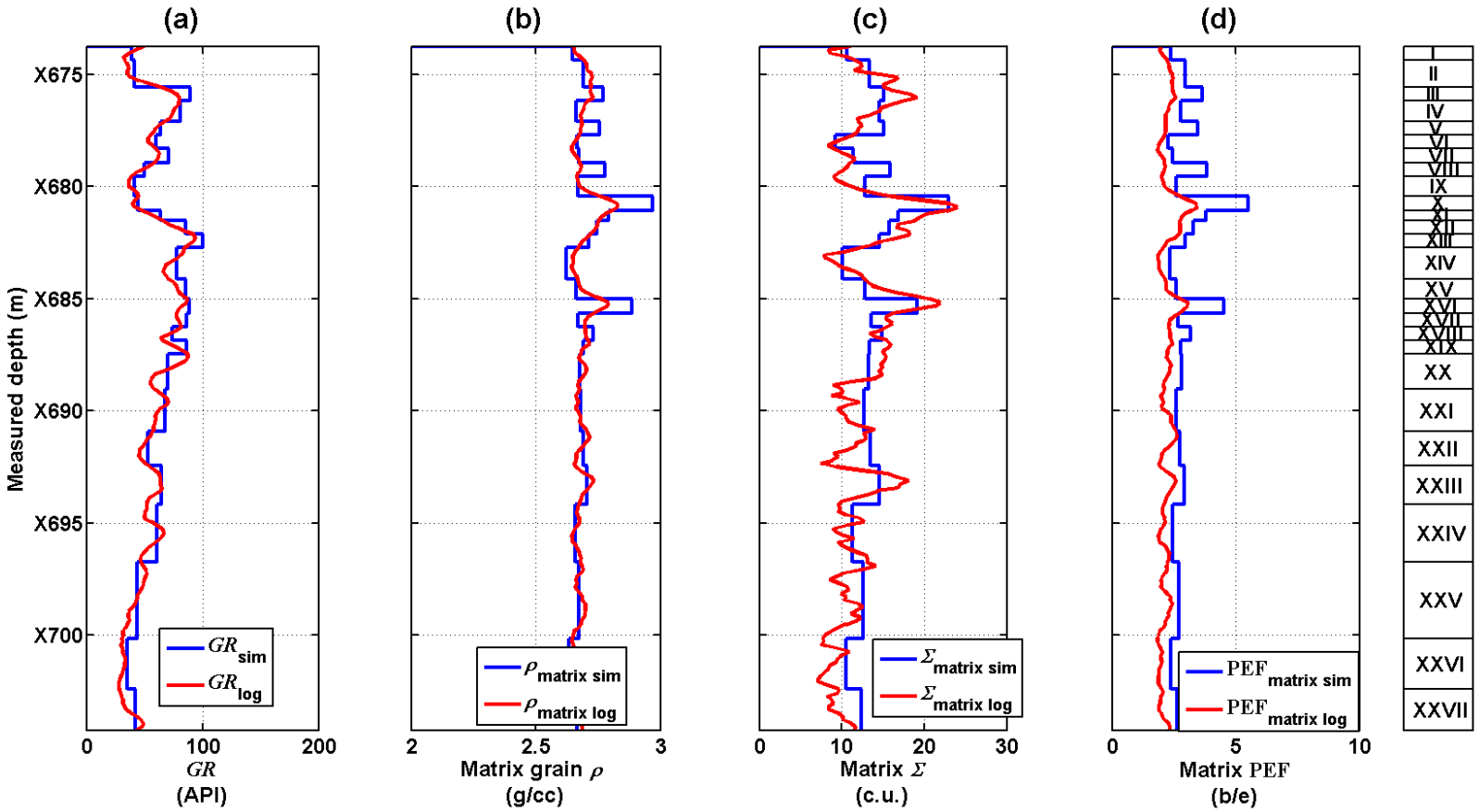

Figure 5.25: Panel (a) shows the comparison between model and simulated gamma ray, panel (b) displays the comparison between model and simulated matrix density, panel (c) exhibits the comparison between model and simulated matrix Sigma, and panel (d) describes the comparison between model and simulated matrix PEF for Field Case No. 2. Simulated and log values are shown as blue and red solid lines, respectively. I to XXVII identify distinct layers in the field case.

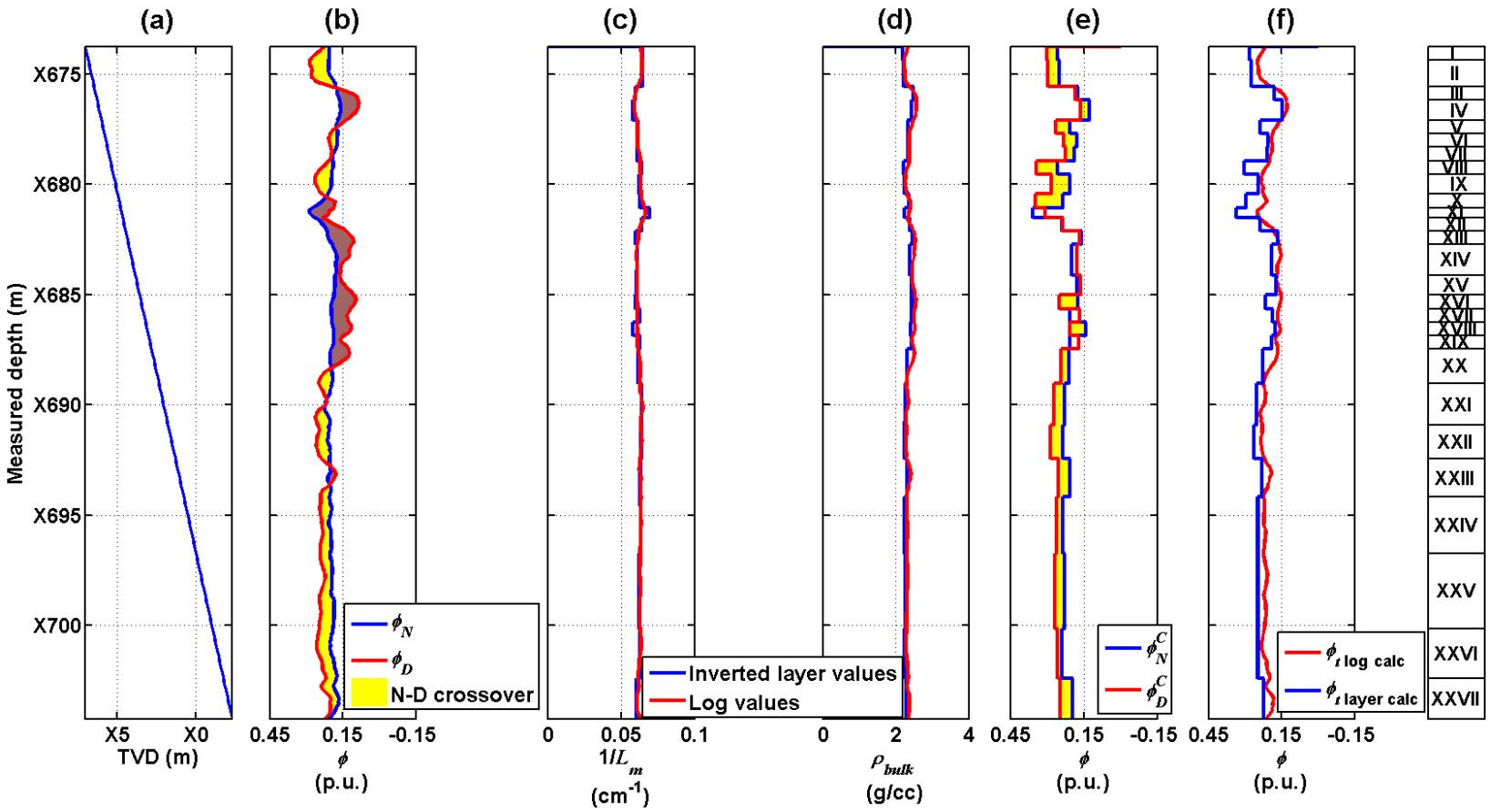

Figure 5.26: Panel (a) describes an inverted well curtain section, panel (b) shows measured neutron and density porosity logs where crossover is indicated by yellow shading and the brown shading describes matrix effects on measured porosity logs, panel (c) displays inverted layer (blue solid line) and log-derived (red solid line) inverse of migration length values, panel (d) shows inverted layer (blue solid line) and log-derived (red solid line) bulk density layer values, panel (e) exhibits matrix-corrected neutron-density crossover, and panel (f) displays calculated total porosity for Field Case No. 2. I to XXVII identify distinct layers in the field case.

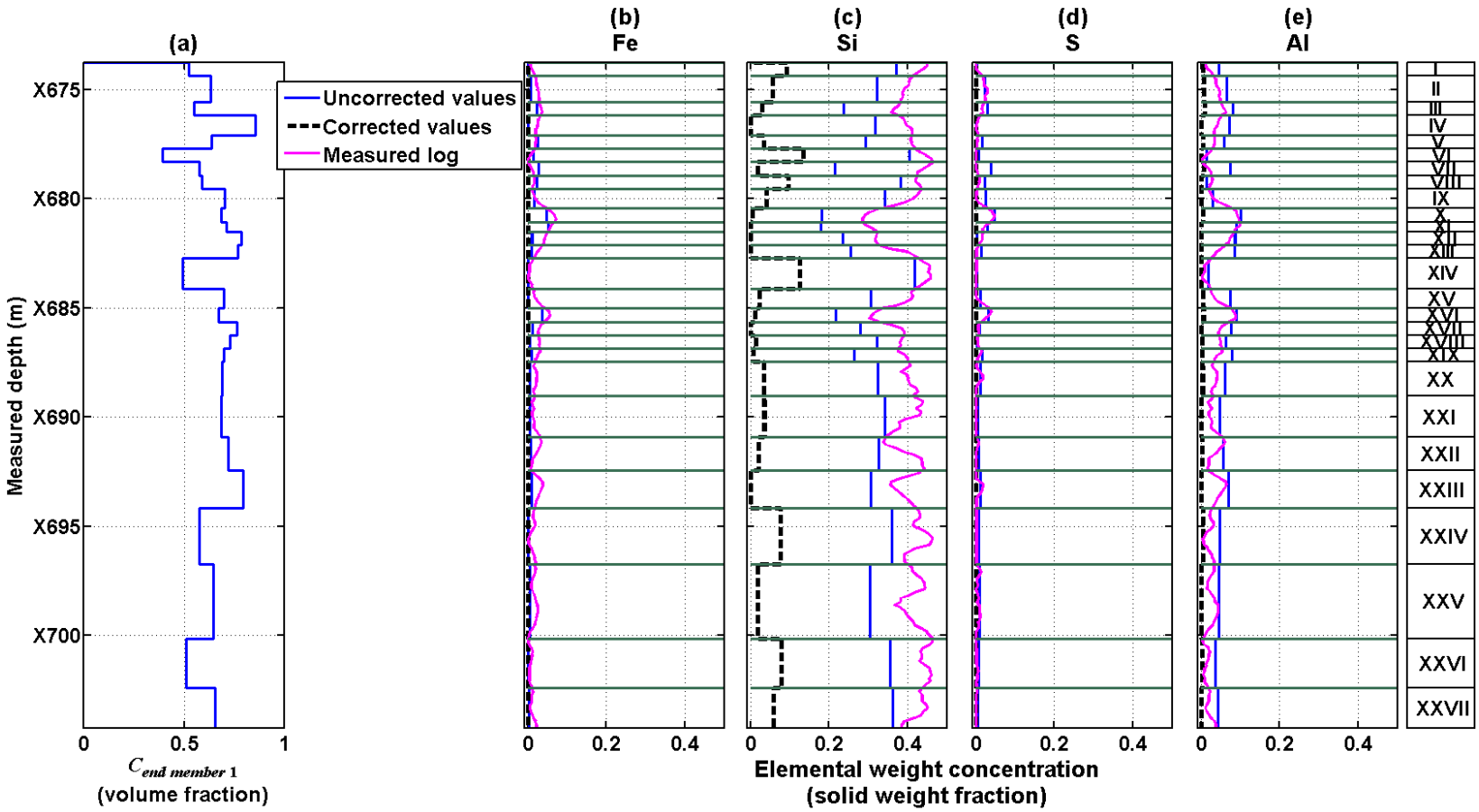

Figure 5.27: Panel (a) displays the volumetric concentration of *end member* 1: shale. Panels (b) to (e) show the comparison between corrected (sand) layer elemental weight concentrations (black solid lines) and uncorrected (inverted) values (blue solid lines) for Field Case No. 2. Magenta solid lines describe measured elemental weight concentration logs; Fe Si, S, and Al are the elements iron, silicon, sulfur, and aluminum, respectively, while I to XXVII identify distinct layers in the field case.

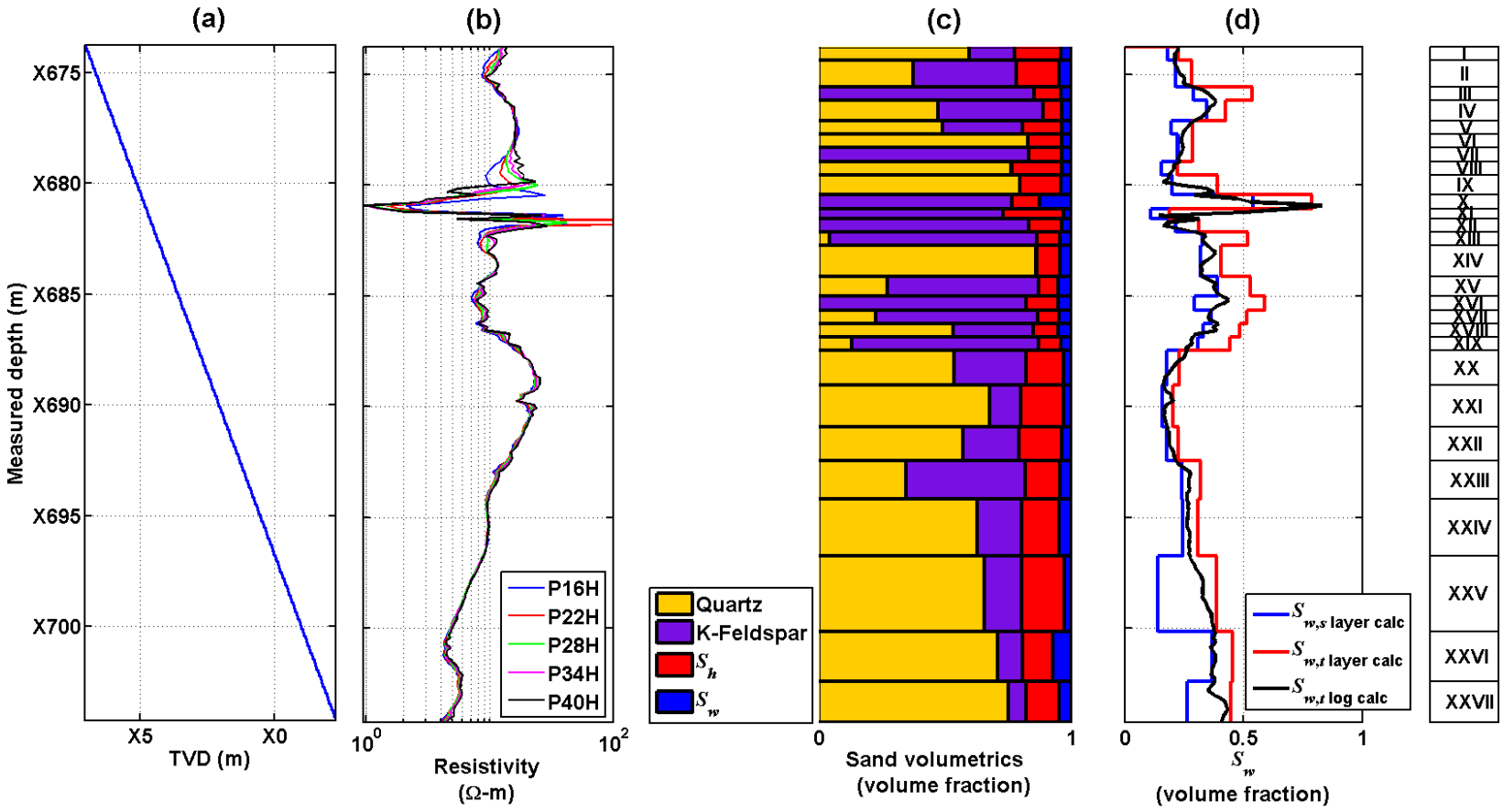

Figure 5.28: Panel (a) describes an inverted well curtain section, panel (b) displays measured resistivity values, panel (c) shows volumetric compositions in sand laminations, and panel (d) exhibits calculated water saturation in sand laminations (blue solid lines) and total water saturation (red solid lines) for Field Case No. 2. I to XXVII identify distinct layers in the field case.

Chapter 6: Summary, Conclusions, and Recommendations

This final chapter summarizes the developments and technical contributions advanced by the research in this dissertation. I also describe general conclusions deduced from results and propose recommendations for future work.

6.1 SUMMARY

Until now, there has been only limited research on the numerical interpretation of spectroscopy measurements. The motivation behind this dissertation was therefore to introduce numerical methods that improve the interpretation of spectroscopy measurements and thereby facilitate spectroscopy-based petrophysical interpretation workflows. To permit the analysis of complex geometries such as high-angle/horizontal (HA/HZ) wells, most of the research advanced in this dissertation pertains to the logging-while-drilling (LWD) spectroscopy tool because of its ability to log extremely complicated geometries.

The first part of the dissertation focused on the development of a forward model that rapidly simulates neutron-induced gamma-ray spectroscopy measurements (elemental relative yields, elemental weight concentrations, mineral volumetric concentrations, and mineral weight concentrations), in which measured gamma rays are generated during high-energy inelastic neutron scattering or low-energy thermal neutron capture interactions. The forward model simulates elemental absolute yield logs by a first-order perturbation of layer elemental absolute yields for inelastic and capture

measurement modes, where perturbation is based on the variation of flux sensitivity functions (FSFs) with respect to the spectroscopy-driven nuclear property (migration length). Simulated elemental absolute yields were converted into elemental relative yields, elemental weight concentrations, mineral volumetric concentrations, and mineral weight concentrations through processing methods that include oxide closure and inversion models. Simulation outputs of elemental and mineral concentrations obtained with the forward model were validated with full Monte Carlo nuclear calculations. Monte Carlo calculations were authenticated through benchmarking Monte Carlo simulated elemental spectra with corresponding laboratory-derived spectra.

In the second part of the dissertation, I developed a spectroscopy-based petrophysical workflow that can be applied to tools where the model geometry detail is not available. Mineralogy was quantified depthwise through depth-by-depth joint matrix inversion of spectroscopy elemental weight logs and other lithology-sensing logs such as gamma ray, matrix density, matrix Sigma, and photoelectric factor (PEF). Estimated mineral concentrations were used to improve the quantification of porosity and hydrocarbon saturation by correcting the assumption of a homogeneous matrix in measured neutron and density porosity logs. Several field cases that include core measurements as well as synthetic cases were used to establish the accuracy and flexibility of the developed workflow. It should be noted that these methods do not address geometrical effects due to the absence of the tool model geometry. If the specific tool model is available, interpretation techniques outlined in the third and fourth parts of

this dissertation, which account for geometrical effects, can be readily implemented in such a tool.

The third part of the dissertation introduced a nonlinear inversion method and a spectroscopy mixing law that improve the quantitative estimation of layer elemental relative yields and weight concentrations. The inversion aspect of the interpretation algorithm was rendered efficient due to the utilization of the spectroscopy fast forward model as opposed to computationally expensive Monte Carlo simulation methods. This algorithm is particularly useful in thin-bedded formations where true layer properties are compromised due to significant shoulder-bed averaging effects. Reductions of shoulder-bed averaging effects as high as 0.3 and 0.27 yield and weight fraction, respectively, were observed in the synthetic and field cases studied.

In the final part of the dissertation, I introduced another nonlinear inversion method, based on the spectroscopy fast-forward model. By this method a solution of mineral concentrations was obtained through a joint interpretation of inelastic or capture elemental relative yields and matrix sensitive logs including gamma ray, PEF, matrix density, and matrix Sigma. This interpretation established solutions of mineralogy that were devoid of shoulder-bed averaging effects and were petrophysically consistent with other well logs. Improved petrophysical calculations of porosity and water saturation were obtained by replacing the assumed homogeneous matrix lithology in neutron and density porosity logs with the estimated mineralogy. In thin-bedded formations, a supplementary interpretation method based on the developed spectroscopy mixing law and a shaly-sand saturation model yielded accurate estimations of mineral and

petrophysical properties. The accuracy and flexibility of the algorithm were validated through synthetic and field cases having different well trajectories, formation geometries, and formation lithologies.

6.2 CONCLUSIONS

This section lists the significant conclusions arising from the research documented in the chapters describing the four parts of this dissertation.

6.2.1 Part One: Fast Numerical Simulation of Logging-While-Drilling Gamma-Ray Spectroscopy Measurements

i. Spectroscopy measurements, including elemental and mineral concentrations, are acquired through the interpretation of gamma rays due to high-energy inelastic neutron scattering or low-energy thermal neutron capture. Both measurement modes assess distinct elemental relative yield logs and can be used to validate elemental weight or mineral concentrations independently.

ii. Inelastic and capture measurements are governed by distinct nuclear transport mechanisms and are differentially impacted by geometrical and environmental effects. Due to the existence of inelastic gamma rays at energy levels higher than those observed for capture gamma rays, inelastic measurements are less affected by shoulder-bed averaging than are capture measurements.

iii. The LWD tool under study does not measure inelastic gamma rays due to low signal-to-noise ratios in the inelastic measurement mode. However, certain elements can only be quantified with inelastic spectra; this limits the number of elements that can

be quantified using the LWD tool. I therefore improved inelastic simulation statistics and included these measurements in the forward numerical simulation method to facilitate robust spectroscopy interpretation using the LWD tool.

iv. Although the methods developed in this dissertation can handle the presence of invasion, invasion effects are not studied because they are negligible in the LWD spectroscopy tool under study. Measurements are acquired almost simultaneously with drilling because the short- spaced gamma-ray spectroscopy detector in the tool is located close to the drill bit, and invasion effects are therefore minimal. Furthermore, the tool has a large collar, steel housing, and a stabilizer that minimize borehole effects. It should also be noted that spectroscopy measurements do not typically consider invasion and other fluid effects because they focus on the solid matrix composition, not on fluid compositions in the borehole or the formation.

v. Accurate fast-forward modeling of spectroscopy elemental and mineral compositions is achieved through first-order perturbation theory, based on a model property of elemental absolute yields. The choice of elemental absolute yields (as opposed to measured gamma-ray spectra) as the modeling parameter circumvents the use of subjective spectral stripping techniques in the estimation of elemental relative yields.

vi. Fast-forward modeling is based on Monte Carlo calculated spectroscopy flux sensitivity function (FSF) maps that arise from inelastic neutron scattering and thermal neutron capture. These maps stem from tracking the spatial importance of inelastic or capture neutrons that have produced gamma rays counted at the detector

and are dependent upon formation migration lengths. Formation migration lengths therefore characterize the perturbation parameter implemented in the forward model.

vii. Monte Carlo simulations, achieved with the Monte Carlo N-Particle code (MCNP), in the presence of the tool model, borehole, and formation, can be modified to enable the tracking of gamma rays from each element in the formation. This allows the direct estimation of elemental relative yields from simulated elemental spectra without the need to employ subjective spectral stripping techniques.

viii. Monte Carlo spectroscopy simulations accurately reproduced shoulder-bed averaging effects that occur in thin-bedded formations for the inelastic and capture measurements modes.

ix. Differences between Monte Carlo and fast simulated logs increase with the complexity of the well trajectory and large perturbations in layer migration lengths. However, these differences are small enough that they do not compromise the reliability of the simulation algorithm in the interpretation of spectroscopy measurements; differences between Monte Carlo and fast simulated spectroscopy logs did not exceed 5% in any of the synthetic cases studied.

x. Results of the implementation of the forward model, in synthetic cases, show that shoulder-bed averaging has the most significant effect on spectroscopy logs, compromising representations of elemental and mineral layer compositions by as much as 170%.

xi. An inversion method is used to quantify mineral concentrations from elemental relative yield logs through the analytical relationship that exists between elemental

relative yields and mineral volumetric concentrations. This approach decreases the assumptions and subjective methods that are typically employed in element-to-mineral transforms. However, it is important to solve for minerals that are known to be present in the formation to avoid underdetermined problems and false representations of non-existing minerals.

6.2.2 Part Two: Improved Mineral and Petrophysical Analysis using Neutron-Capture Gamma-Ray Spectroscopy Logs

i. An inversion method based on the analytical relationship between elemental and mineral concentrations can accurately quantify detailed formation mineralogy.

ii. Although the solution of mineralogy could be posed in terms of elemental relative yields, the use of elemental weight concentrations is more practical in well log interpretation because spectroscopy logs are more commonly delivered as weight logs.

iii. The developed lithology estimation method quantifies mineralogy depth-by-depth and is independent of specific tool model geometry details. Because results do not include tool model geometry details, they do not account or correct for shoulder-bed averaging effects. Estimation of layer mineralogy devoid of shoulder-bed averaging effects can be achieved through the implementation of algorithms, similar to those developed in the LWD spectroscopy tool, in tools where model architecture is available.

iv. The nonlinear inversion method is implemented as a joint interpretation of spectroscopy and matrix-sensitive logs results such that mineralogy yields matrix-sensitive logs that are consistent with corresponding measured field logs.

v. To avoid errors in the estimated mineralogy, elemental weight and lithology-sensing logs used in the interpretation should reflect the composition of formation minerals only. Substantial quality checks should be performed on logs used in the interpretation to ensure that they are not affected by environmental parameters that may propagate errors into the solution.

vi. Calculation of detailed mineral concentration logs facilitates the correction of assumed homogeneous matrix and fluid effects on neutron and density porosity logs and subsequently improves estimations of porosity and hydrocarbon saturation.

vii. Two synthetic and four field cases validate the applicability of the developed workflow in conventional and unconventional formations. In field cases, core measurements appraise the accuracy of estimated mineralogy, porosity, and water saturation. When measured mineral logs are grouped or unreliable, the presence of core data becomes crucial in validating mineralogy results.

viii. An average uniform initial guess equal to the reciprocal of the number of minerals present in the formation, at each depth and for each mineral, is sufficient to estimate mineralogy accurately. However, in underdetermined inversion problems, a reference vector having values estimated from spectroscopy mineral logs or core data is required to improve the stability of the matrix inversion problem.

ix. Commercial software for multi-mineral analysis typically does not use spectroscopy-based petrophysical interpretation workflows or assume non-deterministic and stochastic methods in well log calculations. The method introduced in this part of the dissertation invokes analytical physical relationships into multi-mineral analysis compared to probability functions that are often implemented in commercial solvers.

6.2.3 Part Three: Inversion-Based Interpretation of LWD Gamma-Ray Spectroscopy Measurements

i. A nonlinear gradient-based algorithm that utilizes the spectroscopy fast-forward model (in both inelastic and capture measurement modes) accurately quantifies layer elemental relative yields and weight concentrations.

ii. Tool physics, environmental, and geometrical effects can be included in the estimation method by constructing the Jacobian sensitivity matrix from spectroscopy FSFs and invoking the fast forward model within the inversion algorithm.

iii. The formation geometrical model, including layer thicknesses, well dip, and well azimuth, should be obtained from well logs that are accurately indicative of changes in layer petrophysical properties because significant errors in petrophysical properties arise from perturbations in true bed-boundary locations. As an example, porosity logs may not indicate changes in layer properties due to constant porosity although mineral concentrations may vary significantly. This condition results in the appraisal of fewer layers than are actually present in the formation, and it can cause erroneous estimations of layer elemental concentrations.

iv. The inversion method significantly decreases shoulder-bed averaging effects on elemental relative yield and weight logs. Corrections up to 0.3 yield fraction and 0.27 weight fraction are observed from the inversion-based interpretation of elemental relative yield and weight logs, respectively.

v. Because inelastic spectroscopy logs are less affected by shoulder-bed averaging than are capture spectroscopy logs, estimated layer elemental compositions are more accurate when inversion is achieved using inelastic compared to capture measurements. Regardless of the measurement mode interpreted through inversion, differences between model and estimated elemental compositions do not exceed 0.08 yield fraction or 0.02 weight fraction in synthetic cases.

vi. In field cases, optimal solution convergence is achieved when the initial guess of layer elemental yields or weights is obtained from corresponding bed-center spectroscopy logs and when a reference vector of the same value is included in the inversion.

vii. Error bars indicate a higher degree of uncertainty in elemental compositions estimated within thin beds, as opposed to thick layers, because of the difficulty in resolving the properties of layers that are below the vertical resolution of the LWD spectroscopy tool.

viii. Inversion methods essentially break down when layer thicknesses are below the vertical resolution of the tool. This necessitates the development of an additional interpretation technique to resolve elemental compositions in such laminated systems. A spectroscopy mixing law was used to quantify elemental weight concentrations

within laminations through the linear variation of elemental weight concentrations with respect to the volumetric concentration of an end member of a binary-lithology system. The developed inversion method and spectroscopy mixing law were validated in four synthetic and two field cases that appraise the accuracy and flexibility of the workflow.

ix. It is imperative to ensure that spectroscopy elemental logs are unaffected by environmental effects before estimated elemental compositions are used in any spectroscopy-based petrophysical interpretation. This step is required to ensure that elemental compositions are truly representative of formation properties and do not, for example, reflect components of drilling mud such as sulfur in barite.

6.2.4 Part Four: Inversion-Based Petrophysical Interpretation of LWD Gamma-Ray Spectroscopy Measurements

i. The spectroscopy fast-forward model was successfully and accurately implemented in a nonlinear gradient-based inversion method to quantify layer mineral volumetric and weight concentrations from elemental relative yield or weight logs.

ii. Because the forward model accounts for geometrical effects, the use of the forward model in the inversion method decreases shoulder-bed averaging effects on measured mineral logs (corrections as high as 0.34 mineral volume fraction are observed). The new method thereby facilitates the estimation of true layer mineralogy.

iii. Density image logs are better indicators of changes in layer petrophysical properties than are spectroscopy or gamma-ray image logs when lithology is constant but porosity and fluid saturations are changing.

iv. Mineral concentrations estimated through the inversion of inelastic spectroscopy elemental logs yield more accurate estimations of layer mineral concentrations because inelastic measurements are less affected by shoulder-bed averaging than are capture measurements.

v. Inversion calculations include a joint interpretation of spectroscopy and lithology sensing logs. Thus, they generate mineral concentrations that are petrophysically consistent with other well logs.

vi. Spectroscopy-based petrophysical interpretation improves estimations of porosity and water saturation through the correction of geometrical and petrophysical effects. The geometrical effect of shoulder-bed averaging is corrected through the developed inversion and mixing law methods. Petrophysical effects include the assumption of a homogeneous matrix composition in measured neutron and density porosity logs and are corrected by replacing the homogeneous matrix with inverted mineralogy.

vii. Thin-bed analysis is required in laminated formations to avoid false estimations of mineralogy as well as the underestimation of porosity and hydrocarbon saturation that arises due to averaging of true layer properties. This petrophysical interpretation in laminated formations is based on the developed spectroscopy mixing law and shaly-sand saturation models.

viii. Results from synthetic cases show that spectroscopy-based interpretation methods yield accurate estimations of mineralogy, porosity, and hydrocarbon saturation. The grouping of measured spectroscopy mineral logs into silicates, clays, and carbonates and the presence of shoulder-bed averaging effects in these mineral logs limit their usefulness in validating estimated layer mineralogy. Additional measurements such as core data can be used as an alternative to verify estimated layer mineralogy.

ix. To quantify true formation spectroscopy properties and achieve accurate spectroscopy-based petrophysical interpretation, sufficient quality control checks should be performed on well logs to ensure that they are not compromised by borehole or tool effects.

x. An accurate choice of minerals, obtained through geologic or core data information, should be included in the inversion to prevent false representations of nonexistent minerals or underdetermined estimation problems. In inversion problems that are inadvertently under-determined because the number of elements is still less than that of minerals, even when only minerals actually present in the formation are included in the inversion, solution convergence can be enhanced through the choice of an initial guess and the inclusion of a reference vector obtained from spectroscopy mineral logs, core, or geologic data.

6.3 RESEARCH CONTRIBUTIONS

This section lists the significant contributions that this dissertation introduces into spectroscopy interpretation methods.

i. The main technical contribution of this dissertation is the development of a novel method to numerically simulate spectroscopy elemental and mineral logs in an LWD spectroscopy tool. This method accounts for tool physics, formation, and environmental effects and facilitates the calculation of spectroscopy responses in the complicated well trajectories typically logged by LWD tools, such as in HA/HZ wells.

ii. The spectroscopy forward simulation method is versatile enough to be implemented for any tool model when tool-specific FSFs and elemental sensitivities are defined.

iii. In the absence of tool-specific FSFs and elemental sensitivities, I introduced a tool-independent method that quantifies mineralogy depth by depth. Because this method excludes tool-specific FSFs or elemental sensitivities, geometrical effects are not corrected in the mineralogy solution or in resultant estimations of porosities and water saturations.

iv. This dissertation presented the first robust numerical simulation and interpretation method that accounts for factors that significantly influence spectroscopy measurements such as tool, borehole, shoulder-bed, and well deviation effects. This method facilitated the quantification of true layer elemental and mineral compositions devoid of geometrical effects such as shoulder-bed averaging.

v. I introduced a new method to compute mineralogy that includes a joint interpretation with lithology-sensing logs such that estimated mineralogy is petrophysically consistent with other well-log measurements.

vi. A new method is presented here to correct matrix and fluid effects on measured neutron and density porosity logs based on detailed calculations of mineralogy, thus yielding improved estimations of total porosity and water saturation in conventional and unconventional formations.

vii. Combining interpretation of spectroscopy measurements with nuclear and resistivity logs, to quantify porosity and hydrocarbon saturation, established a petrophysical model that agrees with the physics of nuclear and resistivity measurements. This method corrected geometrical and petrophysical effects on well logs to reveal true formation properties.

viii. Spectroscopy-based petrophysical interpretation in thin-bedded formations requires specialized analysis that has not been previously studied. This dissertation addresses petrophysical interpretation in thin-bedded formations by developing a spectroscopy mixing law and utilizing a shaly-sand saturation model to quantify mineralogy, porosity, and hydrocarbon saturation within laminations.

6.4 RECOMMENDATIONS FOR BEST PRACTICES

The following recommendations outline best practices for the implementation of interpretation methods advanced in the research presented in this dissertation.

i. To accurately assess formation mineralogy from spectroscopy elemental measurements and other lithology-sensing logs (including gamma ray, matrix density, matrix Sigma, and photoelectric factor), these well logs must be indicative solely of rock-formation properties. In general, spectroscopy-based interpretation methods

should only be performed after quality checks indicate that environmental effects, such as washouts, invasion, tool, or borehole mud do not compromise the reliability of measured logs.

ii. Mineral analysis should be accompanied by validation with additional measurements such as core data, whenever possible, particularly when measured mineral logs are presented in major lithologic groups or are significantly affected by shoulder-bed averaging.

iii. The choice of minerals in the initial guess for matrix inversion should be based on *a priori* knowledge obtained from geologic reports or core data to circumvent the exclusion of existing minerals or the false representations of non-existing minerals in the solution. Minerals that are present in very low concentrations may be excluded from the interpretation given that their omission does not cause significant perturbations in subsequent petrophysical interpretation. Such an approach will minimize the occurrence of unstable mineralogy solutions due to underdetermined inversion problems in which the number of input elemental data is less than the number of minerals in the solution.

iv. In underdetermined inversion problems, in which the number of inversion outputs is more than that of available input data, the algorithm can be stabilized by the inclusion of a reference vector in the inversion cost function. Such a reference vector should be estimated from core, mineral, or geologic data to ensure that the solution converges to unique and stable values.

v. In formations that exhibit anomalous or locally varying mineral chemical properties, the assumption of fixed chemical formulas and properties in matrix inversion may be inaccurate. Core data should be used to calibrate mineral chemical formulas and properties dynamically.

vi. The interpretation of formation lithology from spectroscopy elemental logs should always be performed in conjunction with other lithology-sensing logs to ensure that the estimated mineralogy is consistent with these other well logs. This approach also decreases the non-uniqueness of the mineralogy solution and allows for the accurate estimation of a higher number of minerals.

vii. When possible, inelastic spectroscopy logs should be integrated with capture measurements to ensure more robust spectroscopy interpretation. Inelastic measurements can quantify certain elements (predominantly carbon and oxygen) that are not discernable in the capture measurement mode and exhibit a smaller volume of investigation compared to capture measurements.

viii. The choice of bed boundaries for inversion-based interpretation is optimally obtained based on the variability of both porosity and spectroscopy logs because variations in porosity and lithology do not always occur simultaneously in the subsurface. Other measurement data, such as density, gamma ray, and PEF images, can also be included in the bed-boundary analysis to ensure a consolidated and thorough solution.

ix. When there are no appreciable shoulder-bed averaging effects on measured spectroscopy logs, the depth-by-depth, spectroscopy-based, petrophysical interpretation methods introduced in this dissertation can reliably assess mineral and

petrophysical properties. However, in the presence of significant geometrical effects and laminations, it is necessary to implement inversion and spectroscopy mixing law methods in the estimation of mineralogy, porosity, and hydrocarbon saturation.

x. In the interpretation of field cases, each petrophysical zone needs to be accurately defined and analyzed independently. This approach is due to the assumption in the spectroscopy mixing law that the pure end-member lithology and the interval of interest are located within similar petrophysical zones such that the elemental compositions of the pure end-member lithologies are constant within the interval of interest. Similarly, in the inversion algorithm, there is an implicit assumption of constant geometrical and inversion parameters within each inversion depth window that necessitates separate analysis of each petrophysical zone. This technique also allows for the definition of distinct petrophysical parameters (such as Archie's constants) in each interval under study.

6.5 RECOMMENDATIONS FOR FUTURE WORK

The following are recommendations that could further advance the research introduced in this dissertation.

i. I suggest that interpretation methods, introduced for the LWD tool under study in this dissertation, be implemented in other tools to expand the application of this methodology. In particular, tools that acquire inelastic measurements should be studied because the LWD under study records only capture measurements.

ii. In implementing the interpretation methods developed for the LWD tool into wireline tools, invasion or borehole effects should be studied in detail because wireline tools are more affected by invasion than are LWD tools.

iii. Although Monte Carlo simulated spectra were benchmarked with laboratory data, I further recommend that laboratory experiments be performed to benchmark Monte Carlo or fast simulated spectroscopy elemental and mineral logs. These experiments should include capture as well as inelastic spectra to facilitate the benchmarking of Monte Carlo or fast simulated spectroscopy logs in both measurement modes.

Appendix A: Estimation of Mineral Concentrations from Elemental Relative Yields

Well logs of mineral concentrations can be obtained through nonlinear inversion of simulated elemental relative yield logs or weight concentrations. Inversion is based on the simple forward relationship between elements and minerals, expressed as

$$y_i = \frac{\sum_{j=1}^{n} \frac{Se_i \rho_j C_j N_{ij} MM_i}{MM_j}}{\sum_{i=1}^{m}\sum_{j=1}^{n} \frac{Se_i \rho_j C_j N_{ij} MM_i}{MM_j}}, \quad \text{(A-1)}$$

for inversion using elemental relative yields, and

$$M_i = \frac{\sum_{j=1}^{n} \frac{\rho_j C_j N_{ij} MM_i}{MM_j}}{\sum_{i=1}^{m}\sum_{j=1}^{n} \frac{\rho_j C_j N_{ij} MM_i}{MM_j}}, \quad \text{(A-2)}$$

for inversion using elemental weight concentrations, where subscripts *i* and *j* designate the index for *m* elements and *n* minerals, respectively, ρ_j is mineral density, C_j is mineral volumetric concentration, MM_i is the molar mass of element *i*, MM_j is the molar mass of mineral *j*, and N_{ij} is the number of atoms of the *i-th* element in the *j-th* mineral which is obtained from mineral chemical formulas. For lithology interpretation, this analysis is only performed for formation elements and minerals.

Elemental relative yields or weight concentrations are simulated at each measurement point via equation A-1 beginning with an initial guess of mineral volumetric concentrations. The solution is relatively insensitive to the initial guess and is

taken as a uniform average value. Inversion is restricted only to minerals present in the synthetic model to enhance convergence and decrease non-uniqueness of the solution, particularly in underdetermined cases where the number of input elements is smaller than the number of output minerals.

Errors between relative yields or weight concentrations simulated via equation A-1 or A-2, respectively, and measured logs are estimated from the minimization of the quadratic cost function given by

$$C(\mathbf{x}) = \left\| \mathbf{W}_d \cdot \left[\mathbf{g}(\mathbf{x}) - \mathbf{d}_m \right] \right\|_2^2 + \lambda^2 \left\| \mathbf{x} \right\|_2^2, \quad \text{(A-3)}$$

subject to $0 \le \mathbf{x}_j \le 1$,

and $\sum_{j=1}^{n} \mathbf{x}_j = 1$.

In equation A-3, **g** is the forward simulator expressed by equation A-1, **x** is a vector of mineral volumetric concentrations, $\mathbf{d}_m$ is a vector of measured elemental yield or weight logs, λ is the regularization (stabilization) parameter, $\mathbf{W}_d$ is a data weighting matrix, and *j* designates the mineral index. The regularization parameter is needed to manage potential instabilities in the search of **x** due to non-uniqueness, and noisy or inadequate data, by adjusting the weight given to the error and energy additive terms included in the quadratic cost function in equation A-3.

Iterative nonlinear minimization of the quadratic cost function (equation A-3) is performed using Occam's iterative method modified to include a data-weighting matrix (Hansen, 1994; Aster et al., 2013) given by

$$\left\{\left[\mathbf{J}^T\left(\mathbf{x}^k\right)\cdot\mathbf{W}_d^T\cdot\mathbf{W}_d\cdot\mathbf{J}\left(\mathbf{x}^k\right)\right]+\lambda^2\mathbf{I}\right\}\mathbf{x}^{k+1}=\mathbf{J}^T\left(\mathbf{x}^k\right)\left[\left(\mathbf{W}_d{}^T\cdot\mathbf{W}_d\right)\cdot\hat{\mathbf{e}}\right], \qquad \text{(A-4)}$$

where

$$\hat{\mathbf{e}}=\left[\mathbf{d}_m-\mathbf{g}\left(\mathbf{x}^k\right)+\mathbf{J}\left(\mathbf{x}^k\right)\mathbf{x}^k\right], \qquad \text{(A-5)}$$

$\mathbf{x}^k$ and $\mathbf{x}^{k+1}$ designate the vector of model properties at iteration k and the updated trial model at iteration k+1, respectively, **e** is the vector of data misfit, subscript T indicates transposition, and **J** is the Jacobian or sensitivity matrix which is defined by $\frac{\partial y_i}{\partial C_j}$, where

$$\frac{\partial y_i}{\partial C_j}=\frac{\sum_{i=1}^{m}\frac{Se_i\times\rho_j\times C_j\times N_{ij}\times MM_i}{MM_j}\left[\sum_{i=1}^{m}\frac{Se_i\times\rho_j\times N_{ij}\times MM_i}{MM_j}+\sum_{j=1}^{n}\sum_{ii=1}^{m}\left(\frac{Se_i\times\rho_j\times C_j\times N_{ij}\times MM_i}{MM_j}\right)_{ii\neq i}\right]}{\left[\sum_{j=1}^{n}\sum_{i=1}^{m}\left(\frac{Se_i\times\rho_j\times C_j\times N_{ij}\times MM_i}{MM_j}\right)\right]^2}-$$

$$\frac{\left[\sum_{j=1}^{n}\sum_{ii=1}^{m}\left(\frac{Se_i\times\rho_j\times C_j\times N_{ij}\times MM_i}{MM_j}\right)_{ii\neq i}\right]\left[\frac{Se_i\times\rho_j\times N_{ij}\times MM_i}{MM_j}+\sum_{ii=1}^{m}\left(\frac{Se_i\times\rho_j\times C_j\times N_{ij}\times MM_i}{MM_j}\right)_{ii\neq i}\right]}{\left(\sum_{j=1}^{n}\sum_{i=1}^{m}\frac{Se_i\times\rho_j\times C_j\times N_{ij}\times MM_i}{MM_j}\right)^2}, \qquad \text{(A-6)}$$

for inversion using elemental relative yields and

$$\frac{\partial M_i}{\partial C_j} = \frac{\sum_{i=1}^{m} \frac{\rho_j \times C_j \times N_{ij} \times MM_i}{MM_j} \left[\sum_{i=1}^{m} \frac{\rho_j \times N_{ij} \times MM_i}{MM_j} + \sum_{j=1}^{n} \sum_{ii=1}^{m} \left(\frac{\rho_j \times C_j \times N_{ij} \times MM_i}{MM_j} \right)_{ii \neq i} \right]}{\left[\sum_{j=1}^{n} \sum_{i=1}^{m} \left(\frac{\rho_j \times C_j \times N_{ij} \times MM_i}{MM_j} \right) \right]^2} - \frac{\left[\sum_{j=1}^{n} \sum_{ii=1}^{m} \left(\frac{\rho_j \times C_j \times N_{ij} \times MM_i}{MM_j} \right)_{ii \neq i} \right] \left[\frac{\rho_j \times N_{ij} \times MM_i}{MM_j} + \sum_{ii=1}^{m} \left(\frac{\rho_j \times C_j \times N_{ij} \times MM_i}{MM_j} \right)_{ii \neq i} \right]}{\left(\sum_{j=1}^{n} \sum_{i=1}^{m} \frac{\rho_j \times C_j \times N_{ij} \times MM_i}{MM_j} \right)^2},$$

(A-7)

for inversion using elemental weight concentrations, where subscript *ii* designates the index for *m* elements excluding element *i*. The initial guess is updated every iteration until the norm of the difference between measured and numerically simulated logs is equal to or less than 0.0001 for a maximum of ten iterations. This cut-off in the number of iterations is implemented because sensitivity analysis shows that convergence is typically achieved in fewer than ten iterations.

Through sensitivity analysis I find that the optimal value for the data weighting matrix to minimize the relative error between simulated and measured data is a diagonal matrix with entries of 0.05 corresponding to each element. The regularization (stabilization) parameter in the quadratic cost function is obtained using an L-curve strategy (Hansen, 1994) which calculates a value that best minimizes the norm of the

error between numerically simulated and measured logs at each iteration. The impact of λ progressively diminishes from the cost function expressed in equation A-1 as the algorithm reaches convergence.

I define uncertainty bars with a 95% confidence interval for each inverted parameter using a modification to the covariance approach of evaluating uncertainty bars in nonlinear inverse problems (Aster et al., 2013). The 95% confidence interval is defined as

$$\pm 1.96 q^{-\frac{1}{4}} \sqrt{\left\| \mathbf{W}_d \cdot \mathbf{e}(\mathbf{x}) \right\|_2^2 \cdot diag\left\{ \left[\mathbf{J}^T \cdot \mathbf{W}_d^T \cdot \mathbf{W}_d \cdot \mathbf{J} \right]^{-1} \right\}}, \quad \text{(A-8)}$$

where *diag* describes the diagonal matrix entries and q is a constant equal to the inverse of the fourth root of the number of degrees of freedom in the inversion problem. This approach assumes that the distribution of estimated properties follows a normal distribution. Confidence intervals quantify the stability of inversion results and uncertainty in inverted mineral volumetric compositions due to perturbations in the input data. Mineral weight concentrations, $C_{w,j}$ can be estimated from volumetric compositions as

$$C_{w,j} = \frac{\rho_j C_j}{\sum_{j=1}^{n} \rho_j C_j}, \quad \text{(A-9)}$$

This inversion procedure takes an average of 0.03s CPU time per measurement point due to the simplicity of its governing forward analytical relationship described in equation A-1.

Appendix B: Calculation of Jacobian Matrix Entries

B.1 Matrix Inversion of Spectroscopy Elemental Relative Yield or Weight Logs

The first-order derivative of elemental relative yields with respect mineral volumetric concentrations at a single measurement point, *r*, is given by

$$\frac{\partial y_i}{\partial C_j} = \frac{\sum_{i=1}^{m} FSF_{jac}}{\left(\sum_{j=1}^{n} \sum_{i=1}^{m} FSF_{jac} \frac{Se_i \times \rho_j \times C_j \times N_{ij} \times MM_i}{MM_j} \right)^2} \left[\frac{Se_i \times \rho_j \times C_j \times N_{ij} \times MM_i}{MM_j} \left[\sum_{i=1}^{m} FSF_{jac} \frac{Se_i \times \rho_j \times N_{ij} \times MM_i}{MM_j} + \sum_{j=1}^{n} \sum_{ii=1}^{m} \left(\frac{FSF_{jac}}{\frac{Se_i \times \rho_j \times C_j \times N_{ij} \times MM_i}{MM_j}} \right)_{ii \neq i} \right] \right] -$$

$$\frac{\left[\sum_{j=1}^{n} \sum_{ii=1}^{m} \left(\frac{FSF_{jac}}{\frac{Se_i \times \rho_j \times C_j \times N_{ij} \times MM_i}{MM_j}} \right) \right] \left[FSF_{jac} \frac{Se_i \times \rho_j \times N_{ij} \times MM_i}{MM_j} + \sum_{ii=1}^{m} \left(\frac{FSF_{jac}}{\frac{Se_i \times \rho_j \times C_j \times N_{ij} \times MM_i}{MM_j}} \right)_{ii \neq i} \right]}{\left(\sum_{j=1}^{n} \sum_{i=1}^{m} FSF_{jac} \frac{Se_i \times \rho_j \times C_j \times N_{ij} \times MM_i}{MM_j} \right)^2},$$

(B-1)

for inversion using elemental relative yield logs. The first-order derivative of elemental weight concentrations with respect mineral volumetric concentrations at a single measurement point, *r*, is given by

$$\frac{\partial M_i}{\partial C_j} = \frac{\sum_{i=1}^{m} FSF_{jac}}{\left(\sum_{j=1}^{n} \sum_{i=1}^{m} FSF_{jac} \frac{\rho_j \times C_j \times N_{ij} \times MM_i}{MM_j} \right)^2} \left[\frac{\rho_j \times C_j \times N_{ij} \times MM_i}{MM_j} \left[\sum_{i=1}^{m} FSF_{jac} \frac{\rho_j \times N_{ij} \times MM_i}{MM_j} + \sum_{j=1}^{n} \sum_{ii=1}^{m} \left(\frac{FSF_{jac}}{\frac{\rho_j \times C_j \times N_{ij} \times MM_i}{MM_j}} \right)_{ii \neq i} \right] \right] -$$

$$\frac{\left[\sum_{j=1}^{n} \sum_{ii=1}^{m} \left(\frac{FSF_{jac}}{\frac{\rho_j \times C_j \times N_{ij} \times MM_i}{MM_j}} \right) \right] \left[FSF_{jac} \frac{\rho_j \times N_{ij} \times MM_i}{MM_j} + \sum_{ii=1}^{m} \left(\frac{FSF_{jac}}{\frac{\rho_j \times C_j \times N_{ij} \times MM_i}{MM_j}} \right)_{ii \neq i} \right]}{\left(\sum_{j=1}^{n} \sum_{i=1}^{m} FSF_{jac} \frac{\rho_j \times C_j \times N_{ij} \times MM_i}{MM_j} \right)^2}, \quad \text{(B-2)}$$

for inversion using elemental weight concentration logs, where subscript *i* represents the index for *m* elements, *j* represents the index for *n* minerals, *ii* designates the index for *m* elements excluding element *i*, N_{ij} represents the number of atoms of element, *i* in mineral, *j*; *MM* represents molar mass, and *Se* represents relative detection sensitivity of each element to the production of gamma rays. FSF_{jac} indicates the sensitivity at a single

measurement point to an *f*-th layer and is calculated from the normalized FSF for all materials within the volume of investigation of the detector using the FSF and 3D earth model at a single measurement point in the forward simulation.

B.2 Matrix Inversion of Layer Elemental Relative Yields or Weight Concentrations

The first-order derivative of elemental relative yields with respect mineral volumetric concentrations in each layer, *f*, is given by

$$\frac{\partial y_i}{\partial C_j} = \frac{\sum_{i=1}^{m} \frac{Se_j \times \rho_j \times C_j \times N_{ij} \times MM_i}{MM_j} \left[\sum_{i=1}^{m} \frac{Se_j \times \rho_j \times N_{ij} \times MM_i}{MM_j} + \sum_{j=1}^{n} \sum_{ii=1}^{m} \left(\frac{Se_j \times \rho_j \times C_j \times N_{ij} \times MM_i}{MM_j} \right)_{ii \neq i} \right]}{\left(\sum_{j=1}^{n} \sum_{i=1}^{m} \frac{Se_j \times \rho_j \times C_j \times N_{ij} \times MM_i}{MM_j} \right)^2} - \frac{\left[\sum_{j=1}^{n} \sum_{ii=1}^{m} \left(\frac{Se_j \times \rho_j \times C_j \times N_{ij} \times MM_i}{MM_j} \right) \right] \left[\sum_{i=1}^{m} \frac{Se_j \times \rho_j \times N_{ij} \times MM_i}{MM_j} + \sum_{j=1}^{n} \sum_{ii=1}^{m} \left(\frac{Se_j \times \rho_j \times C_j \times N_{ij} \times MM_i}{MM_j} \right)_{ii \neq i} \right]}{\left(\sum_{j=1}^{n} \sum_{i=1}^{m} \frac{Se_j \times \rho_j \times C_j \times N_{ij} \times MM_i}{MM_j} \right)^2},$$

(B-3)

for inversion using layer elemental relative yields. The first-order derivative of elemental relative yields with respect mineral volumetric concentrations in each layer, *f*, is given by

$$\frac{\partial M_i}{\partial C_j} = \frac{\sum_{i=1}^{m} \frac{\rho_j \times C_j \times N_{ij} \times MM_i}{MM_j} \left[\sum_{i=1}^{m} \frac{\rho_j \times N_{ij} \times MM_i}{MM_j} + \sum_{j=1}^{n} \sum_{ii=1}^{m} \left(\frac{\rho_j \times C_j \times N_{ij} \times MM_i}{MM_j} \right)_{ii \neq i} \right]}{\left(\sum_{j=1}^{n} \sum_{i=1}^{m} \frac{\rho_j \times C_j \times N_{ij} \times MM_i}{MM_j} \right)^2} -$$

$$\frac{\left[\sum_{j=1}^{n} \sum_{ii=1}^{m} \left(\frac{\rho_j \times C_j \times N_{ij} \times MM_i}{MM_j} \right)_{ii \neq i} \right] \left[\frac{\rho_j \times N_{ij} \times MM_i}{MM_j} + \sum_{ii=1}^{m} \left(\frac{\rho_j \times C_j \times N_{ij} \times MM_i}{MM_j} \right)_{ii \neq i} \right]}{\left(\sum_{j=1}^{n} \sum_{i=1}^{m} \frac{\rho_j \times C_j \times N_{ij} \times MM_i}{MM_j} \right)^2},$$

(B-4)

for inversion using layer elemental weight concentrations.

Measured aluminum spectra are weak but strongly correlated with spectra from other elements, particularly iron. Aluminum is therefore not directly simulated or included in the inversion but modeled from other elemental weight concentrations (Herron and Herron, 1996). The aluminum modeling equation is given by

$$M_{Aluminum} = 0.38\left(1 - 2.139 M_{Silicon} - 2.497 M_{Calcium} - 1.99 M_{Iron}\right), \qquad \text{(B-5)}$$

for the LWD spectroscopy tool under study, where $M_{Aluminum}$, $M_{Silicon}$, $M_{Calcium}$, and M_{Iron} represent the solid weight fraction of aluminum, silicon, calcium, and iron respectively.

The Jacobian matrix entries $\frac{\partial y_{Al}}{\partial C_j}$ and $\frac{\partial M_{Al}}{\partial C_j}$ are therefore calculated from equation B-5 in the estimation of mineralogy.

List of Symbols

a	Archie's Winsauer constant
Al	Aluminum chemical symbol
AT10	Array induction two foot A10 resistivity measurements
AT20	Array induction two foot A20 resistivity measurements
AT30	Array induction two foot A30 resistivity measurements
AT60	Array induction two foot A60 resistivity measurements
AT90	Array induction two foot A90 resistivity measurements
C	Carbon chemical symbol
$C(\mathbf{x})$	Quadratic cost function
C_j	Volumetric concentration of mineral j (fraction)
$C_{end\ member\ 1}$	Volumetric concentration of first end member of laminated sequence (fraction)
$C_{end\ member\ 2}$	Volumetric concentration of second end member of laminated sequence (fraction)
C_{sh}	Volumetric concentration of shale (fraction)
$C_{w,j}$	Mineral, j-th weight concentration (fraction)
Ca	Calcium chemical symbol
Cl	Chlorine chemical symbol
d	Measured spectrum

$\mathbf{d}$	Numerically simulated measurement
$\mathbf{d}_m$	Measured log
$\mathbf{e}$	Vector of data misfit
$\hat{\mathbf{e}}$	Modified vector of data misfit
$\mathbf{E}$	Estimator matrix
F	Depth varying normalization factor
Fe	Iron chemical symbol
g	Number of layers
$\mathbf{g}$	Forward simulator
h	Layer thickness (m)
$\mathbf{J}$	Jacobian matrix
$\mathbf{J}_{y\text{-}C}$	Jacobian matrix of elemental relative yields with respect to mineral volumetric concentrations
$\mathbf{J}_{y\text{-}M}$	Jacobian matrix of elemental relative yields with respect to elemental weight concentrations
$\mathbf{J}_{y-y_{abs}}$	Jacobian matrix of elemental relative yields with respect to elemental absolute yields
$\mathbf{J}_{M\text{-}C}$	Jacobian matrix of elemental weight concentrations with respect to mineral volumetric concentrations
K	Potassium chemical symbol
K	Mass concentration of Potassium (%).

L_d	Diffusion length (cm)
L_m	Migration length (cm)
L_s	Slowing-down length (cm)
m	Number of elements
m	Vector of measured spectrum data
M_i	Weight concentration of element i (fraction)
MeV	Megaelectron volts (10^6 eV)
Mg	Magnesium chemical symbol
MM	Molecular weight
n	Number of minerals
N_{ij}	Number of atoms of element i in mineral j
p	Vector of measured pulse height spectra
q	Number of degrees of freedom
r	Number of measurement points
r	Position vector in 3D space
R	Detector response
R_s	Sand (non-shale) resistivity (Ω-m)
R_{sh}	Shale resistivity (Ω-m)
R_t	Total resistivity (Ω-m)
R_w	Formation water resistivity
S	Sulfur chemical symbol
S_h	Hydrocarbon saturation (fraction)

S_w	Water saturation (fraction)
Se	Elemental relative detection sensitivity
Si	Silicon chemical symbol
t	Number of pulse height channels
T	Temperature
Th	Mass concentration of Thorium (ppm)
U	Mass concentration of Uranium (ppm)
v	Number of gamma-ray energy bins
$\mathbf{W}_d$	Data-weighting matrix
$\mathbf{W}_x$	Model-weighting matrix
x	Vector of model properties
$y_{abs,\,i}$	Absolute yield of element i (Energy integrated spectrum of element i) (fraction)
y_i	Relative yield of element i (fraction)
y	Vector of elemental yields
α	Gamma-ray coefficient
β	Gamma-ray coefficient
ξ	Inverse of migration length (cm^{-1})
γ	Gamma-ray coefficient
λ	Regularization parameter
Ω-m	Ohm-meter
ϕ	Porosity (p.u.)

$\boldsymbol{\psi}$	Vector of MCNP-simulated gamma-ray current spectrum on the detector surface
ρ	Density (g/cc)
Σ	Sigma (c.u.)

List of Acronyms

1D	One Dimensional
2D	Two Dimensional
3D	Three Dimensional
c.u.	capture units
CAR	Carbonate (fraction)
CLA	Clay (fraction)
Cov(x)	Modified covariance matrix
CPU	Computer Processing Unit
DOI	Depth of Investigation
FSAL	Formation Salinity
FSF	Flux Sensitivity Function
FT-IR	Fourier Transform-Infrared spectroscopy
GR	Gamma Ray (API)
HA	High-Angle
HA/HZ	High-Angle/Horizontal

LWD	Logging-While-Drilling
MCNP	Monte Carlo N-Particle Code
MD	Measured Depth (m)
N-D	Neutron-density
$NaCl_{ppm}$	Formation water salinity
p.u.	Porosity units
P16H	Phase Shift Resistivity 16 inch Spacing at 2 MHz, Environmentally Corrected
P22H	Phase Shift Resistivity 22 inch Spacing at 2 MHz, Environmentally Corrected
P28H	Phase Shift Resistivity 28 inch Spacing at 2 MHz, Environmentally Corrected
P34H	Phase Shift Resistivity 34 inch Spacing at 2 MHz, Environmentally Corrected
P40H	Phase Shift Resistivity 40 inch Spacing at 2 MHz, Environmentally Corrected
PEF	Photoelectric Factor (b/e)
PYR	Pyrite (fraction)
QFM	Quartz-Feldspar-Mica group (fraction)
RMS	Root-Mean-Square
SNUPAR	Schlumberger's Nuclear Parameter calculation program
TEMP	Temperature

TOC	Total Organic Carbon Content
TST	True Stratigraphic Thickness
TVD	True Vertical Depth (m)
XRD	X-Ray Diffraction
XRF	X-Ray Fluorescence

Subscripts

abs	Absolute
B	Background
calc	Calculated
D	Density
f	Layer index
g	Number of beds
h	Hydrocarbon
i	Element index
j	Mineral index
jac	Jacobian
log	Log values
m	Migration
n	Total number of minerals
N	Neutron
p	Measurement point index

ref	Reference
R	Detector position
s	Sand (non-shale)
sh	Shale
sim	Simulated
t	Total
w	Water

Superscripts

C	Corrected
k	Iteration number
m	Archie's porosity exponent
n	Archie's saturation exponent
T	Transpose
z	*z*-th order Taylor's series term

References

Abdollah-Pour, R., 2011, Development and application of a 3D equation-of-state compositional fluid-flow simulator in cylindrical coordinates for near-wellbore phenomena: Dissertation, The University of Texas at Austin.

Adiguna, H., 2012, Comparative study for the interpretation of mineral concentrations, total porosity, and TOC in hydrocarbon-bearing shale from conventional well logs: Dissertation, The University of Texas at Austin.

Ajayi, O., C. Torres-Verdín, and W. E. Preeg, 2014, Rapid simulation and inversion-based interpretation of gamma ray spectroscopy logs in high-angle and horizontal wells: Transactions of the Society of Petrophysicists and Well Log Analysts, 55th Annual Logging Symposium, paper VVV.

Allen, L. S., C. W. Tittle, W. R. Mills, and R. L. Caldwell, 1967, Dual-spaced neutron logging for porosity: Geophysics, **32**, no. 1, 60-68, doi: 10.1190/1.1439857.

Archie, G. E., 1942, The electrical resistivity log as an aid in determining some reservoir characteristics: Petroleum Transactions of AIME, **146**, no. 1, 54-62. doi: 10.2118/942054-G.

Aster, R. C., B. Borchers, and C. H. Thurber, 2013, Parameter estimation and inverse problems: Elsevier.

Bishop, M., 2008, Introduction to Chemistry: Chiral Publishing Company.

Booth, T. E. and J. S. Hendricks, 1984, Importance estimation in forward Monte Carlo calculations: Nuclear Technology/Fusion, **5**, 90-100.

Busch, J. M., W. G. Fortney, and L. N. Berry, 1987, Determination of lithology from well logs by statistical analysis: SPE Formation Evaluation, **2**, no. 4, 412-418, doi: 10.2118/14301-PA.

Clavier, C. and D. H. Rust, 1976, MID-plot: a new lithology technique: The Log Analyst, **17**, no. 6, 16-24.

Cuddy, S. J., 2000, Litho-facies and permeability prediction from electrical logs using fuzzy logic: SPE Reservoir Evaluation and Engineering, **3**, no. 4, 319-324, doi: 10.2523/49470-ms.

Cywicka-Jakiel, T., 2007, Improvement of the MCNP-simulated n-gamma spectrometer response function using the new ENDF/B-VI evaluations for thermal neutron capture: Nuclear Instruments and Methods in Physics Research, Section A, **580**, no. 1, 94-97, doi: 10.1016/j.nima.2007.05.045.

Doveton, J. H., 1994, Geologic log analysis using computing methods: AAPG Computer Applications in Geology, no. 2, Tulsa, OK.

Ellis, D. V. and J. M. Singer, 2007, Well logging for earth scientists: Springer.

Eslinger, E. and F. Boyle, 2013, Building a multi-well model for partitioning spectroscopy log elements into minerals using core mineralogy for calibration: Transactions of the Society of Petrophysicists and Well Log Analysts, 54th Annual Logging Symposium, paper HH.

Evans, M. L., 1981, A computer model for calculating gamma-ray pulse-height spectra for logging applications: Gamma-ray logging workshop, Los Alamos National Laboratory, LA-UR-81-400.

Flaum, C. and G. Pirie, 1981, Determination of lithology from induced gamma-ray spectroscopy: Transactions of the Society of Petrophysicists and Well Log Analysts, 22nd Annual Logging Symposium, paper H.

Galford, J. and R. C. Hertzog, 1989, Variance reduction techniques for improved derived elemental concentrations from fitting prompt neutron capture gamma spectra: IEEE Transactions on Nuclear Science, **36**, no. 1, 1232-1236, doi: 10.1109/23.34638.

Galford, J., J. Quirein, S. Shannon, J. Traux, and J. Witkowsky, 2009, Field tests results of a new neutron-induced gamma-ray spectroscopy geochemical logging tool: Society of Petroleum Engineers Annual Technical Conference and Exhibition Proceedings, SPE 123992, doi: 10.2118/123992-ms.

Gaymard, R. and A. Poupon, 1968, Response of neutron and formation density logs in hydrocarbon bearing formations: The Log Analyst, **9**, 3-11.

Gilchrist, W. A., J. A. Quirein, Y. L. Boutemy, and J. R. Tabanou, 1982, Application of gamma ray spectroscopy to formation evaluation: Transactions of the Society of Petrophysicists and Well Log Analysts, 23rd Annual Logging Symposium, paper B.

Givens, N. and H. Zhao, The Barnett shale: not so simple after all, accessed 11/4/2014; http://www.republicenergy.com/?tabid=98.

Gonçalves, C. A., P. K. Harvey, M. A. Lovell, 1995, Application of a multilayer neural network and statistical techniques in formation characterization: Transactions of the Society of Petrophysicists and Well Log Analysts, 36th Annual Logging Symposium, paper FF.

Grau, J. A., J. S. Schweitzer, D. V. Ellis, and R. C. Hertzog, 1989, A geological model for gamma-ray spectroscopy logging measurements: Nuclear Geophysics, **3**, no. 4, 351-359.

Grau, J. A., J. S. Schweitzer, and R. C. Hertzog, 1990, Statistical uncertainties of elemental concentrations extracted from neutron-induced gamma-ray measurements: IEEE Transactions on Nuclear Science, **37**, no. 6, 2175-2178, doi: 10.1109/TNS.1990.574209.

Haley, R. A., 1995, Pulsed-neutron capture log interpretation in laminated formations: a dual-exponential-decay model: Society of Petroleum Engineers Formation Evaluation, **10**, no. 1, 20-25, doi: 10.2118/26126-PA.

Hansen, P. C., 1994, Regularization tools: A Matlab package for analysis and solution of discrete ill-posed problems: Numerical Algorithms, **6**, no. 1, 1-35, doi: 10.1007/bf02149761.

Hardman, R. H. and L. C. Shen, 1987, Charts for correcting effects of formation dip and hole deviation on induction logs: The Log Analyst, **28**, no. 4, 349-356, issn: 0024-581X.

Heidari, Z., C. Torres-Verdín, and W. E. Preeg, 2012, Improved estimation of mineral and fluid volumetric concentrations in thinly-bedded and invaded formations: Geophysics, **77**, no. 3, WA79-WA98, doi: 10.1190/geo2011-0454.1.

Herron, S. L., and M. M. Herron, 1996, Quantitative lithology: an application for open and cased hole spectroscopy: Transactions of the Society of Petrophysicists and Well Log Analysts, 37th Annual Logging Symposium, paper E.

Herron, S. L. and M. M. Herron, 2000, Application of nuclear spectroscopy logs to the derivation of formation matrix density: Transactions of the Society of Petrophysicists and Well Log Analysts, 41st Annual Logging Symposium, paper JJ.

Herron, M. M., S. L., Herron, J. A. Grau, N. V. Seleznev, J. Phillips, A. E. Sherif, S. Farag, J. P. Horkowtiz, T. J. Neville, and K. Hsu, 2002, Real-time petrophysical analysis in siliciclastics from the integration of spectroscopy and triple-combo logging: Society of Petroleum Engineers Annual Technical Conference and Exhibition Proceedings, SPE 77631, doi: 10.2523/77631-ms.

Hertzog, R. C., 1978, Laboratory and field evaluation of an inelastic neutron scattering and capture gamma-ray spectrometry tool: Society of Petroleum Engineers Annual Technical Conference and Exhibition Proceedings, SPE 7430, doi: 10.2118/7430-PA.

Hertzog, R. C., 1979, Neutron-excited gamma-ray spectrometry for well logging: IEEE Transactions on Nuclear Science, vol. **26**, no. 1, 1558-1567, doi: 10.1109/TNS.1979.4330439.

Hertzog, R. C., L. Colson, B. Seeman, M. O'Brien, H. Scott, D. McKeon, P. Wraight, J. Grau, D. Ellis, J. Schweitzer, and M. Herron, 1989, Geochemical logging with spectrometry tools: SPE Formation Evaluation, June issue, 153-162, doi: 10.2118/16792-PA.

Ijasan, O., C. Torres-Verdín, W. E. Preeg, and A. Mendoza, 2011, Rapid modeling of LWD nuclear measurements acquired in high-angle and horizontal wells for improved petrophysical and geometrical interpretation: Transactions of the Society of Petrophysicists and Well Log Analysts, 52nd Annual Logging Symposium, paper R.

Ijasan, O., C. Torres-Verdín, and W. E. Preeg, 2013, Inversion-based petrophysical interpretation of logging-while-drilling nuclear and resistivity measurements: Geophysics, **78**, no. 6, D473-D489, doi: 10.1190/geo2013-0175.1.

Lewis, E. and W. F. Miller, 1993, Introduction to nuclear engineering: American Nuclear Society.

Liu, Z., Torres-Verdín, C., Wang, G. L., Mendoza, A., Zhu, P., and Terry, R., 2007, Joint inversion of density and resistivity logs for the improved petrophysical assessment of thinly-bedded clastic rock formations: Transactions of the Society of Petrophysicists and Well Log Analysts, 48th Annual Logging Symposium, paper VV.

Mayer, C. and A. Sibbit, 1980, Global, a new approach to computer-processed log interpretation: Society of Petroleum Engineers Annual Technical Conference and Exhibition Proceedings, SPE 9341, doi: 10.2523/9341-ms.

McKeon, D. C. and H. D. Scott, 1989, SNUPAR-a nuclear parameter code for nuclear geophysics applications: IEEE Transactions on Nuclear Science, **36**, no. 1, 1215-1219., doi: 10.1109/23.34634.

Mendoza, A., C. Torres-Verdín, and W. Preeg, 2010a, Linear iterative refinement method for the rapid simulation of borehole nuclear measurements: Part I: Vertical wells: Geophysics, **75**, no. 1, E9–E29, doi: 10.1190/1.3267877.

Mendoza, A., C. Torres-Verdín, and W. Preeg, 2010b, Linear iterative refinement method for the rapid simulation of borehole nuclear measurements: Part 2: High-angle and horizontal wells: Geophysics, **75**, no. 1, E79–E90, doi: 10.1190/1. 3335953.

Mendoza, A., O. Ijasan, C. Torres-Verdín, W. E. Preeg, J. Rasmus, R. J. Radtke, and E. Stockhausen, 2012, Inversion-based method for interpretation of logging-while-drilling density measurements in high-angle and horizontal wells: Geophysics, **77**, no. 4, D113–D127, doi: 10.1190/geo2012-0002.1.

Mimoun, J. G., C. Torres-Verdín, and W. E. Preeg, 2011a, Quantitative interpretation of pulsed neutron capture logs: Part 1: Fast numerical simulation: Geophysics, **76**, no.3, E81–E93, doi: 10.1190/1.3569600.

Mimoun, J. G., C. Torres-Verdín, and W. E. Preeg, 2011b, Quantitative interpretation of pulsed neutron capture logs: Part 2: inversion of measurements in thinly-bedded formations: Geophysics, **76**, no.3, E95–E103, doi: 10.1190/1.3569111.

Neville, T. J., O. Faivre, and H. T. Sun, 2005, Integrated interpretation of a rich data set from a new-generation LWD tool: Society of Petroleum Engineers Annual

Technical Conference and Exhibition Proceedings, SPE 97224, doi: 10.2523/97224-ms.

Ortega, E., C. Torres-Verdín, and W. E. Preeg, 2014a, Rapid forward modeling of multidetector logging-while-drilling Sigma measurements: Geophysics, **79**, no.4, D253–D273, doi: 10.1190/geo2014-0031.1.

Ortega, E., 2014b, Inversion-based petrophysical interpretation of multi-detector logging-while-drilling Sigma measurements: Dissertation, The University of Texas at Austin.

Passey, Q. R., K. E. Dahlberg, K. B. Sullivan, H. Yin, Y. H. Xiao, A. G. Guzman-Garcia, and R. A. Brackett, 2004, A systematic approach to evaluate hydrocarbons in thinly bedded reservoirs: Transactions of the Society of Petrophysicists and Well Log Analysts, 45th Annual Logging Symposium, paper NNN.

Passey, Q. R., H. Yin, C. M. Rendeiro, and D. E. Fitz, 2005, Overview of high-angle and horizontal well formation evaluation – Issues, learnings, and future directions: Transactions of the Society of Petrophysicists and Well Log Analysts, 46th Annual Logging Symposium, paper A.

Pemper, R., A. Sommer, P. Guo, D. Jacobi, S. B. Longo, E. Rodriguez, F. Mendez, and X. Han, 2006, A new pulsed neutron sonde for derivation of formation lithology and mineralogy: Society of Petroleum Engineers Annual Technical Conference and Exhibition Proceedings, SPE 102770, doi: 10.2523/102770-ms.

Plumb, R. A., and S. M. Luthi, 1989, Analysis of borehole images and their application to geologic modeling of an eolian reservoir: Society of Petroleum Engineers Formation Evaluation, **4**, no. 4, 505-514.

Poupon, A., M. E. Loy, and M. P. Tixier, 1954, A contribution to electrical log interpretation in shaly sands: Journal of Petroleum Technology, **6**, no. 6, 27-34.

Poupon, A. and J. Leveaux, 1971, Evaluation of water saturation in shaly formations: The Log Analyst, **12**, no. 4, 3-8.

Quirein, J., S. Kimminau, J. LaVigne, J. Singer, and F. Wendel, 1986, A coherent framework for developing and applying multiple formation evaluation models: Transactions of the Society of Petrophysicists and Well Log Analysts, 27th Annual Logging Symposium, paper DD.

Radtke, R. J., M. Lorente, B. Adolph, M. Berheide, S. Fricke, J. Grau, S. Herron, J. Horkowitz, B. Jorion, D. Madio, D. May, J. Miles, L. Perkins, O. Philip, B. Roscoe, B. Rose, D. Rose, and Stoller, C., 2012, A new capture and inelastic spectroscopy tool takes geochemical logging to the next level: Transactions of the Society of Petrophysicists and Well Log Analysts, 53rd Annual Logging Symposium, paper AAA.

Rasmus, J., R. Altman, T. Barber, M. Javalagi, 2009, Workflow for determining true formation resistivity in HAHZ wells: Transactions of the Society of Petrophysicists and Well Log Analysts, 50th Annual Logging Symposium.

Sanchez-Ramirez, J. A., C. Torres-Verdín, G. L. Wang, A. Mendoza, D. Wolf, Z. Liu, and G. Schell, 2009, Field examples of the combined petrophysical inversion of

gamma-ray, density, and resistivity logs acquired in thinly-bedded clastic rock formations: Transactions of the Society of Petrophysicists and Well Log Analysts, 50th Annual Logging Symposium, paper DDD.

Sarg, J. F., 2012, The Bakken-an unconventional petroleum and reservoir system: Oil and Natural Gas Technology Final scientific/technical report.

Schlumberger Limited, 2009, Log interpretation charts: Schlumberger.

Schweitzer, J. S., R. A. Manete, and R. C. Hertzog, 1984, Gamma Ray Spectroscopy Tool: Environmental Effects: Journal of Petroleum Technology, 36, no. 9, 1527–1534, doi: 10.2118/11144-pa.

Tsang, J. S. K. and M. L. Evans, 1983, Monte Carlo computational model for the gamma-ray spectroscopy tool (GST): Society of Petroleum Engineers of AIME Annual Technical Conference and Exhibition Proceedings, SPE 12052, doi: 10.2523/12052-ms.

Uzoh, E. A., A. Mendoza, C. Torres-Verdín, W. E. Preeg, E. J. Stockhausen, and J. C. Rasmus, 2009, Influence of relative dip angle and bed thickness on LWD density images acquired in high-angle and horizontal wells: Petrophysics, **50**, no. 3, 269-293.

Watson, C. C., 1984, Monte Carlo computation of differential sensitivity functions: Transactions of the American Nuclear Society, **46**, 655-656.

Watson, C. C., 1992, A spatial sensitivity analysis technique for neutron and gamma-ray measurements: Transactions of the American Nuclear Society, **65**, 3-4.

Weller, G., T. El-Halawani, I. Tribe, T. K. Webb, C. Stoller, S. Galvin, and G. Scott, 2005, A new integrated LWD platform delivers improved drilling efficiency, well placement, and formation evaluation services: Society of Petroleum Engineers Annual Technical Conference and Exhibition Proceedings, SPE 96652, doi: 10.2523/96652-ms.

Westaway, P., R. Hertzog, and R. E. Plasek, 1980, Neutron-induced gamma ray spectroscopy for reservoir analysis: Society of Petroleum Engineers Annual Technical Conference and Exhibition Proceedings, SPE 9461, doi: 10.2118/9461-PA.

Witkowsky, J., J. Galford, J. Quirein, and J. Truax, 2012, Predicting pyrite and total organic carbon from well logs for enhancing shale reservoir interpretation: Society of Petroleum Engineers Annual Technical Conference and Exhibition Proceedings, SPE 161097, doi: 10.2118/161097-ms.

X-5 Monte Carlo Team, 2005, MCNP — A general Monte Carlo N-particle transport code: Overview and theory, version 5, vol. 1: Los Alamos National Laboratory.

Yin, H., P. Guo, A. Mendoza, 2008, Comparison of processing methods to obtain accurate bulk density compensation and azimuthal density images from dual-detector gamma density measurements in high-angle and horizontal wells: Transactions of the Society of Petrophysicists and Well Log Analysts, 49th Annual Logging Symposium, paper M.

ZuoAn, Z., X. Tang, D. Yu, D. Murray, and H. Zhao, 2010, Use of elemental capture spectroscopy to accurately determine reservoir lithology and porosity in high

pressure and high H_2S environment: Society of Petroleum Engineers Annual Technical Conference and Exhibition Proceedings, SPE 131210, doi: 10.2118/131210-ms.

Vita

Oyinkansola Ajayi received a B.Sc (2007) in Chemical Engineering from the University of Lagos, Nigeria, and an M.Sc. (2013) in Petroleum Engineering from The University of Texas at Austin. In the summer of 2010, she worked as a research intern at ExxonMobil Upstream Research Company. Her work at ExxonMobil focused on modeling and interpretation of neutron-gamma density measurements. She also interned for Schlumberger Houston Formation Evaluation, Sugarland, Texas and Schlumberger-Doll Research, Cambridge, Massachussetts in the summer of 2011 working on the numerical simulation and interpretation of nuclear spectroscopy measurements. In the summer of 2013, she worked as a petrophysics intern in the North America Gas group at BP Americas where she developed new petrophysical interpretation workflows based on spectroscopy measurements. She is a member of SPE and SPWLA.

Permanent e-mail address: oajayi@utexas.edu

This dissertation was typed by Oyinkansola Ajayi